

# ИЗВЕСТИЯ ВЫСШИХ УЧЕБНЫХ ЗАВЕДЕНИЙ ЧЕРНАЯ МЕТАЛЛУРГИЯ

## IZVESTIYA. FERROUS METALLURGY

[fermet.misis.ru](http://fermet.misis.ru)

2023 Том 66 № 3  
Vol. No.

### МЕТАЛЛУРГИЧЕСКИЕ ТЕХНОЛОГИИ

Степень упрочнения и глубина наклепа при маятниковом  
поверхностном пластическом деформировании углеродистой стали

### МАТЕРИАЛОВЕДЕНИЕ

Влияние ускоренного охлаждения после поперечно-винтовой прокатки  
на формирование структуры и низкотемпературную вязкость разрушения  
низкоуглеродистой стали

### ИННОВАЦИИ В МЕТАЛЛУРГИЧЕСКОМ ПРОМЫШЛЕННОМ И ЛАБОРАТОРНОМ ОБОРУДОВАНИИ, ТЕХНОЛОГИЯХ И МАТЕРИАЛАХ

Метод изучения частотной стабильности материалов  
при испытаниях на многоцикловую усталость стали

# IZVESTIYA FERROUS METALLURGY

Scientific and Technical Journal  
Published since January 1958. Issued monthly

2023 Vol. 66 No. 3  
Том № 3

# ИЗВЕСТИЯ ВЫСШИХ УЧЕБНЫХ ЗАВЕДЕНИЙ ЧЕРНАЯ МЕТАЛЛУРГИЯ

Научно-технический журнал  
Издается с января 1958 г. ежемесячно

# IZVESTIYA FERROUS METALLURGY

www.fermet.misis.ru

ISSN 0368-0797 (Print) ISSN 2410-2091 (Online)

## Alternative title:

Izvestiya vuzov. Chernaya metallurgiya

## Founders:



## Editorial Board:

**German V. Ashikhmin**, Dr. Sci. (Eng.), Prof., JSC "Institute Tsvetmetobrabotka", Moscow

**Sailaubai O. Baisanov**, Dr. Sci. (Eng.), Prof., Abishev Chemical-Metallurgical Institute, Karaganda, Republic of Kazakhstan

**Vladimir D. Belov**, Dr. Sci. (Eng.), Prof., NUST MISIS, Moscow

**Anatolii A. Brodov**, Cand. Sci. (Econ.), Bardin Central Research Institute for Ferrous Metallurgy, Moscow

**Ilya V. Chumanov**, Dr. Sci. (Eng.), Prof., South Ural State Research University, Chelyabinsk

**Andrei N. Dmitriev**, Dr. Sci. (Eng.), Prof., Academician, RANS, A.M. Prokhorov Academy of Engineering Sciences, Institute of Metallurgy, Ural Branch of RAS, Ural Federal University, Yekaterinburg

**Aleksei V. Dub**, Dr. Sci. (Eng.), Prof., JSC "Science and Innovations", Moscow

**Mikhail I. Filonov**, Dr. Sci. (Eng.), Prof., NUST MISIS, Moscow

**Sergei M. Gorbatyuk**, Dr. Sci. (Eng.), Prof., NUST MISIS, Moscow

**Konstantin V. Grigorovich**, Academician of RAS, Dr. Sci. (Eng.), Baikov Institute of Metallurgy and Materials Science of RAS, Moscow

**Victor E. Gromov**, Dr. Sci. (Eng.), Prof., Siberian State Industrial University, Novokuznetsk

**Aleksei G. Kolmakov**, Dr. Sci. (Eng.), Corresponding Member of RAS, Baikov Institute of Metallurgy and Materials Science of RAS, Moscow

**Valerii M. Kolokol'tsev**, Dr. Sci. (Eng.), Prof., Magnitogorsk State Technical University, Magnitogorsk

**Mariya V. Kostina**, Dr. Sci. (Eng.), Baikov Institute of Metallurgy and Materials Science of RAS, Moscow

**Konstantin L. Kosyrev**, Dr. Sci. (Eng.), Prof., JSC "NPO "TSNIITMash", Moscow

**Yuliya A. Kurganova**, Dr. Sci. (Eng.), Prof., Bauman Moscow State Technical University, Moscow

**Linn Horst**, Linn High Therm GmbH, Hirschbach, Germany

**Vladimir I. Lysak**, Academician of RAS, Dr. Sci. (Eng.), Prof., Rector, Volgograd State Technical University, Volgograd

**Valerii P. Meshalkin**, Dr. Sci. (Eng.), Academician of RAS, Prof., D.I. Mendeleyev Russian Chemical-Technological University, Moscow

**Radik R. Mulyukov**, Dr. Sci. (Phys.-Chem.), Prof., Corresponding Member of RAS, Institute of Metals Superplasticity Problems of RAS, Ufa

**Sergei A. Nikulin**, Dr. Sci. (Eng.), Prof., Corresponding Member of RANS, NUST MISIS, Moscow

## Editor-in-Chief:

**Leopol'd I. Leont'ev**, Academician, Adviser of the Russian Academy of Sciences; Dr. Sci. (Eng.), Prof., National University of Science and Technology "MISIS"; Chief Researcher, Institute of Metallurgy UB RAS, Moscow

## Deputy Editor-in-Chief:

**Evgenii V. Protopopov**, Dr. Sci. (Eng.), Prof., Siberian State Industrial University, Novokuznetsk

## Editorial Addresses:

4 Leninskii Ave., Moscow 119049, Russian Federation  
National University of Science and Technology "MISIS"  
Tel.: +7 (495) 638-44-11

E-mail: fermet.misis@mail.ru, ferrous@isis.ru

42 Kirova Str., Novokuznetsk, Kemerovo Region – Kuzbass  
654007, Russian Federation  
Siberian State Industrial University  
Tel.: +7 (3843) 74-86-28  
E-mail: redjizvz@sibsiu.ru

**Asylbek Kh. Nurumgaliev**, Dr. Sci. (Eng.), Prof., Karaganda State Industrial University, Karaganda, Republic of Kazakhstan

**Oleg I. Ostrovski**, Dr. Sci. (Eng.), Prof., University of New South Wales, Sidney, Australia

**Loris Pietrelli**, Dr., Scientist, Italian National Agency for New Technologies, Energy and Sustainable Economic Development, Rome, Italy

**Igor' Yu. Pyshmintsev**, Dr. Sci. (Eng.), Russian Research Institute of the Pipe Industry, Chelyabinsk

**Andrei I. Rudskoi**, Academician of RAS, Dr. Sci. (Eng.), Prof., Rector, Peter the Great Saint-Petersburg Polytechnic University, Saint-Petersburg

**Oleg Yu. Sheshukov**, Dr. Sci. (Eng.), Prof., Ural Federal University, Yekaterinburg

**Laura M. Simonyan**, Dr. Sci. (Eng.), Prof., NUST MISIS, Moscow

**Robert F. Singer**, Dr. Sci. (Eng.), Prof., Friedrich-Alexander University, Germany

**Boris A. Sivak**, Cand. Sci. (Eng.), Prof., VNIIMTMASH Holding Company, Moscow

**Leonid A. Smirnov**, Dr. Sci. (Eng.), Prof., Academician of RAS, OJSC "Ural Institute of Metals", Yekaterinburg

**Sergei V. Solodov**, Cand. Sci. (Eng.), NUST MISIS, Moscow

**Speidel Marcus**, Dr. Natur. Sci., Prof., Swiss Academy of Materials, Switzerland

**Nikolai A. Spirin**, Dr. Sci. (Eng.), Prof., Ural Federal University, Yekaterinburg

**Tang Guoi**, Institute of Advanced Materials of Tsinghua University, Shenzhen, China

**Mikhail V. Temlyantsev**, Dr. Sci. (Eng.), Prof., Siberian State Industrial University, Novokuznetsk

**Ekaterina P. Volynkina**, Dr. Sci. (Eng.), Advisor, ALE "Kuzbass Association of Waste Processors", Novokuznetsk

**Aleksei B. Yur'ev**, Dr. Sci. (Eng.), Rector, Siberian State Industrial University, Novokuznetsk

**Vladimir S. Yusupov**, Dr. Sci. (Eng.), Prof., Baikov Institute of Metallurgy and Materials Science of RAS, Moscow

**Vladimir I. Zhuchkov**, Dr. Sci. (Eng.), Prof., Institute of Metallurgy, Ural Branch of RAS, Ural Federal University, Yekaterinburg

**Michael Zinigrad**, Dr. Sci. (Physical Chemistry), Prof., Rector, Ariel University, Israel

**Vladimir I. Zolotukhin**, Dr. Sci. (Eng.), Prof., Tula State University, Tula

*In accordance with paragraph 5 of the Rules for the formation of the Higher Attestation Commission list journal "Izvestiya. Ferrous metallurgy" is included in the list of leading peer-reviewed scientific journals, publication in which is taken into account in the defense of candidate and doctoral dissertations, as indexed in international data bases.*

**Indexed:** Scopus, Russian Science Citation Index (RSCI), Research Bible, Chemical Abstracts, OCLC and Google Scholar

Registered in Federal Service for Supervision in the Sphere of Mass Communications **PI number FS77-35456.**



Articles are available under Creative Commons Attribution 4.0 License.

# ИЗВЕСТИЯ ВЫСШИХ УЧЕБНЫХ ЗАВЕДЕНИЙ ЧЕРНАЯ МЕТАЛЛУРГИЯ

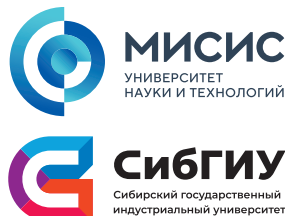
www.fermet.misis.ru

ISSN 0368-0797 (Print) ISSN 2410-2091 (Online)

## Варианты названия:

Известия вузов. Черная металлургия  
Izvestiya. Ferrous Metallurgy

## Учредители:



## Главный редактор:

**Леопольд Игоревич Леонтьев**, академик РАН, советник, Президиум РАН; д.т.н., профессор, Национальный исследовательский технологический университет «МИСИС»; главный научный сотрудник, Институт металлургии УрО РАН, г. Москва

## Заместитель главного редактора:

**Евгений Валентинович Протопопов**, д.т.н., профессор, Сибирский государственный индустриальный университет, г. Новокузнецк

## Адреса редакций:

Россия, 119049, Москва, Ленинский просп., д. 4, стр. 1  
Национальный исследовательский технологический университет «МИСИС»,  
Тел.: +7 (495) 638-44-11  
E-mail: fermet.misis@mail.ru, ferrous@mis.ru

Россия, 654007, Новокузнецк,  
Кемеровская обл. – Кузбасс, ул. Кирова, зд. 42  
Сибирский государственный индустриальный университет,  
Тел.: +7 (3843) 74-86-28  
E-mail: redjizvz@sibsiu.ru

## Редакционная коллегия:

**Г. В. Ашихмин**, д.т.н., профессор, ОАО «Ин-т Цветметобработка», г. Москва  
**С. О. Байсанов**, д.т.н., профессор, ХМИ им. Ж.Абишева, г. Караганда, Республика Казахстан  
**В. Д. Белов**, д.т.н., профессор, НИТУ МИСИС, г. Москва  
**А. А. Бродов**, к.экон.н., ФГУП «ЦНИИчермет им. И.П. Бардина», г. Москва  
**Е. П. Волынкина**, д.т.н., советник, ОЮЛ «Кузбасская Ассоциация переработчиков отходов», г. Новокузнецк  
**С. М. Горбатюк**, д.т.н., профессор, НИТУ МИСИС, г. Москва  
**К. В. Григорович**, академик РАН, д.т.н., ИМЕТ им. А.А. Байкова РАН, г. Москва  
**В. Е. Громов**, д.ф.-м.н., профессор, СибГИУ, г. Новокузнецк  
**А. Н. Дмитриев**, д.т.н., профессор, академик РАЕН, академик АИН РФ, г. Екатеринбург  
**А. В. Дуб**, д.т.н., профессор, ЗАО «Наука и инновации», г. Москва  
**В. И. Жучков**, д.т.н., профессор, ИМЕТ УрО РАН, г. Екатеринбург  
**Р. Ф. Зингер**, д.т.н., профессор, Институт Фридриха-Александра, Германия  
**М. Зиниград**, д.т.н., профессор, Институт Ариэля, Израиль  
**В. И. Золотухин**, д.т.н., профессор, ТулГУ, г. Тула  
**А. Г. Колмаков**, д.т.н., чл.-корр. РАН, ИМЕТ им. А.А. Байкова РАН, г. Москва  
**В. М. Колокольцев**, д.т.н., профессор, МГТУ им. Г.И. Носова, г. Магнитогорск  
**М. В. Костина**, д.т.н., ИМЕТ им. А.А. Байкова РАН, г. Москва  
**К. Л. Косырев**, д.т.н., профессор, АО «НПО «ЦНИИТМаш», г. Москва  
**Ю. А. Курганова**, д.т.н., профессор, МГТУ им. Н.Э. Баумана, г. Москва  
**Х. Линн**, ООО «Линн Хай Терм», Германия  
**В. И. Лысак**, академик РАН, д.т.н., профессор, ВолгГТУ, г. Волгоград

**В. П. Мешалкин**, академик РАН, д.т.н., профессор, РХТУ им. Д.И. Менделеева, г. Москва  
**Р. Р. Мулюков**, д.ф.-м.-н., профессор, чл.-корр. ФГБУН ИПСМ РАН, г. Уфа  
**С. А. Никулин**, д.т.н., профессор, чл.-корр. РАЕН, НИТУ МИСИС, г. Москва  
**А. Х. Нурумгалиев**, д.т.н., профессор, КГИУ, г. Караганда, Республика Казахстан  
**О. И. Островский**, д.т.н., профессор, Университет Нового Южного Уэльса, Сидней, Австралия  
**Л. Пиетрелли**, д.т.н., Итальянское национальное агентство по новым технологиям, энергетике и устойчивому экономическому развитию, Рим, Италия  
**И. Ю. Пышминцев**, д.т.н., РосНИТИ, г. Челябинск  
**А. И. Рудской**, академик РАН, д.т.н., профессор, СПбПУ Петра Великого, г. Санкт-Петербург  
**Б. А. Сивак**, к.т.н., профессор, АО АХК «ВНИИМЕТМАШ», г. Москва  
**Л. М. Симонян**, д.т.н., профессор, НИТУ МИСИС, г. Москва  
**Л. А. Смирнов**, академик РАН, д.т.н., профессор, ОАО «Уральский институт металлов», г. Екатеринбург  
**С. В. Солодов**, к.т.н., НИТУ МИСИС, г. Москва  
**Н. А. Спирин**, д.т.н., профессор, УрФУ, г. Екатеринбург  
**Г. Танг**, Институт перспективных материалов университета Циньхуа, г. Шеньжень, Китай  
**М. В. Темляницев**, д.т.н., профессор, СибГИУ, г. Новокузнецк  
**М. Р. Филонов**, д.т.н., профессор, НИТУ МИСИС, г. Москва  
**И. В. Чуманов**, д.т.н., профессор, ЮУрГУ, г. Челябинск  
**О. Ю. Шешуков**, д.т.н., профессор УрФУ, г. Екатеринбург  
**М. О. Шпайдель**, д.ест.н., профессор, Швейцарская академия материаловедения, Швейцария  
**А. Б. Юрьев**, д.т.н., ректор, СибГИУ, г. Новокузнецк  
**В. С. Юсупов**, д.т.н., профессор, ИМЕТ им. А.А. Байкова РАН, г. Москва

В соответствии п. 5 Правил формирования перечня ВАК журнал «Известия вузов. Черная металлургия» входит в перечень ведущих рецензируемых научных журналов и изданий, публикация в которых учитывается при защитах кандидатских и докторских диссертаций как индексируемый в МБД.

**Индексирование:** Scopus, Russian Science Citation Index (RSCI), Research Bible, Chemical Abstracts, OCLC и Google Scholar

Зарегистрирован Федеральной службой по надзору в сфере связи и массовых коммуникаций ПИ № ФС77-35456.



Статьи доступны под лицензией Creative Commons Attribution 4.0 License.



CONTENTS

СОДЕРЖАНИЕ

METALLURGICAL TECHNOLOGIES

- Zaides S.A., Ho Minh Quan. Degree and depth of hardening under pendulum surface plastic deformation of carbon steel ..... 272
- Shalaevskii D.L. Investigation of thermal mode of hot-rolling mill working rolls in order to improve the accuracy of calculating the thermal profile of their barrels' surface ..... 283
- Fastyskovskii A.R., Glukhov M.I., Vakhrolomeev V.A. Reserves for reducing energy consumption when rolling section bars on modern rolling mills ..... 290

MATERIAL SCIENCE

- Anosov M.S., Shatagin D.A., Chernigin M.A., Mordovina Yu.S., Anosova E.S. Structure formation of Np-30KhGSA alloy in wire and arc additive manufacturing ..... 294
- Burkov A.A., Kulik M.A. Electrospark deposition of metal-loceramic Fe-Al/HfC coating on steel 1035 ..... 302
- Gordienko A.I., Vlasov I.V., Pochivalov Yu.I. Effect of accelerated cooling after cross-helical rolling on formation of structure and low-temperature fracture toughness of low-carbon steel ..... 311
- Barannikova S.A., Li Yu.V. Patterns of localized deformation at pre-fracture stage in carbon steel – stainless steel bimetal ..... 320
- Porfir'ev M.A., Gromov V.E., Kryukov R.E. Evolution of structural-phase state and properties of hypereutectoid steel rails at long-term operation ..... 327

PHYSICO-CHEMICAL BASICS  
OF METALLURGICAL PROCESSES

- Bol'shov L.A., Korneichuk S.K., Bol'shova E.L. Wagner interaction coefficients of nitrogen with chromium and molybdenum in liquid nickel-based alloys ..... 330

Materials of the International  
Scientific Conference "PHYSICO-CHEMICAL  
FOUNDATIONS OF METALLURGICAL PROCESSES"  
named after Academician A.M. Samarin,  
Vyksa, October 10 – 14, 2022

- Khoroshilov A.D., Somov S.A., Katolikov V.D., Murysev V.A., Bocherikov R.E., Yarmukhametov M.R. Using calcium-containing injection wire filled with electrolytic calcium in steel ladle treatment ..... 337

МЕТАЛЛУРГИЧЕСКИЕ ТЕХНОЛОГИИ

- Зайдес С.А., Хо Минь Куан. Степень упрочнения и глубина наклепа при маятниковом поверхностном пластическом деформировании углеродистой стали .. 272
- Шалаевский Д.Л. Исследование теплового режима рабочих валков стана горячей прокатки с целью повышения точности расчета температур поверхностей их бочек ..... 283
- Фастыковский А.Р., Глухов М.И., Вахроломеев В.А. Резервы снижения энергопотребления при прокатке сортовых профилей на современных прокатных станах ..... 290

МАТЕРИАЛОВЕДЕНИЕ

- Аносов М.С., Шатагин Д.А., Чернигин М.А., Мordovina Ю.С., Аносова Е.С. Структурообразование сплава Нп-30ХГСА при аддитивном электродуговым выращивании ..... 294
- Бурков А.А., Кулик М.А. Электроискровое осаждение металлокерамического Fe-Al/HfC покрытия на сталь 35 ..... 302
- Гордиенко А.И., Власов И.В., Почивалов Ю.И. Влияние ускоренного охлаждения после поперечно-винтовой прокатки на формирование структуры и низкотемпературную вязкость разрушения низкоуглеродистой стали ..... 311
- Баранникова С.А., Ли Ю.В. Картины локализации деформации на стадии предразрушения в биметалле углеродистая сталь – нержавеющая сталь ..... 320
- Порфирьев М.А., Громов В.Е., Крюков Р.Е. Эволюция структурно-фазового состояния и свойств рельсов из заэвтектидной стали при длительной эксплуатации ..... 327

ФИЗИКО-ХИМИЧЕСКИЕ ОСНОВЫ  
МЕТАЛЛУРГИЧЕСКИХ ПРОЦЕССОВ

- Большов Л.А., Корнейчук С.К., Большова Э.Л. Вагнеровские параметры взаимодействия азота с хромом и молибденом в жидких сплавах на основе никеля ... 330

По материалам Международной научной  
конференции «ФИЗИКО-ХИМИЧЕСКИЕ  
ОСНОВЫ МЕТАЛЛУРГИЧЕСКИХ ПРОЦЕССОВ»  
им. академика А.М. Самарина,  
Выкса, 10 – 14 октября 2022 г.

- Хорошилов А.Д., Сомов С.А., Католиков В.Д., Мurysev В.А., Бочерилов Р.Е., Ярмахаметов М.Р. Опыт применения кальцийсодержащей инъекционной проволоки с наполнителем из электролитического кальция на этапе внепечной обработки стали ..... 337

**CONTENTS (*Continuation*)**

**СОДЕРЖАНИЕ (*продолжение*)**

Podusovskaya N.V., Komolova O.A., Grigorovich K.V., Pavlov A.V., Aksenova V.V., Rumyantsev B.A., Zheleznyi M.V. Lead and zinc selective extraction from EAF dust while heating in resistance furnace with flowing argon ..... 344

Подусовская Н.В., Комолова О.А., Григорович К.В., Павлов А.В., Аксенова В.В., Румянцев Б.А., Железный М.В. Изучение селективного извлечения свинца и цинка из пыли ДСП при нагреве в печах сопротивления в токе аргона ..... 344

**SUPERDUTY STEEL**

**СТАЛИ ОСОБОГО НАЗНАЧЕНИЯ**

Nikulin S.A., Rogachev S.O., Belov V.A., Shplis N.V., Komissarov A.A., Turilina V.Yu., Nikolaev Yu.A. Structure and properties of steels for manufacture of core catcher vessel of nuclear reactor ..... 356

Никулин С.А., Рогачев С.О., Белов В.А., Шплис Н.В., Комиссаров А.А., Турилина В.Ю., Николаев Ю.А. Структура и свойства сталей для конструкции устройства локализации расплава атомных реакторов ..... 356

**INNOVATIONS IN METALLURGICAL  
INDUSTRIAL AND LABORATORY  
EQUIPMENT, TECHNOLOGIES  
AND MATERIALS**

**ИННОВАЦИИ В МЕТАЛЛУРГИЧЕСКОМ  
ПРОМЫШЛЕННОМ И ЛАБОРАТОРНОМ  
ОБОРУДОВАНИИ, ТЕХНОЛОГИЯХ  
И МАТЕРИАЛАХ**

Myl'nikov V.V., Dmitriev E.A. A method for studying the frequency stability of materials during tests for multi-cycle fatigue of steel ..... 367

Мыльников В.В., Дмитриев Э.А. Метод изучения частотной стабильности материалов при испытаниях на многоцикловую усталость стали ..... 367

**INFORMATION TECHNOLOGIES  
AND AUTOMATIC CONTROL  
IN FERROUS METALLURGY**

**ИНФОРМАЦИОННЫЕ ТЕХНОЛОГИИ  
И АВТОМАТИЗАЦИЯ  
В ЧЕРНОЙ МЕТАЛЛУРГИИ**

Troitskii D.V., Gamin Yu.V., Galkin S.P., Budnikov A.S. Parametric model of a three-roll unit of radial-shear rolling mini-mill ..... 376

Троицкий Д.В., Гамин Ю.В., Галкин С.П., Будников А.С. Параметрическая модель трехвалкового узла мини-стана радиально-сдвиговой прокатки ..... 376



UDC 621.787.4

DOI 10.17073/0368-0797-2023-3-272-282



Original article

Оригинальная статья

## DEGREE AND DEPTH OF HARDENING UNDER PENDULUM SURFACE PLASTIC DEFORMATION OF CARBON STEEL

S. A. Zaides, Ho Minh Quan

Irkutsk National Research Technical University (83 Lermontova Str., Irkutsk 664074, Russian Federation)

✉ minhqvanho2605@gmail.com

**Abstract.** The article discusses influence of the main technological parameters of pendulum surface plastic deformation (SPD) on the mechanical properties of surface layer of cylindrical parts made of carbon steel. Using the hardness tester HBRV-187.5 and the microhardness tester HVM-G21, we determined hardness of the surface layer, microhardness and depth of the work-hardened layer of hardened parts. In addition, the results of calculating the hardening degree are presented, which is important information for evaluating the effectiveness of SPD method in terms of improving the metal mechanical properties. Experimental studies showed that after pendulum SPD (at different processing modes), hardness of the surface layer increases by 9 – 12 % compared to hardness of the original surface, and the microhardness increases by 1.5 – 1.7 times, which leads to a significant hardening of the cylindrical billet surface layer. Depth of the hardened layer varies in the range of 0.9 – 1.1 mm, while the hardening degree is 45 – 65 %. Using the software package Statistica 10.1, which allows solving optimization problems based on statistical analysis and building an optimization model, we determined the optimal modes of hardening by pendulum SPD. These modes simultaneously provide both the maximum depth of the hardened layer and the highest hardening degree of the surface layer. They are formed under the following processing modes: radial interference  $t = 0.15 - 0.2$  mm; longitudinal feed  $s = 0.07 - 0.11$  mm/rev; billet rotation frequency  $n_b = 160 - 200$  min<sup>-1</sup>; frequency of the working tool pendulum movement  $n_t = 110 - 130$  strokes/min; angular amplitude of the working tool  $\alpha = 35 - 40^\circ$ . According to the results of experimental data and numerical calculations, it was established that the average grain size in pendulum SPD decreases by 30 – 40 % compared to the initial size, and the dislocation density increases by 2.5 times.

**Keywords:** carbon steel, hardening degree, hardening depth, surface plastic deformation, hardness, microhardness, processing mode, surface layer, statistical calculation

**For citation:** Zaides S.A., Ho Minh Quan. Degree and depth of hardening under pendulum surface plastic deformation of carbon steel. *Izvestiya. Ferrous Metallurgy*. 2023;66(3):272–282. <https://doi.org/10.17073/0368-0797-2023-3-272-282>

## СТЕПЕНЬ УПРОЧНЕНИЯ И ГЛУБИНА НАКЛЕПА ПРИ МАЯТНИКОВОМ ПОВЕРХНОСТНОМ ПЛАСТИЧЕСКОМ ДЕФОРМИРОВАНИИ УГЛЕРОДИСТОЙ СТАЛИ

С. А. Зайдес, Хо Минь Куан

Иркутский национальный исследовательский технический университет (Россия, 664074, Иркутск, ул. Лермонтова, 83)

✉ minhqvanho2605@gmail.com

**Аннотация.** В статье рассматривается влияние основных технологических параметров маятникового поверхностного пластического деформирования (ППД) на механические свойства поверхностного слоя цилиндрических деталей из углеродистой стали. С использованием твердомера HBRV-187,5 и микротвердомера HVM-G21 определены твердость поверхностного слоя, микротвердость и глубина наклепанного слоя упрочненных деталей. Представлены результаты по расчету степени упрочнения, которые являются важной информацией для оценки эффективности способа ППД с точки зрения улучшения механических свойств металла. Экспериментальные исследования показали, что после маятникового ППД (при разных режимах обработки) твердость поверхностного слоя повышается на 9 – 12 % по сравнению с твердостью исходной поверхности, а микротвердость возрастает в 1,5 – 1,7 раз, что приводит к значительному упрочнению поверхностного слоя цилиндрической заготовки. Глубина упрочненного слоя варьируется в интервале 0,9 – 1,1 мм, при этом степень упрочнения составляет 45 – 65 %. С помощью программного пакета Statistica 10.1, позволяющего решать задачи оптимизации на основе статистического анализа, построена модель оптимизации и определены оптимальные режимы упрочнения при маятниковом ППД, обеспечивающие одновременно и максимальную глубину упрочненного слоя, и наибольшую степень упрочнения поверхностного слоя. Оптимальные режимы упрочнения формируются при следующих режимах обработки: радиальный натяг  $t = 0,15 \div 0,2$  мм; продольная подача  $s = 0,07 \div 0,11$  мм/об; частота вращения заготовки  $n_z = 160 \div 200$  мин<sup>-1</sup>; частота маятникового движения рабочего инструмента  $n_{ин} = 110 \div 130$  дв.ход/мин; угловая амплитуда рабочего инструмента  $\alpha = 35 \div 40^\circ$ . По результатам экспериментальных

данных и численных расчетов установлено, что средний размер зерен при маятниковом ППД уменьшается на 30 – 40 % по сравнению с исходным размером, а плотность дислокаций возрастает в 2,5 раза.

**Ключевые слова:** углеродистая сталь, степень упрочнения, глубина наклепа, поверхностное пластическое деформирование, твердость, микротвердость, режимы обработки, поверхностный слой, статистический расчет

**Для цитирования:** Зайдес С.А., Хо Минь Куан. Степень упрочнения и глубина наклепа при маятниковом поверхностном пластическом деформировании углеродистой стали. *Известия вузов. Черная металлургия*. 2023;66(3):272–282.

<https://doi.org/10.17073/0368-0797-2023-3-272-282>

## INTRODUCTION

The reliability of mechanical products largely depends on the quality of their components. This quality encompasses not only the dimensional accuracy and surface finish of the parts but also the mechanical properties of the surface layer exposed to various loads and thermal effects. Reliability can be enhanced through better materials, design, manufacturing, and operational practices. As indicated in references [1 – 3], improvements in the manufacturing process yield the most favorable outcomes.

In order to enhance the performance characteristics of the surface layer of machine parts, the technology of finishing-hardening treatment through surface plastic deformation (SPD) treatments are extensively employed [4 – 6].

Plastic deformation alters the structure of the metal surface layer. It significantly increases the number of dislocations, vacancies, and other defects in the lattice. Grains are fragmented and clustered, leading to changes in the size and shape of grains within the surface layer. Elastoplastic deformation resulting from machining alters the physical and chemical properties of the metal surface layer [7 – 9].

Plastic deformation induces hardness in the metal, with hardness diminishing linearly with depth. For example, Mitrofanova K. et al. [10] reported that parts made from grade 45 steel, after spinning with a variable-radius roller tool, possess a hardened layer approximately 1.1 mm deep. The microhardness within the region of plastic deformation remains relatively low, at approximately *HV*. Smoothing grade 45 steel components with a diamond tool leads to a tenfold increase in tangential stress. The depth of the hardened layer ranges from 0.05 to 0.40 mm (as the smoothing force escalates from 50 to 200 N). The dislocation density within the hardened surface layer signifies the extent of grain refinement, witnessing an increase of 40 to 70 % [11].

Metal hardening through surface plastic deformation enhances the parts' performance by increasing wear resistance, contact strength, and reliability of the press fits [12 – 14].

The key surface quality indicators are hardness and the depth of the hardened layer [15 – 17]. The extent of hardening depth correlates with roller pressure and can

influence various surface layer properties. Deeper hardening improves wear resistance, while in terms of fatigue strength, studies [2; 11; 15; 18] suggest that residual compressive stresses decrease as hardening depth increases, which might reduce durability gain.

Significant contributions to analytically estimating hardening depth through SPD have been made by researchers such as Braslavsky V.M., Drozd M.S., Kudryatsev I.V., Matlin M.M., Petushkov G.E. and Heifetz S.G. However, the existing relationships are only applicable to basic forming operations.

Researchers at Irkutsk National Research Technical University have refined surface plastic deformation processes by utilizing more intricate tool motions. The introduced a mechanical hardening process involving a swinging (pendulum) motion of the tool [19]. This process alternates between rolling and sliding actions. In our own work [20], we've assessed the stress increase within the deformation area achievable without raising the radial tool interference and residual stress.

This study aims to discern the impact of variables related to the swinging tool deformation on hardening depth and final hardness, while also evaluating the feasibility of the process.

## MATERIALS AND METHODS

Fig. 1 illustrates the pendulum tool treatment process. In this process, denoted as Pendulum Tool Plastic Deformation (PTPD), the outer surface 1 is rotated about its centerline. The tool is pressed onto the surface and moved with a radial interference  $t$ . The tool is advanced parallel to the part axis. The tool itself takes on the form of a sector 3 with a circular surface 2. This sector-shaped tool is firmly attached to a rocker that oscillates within the  $\alpha$  angle range.

For the experiments, we utilized a 1K62 lathe. The upper carriage was replaced with the sector-shaped tool drive (Fig. 2). The tool's specifications include a sector radius  $R_{\text{sec}} = 65$  mm; an edge fillet radius  $r_{\text{tool}} = 3$  mm; and it's made of R18 HSS material. The lubricant used was I-40A industrial oil, commonly employed in hardening processes.

We machined cylindrical samples with a 25 mm diameter, using medium-carbon steel grade 45 and measured

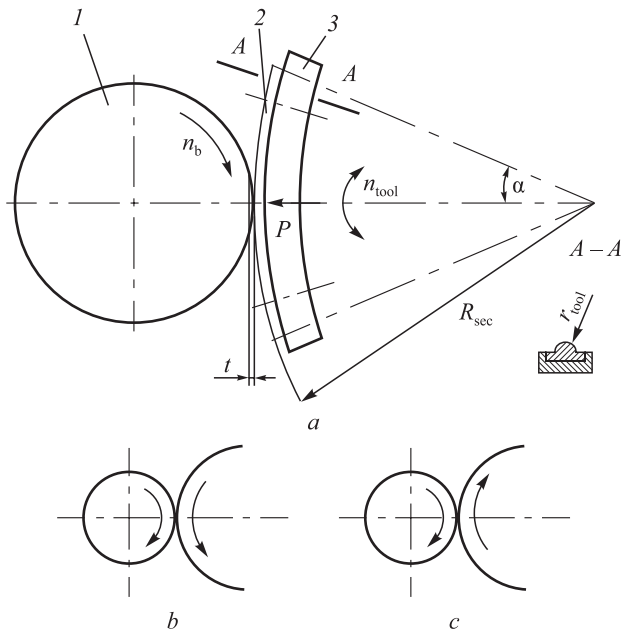


Fig. 1. Scheme of pendulum surface plastic deformation (a):  
1 – billet; 2 – deforming element; 3 – working sector of the tool;  
b – rolling scheme; c – sliding scheme in the contact zone

Рис. 1. Схема маятникового поверхностного пластического деформирования (а):

1 – заготовка; 2 – деформирующий элемент;  
3 – рабочий сектор инструмента;

b – схема качения; c – схема скольжения в зоне контакта

the resulting hardening depth and final hardness. These samples were designed with six equally spaced grooves to demarcate six segments of the same length and diameter. We tailored the process variables to treat conducting tests for five different sets of variables per sample. Each set of process variables was applied to three samples, and the curves illustrate the mean values.

In order to eliminate any runout, the sample was clamped within the three-jaw chuck of the lathe and additionally supported by the tailstock center. The cylindrical surface of the sample was machined to a 25 mm diameter (with parameters:  $s = 0.17$  mm/rev, rpm = 620,  $t = 0.5$  mm) and subsequently subjected to hardening via plastic deformation.

Before conducting the tests, we performed hardening on a pilot batch of samples to establish the baseline plastic deformation mode. The foundational process variables were determined as follows: radial interference  $t = 0.07$  mm; longitudinal feed  $s = 0.07$  mm/rev; billet rotation frequency  $n_b = 100$  rpm; tool angular amplitude  $\alpha = \pm 20^\circ$ ; and tool frequency  $n_{\text{tool}} = 55$  double strokes/min.

After the hardening process using the pendulum tool, the cylindrical samples were slice into thin sections utilizing a Discotom-10 metallographic cutting machine. These sections were then positioned within molds and filled with Aka-Resin Acrylic epoxy resin powder, subsequently compressed on a POLYLAB S50A automatic press. Following this, the sample sections underwent grinding and polishing on a Tegramin-25 automatic grinding and polishing machine, employing water cooling to achieve a mirror-like shine. In order to reveal the microstructure, the thin sections of the steel grade 45 samples were subjected to etching using a solution of 5 % nitric acid ( $\text{HNO}_3$ ) mixed with alcohol.

The Rockwell hardness of the surface layer was measured using an HBRV-187.5 hardness tester. For each segment of the sample, hardness was measured at six distinct points, situated on two circumferences. The hardness value for each segment was determined as the average of these six measurements.

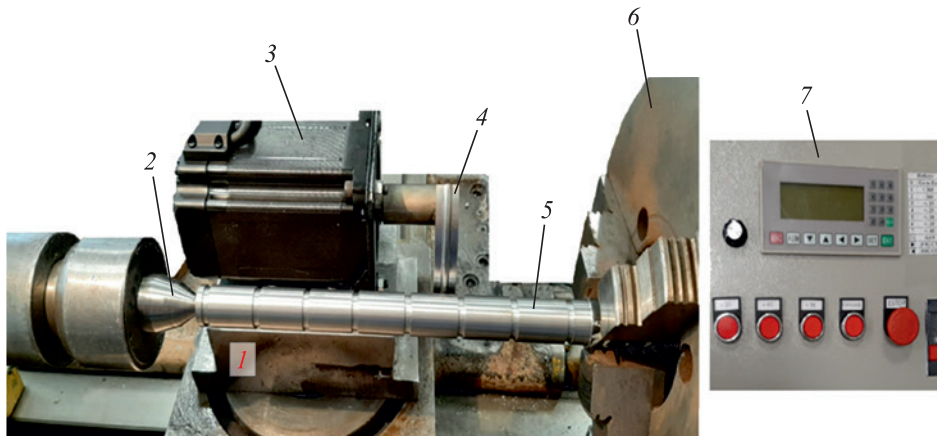


Fig. 2. General view of the device for pendulum surface plastic deformation (SPD) of cylindrical parts' outer surfaces:  
1 – base; 2 – rear center; 3 – motor-reducer; 4 – sectorial working tool with a rounding radius; 5 – processed sample;  
6 – three-jaw chuck; 7 – control panel for the working tool movement

Рис. 2. Общий вид устройства для маятникового ППД наружных поверхностей цилиндрических деталей:

1 – основание; 2 – задний центр; 3 – мотор-редуктор; 4 – секторальный рабочий инструмент с радиусом скругления;

5 – обрабатываемый образец; 6 – трехкулачковый патрон; 7 – панель управления параметрами движения рабочего инструмента



Microhardness measurements were conducted using an HMV-G21 microhardness meter, adhering to GOST R ISO 6507-1-2007 standards. The instrument employed a diamond Vickers pyramid penetrator to indent a flat section of the sample. The  $HV_{0.2}$  scale was employed, with a rated load of 1.961 N and a holding time of 5 s. Microhardness readings were taken at three points evenly spaced around the circumference. Mean hardness values were computed and microhardness vs. process variable curves were plotted for each process variable (as shown in the curves below).

The microstructure of the hardened samples was examined using a MET-2 metallographic microscope. A  $\times 500$  magnification of the metal's structure was observed on a computer screen utilizing the ToupView software. The grain size was estimated as the mean of the maximum and minimum grain dimensions. Obtaining consistent results with minimal error required 5 to 7 measurements, and at least 10 measurements were taken for each grain.

## EXPERIMENTAL RESULTS

Let us examine the essential physical and mechanical properties of the hardened surface, such as surface layer hardness, microhardness and hardening depth, and their correlations with the process variables within the pendulum tool treatment process.

**Surface Layer Hardness.** In Table 1, we present the surface hardness values following the pendulum tool treatment in relation to the key process variables.

Based on the available experimental outcomes, it is evident that the surface layer hardness experiences an average increase of 9 to 12 %. Notably, the process variables with substantial impact on hardness augmentation include radial interference, longitudinal feed, bil-

let rotation frequency rpm, pendulum frequency, and the amplitude of angular tool movement.

**Microhardness of the Hardened Layer.** Microhardness measurements provide insights into both absolute hardness and the depth of hardening. As depicted in Fig. 3, the distribution of microhardness across the cross-section of the hardened part (under the baseline process mode) is showcased. Notably, the initial microhardness of the sample after turning ranged between 210 to 215  $HV_{0.2}$ . Subsequent to the pendulum tool treatment, microhardness at a depth of 50  $\mu\text{m}$  beneath the surface surged to 320  $HV_{0.2}$ .

It should be noted that the microhardness decreases towards the centerline of the cylindrical part. At a certain depth, it becomes equal to the initial microhardness of the part metal. The increased depth of the microhardness layer is approximately 0.88 mm (Fig. 3). Fig. 3 illustrates the distribution of microhardness across the depth of the hardened layer.

Table 2 outlines the relationships between the key process variables, maximum microhardness and hardening depth.

Fig. 4 displays the curves of microhardness and hardening depth against the key process variables ( $s$ ,  $t$ ,  $n_b$ ,  $n_{\text{tool}}$ ) curves.

The study revealed that as the radial interference increases from 0.05 to 0.20 mm, the microhardness of the surface layer increases by approximately 12 %, whereas the increase in hardening depth is approximately 35 %. With an increase in longitudinal feed from 0.07 to 0.23 mm/rev, there is a decrease in microhardness by 3 to 5 % and a decrease in hardening depth by 7 to 8 %. Furthermore, elevating the billet rotation frequency RPM (from 80 to 200) and the frequency of the pendulum tool (from 40 to 120 double strokes per min) also results in

Table 1

### Hardness of the surface layer of cylindrical parts under pendulum SPD (initial hardness $HRB_{\text{in}} = 84.8$ )

Таблица 1. Твердость поверхностного слоя цилиндрических деталей при маятниковом ППД (исходная твердость  $HRB_{\text{исх}} = 84,8$ )

Longitudinal feed, mm/rev	0.07	0.11	0.13	0.17	0.23
Hardness, HRB	94.1	93.7	93.5	93.2	93.0
Radial interference, mm	0.05	0.07	0.10	0.15	0.20
Hardness, HRB	93.7	94.1	94.3	94.6	94.8
Billet rotation frequenc, rpm	80	100	125	160	200
Hardness, HRB	93.8	94.1	94.2	94.8	95.6
Pendulum tool frequency, double strokes/min	40	55	80	100	120
Hardness, HRB	93.6	94.1	94.3	94.6	94.7
Range of the angular tool movement, deg	$\pm 15$	$\pm 20$	$\pm 25$	$\pm 30$	$\pm 37$
Hardness, HRB	93.8	94.1	94.3	94.5	94.8

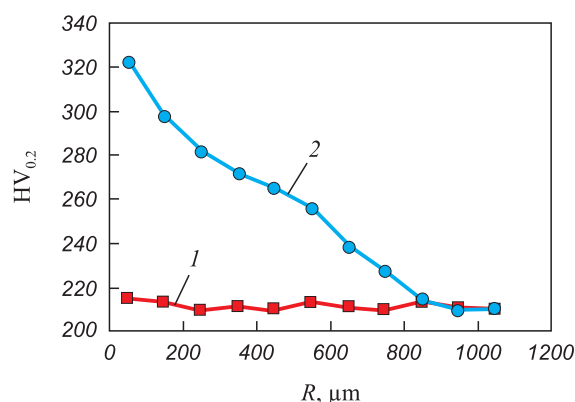


Fig. 3. Distribution of microhardness over the surface layer depth under pendulum SPD (in basic processing modes):  
1 – before pendulum SPD; 2 – after pendulum SPD

Рис. 3. Распределение микротвердости по глубине поверхностного слоя при маятниковом ППД (в базовых режимах обработки):  
1 – до МППД; 2 – после МППД

a microhardness increase of 10 to 14 % and an increase in hardening depth by 15 to 18 %. The variation in angular amplitude has minimal effect on microhardness and hardening depth.

The rate of hardening ( $CH$ ) in the surface layer after plastic deformation can be estimated using the following equation:

$$CH = \frac{HV_2 - HV_1}{HV_1} \cdot 100 \% \quad (1)$$

where  $HV_1$  represents the initial microhardness of the surface layer;  $HV_2$  is the microhardness after treatment.

Table 3 presents the estimated hardness values in relation to the key process variables.

The data suggest that under baseline conditions, the hardening rate is approximately 50 %. By adjusting the process variables, the hardening rate can be varied

within the range of 45 to 65 %. Fig. 5 illustrates the curves depicting the relationship between hardening rate and key process variables ( $s$ ,  $t$ ,  $n_b$ ,  $n_{tool}$ ).

To determine the optimal treatment mode for pendulum tool, with the aim of achieving the maximum depth of the hardened layer and hardening rate, we utilized the Statistica 10.1 software package. This software is extensively employed for statistical analysis within the manufacturing field. Utilizing Statistica 10.1, we derived single-factor equations (2) and (3) that correspond to the curves depicted in Figs. 4 and 5. The depth of the hardened layer and the hardening rate are the variables targeted for optimization:

$$h = \begin{cases} 7.3s^2 + 3s + 2.1; \\ 69t^2 + 17t + 7.8; \\ 0.05n_{tool}^2 + 1.6n_{tool} + 6.6; \\ 0.87n_b^2 + 0.4n_b + 0.9; \end{cases} \quad (2)$$

$$CH = \begin{cases} 9.3s^2 + 5s + 25; \\ 9.9t^2 + 1.7t + 5; \\ 0.7n_{tool}^2 + 0.5n_{tool} + 6; \\ 7.9n_b^2 + 0.3n_b + 4. \end{cases} \quad (3)$$

Figs. 6 and 7 illustrate the optimization results generated by Statistica 10.1.

Table 4 summarizes the statistical analysis and optimization undertaken for the depth of the hardened layer and the hardening rate. It was observed that certain sets of process variables yield the highest values for both the depth of the hardened layer (approximately 1.1 mm) and the hardening rate (about 65 %). This phenomenon arises from the clear relationship between the depth, hardening rate (HR), and each individual process vari-

Table 2

### Microhardness ( $HV_{0.2}$ ) on the surface and hardening depth ( $h$ ) under pendulum SPD

Таблица 2. Микротвердость ( $HV_{0.2}$ ) на поверхности и глубина наклепа ( $h$ ) при маятниковым ППД

Longitudinal feed, mm/rev	0.07	0.11	0.13	0.17	0.23
Microhardness/depth, mm	323/0.88	317/0.86	313/0.85	307/0.82	305/0.81
Radial interference, mm	0.05	0.07	0.10	0.15	0.20
Microhardness/depth, mm	306/0.81	323/0.88	333/0.94	339/1.01	348/1.10
Billet rotation frequency, rpm	80	100	125	160	200
Microhardness/depth, mm	320/0.86	323/0.88	325/0.89	328/0.91	330/0.93
Pendulum tool frequency, double strokes/min	40	55	80	100	120
Microhardness/depth, mm	317/0.85	323/0.88	327/0.91	334/0.94	339/0.98
Amplitude of the angular tool movement, deg	±15	±20	±25	±30	±37
Microhardness/depth, mm	316/0.87	323/0.88	325/0.89	327/0.90	329/0.91

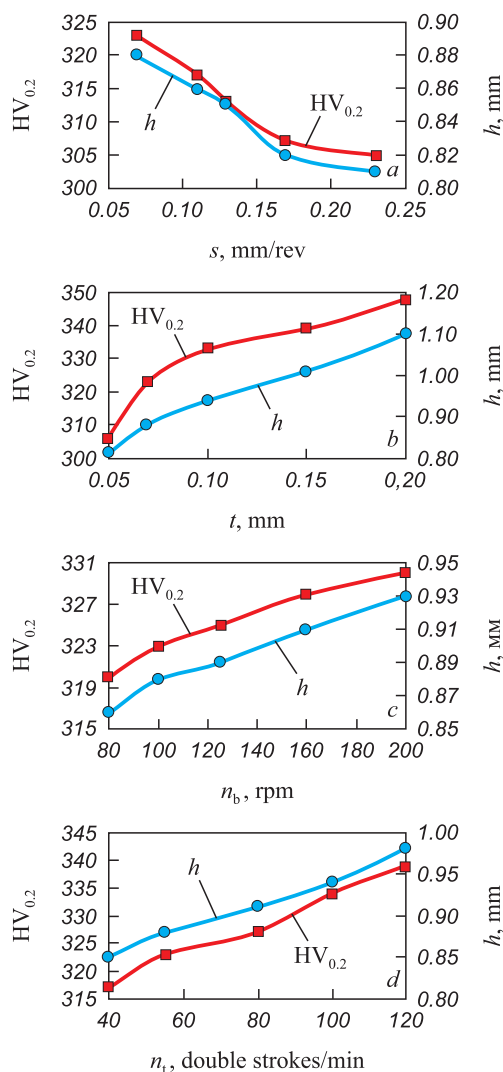


Fig. 4. Dependence of microhardness and hardening depth on the main parameters of pendulum SPD:

$$s (a); t (\bar{b}); n_b (\bar{c}); n_t (\bar{d})$$

Рис. 4. Зависимость микротвердости и глубины упрочнения от основных параметров маятниковой ППД:

$$s (a); t (\bar{b}); n_b (\bar{c}); n_t (\bar{d})$$

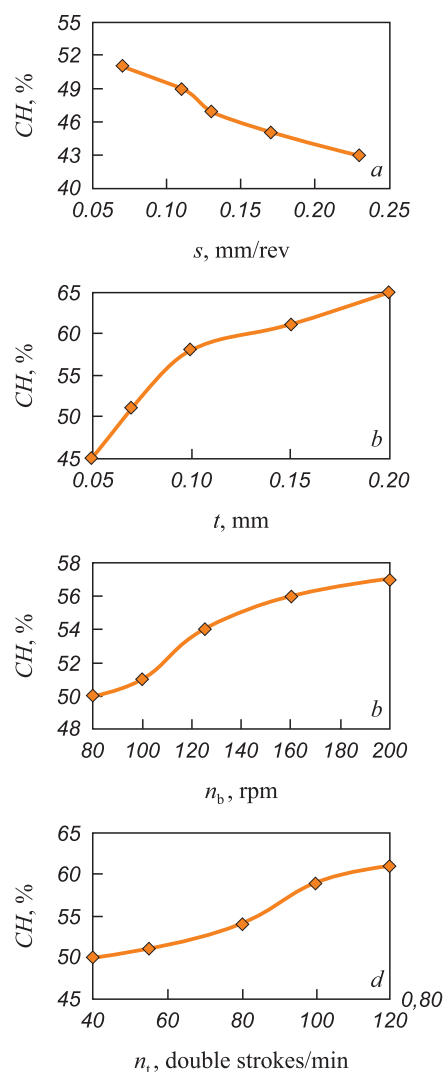


Fig. 5. Dependence of hardening degree on the main parameters of pendulum SPD:

$$s (a); t (\bar{b}); n_b (\bar{c}); n_t (\bar{d})$$

Рис. 5. Зависимость степени упрочнения от основных параметров маятниковой ППД:

$$s (a); t (\bar{b}); n_b (\bar{c}); n_t (\bar{d})$$

Table 3

### Influence of the main parameters of pendulum SPD on hardening degree

Таблица 3. Влияние основных параметров маятниковой ППД на степень упрочнения

Longitudinal feed, mm/rev	0.07	0.11	0.13	0.17	0.23
Hardening rate, %	51	49	47	45	43
Radial interference, mm	0.05	0.07	0.10	0.15	0.20
Hardening rate, %	45	51	58	61	65
Billet rotation frequency, rpm	80	100	125	160	200
Hardening rate, %	50	51	54	56	57
Pendulum tool frequency, double strokes/min	40	55	80	100	120
Hardening rate, %	50	51	54	59	61
Amplitude of the angular tool movement, deg	±15	±20	±25	±30	±37
Hardening rate, %	50	51	53	55	56

able. For instance, the parameters  $h$  and HR exhibit a direct proportionality with  $\alpha$ ,  $t$ ,  $n_b$ ,  $n_{\text{tool}}$  while displaying an inverse proportionality with the longitudinal feed  $s$ .

## RESULTS AND DISCUSSION

The phenomenon responsible for the strengthening of the metal is the impeding of dislocation motion. One method to hinder the motion of dislocations involves refining the grain structure. The accumulation of dislocations along grain boundaries obstructs the movement of dislocations, ultimately leading to the hardening of the metal [21 – 23]. Evaluating the effectiveness of the proposed mechanical hardening process can be achieved by assessing the improvements in the mechanical properties of the surface layer, primarily through changes in grain sizes and dislocation density (which is closely tied to the dimensions of the intergranular boundaries). Table 5 provides an analysis of the microstructure properties observed on the surface of the sample and at its centerline.

For components made from steel grade 45, the microstructure of the surface layer comprises dark spots indicating pearlite, and light spots representing ferrite.

The grain sizes within the core of the part that hasn't been subjected to plastic deformation show minimal variation, remaining in the range of approximately 50 to 70  $\mu\text{m}$ . Both the radial and axial cross-sections of the grains exhibit nearly identical features. Conversely, on the surface, the grain structure appears finer due to direct exposure to grinding and the effects of mechanical hardening. In this region, the microstructure primarily consists of grains compressed in the radial direction (the main deformation direction) and elongated along the axial direction (aligned with the direction of plastic flow). The concentration of pearlite grains is heightened, evident from the greater microhardness observed in the surface layer (as outlined in Table 5). The average widths of the grains measure 25  $\mu\text{m}$  for ferrite and 30  $\mu\text{m}$  for pearlite, while the average lengths are 35  $\mu\text{m}$  for ferrite and 40  $\mu\text{m}$  for pearlite.

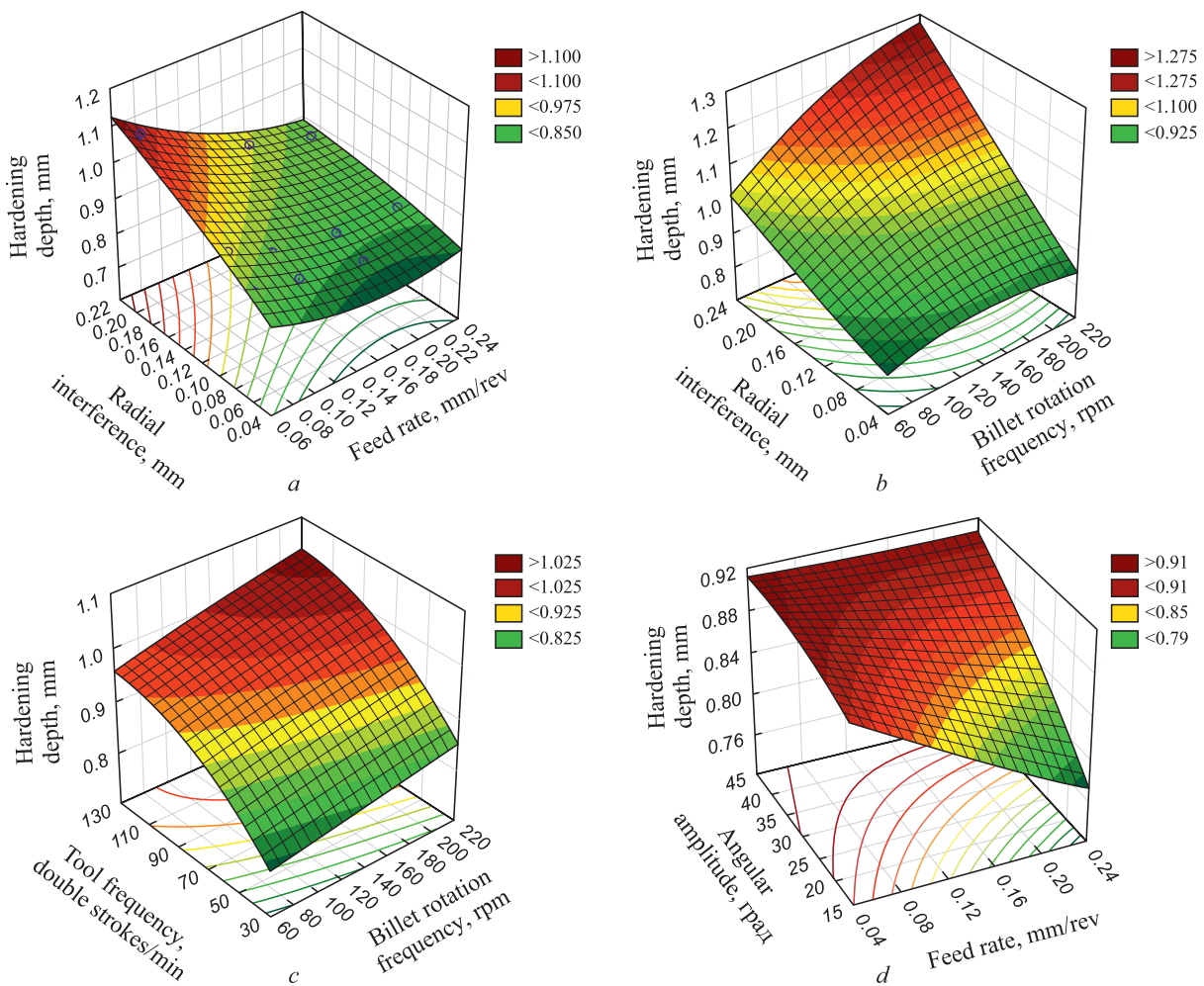


Fig. 6. Depth response surfaces of the hardened layer of cylindrical surfaces under pendulum SPD depending on:  $t$  and  $s$  (a);  $t$  and  $n_b$  (b);  $n_t$  and  $n_b$  (c);  $\alpha$  and  $s$  (d)

Рис. 6. Поверхности отклика глубины упрочненного слоя цилиндрической поверхности при маятниковом ППД в зависимости от:  $t$  и  $s$  (a);  $t$  и  $n_b$  (б);  $n_{\text{ин}}$  и  $n_b$  (в);  $\alpha$  и  $s$  (г)



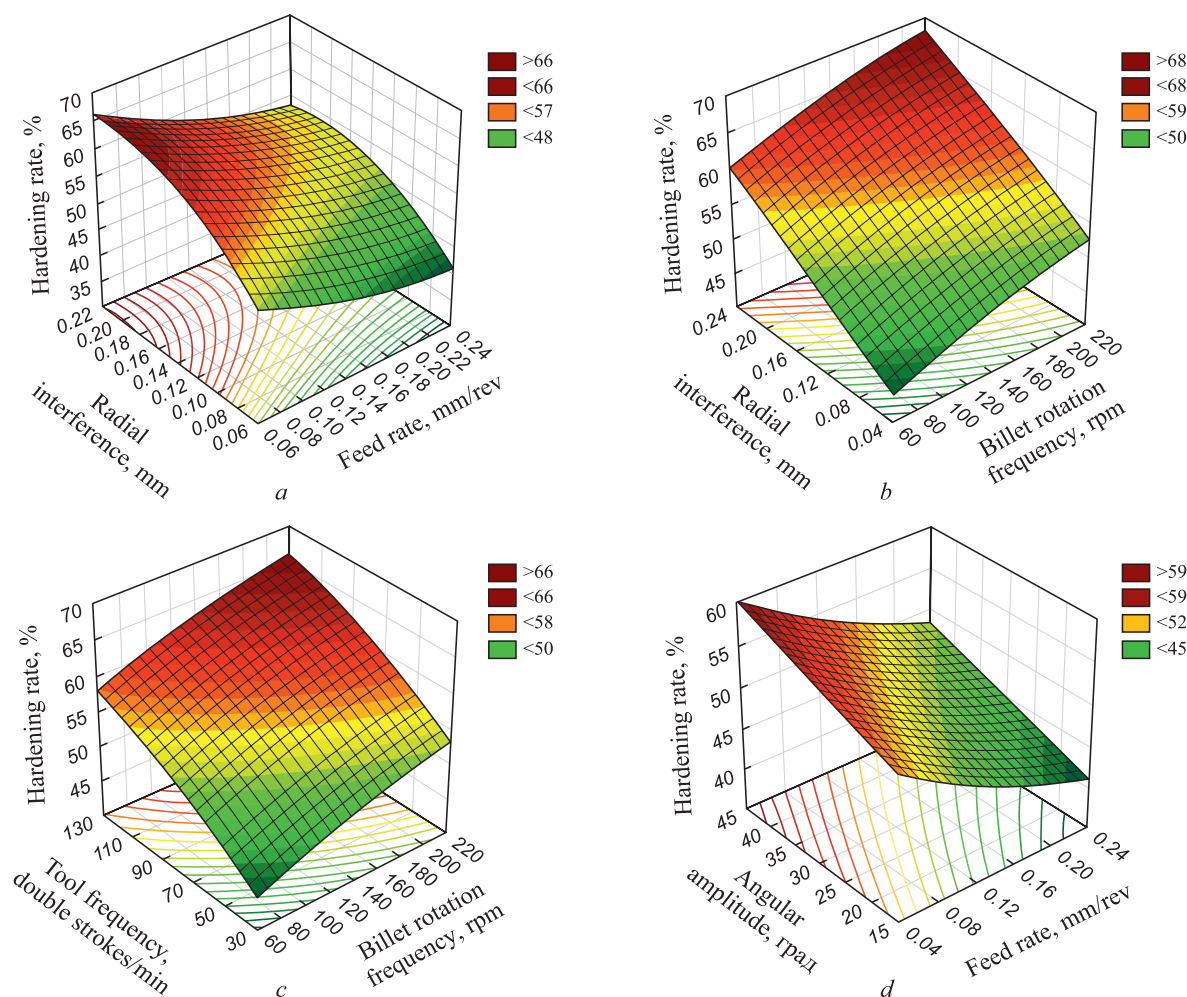


Fig. 7. Response surfaces of hardening degree of cylindrical surface under pendulum SPD depending on:  $t$  and  $s$  (a);  $t$  and  $n_b$  (b);  $n_t$  and  $n_b$  (c);  $\alpha$  and  $s$  (d)

Рис. 7. Поверхности отклика степени упрочнения цилиндрической поверхности при маятниковом ППД в зависимости от:  $t$  и  $s$  (a);  $t$  и  $n_b$  (б);  $n_{\text{ин}}$  и  $n_b$  (в);  $\alpha$  и  $s$  (г)

It is evident that the treatment leads to a reduction in grain sizes within the hardened layers by approximately 30 to 40 %. Additionally, the notable increase in the concentration of fine, hard pearlite grains contributes to the heightened microhardness of the surface layer.

Theoretical investigations [21; 22] highlight that the hardening process of the surface layer can be compre-

hended through the lens of dislocation theory. According to this theory, metal hardening arises from the development of denser dislocation substructures and enhanced shear resistance within the lattice. Drankin B. et al. [22] substantiated that the creation of low-angle grain boundaries, coupled with an augmented dislocation density, curtails grain movement and reinforces the metal. This implies

Table 4

**Parameters and modes of pendulum SPD providing an increase in physical and mechanical properties of the surface layer**

Таблица 4. Параметры и режимы маятникового ППД, обеспечивающие повышение механических свойств поверхностного слоя

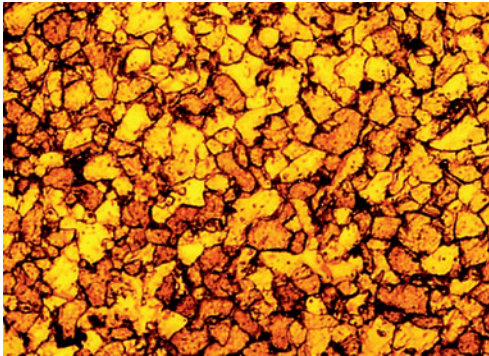
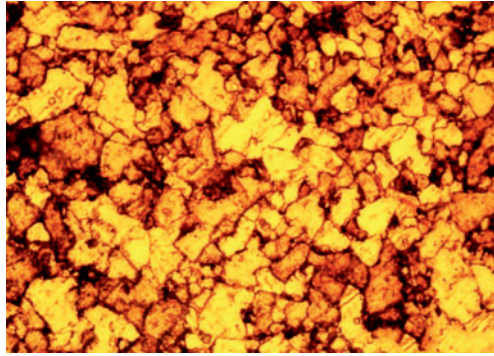
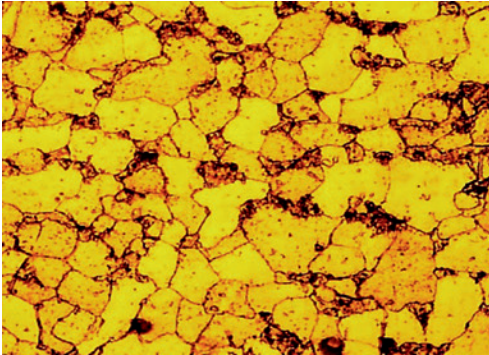
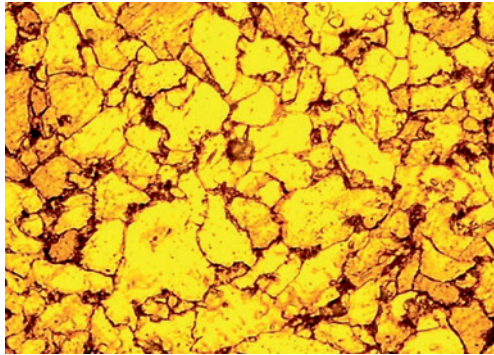
Layer properties	Process variables					Optimized variables	
	$t$ , mm	$s$ , mm/rev	$\alpha$ , deg	$n_{\text{tool}}$ , double strokes/min	$n_b$ , rpm	$h$ , mm	$CH$ , %
$h$ , mm	0.15 – 0.20	0.07 – 0.11	35 – 40	120 – 130	160 – 200	1.0 – 1.1	50 – 60
$CH$ , %	0.15 – 0.20	0.07 – 0.11	35 – 40	110 – 130	180 – 200	1.0 – 1.1	61 – 65



Table 5

Microstructure of the hardened layer (steel 45) after pendulum SPD

Таблица 5. Микроструктура упрочненного слоя (сталь 45) после маятникового ППД

Section	Microstructure of a hardened sample, 45 steel grade (×500)	
	Cross section	Longitudinal section
Surface area		
Core area		

that a higher dislocation density corresponds to increased hardness of the metal. Sulima A. et al. [23] introduced the equation for dislocation density:

$$\rho = \left( \frac{0.27(HV_2 - HV_1)}{amGb} \right)^2 + \rho_0, \quad (4)$$

where  $HV_1$  represents the initial surface microhardness;  $HV_2$  is the surface microhardness post plastic deformation;  $\rho_0 = 10^8 \text{ cm}^{-2}$  is the initial dislocation density for carbon steels. Works [22; 23] present an inter-dislocation interaction parameter for ferritic steel as  $\alpha = 0.32$ . G. Taylor estimated parameters for diverse polycrystal lattice types. They are: for BCC metal lattice  $m = 2.75$ ; for steel grade 45 the shear modulus  $G = 78,000 \text{ MPa}$ ; the Burgers vector  $b = 3 \cdot 10^{-8} \text{ cm}$ .

With the given values, we calculated the dislocation density 50  $\mu\text{m}$  beneath the surface following pendulum tool treatment in the baseline mode, resulting in a value of  $2.28 \cdot 10^8 \text{ cm}^{-2}$ .

This indicates that the pendulum tool treatment escalates dislocation density by a factor of 2.2 to 2.5. We compared these outcomes with values reported in [11; 12]. These studies indicate a 26 % increase in dislocation den-

sity after treatment with a standard roller and a 150 % increase after treatment with a two-radius roller.

In conclusion, it is imperative to note that the proposed pendulum tool process integrates both rolling and sliding, a unique characteristic not present in other existing hardening methods. Such a combination effectively reduces surface micro-roughness and enhances the mechanical properties of the surface layer.

## CONCLUSION

We have introduced a novel mechanical hardening process and developed the corresponding tooling. This process contributes to a notable increase in the hardness of the surface layer, achieving enhancements of approximately 9 to 12 % over the initial hardness.

Particularly significant is the microhardness elevation, ranging from 50 to 70 %. The resultant hardening depth lies within the range of 0.9 to 1.1 mm, and the corresponding hardening rate varies between 45 and 65 %.

By identifying optimal values for the process variables ( $n_b = 160 \div 200 \text{ min}^{-1}$ ;  $n_{\text{tool}} = 110 \div 130$  double strokes/min;  $t = 0.15 \div 0.2 \text{ mm}$ ;  $s = 0.07 \div 0.11 \text{ mm/rev}$ ;  $\alpha = 35 \div 40^\circ$ ), we have successfully determined the set-

tings that yield the maximum depth of the hardened layer and hardening rate.

We have elucidated the rationale behind the improvement in surface layer properties, supported by both experimental findings and simulations. The research has revealed that, post-treatment, the average grain size experiences a reduction of 30 to 40 %, while the dislocation density undergoes a substantial increase of 150 %.

## REFERENCES / СПИСОК ЛИТЕРАТУРЫ

- Laouar L., Hamadache H., Saad S., Bouchelaghem A., Mekhilef S. Mechanical surface treatment of steel – Optimization parameters of regime. *Physics Procedia*. 2009;2(3): 1213–1221. <https://doi.org/10.1016/j.phpro.2009.11.084>
- Gorbunov A.V., Gorbunov V.F. Rationale for non-rigid shaft hardening depth under surface plastic deformation by centrifugal roller. *Vestnik IrGTU*. 2012;9(68):29–33. (In Russ.). Горбунов А.В., Горбунов В.Ф. Обоснование глубины упрочнения нежестких валов при поверхностной пластической деформации центробежным обкатником. *Вестник ИрГТУ*. 2012;9(68):29–33.
- Zhang Z. Theoretical prediction of cross-sectional deformation of circular thin-walled tube in large elastic–plastic deformation stage under lateral compression. *Thin-Walled Structures*. 2022;180:109957. <https://doi.org/10.1016/j.tws.2022.109957>
- Biswas S., Alavi S.H., Sedai B., Blum F.D., Harimkar S.P. Effect of ultrasonic vibration-assisted laser surface melting and texturing of Ti-6Al-4V ELI alloy on surface properties. *Journal of Materials Science & Technology*. 2019;35(2): 295–302. <https://doi.org/10.1016/j.jmst.2018.09.057>
- Li Y.B., Zhang Q.X., Qi L., David S.A. Improving austenitic stainless steel resistance spot weld quality using external magnetic field. *Science and Technology of Welding and Joining*. 2018;23(7):619–627. <https://doi.org/10.1080/13621718.2018.1443997>
- DiGiovanni C., Biro E., Zhou N.Y. Impact of liquid metal embrittlement cracks on resistance spot weld static strength. *Science and Technology of Welding and Joining*. 2019;24(3):218–224. <https://doi.org/10.1080/13621718.2018.1518363>
- Grzesik W., Rech J., Żak K. High-precision finishing hard steel surfaces using cutting, abrasive and burnishing operations. *Procedia Manufacturing*. 2015;1:619–627. <https://doi.org/10.1016/j.promfg.2015.09.048>
- Chen X.S., Li Q., Fei S.M. Constrained model predictive control in ball mill grinding process. *Powder Technology*. 2008;186(1):31–39. <https://doi.org/10.1016/j.powtec.2007.10.026>
- Roux J.D.L., Craig I.K. Requirements for estimating the volume of rocks and balls in a grinding mill. *IFAC-PapersOnLine*. 2017;50(1):1169–1174. <https://doi.org/10.1016/j.ifacol.2017.08.403>
- Mitrofanova K.S. Investigating the quality of steel 45 surface layer after surface plastic deformation with a mill-radius roller. In: *Proceedings of the Conf. "Innovations in Mechanical Engineering"*. 2019:639–787. (In Russ.). Митрофанова К.С. Исследование качества поверхностного слоя стали 45 после поверхностного пластического деформирования мультирадиусным роликом. *Сборник трудов конференции «Инновации в машиностроении»*. 2019:639–787.
- Zaides S.A. *Handbook on Surface Plastic Deformation Processes*. Irkutsk: IRNITU; 2021:504. (In Russ.). Зайдес С.А. *Справочник по процессам поверхностного пластического деформирования*. Иркутск: Изд-во ИРНТУ; 2021:504.
- Cuong N.K. *Improving the quality of low-rigid shafts by surface plastic deformation in cramped conditions: Cand. Tech. Sci. Diss.* Irkutsk; 2018:149. (In Russ.). Кьонг Н.К. *Повышение качества мало жестких валов поверхностным пластическим деформированием в стесненных условиях: Дис. ...канд. техн. наук*. Иркутск, 2018:149.
- Yaman N., Sunay N., Kaya M., Kaynak Y. Enhancing surface integrity of additively manufactured Inconel 718 by roller burnishing process. *Procedia CIRP*. 2022;108:681–686. <https://doi.org/10.1016/j.procir.2022.03.106>
- Frihat M.H., Al Quran F.M.F., Al-Odat M.Q. Experimental investigation of the influence of burnishing parameters on surface roughness and hardness of brass alloy. *Material Science & Engineering*. 2015;5(1):1–4. <https://doi.org/10.4172/2169-0022.1000216>
- Ezhelev A.V., Bobrovskii I.N., Luk'yanov A.A. Analysis of processing ways by superficial and plastic deformation. *Fundamental'nye issledovaniya*. 2012;(6–3):642–646. (In Russ.). Ежелев А.В., Бобровский И.Н., Лукьянов А.А. Анализ способов обработки поверхностно-пластическим деформированием. *Фундаментальные исследования*. 2012;(6–3): 642–646.
- Kotenok V.I., Podobedov S.I. Energy-efficient design of rolls for ball-rolling mills. *Metallurgist*. 2001;45(9–10):363–367.
- Tomczak J., Pater Z., Bulzak T. The flat wedge rolling mill for forming balls from heads of scrap railway rails. *Archives of Metallurgy and Materials*. 2018;63(1):5–12. <https://doi.org/10.24425/118901>
- Chumachenko E.N., Aksenov S.A., Logashina I.V. Mathematical modeling and energy conservation for rolling in passes. *Metallurgist*. 2010;(8):498–503.
- Zaides S.A., Ho Minh Quan. *Method for surface-plastic deformation of outer surface of a part in the form of body of revolution*. Paten RF no. 2757643. Publ. 19.10.2021. (In Russ.). Пат. 2757643 RU. *Способ поверхностно-пластического деформирования наружной поверхности детали в виде тела вращения* / Зайдес С.А., Хо Минь Куан; заявл. 04.02.2021; опубл. 19.10.2021.
- Zaides S.A., Kho Min' Kuan. Pendulum surface plastic deformation of cylindrical blanks. *Izvestiya. Ferrous Metallurgy*. 2022;65(5):344–353. (In Russ.). <https://doi.org/10.17073/0368-0797-2022-5-344-353>

Зайдес С.А., Хо Минь Куан. Маятниковое поверхностное пластическое деформирование цилиндрических заготовок. *Известия вузов. Черная металлургия*. 2022;65(5):344–353. <https://doi.org/10.17073/0368-0797-2022-5-344-353>

21. Prikhod'ko V.M., Petrova L.G., Chudina O.V. *Metallophysical Foundations for Hardening Technologies Development*. Moscow: Mashinostroyeniye; 2003:384. (In Russ.).  
Приходько В.М., Петрова Л.Г., Чудина О.В. *Металлофизические основы разработки упрочняющих технологий*. Москва: Машиностроение; 2003:384.
22. Drapkin B.M., Kononenko V.K., Bez'yazychnyi V.F. *Properties of Alloys in Extreme State*. Moscow: Mashinostroyeniye; 2004:256. (In Russ.).

Драпкин Б.М., Кононенко В.К., Безъязычный В.Ф. *Свойства сплавов в экстремальном состоянии*. Москва: Машиностроение; 2004:256.

23. Sulima A.M., Shulov V.A., Yagodkin Yu.D. *Surface Layer and Operational Properties of Machine Parts*. Moscow: Mashinostroyeniye; 1988:146–149. (In Russ.).

Сулима А.М., Шулов В.А., Ягодкин Ю.Д. *Поверхностный слой и эксплуатационные свойства деталей машин*. Москва: Машиностроение; 1988:146–149.

## Information about the Authors

## Сведения об авторах

**Семен Азикович Зайдес**, д.т.н., профессор кафедры материаловедения, сварочных и аддитивных технологий, Иркутский национальный исследовательский технический университет

**E-mail:** zsa@istu.edu

**Хо Минь Куан**, аспирант кафедры материаловедения, сварочных и аддитивных технологий, Иркутский национальный исследовательский технический университет

**ORCID:** 0000-0002-0488-0290

**E-mail:** minhquanho2605@gmail.com

**Semen A. Zaides**, Dr. Sci. (Eng.), Prof. of the Chair of Materials Science, Welding and Additive Technologies, Irkutsk National Research Technical University

**E-mail:** zsa@istu.edu

**Ho Minh Quan**, Postgraduate of the Chair of Materials Science, Welding and Additive Technologies, Irkutsk National Research Technical University

**ORCID:** 0000-0002-0488-0290

**E-mail:** minhquanho2605@gmail.com

Received 27.01.2023

Revised 21.03.2023

Accepted 11.04.2023

Поступила в редакцию 27.01.2023

После доработки 21.03.2023

Принята к публикации 11.04.2023





UDC 621.771.01

DOI 10.17073/0368-0797-2023-3-283-289



Original article

Оригинальная статья

## INVESTIGATION OF THERMAL MODE OF HOT-ROLLING MILL WORKING ROLLS IN ORDER TO IMPROVE THE ACCURACY OF CALCULATING THE THERMAL PROFILE OF THEIR BARRELS' SURFACE

D. L. Shalaevskii

Cherepovets State University (5 Lunacharskogo Ave., Cherepovets, Vologda Region 162600, Russian Federation)

shal-dmitrij@yandex.ru

**Abstract.** Thermal mode of the working roll barrel in a hot-rolling mill is a significant technological factor that affects the steel strip quality, its cross section, and durability of working rolls. A reliable calculation of the temperature mode parameters makes it possible to determine the thermal profile shape and the best profiling of the roll barrel surface, as well as to reduce defects in steel strip flatness. The most common is the balance model of roll thermal mode. Its accuracy is largely determined by thermophysical constants, in particular, the heat transfer coefficients of the rolls: contact – with the strip and convective – with cooling water. There are various data on the values and methods for calculating these coefficients, but most of them do not take into account the presence of pauses in rolling rhythm of the finishing group of stands, the duration of which is significant. Failure to take this factor into account entails significant errors in calculations of the thermal mode. A passive experiment was carried out, during which surface temperatures of the working rolls' barrels were measured using a thermocouple at several points along their length immediately after they fell out. Also, the parameters of steel strip rolling before roll change were determined: rolling rhythm coefficients, strip reduction in stands, water consumption for cooling rolls and some others. As a result, an empirical equation was obtained for calculating the contact heat transfer coefficient, taking into account the main technological factors. The use of refined coefficients for calculating the temperatures of the roll barrel significantly increased the accuracy of predicting the thermal mode, in particular, the thermal profile of the working roll, based on values of the rolling parameters.

**Keywords:** CCM, thermal mode, continuous hot rolling, steel strip, flatness, cross section shape, contact heat transfer coefficient, working roll barrel, surface temperature, thermal profile, balance equations

**For citation:** Shalaevskii D.L. Investigation of thermal mode of hot-rolling mill working rolls in order to improve the accuracy of calculating the thermal profile of their barrels' surface. *Izvestiya. Ferrous Metallurgy*. 2023;66(3):283–289.  
<https://doi.org/10.17073/0368-0797-2023-3-283-289>

## ИССЛЕДОВАНИЕ ТЕПЛООВОГО РЕЖИМА РАБОЧИХ ВАЛКОВ СТАНА ГОРЯЧЕЙ ПРОКАТКИ С ЦЕЛЮ ПОВЫШЕНИЯ ТОЧНОСТИ РАСЧЕТА ТЕМПЕРАТУР ПОВЕРХНОСТЕЙ ИХ БОЧЕК

Д. Л. Шалаевский

Череповецкий государственный университет (Россия, 162600, Вологодская обл., Череповец, пр. Луначарского, 5)

shal-dmitrij@yandex.ru

**Аннотация.** Тепловой режим бочки рабочего вала непрерывного стана горячей прокатки – значимый фактор технологии, который влияет на качество формы стальной полосы, ее поперечное сечение, стойкость рабочих валков. Достоверный расчет параметров температурного режима позволяет определить форму теплового профиля и наилучшую профилировку поверхности бочки вала, добиться уменьшения дефектов планшестности готового проката. Наиболее распространенной является балансная модель теплового режима вала, точность которой в значительной степени определяется теплофизическими постоянными, в частности коэффициентами теплообмена валков: контактного – с полосой и конвективного – с охлаждающей водой. Имеются различные сведения о значениях и методах расчета этих коэффициентов, но большинство из них не учитывают наличие пауз в ритме прокатки чистовой группы клетей, длительность которых значительна. Отсутствие учета этого фактора влечет за собой существенные ошибки в расчетах теплового режима бочки вала. Проведен пассивный эксперимент, в ходе которого с помощью термопары измерены температуры поверхностей бочек рабочих валков в нескольких точках по их длине сразу же после вывалки. Также определены параметры прокатки стальных полос перед перевалкой: коэффициенты ритма прокатки, обжатия полосы в клетях, расходы воды на охлаждение валков и некоторые другие параметры. В результате получено эмпирическое уравнение для расчета коэффициента контактного теплообмена, учитывающее основные факторы технологии, в том числе длительность пауз в ритме прокатки. Использование уточненных коэффициентов для расчета температур

бочки валка значительно повысило точность прогнозирования теплового режима, в частности теплового профиля рабочего валка, по значениям параметров прокатки.

**Ключевые слова:** непрерывный стан, тепловой режим, горячая прокатка, стальные полосы, плоскостность, форма поперечного профиля, коэффициент контактного теплообмена, бочка рабочего валка, температура поверхности, тепловой профиль, уравнения теплового баланса

**Для цитирования:** Шалаевский Д.Л. Исследование теплового режима рабочих валков стана горячей прокатки с целью повышения точности расчета температур поверхностей их бочек. *Известия вузов. Черная металлургия*. 2023;66(3):284–289.

<https://doi.org/10.17073/0368-0797-2023-3-283-289>

## INTRODUCTION

Numerous studies have been conducted on the temperature profiles of roll body in continuous rolling mills. Garber E. et al. [1] proposed a thermal analysis approach for broad-strip hot rolling mill rolls. Their method incorporated heat balance equations for work rolls (WR) and backup rolls (BR) considering heat exchange between the rolls, strip, cooling water, and the environment. The accuracy of their simulation heavily relied on empirically estimated heat transfer coefficients. However, a disadvantage of their model was the insufficient consideration of rolling downtime. To address this, the fraction of operating time during the lead time was multiplied by the roll body temperature, leading to significant errors during extended downtime. Despite this limitation, the simulation model was relatively simple, valid to a certain extent, and had potential for improvement.

Bel'skii S. et al. [2] employed a simplified model to estimate the temperature profile of hot-rolling work rolls. They obtained an exact solution for the thermal conductivity equation and measured the temperature distribution along the roll body after rolling.

Antonyuk V. et al. [3] introduced a new design for cooling system headers aimed at reducing the work roll body temperature to an acceptable level. However, their study lacked any theoretical analysis of the proposed upgrade, and it remained unclear whether the design could be applied to cooling systems of other rolling mills.

Garber E. et al. [4] demonstrated the significant impact the roll body temperature profile on the accuracy of strip cross-section shape [4]. The model presented in [3] could be applied with adjustments specific to the rolling mill and actual downtime.

Several studies have focused on temperature profiles in broad-strip rolling mill.

Hamraoui M. et al. [5] simulated the strip temperature distribution in the steady-state mode, representing work rolls as heated hollow cylinders in contact with the strip and cooled by convection on the outer and axial hole surface. They proposed a model linking roll temperature to its rotation speed and heat exchange with the environment.

Johnson R. et al. [6] investigated the unsteady thermal field of the roll at different time intervals, assuming heat transfer solely on the roll surface. Their resulting

thermal field model enabled temperature prediction at any point within the roll body.

Campos A. et al. [7] developed a real-time simulation model to estimate the temperature and thermal expansion of hot-rolling mill work rolls. Additionally, they designed an intelligent system to control the cooling water flow rate for work rolls.

Hlady C. et al. [8] determined the heat transfer coefficient for hot rolling of aluminum-magnesium alloys in a laboratory mill. They placed thermocouples inside the rolling strip and obtained coefficient values ranging from 200 to 450 kW/(m<sup>2</sup>·°C) through inverse modeling.

Zhang X. et al. [9] created a finite-difference model to simulate the thermal expansions of CVC work rolls during hot strip rolling. Their simulation considered heat release resulting from strip deformation and friction, as well as convective heat exchange with the environment.

Prediction of temperature distribution in work rolls holds great importance for mill designers. Serajzadeh S. et al. [10] estimated the temperature and heat transfer coefficients of hot-rolling roll. By utilizing the differential equation of thermal conductivity for cylinders, they derived a nonstationary thermal model which provided reasonably accurate estimates of work roll temperature.

Mercado-Solis R. et al. [11] examined surface defects in work roll bodies caused by temperature stress. They studied heat damage to hot-rolling mill work rolls using a test bench that simulated the first stands. Two steel grades were tested: high-speed tool steel and high-carbon chromium steel. Their FEM model predicted temperature distribution across the roll volume.

Hwang S. et al. [12] presented a FEM approach to analyze the thermal and mechanical behavior of hot strip rolls.

Kotrbaček P. et al. [13] conducted a study on the impact of roll temperature on roll body wear.

Arif A. et al. [14] examined the temperature distribution in the work roll when it comes into contact with the strip during cold rolling. They proposed a FEM approach to simulate the inhomogeneous heat flow at the interface between the roll body and strip.

In his monograph, Garber E. [15] provided a comprehensive review of existing simulation models for cooling broad-strip rolling mill rolls. The monograph also includes an analysis of the roll cooling system and dis-



cusses the adaptation of simulation models to specific rolling mill.

# PROBLEM STATEMENT. MATERIALS AND METHODS

In most cases, the temperature distribution across the surface of WR body is symmetric relative to the roll body's midline. This symmetry is maintained up to approximately two-thirds of the average strip width [1]. The roll surface temperature experiences a slight decrease towards the strip edges, while the roll ends are only a few degrees hotter than the cooling water. To predict the temperature profile, it is necessary to determine the actual temperature at the middle of the roll body. This temperature can be obtained using available temperature distribution models.

The heat balance model [16; 17] utilized to calculate the temperature at the middle of the roll body surface in 4-high mill stands.

This model employs thermal balance equations for the WR and BR, assuming that the average temperature field over the rolling lead time remains constant. According to this model, the entire heat energy generated is transferred through contact heat exchange to the backup roll and through convective heat exchange to either the cooling water or the environment.

Fig. 1 illustrates the heat flows in the radial plane of the rolls for a 4-high mill stand. Based on Fig. 1 and the aforementioned patterns of roll-to-roll, roll-to-cooling water, and roll-to-environment heat exchange, the quasi-stationary heat balance can be represented by the following two equations:

– for the work roll:

$$Q_{wr} - Q_{cool,wr}^{in} - Q_{cool,wr}^{out} - Q_{br} = 0; \quad (1)$$

– for the backup roll:

$$Q_{br} - Q_{cool,br} - Q_{br,env} = 0. \quad (2)$$

In these equations, the heat amounts are defined as follows:  $Q_{wr}$  represents the heat supplied to the WR from the strip through contact and partially radiant heat exchange;  $Q_{cool,wr}^{in}$  and  $Q_{cool,wr}^{out}$  denote the amounts of heat removed from the WR by the cooling water at the inlet and outlet of the stand;  $Q_{br}$  represents the heat transferred from the WR to BR through contact heat exchange;  $Q_{br,cool}$  represents the heat removed by the cooling water from the backup roll;  $Q_{br,env}$  represents the heat released by the backup roll to the environment (air).

By substituting the heat balance components in the equations above they are reduced to a system of two linear equations in the unknown average temperatures of the WR ( $t_{av,wr,i}$ ) and BR ( $t_{av,br,i}$ ):

$$\begin{cases} A_1 t_{wr} + B_1 t_{br} = D_1; \\ A_2 t_{wr} + B_2 t_{br} = D_2. \end{cases}$$

The coefficients of the system of equations are expressed as follows:

$$\begin{cases} A_1 = \alpha_{cont.ht.wr} l_{si} + \frac{\pi - \varphi_4 - \varphi_1}{2} D_{wri} \alpha_{1wri}^{in} + \\ + \frac{\pi - \varphi_2}{2} D_{wri} \alpha_{1wri}^{out} + \alpha_{cont.ht.br} b_{bri}; \\ A_2 = B_1 = -\alpha_{cont.ht.br} b_{bri}; \\ B_2 = \frac{\varphi_5}{2} D_{bri} \alpha_{1br} + \alpha_{cont.ht.br} b_{bri} + (2\pi - \varphi_5) \frac{D_{bri}}{2} \alpha_{br,env}; \\ D_1 = \alpha_{cont.ht.wr} l_{si} t_s + \frac{\pi - \varphi_4 - \varphi_1}{2} D_{wri} \alpha_{1wri}^{in} t_{cool1} + \\ + \frac{\pi - \varphi_2}{2} D_{wri} \alpha_{1wri}^{out} t_{cool1}; \\ D_2 = \frac{\varphi_5}{2} D_{bri} \alpha_{1br} t_{cool1} + (2\pi - \varphi_5) \frac{D_{bri}}{2} \alpha_{br,env} t_{env}. \end{cases}$$

The input values for the system of equations are as follows:

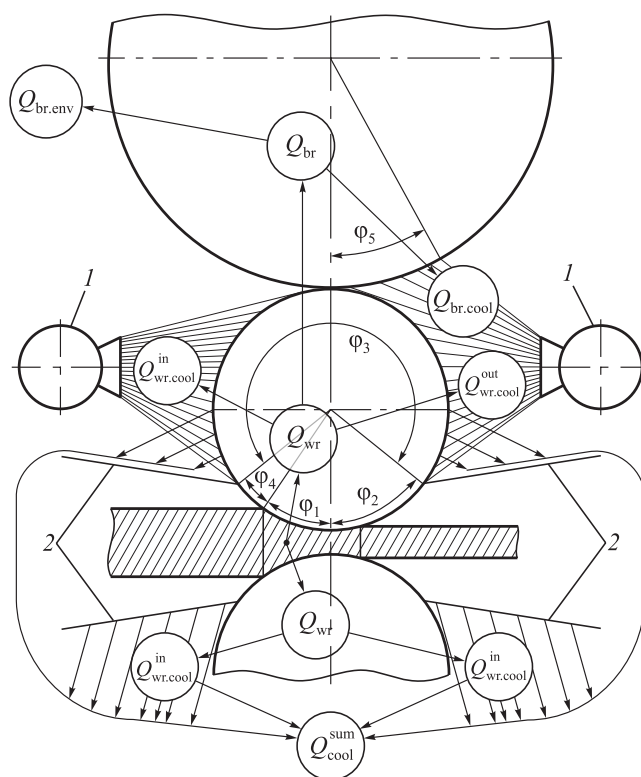


Fig. 1. Scheme of heat flows in the “quarto” stand:

1 – collector with nozzles of the roll cooling system;

2 – wiring-water cutters from the rolled strip

Рис. 1. Схема тепловых потоков в клети «кварто»:

1 – коллектор с форсунками системы охлаждения валков;

2 – проводки-отсекатели воды от прокатываемой полосы

– contact heat transfer coefficients:  $\alpha_{\text{cont.ht.wr}}$  strip to WR;  $\alpha_{\text{cont.ht.br}}$  WR to BR;

– convective heat transfer coefficients:  $\alpha_{\text{lwr},i}^{\text{in}}$ ,  $\alpha_{\text{lwr},i}^{\text{out}}$  WR to cooling water at the stand inlet and outlet;  $\alpha_{\text{lbr}}$  BR to the cooling water;  $\alpha_{\text{br,env}}$  BR to the air (all the heat transfer coefficients are in  $\text{W}/(\text{m}^2 \cdot ^\circ\text{C})$ );

–  $\varphi_1$  to  $\varphi_5$  are the WR and BR circumference angles in radians which define sectors with different heat transfer coefficients (refer Fig. 1);

– other values:  $D_{\text{wri}}$ ,  $D_{\text{bri}}$  mid-body diameters of the  $i^{\text{th}}$  stand WR and BR, m;  $l_{\text{sl}}$  length deformation area for the  $i^{\text{th}}$  stand, m (pre-estimated using the rolling force model);  $b_{\text{bri}}$  width of the elastic contact area between the WR and BR, m (estimated using the Hertzian equations from elasticity theory);  $t_{\text{cool}}$  temperature of the cooling water supplied to the rolls,  $^\circ\text{C}$ ;  $t_{\text{out},i}$  strip temperature as it leaves the deformation area of the  $i^{\text{th}}$  stand (pre-estimated with the partial strip temperature model);  $t_{\text{env}}$  ambient (air) temperature,  $^\circ\text{C}$ .

The WR and BR heat balance equations were solved using Cramer's rule:

$$\left. \begin{aligned} t_{\text{wr}} &= \frac{B_2 D_1 - B_1 D_2}{A_1 B_2 - A_2 B_1}; \\ t_{\text{br}} &= \frac{A_1 D_2 - A_2 D_1}{A_1 B_2 - A_2 B_1}. \end{aligned} \right\} \quad (3)$$

The reliability of roll temperature estimation depends on the contact and convective heat transfer coefficients:

$\alpha_{\text{cont.ht.wr}}$ ,  $\alpha_{\text{cont.ht.br}}$ ,  $\alpha_{\text{lwr},i}^{\text{in}}$ ,  $\alpha_{\text{lwr},i}^{\text{out}}$ ,  $\alpha_{\text{lbr}}$ ,  $\alpha_{\text{br,env}}$ .

Garber E. et al. [16; 17] presented equations for the  $\alpha_{\text{lwr},i}^{\text{in}}$ ,  $\alpha_{\text{lwr},i}^{\text{out}}$ ,  $\alpha_{\text{lbr}}$ ,  $\alpha_{\text{br,env}}$  coefficients. The convective heat transfer coefficients between BR and cooling water, and BR and environment (air) in these papers are:  $\alpha_{\text{lbr}} = 1500 \text{ W}/(\text{m}^2 \cdot ^\circ\text{C})$ ;  $\alpha_{\text{br,env}} = 400 \text{ W}/(\text{m}^2 \cdot ^\circ\text{C})$ , the contact heat transfer coefficient between WR and BR  $\alpha_{\text{cont.ht.br}} = 40 \text{ kW}/(\text{m}^2 \cdot ^\circ\text{C})$ .

The equation for the convective heat transfer coefficient between WR and cooling water is given by [17]

$$\alpha_{\text{lwr},i} \approx \alpha_{\text{lwr},i}^{\text{out}} = 21 V_{11} + 21,000 p_{\text{cool}} - 0.04 V_{11}^2 - 71 p_{\text{cool}}^2 - 14,590, \text{ W}/(\text{m}^2 \cdot ^\circ\text{C}), \quad (4)$$

where  $V_{11}$  is the water spraying intensity over the roll body width  $\left( V_{11} = \frac{V}{\varphi_3 R b_s}, \text{ m}^3/(\text{s} \cdot \text{m}^2), V \text{ is the total volume of water supplied to the WRs of the } i^{\text{th}} \text{ stand, m}^3/\text{s}; b_s \text{ is the strip width, m}; p_{\text{cool}} \text{ is the WR cooling water pressure, atm.} \right.$

The roll-to-strip contact heat transfer coefficient  $\alpha_{\text{cont.ht.wr}}$  depends on:

– the length of the deformation area, which in turn is determined by the contact stress;

– the roll body-to-strip contact period expressed as the downtime ratio:  $K_{\text{dr}} = \frac{\tau_{\text{lt}}}{\tau_{\text{lt}} + \tau_{\text{dr}}}$  ( $\tau_{\text{lt}}$  is the lead time, s;  $\tau_{\text{dr}}$  is the downtime when there is no strip in the deformation area, s);

– the roll body diameter (assumed constant for the specific rolling mill and stand);

– the presence of slag between the strip and the roll surface.

It is important to emphasize that the accuracy of the  $\alpha_{\text{cont.ht.wr}}$  contact heat transfer coefficient will greatly influence the accuracy of work roll temperature estimation and other temperature-dependent process properties.

The determination of  $\alpha_{\text{cont.ht.wr}}$  can be achieved by utilizing experimental data of process variables, stand properties, and experimental studies of roll body surface temperature.

Papers [16 – 18] provide such input data for calculating the  $\alpha_{\text{cont.ht.wr}}$  coefficient in the finishing stands of a broad-strip cold and hot rolling mill. The literature reports temperatures of work roll body surfaces that are measured using thermocouples immediately after the work rolls are removed from the stand. Fig. 2 illustrates bar graphs depicting the temperature distribution in the middle of the WR body for the finishing stand of the 2000 model broad-strip rolling mill.

Fig. 2 indicates that the roll body temperature generally decreases from the first stand to the last finishing stand. This can be attributed to the lower strip temperature in these stands. However, the second and third stands deviate from this trend. Fig. 3 demonstrates that the average flow rates of water supplied to the roll body surfaces are highest compared to the flow rates in the other stands.

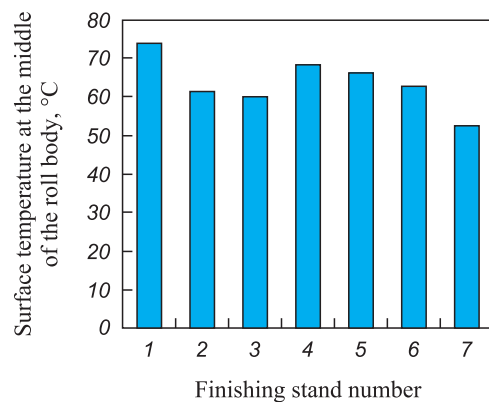


Fig. 2. Temperatures of the working rolls barrels' surfaces in the stands of finishing group

Рис. 2. Температуры поверхностей бочек рабочих валков в клетях чистовой группы

To derive an analytic equation for the WR-to-strip contact heat exchange coefficient we determined the coefficient values that minimize the discrepancy between measured and estimated temperatures using the heat balance model. Subsequently, they selected the most suitable equation for  $\alpha_{\text{cont.ht.wr}}$  and validated its performance.

## RESULTS AND DISCUSSION

We conducted regression analysis on the experimental data to develop an equation for the WR-to-strip contact heat exchange coefficient in the deformation areas of the finishing stands in the broad-strip rolling mill. The resulting equation is as follows:

$$\alpha_{\text{cont.ht.wr}} = 6.6 p_{\text{avgi}} + 10^3(70.7K_{\text{dr}} - 48.2K_{\text{dr}}^2 - 22.75), \text{ W/(m}^2\cdot\text{°C)},$$

where  $p_{\text{avgi}}$  represents the average contact pressure at the center of deformation;  $K_{\text{dr}}$  denotes the downtime ratio.

The ranges of the values used to establish the expression for  $\alpha_{\text{cont.ht.wr}}$  are as follows:  $K_{\text{dr}} = 0.46 - 0.90$ ;  $p_{\text{avgi}} = 200 - 600$  MPa.

The equation includes significant factors which were determined based on the results of Student's  $t$ -test with an  $\alpha$  significance level.

To validate the equation for the heat transfer coefficient, Fisher's criterion was employed. Both the heat balance model and the  $\alpha_{\text{cont.ht.wr}}$  equation were validated using a statistically significant dataset. The average  $t_{\text{avg.wri}}$  (discrepancy between the estimated and measured value) was 8.01 %. The maximum discrepancy was 16.7 %, the minimum was 1.53 %, and  $R^2 = 0.87$ .

Consequently, the expression for the contact heat transfer coefficient can be considered reliable. The heat balance

model can be utilized to estimate the roll temperature profile and other properties, such as the dimensions of the strip cross-section or the optimal shape of the WR body, in broad-strip rolling mills [19]. This approach can also be applied to estimate the cross-section shape of cold-rolled strips [20].

Based on the experimental data and the equation for the WR-to-strip contact heat exchange coefficient, we conducted an analysis to estimate the impact of the downtime ratio and contact pressure on the heat exchange intensity between the WR and strip (Fig. 4). The results depicted in Fig. 4 indicate that the downtime ratio and contact pressure, when within the acceptable ranges, can exert a significant influence on the contact heat transfer coefficient and, consequently, the heat profile of the roll. Specifically, the downtime ratio demonstrates the most substantial effect on the WR-to-strip heat exchange, particularly when the downtime ratio falls below 0.6.

## CONCLUSIONS

The roll body temperature plays a crucial role in hot rolling processes as it impacts various aspects such as the shape and dimensions of the rolled steel and the lifespan of the roll itself. To achieve an accurate estimation of the roll temperature and obtain its temperature profile, it is essential to employ a reliable heat balance model. This model enables the determination of the optimal shape of the roll body and aids in minimizing flatness defects. The accuracy of the heat balance model heavily relies on the constants associated with heat transfer coef-

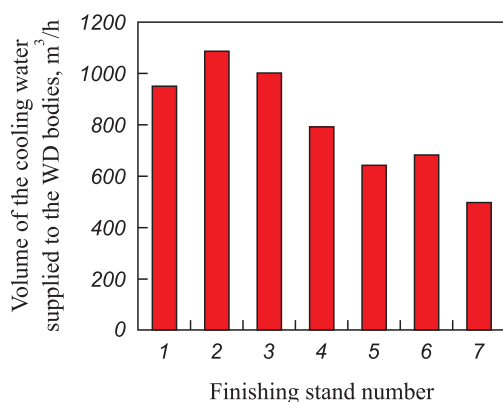


Fig. 3. Water consumption for cooling the working rolls barrels' surfaces in the stands of finishing group

Рис. 3. Расходы воды на охлаждение поверхностей бочек рабочих валков в клетях чистовой группы

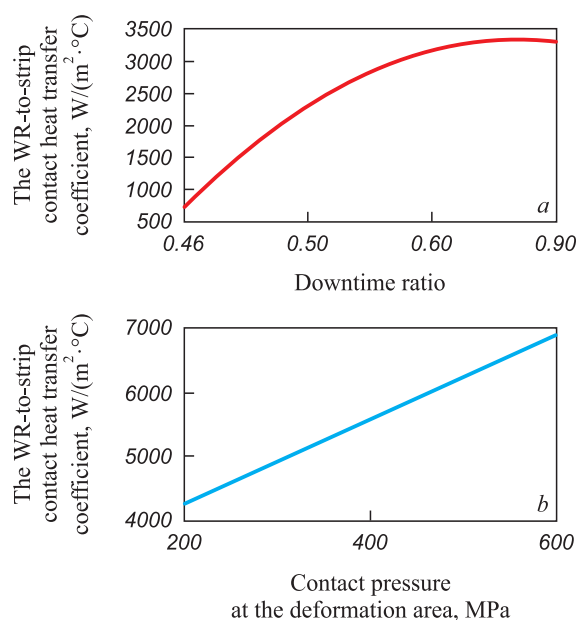


Fig. 4. Influence of rolling factors on the coefficient of contact heat transfer

Рис. 4. Влияние факторов прокатки на коэффициент контактного теплообмена

ficients. In the context of roll temperature estimation, there are two types of heat transfer that are of particular importance: contact heat transfer between the roll and the strip, and convective heat transfer between the roll and the cooling water. The available literature sources provide diverse values and equations for the contact and convective heat transfer coefficients in roll temperature analysis. However, many of these sources overlook the impact of long breaks during the operation of the finishing stand. As a result, significant errors can arise in the analysis of roll temperature.

To address this issue, we conducted measurements of the actual roll body temperature at multiple points along the roll length using thermocouple immediately after rolling. Additionally, we collected data on various rolling process variables, such as downtime ratio, reduction ratio for each stand, cooling water flow rate, and others, prior to the transfer of the steel strip. Based on these measurements and process variable values, we derived an empirical equation for the contact heat transfer coefficient that incorporates the key process variables, including the downtime ratio. By utilizing these refined coefficients, we significantly improved the accuracy of the roll temperature profile obtained from the process variable values.

Our findings indicate that the downtime ratio and contact pressure, when within acceptable ranges, exert a substantial influence on the contact heat transfer coefficient and, consequently, the heat profile of the roll body. Particularly, the downtime ratio exhibits the most significant impact on the heat exchange between the work roll and the strip, especially when the downtime ratio is below 0.6.

## REFERENCES / СПИСОК ЛИТЕРАТУРЫ

- Garber E.A., Khlopotin M.V., Traino A.I., Popov E.S., Savinykh A.F. Simulation of the thermal conditions of rolls in a wide-strip hot-rolling mill to determine their effective cooling conditions. *Russian Metallurgy (Metally)*. 2009;(3):208–219.  
Гарбер Э.А., Хлопотин М.В., Траино А.И., Попов Е.С., Савиных А.Ф. Моделирование теплового режима валков широкополосного стана горячей прокатки для определения эффективных режимов их охлаждения. *Металлы*. 2009;(3):34–47.
- Bel'skii S.M., Mazur I.P., Astakhov A.A. Simplified computational procedure of thermal profiling of working rolls of hot-rolling mill. *Proizvodstvo prokata*. 2018;(2):3–6. (In Russ.).  
Бельский С.М., Мазур И.П., Астахов А.А. Упрощенная методика вычисления тепловой профилировки рабочих валков стана горячей прокатки. *Производство проката*. 2018;(2):3–6.
- Antonyuk V.V., Fedin A.G., Mustafin V.A., Dema R.R., Platov S.I., Amirov R.N., Koldin A.V. Kharchenko M.V. Setting up and controlling the thermal state of working rolls in the 2000 wide-strip hot-rolling mill of PJSC “Magnitogorsk Iron and Steel Works”. In: *Proceedings of the XI Int. Congress of Rollers*. Vol. 2. 2017. (In Russ.).  
Антонюк В.В., Федин А.Г., Мустафин В.А., Дема Р.Р., Платов С.И., Амиров Р.Н., Колдин А.В. Харченко М.В. Опыт настройки и управления тепловым состоянием рабочих валков широкополосного стана 2000 горячей прокатки ПАО «Магнитогорский металлургический комбинат». *Материалы XI Международного конгресса прокатчиков*. Том 2. 2017.
- Garber E.A., Mishnev P.A., Shalaevskii D.L., Paligin R.B., Mikheeva I.A., Bolobanova N.L. New methods for modeling and reducing the non-flatness of steel strips during hot rolling on wide-strip mills. In: *Proceedings of the Int. Sci. Seminar “Scientific and Technological Progress in Metallurgy – 2013”*. 2014:70–82. (In Russ.).  
Гарбер Э.А., Мишнев П.А., Шалаевский Д.Л., Палигин Р.Б., Михеева И.А., Болобанова Н.Л. Новые методы моделирования и уменьшения неплоскостности стальных полос при горячей прокатке на широкополосных станах. *Материалы Международного научного семинара «Научно-технический прогресс в металлургии – 2013»*. 2014:70–82.
- Hamraoui M. Thermal behaviour of rollers during the rolling process. *Applied Thermal Engineering*. 2009;29(11–12):2386–2390.  
<https://doi.org/10.1016/j.applthermaleng.2008.12.013>
- Johnson R.E., Keanini R.G. An asymptotic model of work roll heat transfer in strip rolling. *International Journal of Heat and Mass Transfer*. 1995;41(6–7):871–879.  
[https://doi.org/10.1016/S0017-9310\(97\)00175-0](https://doi.org/10.1016/S0017-9310(97)00175-0)
- Campos A.M., Garcia D.F., Usamentiaga R., de Abajo N., Gonzalez J.A. Real time model for the intelligent control of cooling systems for hot strip mill work rolls. *26<sup>th</sup> Annual Conference of the IEEE*. 2000.  
<https://doi.org/10.1109/IECON.2000.972272>
- Hlady C.O., Brimacombe J.K., Samarasekera I.V., Hawbolt E.B. Heat transfer in the hot rolling of the metal. *Metallurgical and Material Transactions B*. 1995;26:1019–1027.  
<https://doi.org/10.1007/BF02654104>
- Zhang X.M., Yang Z.Y., Tieu A.K., Liu X.N., Wang G.D. Numerical modeling of the thermal deformation of CVC work rolls in hot strip rolling. *Journal of Material Processing Technology*. 2002;130–131:219–223.  
[https://doi.org/10.1016/S0924-0136\(02\)00736-7](https://doi.org/10.1016/S0924-0136(02)00736-7)
- Serajzadeh S., Karemi Taheri A., Mucciardi F. Unsteady state work-roll temperature distribution during continuous hot slab rolling. *International Journal of Mechanical Sciences*. 2002;44(12):2447–2462.  
[https://doi.org/10.1016/S0020-7403\(02\)00179-0](https://doi.org/10.1016/S0020-7403(02)00179-0)
- Mercado-Solis R.D., Talamantes-Silva J., Beynon J.H., Hernandez-Rodriguez M.A.L. Modelling surface thermal damage to mill rolls. *Wear*. 2007;263(17–20):1560–1567.  
<https://doi.org/10.1016/j.wear.2006.12.062>
- Hwang S.M., Sun C.G., Ryoo S.R., Kwak W.J. An integrated FE process model for prevision analysis of the thermo-mechanical behaviours of rolls and strip in hot strip rolling. *Computer Methods in Applied Mechanics and Engineering*. 2002;191:4015–4033.  
[https://doi.org/10.1016/S0045-7825\(02\)00298-0](https://doi.org/10.1016/S0045-7825(02)00298-0)
- Kotrbaček P., Horsky J., Raudensky M., Pohanka M. Experimental study of heat transfer in hot rolling. *Revue de Métal-*



- lurgie*. 2006;103(7–8):333–341.  
<https://doi.org/10.1051/metal:2006134>
14. Arif A.F., Khan O., Zubair S.M. Prediction of roll temperature with a non-uniform heat flux at tool and workpiece interface. *Heat and Mass Transfer*. 2004;41(1):75–94.  
<https://doi.org/10.1007/s00231-004-0508-6>
  15. Garber E.A. *Modeling and Improvement of Thermal Mode and Forming of Rolls: Monograph*. Cherepovets: ChSU; Moscow: Teplotekhnika; 2013:114. (In Russ.).  
 Гарбер Э.А. *Моделирование и совершенствование теплового режима и профилировок валков: Монография*. Череповец: ЧГУ; Москва: Теплотехник; 2013:114.
  16. Garber E.A., Khlopotin M.V., Savinykh A.F., Kozhevnikov A.V., Golovanov A.V., Smirnov V.S. Industrial tests of improved crowning of work rolls in wide-strip hot rolling mill. *Proizvodstvo prokata*. 2008;(4):18–22. (In Russ.).  
 Гарбер Э.А., Хлопотин М.В., Савиных А.Ф., Кожевников А.В., Голованов А.В., Смирнов В.С. Промышленные испытания усовершенствованных профилировок рабочих валков на широкополосном стане горячей прокатки. *Производство проката*. 2008;(4):18–22.
  17. Garber E.A., Khlopotin M.V., Popov E.S., Savinykh A.F., Golovanov A.V. Improving the efficiency of cooling rolls in a wide-strip hot rolling mill using adaptive mathematical models of heat balance. *Proizvodstvo prokata*. 2009;(4):12–24. (In Russ.).  
 Гарбер Э.А., Хлопотин М.В., Попов Е.С., Савиных А.Ф., Голованов А.В. Повышение эффективности охлаждения валков широкополосного стана горячей прокатки с использованием адаптивных математических моделей теплового баланса. *Производство проката*. 2009;(4):12–24.
  18. Garber E.A. *Станы холодной прокатки*. Москва: Черметинформация; 2004.  
 Garber E.A. *Cold Rolling Mills*. Moscow: Chermetininformatsiya; 2004. (In Russ.).
  19. Garber E.A., Mishnev P.A., Shalaevskii D.L., Paligin R.B., Mikhreeva I.A., Bolobanova N.L. Modeling and reduction of strips non-flatness during hot rolling at the stage of setting up a wide-strip mill. *Proizvodstvo prokata*. 2014;(3):7–13. (In Russ.).  
 Гарбер Э.А., Мишнев П.А., Шалаевский Д.Л., Палигин Р.Б., Михеева И.А., Болобанова Н.Л. Моделирование и уменьшение неплоскостности полос при горячей прокатке на стадии настройки широкополосного стана. *Производство проката*. 2014;(3):7–13.
  20. Shalaevskii D.L., Korepina K.P. Influence of cross profile of cold rolled strips on occurrence of flatness defects. *Chernye metally*. 2022;(3):56–59. (In Russ.).  
 Шалаевский Д.Л., Корепина К.П. Исследование влияния поперечного профиля холоднокатаных полос на возникновение дефектов планшетности. *Черные металлы*. 2022;(3):56–59.

## Information about the Author

## Сведения об авторе

**Dmitrii L. Shalaevskii**, Cand. Sci. (Eng.), Assist. Prof. of the Chair of Metallurgy, Mechanical Engineering and Technological Equipment, Cherepovets State University  
**ORCID:** 0000-0002-0443-4135  
**E-mail:** shal-dmitrij@yandex.ru

**Дмитрий Леонидович Шалаевский**, к.т.н., доцент кафедры металлургии, машиностроения и технологического оборудования, Череповецкий государственный университет  
**ORCID:** 0000-0002-0443-4135  
**E-mail:** shal-dmitrij@yandex.ru

Received 23.11.2022  
 Revised 27.01.2023  
 Accepted 11.03.2023

Поступила в редакцию 23.11.2022  
 После доработки 27.01.2023  
 Принята к публикации 11.03.2023





UDC 621.771.01

DOI 10.17073/0368-0797-2023-3-290-293

Short report  
Краткое сообщение

## RESERVES FOR REDUCING ENERGY CONSUMPTION WHEN ROLLING SECTION BARS ON MODERN ROLLING MILLS

A. R. Fastyskovskii , M. I. Glukhov, V. A. Vakhrolomeev

Siberian State Industrial University (42 Kirova Str., Novokuznetsk, Kemerovo Region – Kuzbass 654007, Russian Federation)

fastikovsky@mail.ru

**Abstract.** Metallurgical production is a highly energy-intensive process, and the search for solutions to reduce energy costs remains an urgent task for all stages. In this regard, the production of finished rolled products is considered as the most promising direction for the implementation of energy-saving technologies. There are two ways to reduce energy costs in hot rolling of section bars: saving energy for heating and improving the use of the main equipment to reduce intermediate energy costs. Due to the difference in silt conditions at the moment of capture and at the steady stage of the rolling process, a reserve of retracting friction forces arises, which can be used for additional shaping in non-drive devices and thereby increase the efficiency of the main equipment and reduce overall energy costs. For the practical implementation of the proposed concept, dependence was obtained that makes it possible to estimate the power potential that is not used at the steady stage of the rolling process. Using the obtained dependence, it was found that when rolling in smooth rolls, the potential of friction forces is used only by 50 – 60 %, and when rolling in calibers, by 35 – 40 %. It was experimentally established that during the rolling of shaped sections in passes with an elongation ratio of less than 1.10 – 1.15, more than 50 % of the energy is spent on idling. However, by replacing drive stands in these passes with non-drive cassettes (in continuous groups), it is possible to increase the efficiency of adjacent stands by 4 – 5 % and reduce energy costs.

**Keywords:** energy consumption, section bar, non-drive stand, idling, efficiency**For citation:** Fastyskovskii A.R., Glukhov M.I., Vakhrolomeev V.A. Reserves for reducing energy consumption when rolling section bars on modern rolling mills. *Izvestiya. Ferrous Metallurgy*. 2023;66(3):290–293. <https://doi.org/10.17073/0368-0797-2023-3-290-293>

## РЕЗЕРВЫ СНИЖЕНИЯ ЭНЕРГОПОТРЕБЛЕНИЯ ПРИ ПРОКАТКЕ СОРТОВЫХ ПРОФИЛЕЙ НА СОВРЕМЕННЫХ ПРОКАТНЫХ СТАНАХ

А. Р. Фастыковский , М. И. Глухов, В. А. Вахроломеев

Сибирский государственный индустриальный университет (Россия, 654007, Кемеровская область – Кузбасс, Новокузнецк, ул. Кирова, 42)

fastikovsky@mail.ru

**Аннотация.** Металлургическое производство является высокоэнергоёмким процессом, поэтому поиск решений по снижению энергозатрат остается актуальной задачей для всех переделов. В этом плане производство готовой прокатной продукции рассматривается как наиболее перспективное направление для реализации энергосберегающих технологий. Возможны два пути снижения энергозатрат при горячей прокатке сортовых профилей: экономия энергии на нагрев и улучшение использования основного оборудования для снижения промежуточных затрат энергии. Ввиду разности силовых условий в момент захвата и на установившейся стадии процесса прокатки возникает резерв втягивающих сил трения, который можно использовать для дополнительного формоизменения в неприводных устройствах и тем самым повысить эффективность основного оборудования и снизить общие энергозатраты. Для практической реализации предложенной концепции была получена зависимость, позволяющая оценить потенциал мощности, который не используется на установившейся стадии процесса прокатки. С применением полученной зависимости было установлено, что при прокатке в гладких валах потенциал сил трения используется только на 50 – 60 %, а при прокатке в калибрах – на 35 – 40 %. Экспериментально установлено, что при прокатке фасонных профилей в пропусках с коэффициентом вытяжки менее 1,10 – 1,15 более 50 % энергии затрачивается на холостой ход. Однако заменив в этих пропусках приводные клетки на неприводные кассеты (в непрерывных группах), можно повысить коэффициент полезного действия рядом стоящих клеток на 4 – 5 % и снизить энергозатраты.

**Ключевые слова:** энергопотребление, сортовые профили, неприводная клетка, холостой ход, коэффициент полезного действия**Для цитирования:** Фастыковский А.Р., Глухов М.И., Вахроломеев В.А. Резервы снижения энергопотребления при прокатке сортовых профилей на современных прокатных станах. *Известия вузов. Черная металлургия*. 2023;66(3):290–293. <https://doi.org/10.17073/0368-0797-2023-3-290-293>

Metallurgical production is considered one of the most energy-intensive industries, consuming up to 90 % of coking coal, 50 % of generated electricity, and 25 % of natural gas [1]. The final stage of metallurgical processing, known as rolling production, requires a significant amount of fuel for both heating the billet before rolling (1.30–1.65 GJ/t) and during the rolling process itself (0.45–1.20 GJ/t) [2]. These figures convincingly highlight the importance of efforts to reduce energy costs in rolled product manufacturing.

Enhancing the utilization of friction forces within the deformation zone of a rolling stand represents a key opportunity for reducing energy consumption in the production of section bars on modern continuous rolling mills [3–5]. By doing so, the overall efficiency of the primary rolling equipment can be increased. To implement this approach, additional non-driven devices, located in close proximity to the drive stands, can be employed for the deformation or longitudinal separation of the strip [6–9].

It is widely recognized that the rolling process relies on friction forces between the metal and the rolls. The more effectively these friction forces are harnessed during the forming process, the higher the process efficiency and the more efficiently energy is utilized. However, the varying force conditions during the initial gripping of the metal by the rolls and during the steady stage of the rolling process create circumstances where the potential of friction forces within the deformation zone is not fully realized. Addressing this issue necessitates the use of continuous devices, such as rolls and dividing devices, which facilitate additional work to be performed.

In order to quantify the untapped potential of friction forces during the steady stage of the rolling process, we can calculate the unused power ( $\Delta N$ ) by considering the disparity in friction coefficients between the gripping phase ( $\mu_g$ ) and the steady stage ( $\mu_s$ ) of hot rolling, where  $\mu_g/\mu_s \approx 1.2 \div 1.4$  [10]. This can be determined using the equation:

$$\Delta N = N_s - N_d,$$

where  $N_s$  represents the power that can be generated by friction forces during the steady stage of hot rolling;  $N_d$  is the power required for deformation in the driven stand.

The maximum power generated by friction forces during the steady stage of hot rolling (assuming a zero-length advance zone) can be calculated using the equation:

$$N_s = 2p_{\text{avg}}\mu_s b_{\text{avg}} l_d v,$$

where  $p_{\text{avg}}$  denotes the average normal pressure;  $b_{\text{avg}}$  represents the average strip width;  $l_d$  is the length of contact arc;  $v$  is the rolling speed.

To determine the power required during deformation, we utilize the well-known Fink equation [11], with the substitution:

$$\Delta h \approx h_{\text{avg}} \ln \left( \frac{h_0}{h_1} \right),$$

where  $\Delta h$  is the absolute reduction;  $h_{\text{avg}}$  is the average strip height;  $h_0$  and  $h_1$  refer to the strip height before and after rolling in the driven stand, respectively.

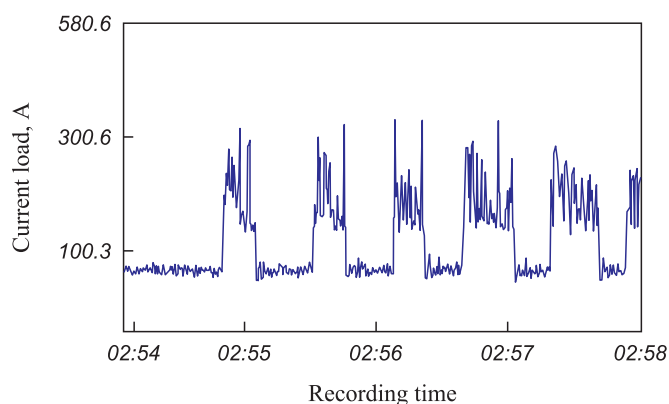
It should be noted that this assumption introduces an error of 1–3 % for degrees of deformation up to 60 %. After appropriate transformations and incorporating the  $\mu_g/\mu_s$  ratio, we obtain:

$$\Delta N = p_{\text{avg}} b_{\text{avg}} v (1.54\mu_g l_d - \Delta h).$$

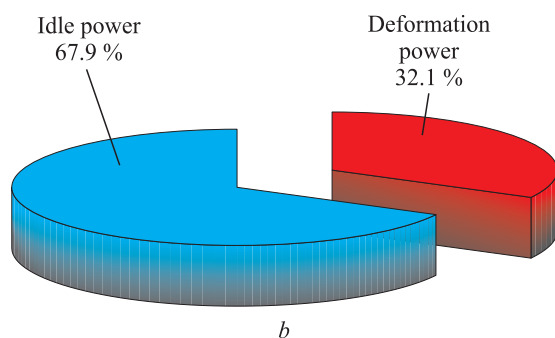
The obtained  $\Delta N$  value makes it possible to estimate the unused potential of friction forces in the deformation zone during hot rolling. The calculations reveal that, when rolling a rectangular strip on smooth rolls, only 50–60 % of the maximum potential of friction forces is utilized under maximum reductions and 35–40 % in subsequent passes due to differences in force conditions between gripping and the steady stage of rolling. This inefficiency significantly impacts the rolling process, resulting in increased energy consumption. Therefore, the implementation of non-driven devices for deformation and longitudinal separation is recommended.

To enhance the efficiency of rolling bars, a more complete utilization of the potential of friction forces can be achieved by replacing driven stands with non-driven ones in sections where the elongation coefficient falls below 1.10–1.15. Fig. 1, *a* presents a diagram illustrating the recording of the current of the main engine in the second stand of a medium-section mill during the production of angle No. 9, with a drawing ratio of 1.03. Fig. 1, *b* depicts the power distribution for this case, with the majority of power being used for idling (67.9 %), while only a small fraction (32.1 %) is allocated to product formation. To address this issue, the implementation of a non-driven stand, specifically a cassette, in place of the drive stand for the given pass can be considered. This adjustment enables the redistribution of power for product deformation across adjacent stands from the same group without the need for stopping. Such an approach will lead to a reduction in energy costs by minimizing idle power consumption and an increase in the efficiency of adjacent stands (Fig. 2).

The medium-section mill being considered has an assortment comprising 83 % of shaped profiles, such as angles, beams, and channels. Within this assortment, there are sections with an elongation ratio of less than 1.10–1.15, indicating areas where improvement is needed. By incorporating non-driven stands



a



b

Fig. 1. Energy costs during rolling in the second stand of the middle-grade mill with drawing coefficient 1.03:

a – current diagram of the main motor;

b – energy balance in the considered stand

Рис. 1. Энергозатраты при прокатке во второй клетке среднесортного стана с коэффициентом вытяжки 1,03:

a – токовая диаграмма главного двигателя;

b – энергетический баланс в рассматриваемой клетке

in these passes, and with an annual production output of 1.4 million tons of finished products, energy savings of up to 0.75 kWh/t can be achieved. In monetary terms, this translates to an annual savings of 4.8 million rubles. Additionally, the use of non-driven stands in the form of cassettes results in reduced metal consumption, costs, depreciation deductions, and operating expenses compared to traditional rolling stands. This provides an additional benefit of 15 million rubles per year. Considering the costs associated with manufacturing the new equipment, the investment in non-driven stands is projected to have a payback period of 0.8 years.

## CONCLUSIONS

During the steady state stage of hot rolling, there exists an untapped potential of frictional forces in the deformation zone due to the differing force conditions between gripping and the steady state stage of the process. This inefficient utilization of energy can result in suboptimal performance.

In order to enhance the efficient utilization of frictional forces in the deformation zone during the steady

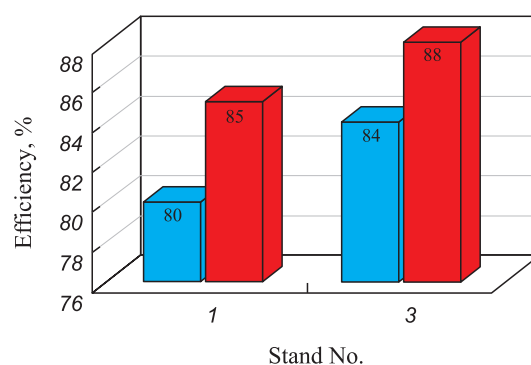


Fig. 2. Change in efficiency of 1 and 3 stands when replacing the second stand with a non-drive stand – cassette

Рис. 2. Изменение коэффициента полезного действия 1 и 3 клетей при замене второй клетки неприводной клетью – кассетой

stage of the rolling process, it is proposed to incorporate non-driven devices in close proximity to the driving stands for additional deformation and longitudinal separation. Research indicates that when the drawing ratio falls below 1.10 – 1.15, it is advisable to replace the drive stands with non-drive stands. This approach not only reduces energy consumption and operating costs but also enhances the efficiency of the primary equipment.

## REFERENCES / СПИСОК ЛИТЕРАТУРЫ

1. Volkova I.A. Review of new directions for energy. *Metal-lurg.* 2005;(8):32–36. (In Russ.).  
Волкова И.А. Новые направления энергосбережения в металлургии. *Металлург.* 2005;(8):32–36.
2. Dubina O.V. Dynamics of energy consumption in rolling shops. *Proizvodstvo prokata.* 2003;(1):29–32. (In Russ.).  
Дубина О.В. Динамика потребления энергоресурсов в прокатных цехах. *Производство проката.* 2003;(1):29–32.
3. Fastyskovskii A.R., Fastyskovskii D.A. Evaluation of the possibilities of contact friction forces in order to intensify the rolling process at an established stage. *Proizvodstvo prokata.* 2013;(7):9–12. (In Russ.).  
Фастыковский А.Р., Фастыковский Д.А. Оценка возможностей контактных сил трения с целью интенсификации процесса прокатки на установившейся стадии. *Производство проката.* 2013;(7):9–12.
4. Matsuo G., Suzuki M. The latest technology of multi-slit rolling. *SEA. ISI Quaterly.* 1995;(3):49–58.
5. Sidelnikov S.B., Galiev R.I., Bepalov V.M., Samchuk A.P. Determining power–energy parameters of combined rolling–extrusion process for low-plastic aluminium alloys. *Non-Ferrous Metals.* 2018;44(1):30–36.  
<https://doi.org/10.17580/nfm.2018.01.06>
6. Sidelnikov S., Galiev R., Lopatina E., Samchuk A. Analysis of energy–force parameters of combined processing for receiving modifying bars from Al–5Ti–1B alloy. *Non-Ferrous Metals.* 2017;42(1):30–35.  
<https://doi.org/10.17580/nfm.2017.01.07>
7. Fastyskovskii A.R. Region for extrolling and effective deformation modes. *Russian Journal of Non-Ferrous Metals.*

2011;52(3):230–233.

<https://doi.org/10.3103/S1067821211030084>

8. Grzyb R., Misiolek Z. The concept and the theoretical fundamentals of a new combined process of rolling and extrusion. *Archiwum Hutnictwa*. 1983;28(3):305–319.
9. Grzyb R., Misiolek Z. The experimental investigations on the force parameters and metal flow in the combined process of rolling and extrusion. *Archiwum Hutnictwa*. 1983;28(3): 321–340.
10. Grudev A.P. *Theory of Rolling*. Moscow: Internet Engineering; 2001:280. (In Russ.).  
Грудев А.П. *Теория прокатки*. Москва: Интернет Инжиниринг; 2001:280.
11. Nikitin G.S. *Theory of Continuous Longitudinal Rolling*. Moscow: Bauman Moscow State Technical University; 2009:399. (In Russ.).  
Никитин Г.С. *Теория непрерывной продольной прокатки*. Москва: МГТУ им. Н.Э. Баумана; 2009:399.

## Information about the Authors

**Andrei R. Fastyskovskii**, Dr. Sci. (Eng.), Prof. of the Chair “Metal Forming and Metal Science. OJSC “EVRAZ ZSMK”, Siberian State Industrial University

ORCID: 0000-0001-9259-9038

E-mail: fastikovsky@mail.ru

**Maksim I. Glukhov**, Postgraduate of the Chair “Metal Forming and Metal Science. OJSC “EVRAZ ZSMK”, Siberian State Industrial University  
E-mail: Gluhovmx@yandex.ru

**Vladimir A. Vakhrolomeev**, Postgraduate of the Chair “Metal Forming and Metal Science. OJSC “EVRAZ ZSMK”, Siberian State Industrial University  
E-mail: wladimir170581@mail.ru

## Сведения об авторах

**Андрей Ростиславович Фастыковский**, д.т.н., профессор кафедры «Обработка металлов давлением и металловедение. ЕВРАЗ ЗСМК», Сибирский государственный индустриальный университет

ORCID: 0000-0001-9259-9038

E-mail: fastikovsky@mail.ru

**Максим Ильич Глухов**, аспирант кафедры «Обработка металлов давлением и металловедение. ЕВРАЗ ЗСМК», Сибирский государственный индустриальный университет  
E-mail: Gluhovmx@yandex.ru

**Владимир Анатольевич Вахроломеев**, аспирант кафедры «Обработка металлов давлением и металловедение. ЕВРАЗ ЗСМК», Сибирский государственный индустриальный университет  
E-mail: wladimir170581@mail.ru

## Contribution of the Authors

**A. R. Fastyskovskii** – formulation and solution of the problem of determining the power reserve during rolling at a steady stage of the process, theoretical analysis of the prospects for using the reserve of friction forces during rolling, justification of the extraction coefficients at which it is advisable to replace the drive rolling stands with non-drive devices, formulation of conclusions based on the results of research.

**M. I. Glukhov** – obtaining and analyzing experimental results, evaluating the economic effect of using the reserve of friction forces on the operating mill.

**V. A. Vakhrolomeev** – analysis of literary data, design of the graphic part, evaluation of the possibility of increasing the efficiency when using the reserve of friction forces.

## Вклад авторов

**А. Р. Фастыковский** – постановка и решение задачи по определению резерва мощности при прокатке на установившейся стадии процесса; теоретический анализ перспектив использования резерва сил трения при прокатке; обоснование коэффициентов вытяжки, при которых целесообразно приводные прокатные клетки заменять неприводными устройствами; формулирование выводов по результатам исследований.

**М. И. Глухов** – получение и анализ экспериментальных результатов, оценка экономического эффекта от использования резерва сил трения на действующем стане.

**В. А. Вахроломеев** – анализ литературных данных, оформление графической части, оценка возможности увеличения коэффициента полезного действия при использовании резерва сил трения.

Received 23.06.2022

Revised 01.03.2023

Accepted 10.03.2023

Поступила в редакцию 23.06.2022

После доработки 01.03.2023

Принята к публикации 10.03.2023





UDC 621.791.927.5

DOI 10.17073/0368-0797-2023-3-294-301



Original article

Оригинальная статья

## STRUCTURE FORMATION OF Np-30KhGSA ALLOY IN WIRE AND ARC ADDITIVE MANUFACTURING

M. S. Anosov, D. A. Shatagin, M. A. Chernigin,  
Yu. S. Mordovina<sup>✉</sup>, E. S. Anosova

■ R.E. Alekseev Nizhny Novgorod State Technical University (24 Minina Str., Nizhny Novgorod 603022, Russian Federation)

✉ ips4@nntu.ru

**Abstract.** The use of metallic products 3D-printing is a modern, promising technology that improves production efficiency. However, using this technology is associated with a number of problems, for example, with increased microstructural heterogeneity and defects in metal. Therefore, it is necessary to carry out researches to identify 3D-printing modes ensuring the most homogeneous, stable and non-defect structure. In this work, a study was made of the process of structure formation of 30KhGSA steel in the process of Wire and Arc Additive Manufacturing (WAAM) under various printing modes. Microstructural analysis, microhardness measurement and fractal analysis were used for assessment of the obtained billets. In all surfacing modes, a significant structural inhomogeneity of the deposited billet was revealed, which is explained by the thermal effect of the deposited layer on the already crystallized metal. Nevertheless, we found the mode that gives the most favorable microstructure in terms of its uniformity and equiaxed grains. With an increase in WAAM heat input values, an increase in the productivity of the process is observed and a decrease in the number of pores in the material is recorded. However, when the heat input of the surfacing process exceeds 1000 J/mm, the structural inhomogeneity of the material increases and its microhardness significantly decreases. Based on the studies, as a WAAM 3D-printing mode for Np-30KhGSA alloy, a mode with a heat input of about 920 J/mm can be chosen, which provides the lowest structural inhomogeneity and a sufficiently high productivity of the growth process with the absence of defects in the form of pores and elements of not melted wire.

**Keywords:** electric arc surfacing, surfacing heat input, thermal cycle, microstructure, 30KhGSA, WAAM

**Acknowledgements:** The work was supported by the Russian Science Foundation, grant No. 22-79-00095 “Development of scientific and technological foundations for the structure formation of structural materials obtained by wire arc additive manufacturing for the formation of mechanical properties under fatigue using artificial intelligence approaches”.

**For citation:** Anosov M.S., Shatagin D.A., Chernigin M.A., Mordovina Yu.S., Anosova E.S. Structure formation of Np-30KhGSA alloy in wire and arc additive manufacturing. *Izvestiya. Ferrous Metallurgy*. 2023;66(3):294–301. <https://doi.org/10.17073/0368-0797-2023-3-294-301>

## СТРУКТУРООБРАЗОВАНИЕ СПЛАВА Нп-30ХГСА ПРИ АДДИТИВНОМ ЭЛЕКТРОДУГОВОМ ВЫРАЩИВАНИИ

М. С. Аносов, Д. А. Шатагин, М. А. Чернигин,  
Ю. С. Мордовина<sup>✉</sup>, Е. С. Аносова

■ Нижегородский государственный технический университет им. Р.Е. Алексеева (Россия, 603022, Нижний Новгород, ул. Минина, 24)

✉ ips4@nntu.ru

**Аннотация.** Использование 3D-печати изделий из металлических материалов является современной перспективной технологией, способствующей повышению производственной эффективности. Однако применение данной технологии сопряжено с рядом проблем, например, с повышенной микроструктурной неоднородностью и дефектностью металла. В связи с этим требуется проведение исследований, направленных на выявление таких режимов 3D-печати, которые бы обеспечили получение наиболее однородной, стабильной и бездефектной структуры. В работе изучено структурообразование стали марки 30ХГСА в процессе аддитивной электродуговой наплавки при различных режимах печати. Для оценки качества полученных заготовок применялись микроструктурный и фрактальный анализы, а также измерение микротвердости. При всех режимах наплавки выявлена значительная структурная неоднородность наплавленной заготовки, которая объясняется термическим воздействием наплавленного слоя на уже закристаллизовавшийся металл. Тем не менее, установлен режим, который дает наиболее благоприятную микроструктуру с точки зрения ее однородности и равноосности зерен. При увеличении значений погонной энергии процесса аддитивного электродугового выращивания наблюдается увеличение производительности процесса и фиксируется уменьшение количества пор в материале. Однако при значениях погонной энергии процесса

наплавки свыше 1000 Дж/мм увеличивается структурная неоднородность материала и значительно снижается его микротвердость. Исходя из проведенных исследований, в качестве режима 3D-печати электродуговой наплавкой для сплава Nп-30ХГСА может быть выбран режим с погонной энергией порядка 920 Дж/мм. Он обеспечивает наименьшую структурную неоднородность и достаточно высокую производительность процесса выращивания с отсутствием дефектов в виде пор и элементов нерасплавившейся проволоки.

**Ключевые слова:** электродуговая наплавка, погонная энергия наплавки, термический цикл, микроструктура, микротвердость, фрактальный анализ, 30ХГСА, WAAM

**Благодарности:** Исследование выполнено при поддержке гранта Российского научного фонда № 22-79-00095 «Разработка научно-технологических основ структурирования конструкционных материалов, полученных путем аддитивного электродугового выращивания для формирования механических свойств при усталости с использованием подходов искусственного интеллекта».

**Для цитирования:** Аносов М.С., Шатагин Д.А., Чернигин М.А., Мордовина Ю.С., Аносова Е.С. Структурирование сплава Nп-30ХГСА при аддитивном электродуговом выращивании. *Известия вузов. Черная металлургия*. 2023;66(3):295–301.

<https://doi.org/10.17073/0368-0797-2023-3-294-301>

## INTRODUCTION

In contemporary manufacturing business, the rapid introduction of new products and optimal utilization of material are crucial requirements [1 – 2]. Wire or powder-based additive manufacturing is a method that can fulfill these requirement [3 – 4].

Numerous 3D-printing technologies exist, but in our assessment, Wire and Arc Additive Manufacturing (WAAM) holds significant promise due to its favorable productivity, low energy consumption, and superior mechanical properties compared to other 3D-printing processes [5 – 7].

Metal components produced through 3D-printing find extensive applications [8]. However, the limited knowledge concerning the structure, mechanical properties and chemical composition changes during 3D printing hampers their widespread adoption [9]. The geometry, chemical composition, and mechanical properties of the deposited material largely depend on the wire composition, 3D-printing conditions, and the duration of interlayer dwell time (thermal cycle properties). During 3D-printing, the newly deposited layer partially melts the previous layer, leading to changes in the structure of the unmelted metal below. Consequently, significant heterogeneity can arise across the thickness of the deposition layer. Fractal analysis, as proposed in papers [10 – 13], can be utilized to estimate this heterogeneity. Anisotropy in mechanical properties and residual stress can be minimized through mechanical or heat treatment [14 – 16].

The objective of this study is to examine the impact of WAAM conditions on the mechanical properties and formation of the metal structure.

## MATERIALS AND METHODS

We conducted a study on printed parts manufactured from the 30KhGSA alloy using a WAAM test bench [17]. The 30KhGSA alloy is widely employed for the production of robust components subjected to dynamic loads and/or high temperatures. Additionally, it finds application in repair welding, and surfacing processes [18]. The chemical composition of the wire is provided in Table 1.

To manufacture the samples, we employed a computer-controlled WAAM process. Various printing conditions were deliberately modified, resulting in the creation of nine wall-shaped samples. Each sample was deposited in a single pass, with a width equivalent to the width of the deposited material. The samples consisted of ten layers in total, and the deposition of metal drops was accomplished through electric arc short circuits. During the WAAM process, a liquid metal drop is initially formed, and the end of the electrode is melted. Subsequently, the drop extends and closes the arc gap. The thin liquid bridge between the electrode and the drop evaporates rapidly due to its high resistance, causing the drop to explode and enters the weld pool. This sequence is repeated throughout the deposition process [19].

The surfacing mode variables include amperage ( $I$ , A), voltage ( $U$ , V), arc gap ( $z$ , mm), wire feed rate ( $V$ , mm/s) and shielding gas flow rate. For all the samples, we maintained a consistent arc gap of 11 mm and a wire feed rate of 200 mm/min, which were determined through preliminary testing. The shielding gas flow rate was not varied during the experiment.

Table 1

### Chemical composition of surfacing wire 30KhGSA

Таблица 1. Химический состав наплавочной проволоки 30ХГСА

Element	C	Mn	Si	P	S	Cr	Ni
Content, %	0.296	1.050	0.950	≤0.025	≤0.025	1.000	0.030

Heat input ( $Q$ ), measured in electric energy per unit of the weld length, was determined according to GOST R ISO 857-1-2009. An energy loss factor of 0.8 was assumed:

$$Q = \frac{0.8IU}{V}.$$

WAAM modes and corresponding heat inputs for each sample are provided in Table 2.

To conduct microstructural analysis, samples were cut out from the deposited walls, reaching the same height as the printed walls. These samples were then polished using a polishing machine, followed by etching in a 4 % aqueous solution of nitric acid.

Chemical composition analysis was performed using a Foundry-Master optical emission analyzer with a sensitivity of approximately 0.001 %.

Microhardness evaluation was carried out using a Fischerscope HM2000 hardness tester. A square-based diamond pyramid indenter with an angle of  $\alpha = 136$  was employed. Microhardness measurements were conducted along the entire height of the deposited wall, applying a 50 g load. The load was held for 10 s, and the distance between adjacent hardness test points was 0.2 mm. Approximately five hardness measurements were taken in each area of interest, and the results were averaged.

Fractal analysis, as demonstrated by Gonchar et al. [20], was utilized to assess the surfacing microstructure and quality. Fractal dimension of the microstructure image was obtained through fractal analysis at different magnifications. A software package for this purpose was developed and registered under No. 2022666922 as

the “Software for Microstructure And Structural Damage Assessment”.

To facilitate comparative analysis, measurements were conducted in three regions of interest: the base, middle, and top of the deposited metal wall.

## RESULTS AND DISCUSSION

In order to assess the surfacing process efficiency, we measured the dimensions of the deposited walls and estimated the cross-section areas of the samples. The results of these measurements are presented in Table 3.

Fig. 1 illustrates the relationships between the cross-section area of the deposited layer (per one deposited bead)  $S_{\text{bead}}$ , and the heat input  $Q$  at different voltage values  $U$ .

These relationships clearly demonstrate the significant impact of input energy and deposition voltage on the speed of the 3D-printing process. For example, increasing the heat input at a constant voltage leads to a substantial and consistent increase in the process speed.

Figs. 2 – 4 depict micrographs of samples 1, 5 and 9, taken at cross-sections along the height of the deposited wall.

The microstructure of the sample 1 wall near the substrate is predominantly composed of tempered bainite (Fig. 2, a). This structure formation can be attributed to the following factors.

- The relatively high cooling rate experienced by the layer in contact with the St3 (DIN analog: USt 37-2) steel grade substrate, which possesses a high thermal conductivity coefficient of 55 W/(m·K) at 20 °C. In compari-

Table 2

### WAAM modes

Таблица 2. Режимы наплавки

Sample No.	1	2	3	4	5	6	7	8	9
$I$ , A	120	160	200	120	160	200	120	160	200
$U$ , V	18	18	18	24	24	24	27	27	27
$Q$ , J/mm	518.4	691.2	864.0	691.2	921.6	1152.0	777.6	1036.8	1296.0

Table 3

### Geometric parameters of the billets obtained by 3D-printing

Таблица 3. Геометрические параметры образцов, полученных при помощи 3D-печати

Billet No.	1	2	3	4	5	6	7	8	9
$H$ , mm	21.0	23.8	30.0	15.0	18.1	21.8	13.5	15.5	17.9
$B$ , mm	8.2	10.0	12.5	10.0	11.8	13.5	10.8	13.3	14.4
$S$ , mm <sup>2</sup>	172.20	238.00	375.00	150.00	213.58	294.30	145.80	206.15	257.76

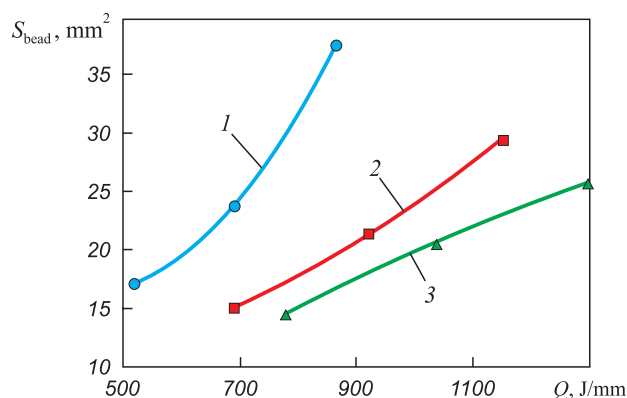


Fig. 1. Dependence of cross-sectional area on the value of surfacing process input energy at different voltage levels in terms of one deposited roller:  
1 – 18 V; 2 – 24 V; 3 – 27 V

Рис. 1. Зависимость площади поперечного сечения в пересчете на один наплавленный валик от величины погонной энергии процесса наплавки при различных уровнях напряжения: 1 – 18 В; 2 – 24 В; 3 – 27 В

son, the thermal conductivity coefficient for 30HGSA is  $38 \text{ W}/(\text{m} \cdot \text{K})$ , while air has a coefficient of  $0.0259 \text{ W}/(\text{m} \cdot \text{K})$ . Consequently, the cooling rate of the deposited metal is higher in contact with the substrate.

- The introduction of heat during the deposition of subsequent layers, leading to both quenching and tempering.

In the middle of the sample, the bainite structure is predominantly maintained, as shown in Fig. 2, *b*. However, other structural components, such as troostosorbite, are also noticeable. The cooling rate of this region after the deposition of a single layer is below the critical rate required for the diffusive decomposition of austenite. The energy input during the deposition of subsequent layers is sufficient for tempering as well.

The microstructure at the top of the sample differs from that at the base. It mainly consists of sorbite and ferrite. This structure can be explained by the following factors:

- cooling occurs in the air, which has a very low thermal conductivity coefficient (as mentioned above), without reaching critical cooling rates necessary for quenching;

- the absence of subsequent heat treatment that would induce phase recrystallization and tempering.

A chemical carbon liquation likely occurs in this region, evidenced by clear stripes (Fig. 2, *c*). The columnar grain structure is a result of heat dissipation as the deposited layer cools. Without subsequent heat treatment, the microstructure remains unchanged. It is important to note that this region exhibits significant non-homogeneity in grain size, which can have adverse effects on the mechanical properties.

Proper heat treatment can eliminate the non-homogeneity in grain size and improve the microstructure.

Normalization or toughening can indeed be employed to address the non-homogeneity and improve the microstructure of the samples.

In the microstructure of sample 5, similar to sample 1, tempered bainite is observed near the substrate (Fig. 3, *a*). The structure transitions from bainite to troostosorbite in the middle, with the top layer consisting of sorbite. The transition between structures in this sample is smoother (Fig. 3, *b*). Importantly, all regions of this sample do not exhibit grain non-homogeneity or columnar grains in the last deposited layer (Fig. 3, *c*).

Sample 9 near the substrate displays a microstructure comprising tempered bainite with inclusions of other structures, such as troostosorbite. The microstructure in this region is generally coarser and more heterogeneous compared to other samples. However, the bainite gradually transforms into troostosorbite from the bottom to the middle of the sample. The middle of the sample contains larger grains compared to samples 1 and 5, likely due to the higher heat input during deposition (Fig. 4, *b*). The top layer of the sample consists of troostite and ferrite, with a highly heterogeneous microstructure across the sample section.

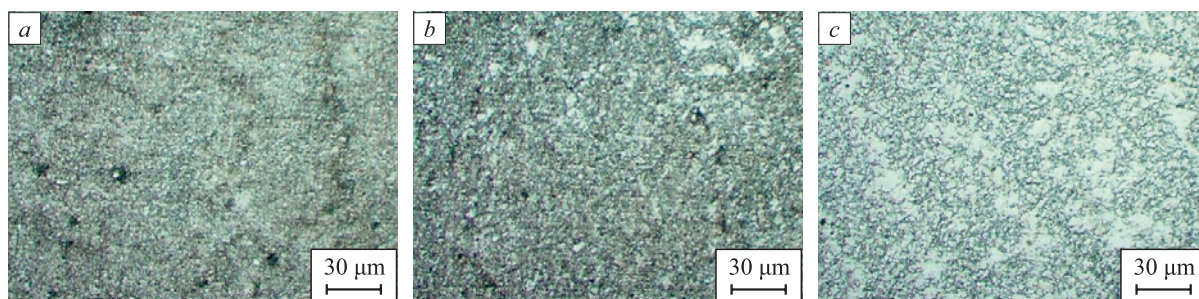


Fig. 2. Microstructure of the deposited wall near the substrate (*a*), in the center of the sample (*b*) and at its apex (*c*) (steel 30KhGSA, sample 1,  $Q = 518.4 \text{ J/mm}$ )

Рис. 2. Микроструктура наплавленной стенки вблизи подложки (*a*), в центре образца (*b*) и в его вершине (*c*) (сталь 30ХГСА, образец 1,  $Q = 518,4 \text{ Дж/мм}$ )



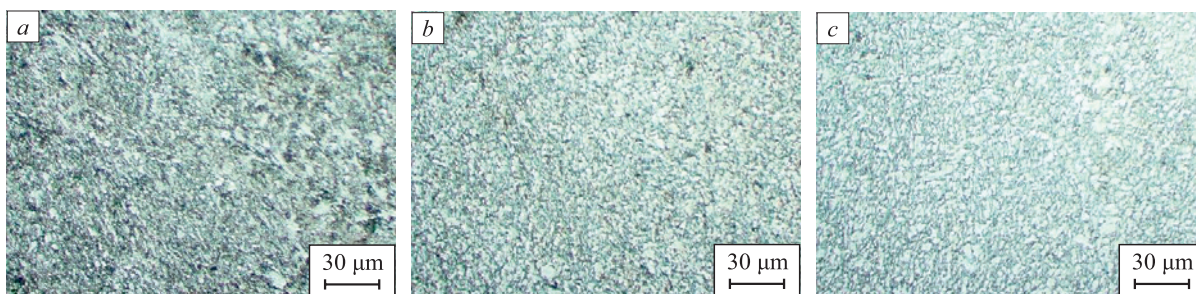


Fig. 3. Microstructure of the deposited wall near the substrate (a), in the center of the sample (b) and at its apex (c) (steel 30KhGSA, sample 5,  $Q = 921.6$  J/mm)

Рис. 3. Микроструктура наплавленной стенки вблизи подложки (a), в центре образца (b) и в его вершине (c) (сталь 30ХГСА, образец 5,  $Q = 921,6$  Дж/мм)

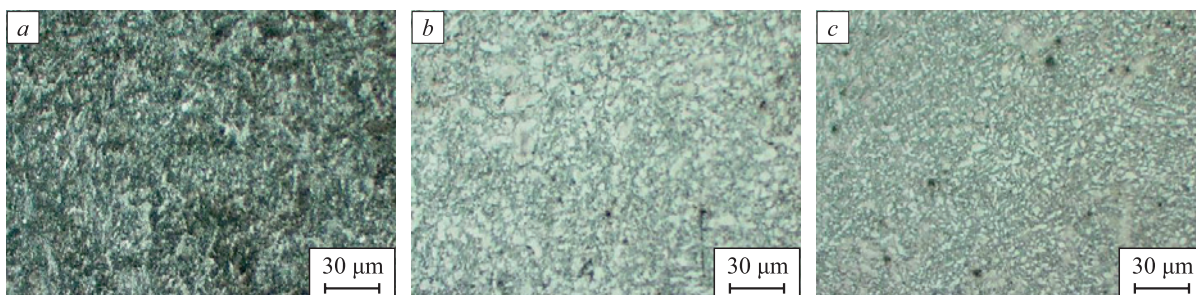


Fig. 4. Microstructure of the deposited wall near the substrate (a), in the center of the sample (b) and at its apex (c) (steel 30KhGSA, sample 9,  $Q = 1296$  J/mm)

Рис. 4. Микроструктура наплавленной стенки вблизи подложки (a), в центре образца (b) и в его вершине (c) (сталь 30ХГСА, образец 9,  $Q = 1296$  Дж/мм)

Through the microstructure analysis of the samples produced under different surfacing modes, it was determined that sample 5 ( $I = 160$  A,  $U = 24$  V,  $Q = 921.6$  J/mm) possesses the most favorable metal structure. The micrographs of the samples did not reveal substantial structural defects commonly found in castings and welded parts, such as large pores or shrinkage cavities. However, micropores, grain non-homogeneity, and a heterogeneous structure were observed. These disadvantages can be mitigated through appropriate heat treatment. It is worth noting that all surfacing modes yielded fine-grained and highly dispersed structures.

Furthermore, the  $D_F$  fractal dimensions of the microstructures obtained under different WAAM conditions along the entire height of the deposited walls were estimated, excluding the first and last layers (machining allowance) (refer to Fig. 5). Variations in the fractal dimensions along the height of the deposited wall indicate significant structural changes, particularly in the sample manufactured at higher energy input.

Fig. 6 illustrates the variations in the  $\Delta D_F$  fractional dimension, which contribute to the structural heterogeneity of the metal along the height of the sample.

The optimal heat input for achieving structural homogeneity along the wall height is approximately 900 J/mm.

At lower heat input values, the structure becomes more heterogeneous, exhibiting a large number of pores and unmelted wire fragments, which is considered unacceptable. Conversely, higher heat input values result in significant heat transfer to the solidified and cooled metal,

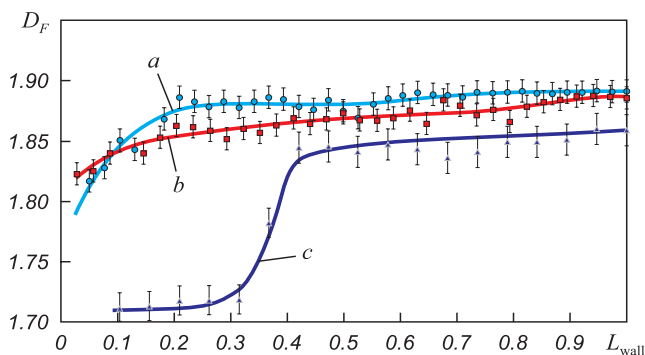


Fig. 5. Dependence of the microstructural image fractal dimension on the fraction of the deposited wall height  $L_w$  at different values of surfacing input energy of: sample 1 –  $Q = 518.4$  J/mm (a); sample 5 –  $Q = 921.6$  J/mm (b); sample 9 –  $Q = 1296$  J/mm (c)

Рис. 5. Зависимость фрактальной размерности изображения микроструктур сплавов от доли высоты наплавленной стенки  $L_{ст}$  при различных значениях погонной энергии наплавки: образец 1 –  $Q = 518,4$  Дж/мм (a); образец 5 –  $Q = 921,6$  Дж/мм (b); образец 9 –  $Q = 1296$  Дж/мм (c)

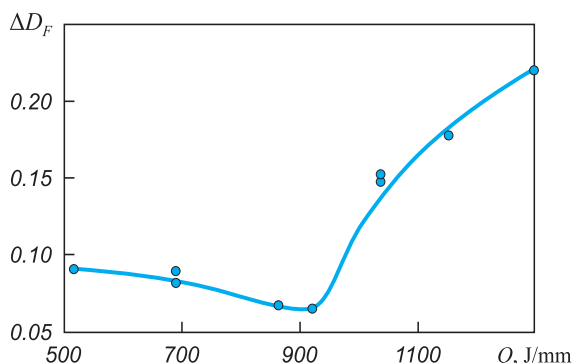


Fig. 6. Spread of the fractal dimension values  $\Delta D_F$  of microstructural images from the values of surfacing input energy

Рис. 6. Величина разброса значений фрактальной размерности  $\Delta D_F$  изображения микроструктуры от погонной энергии наплавки

leading to microstructural changes such as phase recrystallization, hardening, and tempering. These changes cause the metal structure along the wall cross-section to become highly heterogeneous.

In order to assess the effects of surfacing modes on the material properties, microhardness measurements were conducted. Fig. 7 depicts the relationship between microhardness and heat input during the surfacing process.

As shown in Fig. 7, heat input has a notable impact on microhardness. With increasing heat input, the average microhardness decreases monotonically along the height of the sample. This phenomenon is primarily attributed to the elevated temperature in the fusion zone resulting from higher heat input. The increased temperature leads to the burning out of certain chemical elements, particularly carbon, and a subsequent loss of strength. The grain size experiences minimal changes, which is confirmed by the chemical analysis of the samples. For instance, as the heat input surpasses 900 J/mm, the carbon content in the alloy decreases from 0.3 % to 0.2 %, silicon decreases

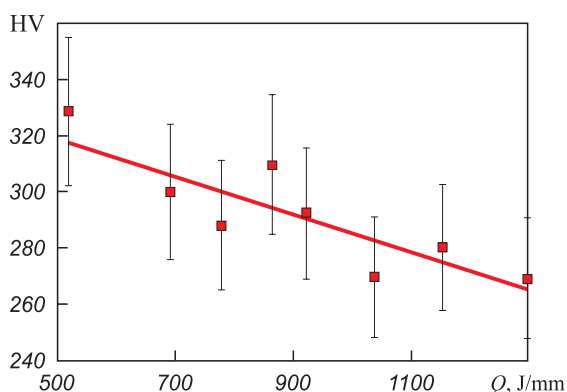


Fig. 7. Dependence of 30KhGSA alloy microhardness on the values of surfacing input energy

Рис. 7. Зависимость микротвердости сплава 30ХГСА от погонной энергии процесса наплавки

from 1 to 0.75 % and magnesium decreases from 1 % to 0.7 %.

The microhardness analysis also reveals the following: samples produced with a heat input of up to 900 J/mm exhibit relatively consistent microhardness along the entire height of the deposited wall. However, at higher heat input levels, the microhardness gradually increases from the base to the top of the sample, with more pronounced differences in the upper layers. The higher hardness observed in the top layers can be attributed to their shorter exposure to critical temperatures, preventing significant tempering from occurring.

## CONCLUSIONS

This study determined that an optimal heat input of approximately 921.6 J/mm is suitable for the WAAM 3D-printing mode for Np-30KhGSA alloy. The specific conditions for achieving this optimal heat input are as follows: amperage of 160 A, voltage of 24 V, and a printing speed of 200 mm/min. The shielding gas used is a mixture of 80 % Ar and 20 % CO<sub>2</sub>, delivered at a flow rate of 15 l/min. Under these optimized process conditions, the microstructure of the printed parts does not exhibit any pores or unmelted wire fragments, indicating a high level of material integrity. Additionally, the printing speed is considered sufficient, as indicated in Table 2, and the level of structural heterogeneity observed is insignificant, as demonstrated in Fig. 4).

## REFERENCES / СПИСОК ЛИТЕРАТУРЫ

1. Jackson M.A., Van Asten A., Morrow J.D., Min S., Pfefferkorn F.E. Energy consumption model for additive-subtractive manufacturing processes with case study. *International Journal of Precision Engineering and Manufacturing-Green Technology*. 2018;5(4):459–466. <https://doi.org/10.1007/s40684-018-0049-y>
2. Pinto-Lopera J.E., Motta J.M.S.T., Absi Alfaro S.C. Real-time measurement of width and height of weld beads in GMAW processes. *Sensors*. 2016;16(9):1500. <https://doi.org/10.3390/s16091500>
3. Li J.L.Z., Alkahari M.R., Rosli N.A.B., Hasan R., Sudin M.N., Ramli F.R. Review of wire arc additive manufacturing for 3D metal printing. *International Journal of Automation Technology*. 2019;13(3):346–353. <https://doi.org/10.20965/ijat.2019.p0346>
4. Kah P., Latifi H., Suoranta R., Martikainen J., Pirinen M. Usability of arc types in industrial welding. *International Journal of Mechanical and Materials Engineering*. 2014;9:15. <https://doi.org/10.1186/s40712-014-0015-6>
5. Ding D., Pan Z., Cuiuri D., Li H. Wire-feed additive manufacturing of metal components: technologies, developments and future interests. *The International Journal of Advanced Manufacturing Technology*. 2015;81:465–481. <https://doi.org/10.1007/s00170-015-7077-3>
6. Wu B., Pan Z., Ding D., Cuiuri D., Li H., Xu J., Norrish J. A review of the wire arc additive manufacturing of metals:



- Properties, defects and quality improvement. *Journal of Manufacturing Processes*. 2018;35:127–139. <https://doi.org/10.1016/j.jmapro.2018.08.001>
7. Anosov M.S., Shatagin D.A., Mikhailov A.M., Andronov D.V. Rationale for the use of 3D-printing technology by electric arc welding to obtain parts in small-scale production. *Actual Problems of Science and Education in the Context of Modern Challenges: Proceedings of the XIII Int. Sci. and Prac. Conf., Moscow, August 15, 2022*. Moscow: Pechatnyi tsekh; 2022:291–295. (In Russ.).  
Аносов М.С., Шатагин Д.А., Михайлов А.М., Андронов Д.В. Обоснование применения технологии 3D-печати электродуговой наплавкой для получения деталей в условиях мелкосерийного производства. *Актуальные проблемы науки и образования в условиях современных вызовов: Сборник материалов XIII Международной научно-практической конференции, Москва, 15 августа 2022 года*. Москва: Печатный цех; 2022:291–295.
  8. Kudryashov V.A., Lapyshev A.A. Creation of additive technologies according to fatigue behaviour of material in aviation engineering. *Izvestiya Samarskogo nauchnogo tsentra Rossiiskoi akademii nauk*. 2018;20(4–3(84)):406–413. (In Russ.).  
Кудряшов В.А., Лапышев А.А. Создание аддитивных технологий с учетом усталостного поведения материала в авиационном инжиниринге. *Известия Самарского научного центра Российской академии наук*. 2018; 20(4–3(84)):406–413.
  9. Kubanova A.N., Sergeev A.N., Dobrovol'skii N.M., Gvozdev A.E., Medvedev P.N., Maliy D.V. Materials and technologies for production products by additive manufacturing. *Chebyshevskii Sbornik*. 2019;20(3):453–477. (In Russ.). <https://doi.org/10.22405/2226-8383-2019-20-3-453-477>  
Кубанова А.Н., Сергеев А.Н., Добровольский Н.М., Гвоздев А.Е., Медведев П.Н., Малий Д.В. Особенности материалов и технологий аддитивного производства изделий. *Чебышевский сборник*. 2019;20(3):453–477. <https://doi.org/10.22405/2226-8383-2019-20-3-453-477>
  10. Garashchenko Y., Glushko A., Kobets O., Harashchenko O. Fractal analysis of structural and phase changes in the metal of welded steam pipe joints. *Advances in Design, Simulation and Manufacturing IV*. DSMIE 2021. *Lecture Notes in Mechanical Engineering*. [https://doi.org/10.1007/978-3-030-77719-7\\_4](https://doi.org/10.1007/978-3-030-77719-7_4)
  11. Krasikova I.E., Krasikov I.V., Kartuzov V.V. Correlation of fractal characteristics of the material structure by electron-microscopic images of the sample surface with their physical and mechanical properties *Elektronnaya mikroskopiya i prochnost' materialov. Seriya: Fizicheskoe materialovedenie, struktura i svoystva materialov*, 2016;(22):3–9. (In Russ.).  
Красикова И.Е., Красиков И.В., Картузов В.В. Корреляция значений фрактальных характеристик структуры материала по электронно-микроскопическим фотографиям поверхности образцов со значениями их физико-механических характеристик. *Электронная микроскопия и прочность материалов. Серия: Физическое материаловедение, структура и свойства материалов*. 2016;(22):3–9.
  12. Zaiser M., Bay K., Hähner P. Fractal analysis of deformation-induced dislocation patterns. *Acta Materialia*. 1999;47(8):2463–2476. [https://doi.org/10.1016/S1359-6454\(99\)00096-8](https://doi.org/10.1016/S1359-6454(99)00096-8)
  13. Kabaldin Y.G., Anosov M.S., Shatagin D.A. Evaluation of the mechanism of the destruction of metals based on approaches of artificial intelligence and fractal analysis. *IOP Conference Series: Materials Science and Engineering*. 2020;709:033076. <https://doi.org/10.1088/1757-899X/709/3/033076>
  14. Rodrigues T.A., Duarte V., Miranda R.M., Santos T.G., Oliveira J.P. Current status and perspectives on wire and arc additive manufacturing (WAAM). *Materials (Basel)*. 2019;12(7):1121. <https://doi.org/10.3390/ma12071121>
  15. Bai X., Zhang H., Wang G. Modeling of the moving induction heating used as secondary heat source in weld-based additive manufacturing. *The International Journal of Advanced Manufacturing Technology*. 2015;77:717–727. <https://doi.org/10.1007/s00170-014-6475-2>
  16. Donoghue J., Antonyamy A.A., Martina F., Colegrove P.A., Williams S.W., Prangnell P.B. The effectiveness of combining rolling deformation with Wire–Arc Additive Manufacture on  $\beta$ -grain refinement and texture modification in Ti–6Al–4V. *Materials Characterization*. 2016;114:103–114. <https://doi.org/10.1016/j.matchar.2016.02.001>
  17. Kabaldin Yu.G., Shatagin D.A., Anosov M.S., Kolchin P.V., Kiselev A.V. Diagnostics of 3D-printing on a CNC machine using machine learning approaches. *Vestnik mashinostroyeniya*. 2021;(1):55–59. (In Russ.). <https://doi.org/10.36652/0042-4633-2021-1-55-59>  
Кабалдин Ю.Г., Шатагин Д.А., Аносов М.С., Колчин П.В., Киселев А.В. Диагностика процесса 3D-печати на станке с ЧПУ с использованием подходов машинного обучения. *Вестник машиностроения*. 2021;(1):55–59. <https://doi.org/10.36652/0042-4633-2021-1-55-59>
  18. Chinakhov D.A. Research and development of technology for welding multilayer joints from 30KhGSA steel, providing guaranteed quality of welded joints with minimal resource and labor costs. *Sovremennye naukoemkie tekhnologii*. 2006;(3):73–75. (In Russ.).  
Чинахов Д.А. Исследование и разработка технологии сварки многослойных соединений из стали 30ХГСА, обеспечивающей гарантированное качество сварных соединений с минимальными ресурсо- и трудозатратами. *Современные наукоемкие технологии*. 2006;(3):73–75.
  19. Atroshchenko V.V., Tefanov V.N., Kraev K.A. On control of metal transfer during welding by consumable electrode with a short circuit of arc interval. *Vestnik Ufmskogo gosudarstvennogo aviatsionnogo tekhnicheskogo universiteta*. 2008;11(2):146–154.  
Атрощенко В.В., Тэфанов В.Н., Краев К.А. К вопросу об управлении переносом электродного металла при дуговой сварке плавящимся электродом с короткими замыканиями дугового промежутка. *Вестник Уфимского государственного авиационного технического университета*. 2008;11(2):146–154.
  20. Gonchar A.V., Kurashkin K.V., Andreeva O.V., Anosov M.S., Klyushnikov V.A. Fatigue life prediction of structural steel using acoustic birefringence and characteristics of persistent slip bands. *Fatigue & Fracture of Engineering Materials & Structures*. 2022;45(1):101–112. <https://doi.org/10.1111/ffe.13586>

## Information about the Authors

**Maksim S. Anosov**, Cand. Sci. (Eng.), Assist. Prof. of the Chair “Technology and Equipment Engineering”, R.E. Alekseev Nizhny Novgorod State Technical University

**E-mail:** anosov-maksim@list.ru

**Dmitrii A. Shatagin**, Cand. Sci. (Eng.), Assist. Prof. of the Chair “Technology and Equipment Engineering”, R.E. Alekseev Nizhny Novgorod State Technical University

**E-mail:** dmitsanych@gmail.com

**Mikhail A. Chernigin**, Engineer, R.E. Alekseev Nizhny Novgorod State Technical University

**E-mail:** dmitsanych@gmail.com

**Yuliya S. Mordovina**, Academic Activity Engineer, R.E. Alekseev Nizhny Novgorod State Technical University

**E-mail:** ips4@nntu.ru

**Ekaterina S. Anosova**, Assistant, R.E. Alekseev Nizhny Novgorod State Technical University

**E-mail:** katena.zav@mail.ru

## Сведения об авторах

**Максим Сергеевич Аносов**, к.т.н., доцент кафедры «Технология и оборудование машиностроения», Нижегородский государственный технический университет им. Р.Е. Алексеева

**E-mail:** anosov-maksim@list.ru

**Дмитрий Александрович Шатагин**, к.т.н., доцент кафедры «Технология и оборудование машиностроения», Нижегородский государственный технический университет им. Р.Е. Алексеева

**E-mail:** dmitsanych@gmail.com

**Михаил Алексеевич Чернигин**, инженер, Нижегородский государственный технический университет им. Р.Е. Алексеева

**E-mail:** dmitsanych@gmail.com

**Юлия Сергеевна Мордовина**, инженер по учебному процессу, Нижегородский государственный технический университет им. Р.Е. Алексеева

**E-mail:** ips4@nntu.ru

**Екатерина Сергеевна Аносова**, ассистент, Нижегородский государственный технический университет им. Р.Е. Алексеева

**E-mail:** katena.zav@mail.ru

## Contribution of the Authors

**M. S. Anosov** – drawing up experimental plan, fractal analysis of images of microstructures, scientific guidance.

**D. A. Shatagin** – surfacing of experimental samples and their mechanical processing.

**M. A. Chernigin** – metallographic analysis, microhardness measurement, chemical analysis of the billets after surfacing.

**Yu. S. Mordovina** – metallographic analysis, microhardness analysis, design and editing of the article.

**E. S. Anosova** – analysis of changes in the alloy chemical composition, analysis of the samples geometry.

## Вклад авторов

**М. С. Аносов** – составление плана экспериментального исследования, фрактальный анализ изображений микроструктур, научное руководство.

**Д. А. Шатагин** – проведение наплавки и механической обработки экспериментальных образцов

**М. А. Чернигин** – металлографический анализ, измерение микротвердости, проведение химического анализа заготовок после наплавки.

**Ю. С. Мордовина** – металлографический анализ, анализ микротвердости, оформление и редактирование статьи.

**Е. С. Аносова** – анализ изменения химического состава сплава и геометрии образцов.

Received 15.03.2023

Revised 19.04.2023

Accepted 24.04.2023

Поступила в редакцию 15.03.2023

После доработки 19.04.2023

Принята к публикации 24.04.2023





UDC 621.762:537.523.4

DOI 10.17073/0368-0797-2023-3-302-310



Original article

Оригинальная статья

## ELECTROSPARK DEPOSITION OF METALLOKERAMIC Fe–Al/HfC COATING ON STEEL 1035

A. A. Burkov, M. A. Kulik

Institute of Materials Science of the Khabarovsk Federal Research Center, Far-Eastern Branch of the Russian Academy of Sciences (153 Tikhookeanskaya Str., Khabarovsk 680000, Russian Federation)

✉ marijka80@mail.ru

**Abstract.** To improve the tribotechnical behavior and heat resistance of steel 1035, composite metalloceramic Fe–Al/HfC coatings were prepared by electrospark deposition. A non-localized anode was used as an electrode consisting of a mixture of iron and aluminum granules with a molar ratio of 3:2 and with the addition of HfC powder. The cathode gain had positive values indicating that HfC powder can be deposited on steel 1035 using the Fe<sub>60</sub>Al<sub>40</sub> anode mixture. Moreover, the cathode gain monotonically increased with the increase in addition of HfC powder to the anode mixture. The coatings structure is represented by a matrix of FeAl intermetallic compound reinforced with HfC grains, which corresponds to the structure of a metalloceramic composite. Concentration of HfC in the coating increased with the addition of HfC powder to the anode mixture. Deposition of Fe–Al/HfC coatings according to the proposed technique allows reducing the friction coefficient of steel 1035 from 6 to 40 vol. %. Depending on the concentration of HfC in the anode mixture, the wear resistance of Fe–Al/HfC coatings varied nonmonotonically with a maximum at 8 vol. %. The use of Fe–Al/HfC coatings makes it possible to increase the wear resistance of the steel surface to 10 times. Comparison of the final weight gain of the samples after 100 h of oxidation resistance tests at a temperature of 700 °C allows us to conclude that electrospark deposition Fe–Al/HfC coatings can increase the oxidation resistance of steel 1035 by 1.7–2.2 times. Analysis of the study results shows that adhesion of Fe–Al composition to HfC is weak. This was reflected in decrease in hardness, wear resistance and oxidation resistance of coatings with an increase in the concentration of HfC in the anode mixture above 8 vol. %.

**Keywords:** electrospark deposition, intermetallic compound FeAl, coating, hafnium carbide, steel 1035, wear, oxidation resistance

**For citation:** Burkov A.A., Kulik M.A. Electrospark deposition of metalloceramic Fe–Al/HfC coating on steel 1035. *Izvestiya. Ferrous Metallurgy*. 2023;66(3):302–310. <https://doi.org/10.17073/0368-0797-2023-3-302-310>

## ЭЛЕКТРОИСКРОВОЕ ОСАЖДЕНИЕ МЕТАЛЛОКЕРАМИЧЕСКОГО Fe–Al/HfC ПОКРЫТИЯ НА СТАЛЬ 35

А. А. Бурков, М. А. Кулик

Институт материаловедения Хабаровского Федерального исследовательского центра Дальневосточного отделения РАН (Россия, 680000, Хабаровск, ул. Тихоокеанская, 153)

✉ marijka80@mail.ru

**Аннотация.** Для улучшения триботехнического поведения и жаростойкости стали 35 были приготовлены методом электроискрового легирования композиционные металлокерамические Fe–Al/HfC покрытия. В качестве электрода использовался нелокализованный анод, состоящий из смеси железных и алюминиевых гранул с молярным соотношением 3:2, и с добавлением порошка карбида гафния. Привес катода имел положительные значения, свидетельствующие о том, что порошок карбида гафния может осаждаться на сталь 35 с использованием анодной смеси Fe<sub>60</sub>Al<sub>40</sub>. Привес катода монотонно увеличивался с ростом добавки порошка HfC в анодную смесь. Структура покрытий представлена матрицей из интерметаллида FeAl, армированной зернами карбида гафния, что соответствует структуре металлокерамического композита. Концентрация карбида гафния в покрытии увеличивалась с ростом добавки порошка HfC в анодную смесь. Осаждение Fe–Al/HfC покрытий по предложенной методике приводит к снижению коэффициента трения стали 35 от 6 до 40 %. В зависимости от концентрации карбида гафния в анодной смеси, износостойкость Fe–Al/HfC покрытий изменялась немонотонно с максимумом при 8 % (об.). Применение Fe–Al/HfC покрытий позволяет повысить износостойкость поверхности стали 35 до 10 раз. Сравнение итогового привеса образцов после 100 ч испытаний на жаростойкость при температуре 700 °C дает возможность заключить, что электроискровые Fe–Al/HfC покрытия способствуют повышению жаростойкости стали 35 от 1,7 до 2,2 раза. Анализ результатов проведенного исследования позволяет сделать заключение о слабой адгезии Fe–Al композиции к карбиду гафния. Это отразилось в снижении твердости, износостойкости и жаростойкости покрытий при повышении концентрации HfC в анодной смеси выше 8 % (об.).

**Ключевые слова:** электроискровое легирование, интерметаллид FeAl, покрытие, карбид гафния, сталь 35, износ, жаростойкость

**Для цитирования:** Бурков А.А., Кулик М.А. Электронное осаждение металлокерамического Fe–Al/HfC покрытия на сталь 35. Известия вузов. Черная металлургия. 2023;66(3):303–310. <https://doi.org/10.17073/0368-0797-2023-3-302-310>

## INTRODUCTION

Steel 1035 is a common structural material used for manufacturing such components as crankshafts, axles, connecting rods, spindles, sprockets, disks, pins, cams, pushrods, etc. [1]. It has such disadvantages as low wear, corrosion, and heat resistance which limits its applications [2]. Protective coatings can improve the heat, corrosion and wear resistance of medium-carbon steels [3; 4].

Metalloceramic matrix composites (MMC) are promising coating materials. They consist of a metal matrix reinforced with hard ceramic particles [5; 6].

Iron aluminides can be an efficient metal matrix in such coatings [7]. They have high heat (up to 1000 °C) and corrosion resistance in oxidizing and reducing environments, since the aluminum content is higher than in steels and heat-resistant alloys [8]. Yürektürk Y. et al. [9] report that Fe–Al coatings make steel component surfaces harder, and enhance wear and corrosion resistance. As noted by Pal M. et al. [10] The thermal expansion coefficient of iron aluminides matches that of most steel grades. For this reason, such coatings have high adhesion [10].

Hafnium carbide (HfC) is one of the hard-melting binary compounds. Toth L. et al. [11] reported that its melting point is 3928 °C. As noted by Hans K. et al. [12], HfC with high heat resistance is used in solar absorber coatings. Zang K. et al. [1] indicated that hafnium carbide is a highly suitable ceramic coating on steel substrates for its unique properties, such as high hardness, thermal and electrical conductivity and chemical stability [13]. For this reason, hafnium carbide can be used as reinforcement in MMC coatings. However, HfC coatings have poor heat resistance [14], since the crystalline hafnium carbide powder oxidizes at 430 °C and up [15]. Therefore, it is combined with a heat-resistant metal matrix to obtain high-temperature, wear-resistant coatings. The combination of solid hafnium carbide and heat-resistant Fe–Al matrix produces a successful MMC coating for steel 1035 parts operated at high temperatures.

We studied electrospray deposition (ESD) of HfC/Fe–Al coatings. It is a simple process with low requirements for the substrate surface finish. ESD results in metallurgical bonding between the coating and the substrate [16]. The authors also successfully applied a WC/Fe–Al coating to stainless steel using a modified electrospray deposition with a bulk electrode (EDBE). We used a bulk electrode made of Fe<sub>40</sub>Al<sub>60</sub> pellets also containing tungsten carbide [7]. This composition was selected since the substrate iron is involved in the formation of the FeAl intermetallic. It was found that aluminum dominated over

iron in the binder composition due to its lower melting point. Therefore, for the deposition of Fe–Al/HfC coatings, we used Fe<sub>60</sub>Al<sub>40</sub> bulk electrodes with a lower aluminum content.

The purpose of this study is to analyze the effect of hafnium carbide powder content in a Fe<sub>60</sub>Al<sub>40</sub> BE on the structure, wear, and heat resistance the of Fe–Al/HfC metal-ceramic electrodeposited coating on a steel 1035 substrate.

## MATERIALS AND METHODS

The substrates were diameter 12 mm, 10 mm high cylinders made of steel 1035. The bulk electrode was made of a mixture of iron and aluminum pellets, and varying amounts of hafnium carbide powder (99.6 % purity, 1.5 ± 0.5 µm average particle diameter). Refer to 1). The powder includes the HfC phase with a small admixture of hafnium metal (Fig. 1). The pellets were cylinders 4 ± 1 mm long cut off steel St3 and aluminum alloy 1188 bars, 4 ± 0.5 mm dia. The ratio of pellets in the BE was such that the iron-to-aluminum molar ratio was 3:2. The IMES-40 pulse generator produced rectangular current pulses, 110 A peak value, at 30 V with a 100 µs duration and a 1000 µs period. The substrate was connected to the negative lead of a pulse generator. A container with Fe<sub>60</sub>Al<sub>40</sub> pellets and HfC powder was connected to the positive lead. The substrate was half-immersed into the pellet layer. See Burkov A. et al. [17] for a detailed description of the bulk electrode electrodeposition test bench. Argon was supplied into the container at a 5 l/min rate, in order to prevent oxidation. The pellets were pretreated, in order to saturate their surface with HfC powder for 10 min. The total coating application time was also 10 min.

The phase composition of the samples was studied using a DRON-7 X-ray diffractometer, CuK<sub>α</sub> band. We used PDWin software to identify the XRD pat-

Table 1

### Composition of non-localized electrode

Таблица 1. Состав нелокализованного электрода

Samples	Pellets ratio, at. %		HfC fraction, vol. %
	Fe	Al	
Hf4	60	40	4
Hf8			8
Hf12			12

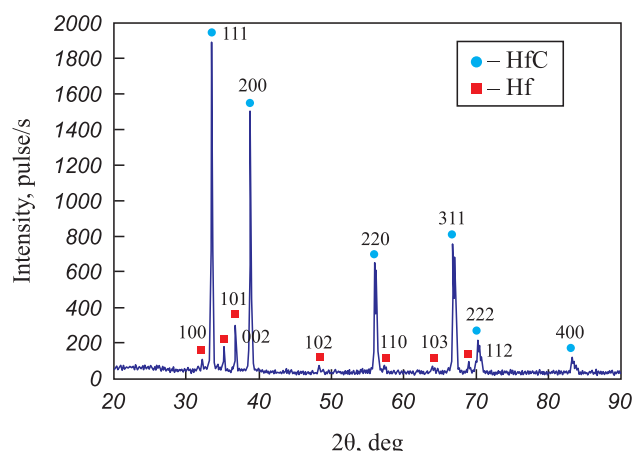


Fig. 1. X-ray diffraction pattern of HfC powder

Рис. 1. Рентгеновская дифрактограмма порошка карбида гафния

terns. The surface microrelief and elemental composition of the sample were analyzed with a Vega 3 LMH scanning electron microscope (SEM) (Tescan, Czech Republic) equipped with an X-max 80 energy dispersive X-ray spectrometer (Oxford Instruments) (EDS). The hardness was measured with a PMT-3M microhardness tester at 0.5 N (Vickers method). Wear resistance was tested according to ASTM G99-17 (dry sliding friction using) an R6M5 HSS disk counterbody sliding at 0.47 m/s under a 25 and 70 N load. At least three measurements were made for each sample. The wear was assessed by the gravimetric method with a 0.1 mg accuracy. The wear rate was estimated as

$$W = \frac{\Delta m}{\rho Pl},$$

where  $\Delta m$  is the mass loss due to abrasion;  $\rho$  is the coating density assumed to be equal to the density of steel 1035;  $P$  is the load;  $l$  is the friction path length.

The samples were wear-tested after each weight measurement, in order to eliminate the error caused by a possible change in the counterbody surface properties. For heat resistance tests, the samples were placed in an oven at 700 °C. The total testing time was 100 h. The samples were held at this temperature for ~6 h, then removed from the oven and cooled to room temperature in a dryer. The samples were placed in a corundum crucible, in order to record the mass of the detached oxides. The sample weight changes were measured with lab scales, with 0.1 mg accuracy.

## RESULTS AND DISCUSSION

Studying the cathode weight evolution during electrospark deposition of new electrode materials is aimed at identifying cathode weight gain and the optimal treatment time. If the cathode loses weight, the process is inef-

ficient. If the relative weight gain is low, the coating will be thin and non-continuous. The EDBE process generates electrical discharges between the steel pellets and the substrate, resulting in liquid metal transfer from the pellet surface to the substrate. Hafnium carbide powder particles occur on the surface of the electrodes at the time of discharge fuse with the metal. It leads to cathode weight gain (Fig. 2, *a*). After two minutes, the cathode weight gain rate slows down for all the bulk electrode materials. This can be explained by the accumulation of defects in the doped layer, and more intense electrical erosion as the number of discharges grows [18]. When the hafnium carbide concentration in the BE material increases from 4 to 12 vol. %, the cathode weight gain increases linearly from 9.96 to 26.1 mg/cm<sup>2</sup>. Such mass transfer can be explained by better conditions for electric discharges and higher discharge frequency with the increase of the HfC powder concentration in the granules. Previously we also observed a positive correlation between the powder concentration in the BE material and the cathode weight gain for Cr<sub>3</sub>C<sub>2</sub>, TaC, and WC powders [19 – 21]. However, this relation can be inversed in other powders [22]. Therefore, further study of the powder composition and particle size distribution effects would be of interest.

Fig. 2, *b* shows the XRD patterns of the coatings. The coatings contain hafnium carbide and intermetallic FeAl phases. This indicates that the coating has a ceramic-metal structure. The metal matrix is iron aluminide FeAl, and hafnium carbide is the reinforcing phase. The concentration of hafnium carbide in the coatings increases in a linear way with the powder content in the bulk electrode material. Note the XRD pattern of the Hf12 coating features only HfC reflexes.

The average thickness of the coatings increases from 30.5 to 43.5 μm as the hafnium carbide powder content in the anode mixture increases (refer to Table 2), which agrees well with the measured cathode weight gain (Fig. 2, *a*). Figs. 3, *a*, *c* show the cross-sections of the Hf4 and Hf12 coatings. All the coatings have a biphasic structure: a dark gray matrix with white inclusions. According to the EDS analysis, the white inclusions are hafnium carbide (Fig. 4). The inclusion size in the HfC/Fe–Al coatings ranges from 0.2 to 7 μm. Figs. 3, *a* and *c* show that the HfC grain density increases with the hafnium carbide powder increase in the BE material, which agrees with the XRD analysis results. According to the EDS analysis results (Fig. 3, *b*, *d*), the concentration of aluminum in the coatings is higher than that of iron. As the iron-aluminum state diagram indicates, this ratio corresponds to the iron aluminide FeAl detected by XRD (Fig. 2, *b*). Therefore, the deposition of HfC powder mixed with iron and aluminum granules by the EDBE process creates a metal-ceramic structure through the introduction of ceramic particles into the metal matrix [23].

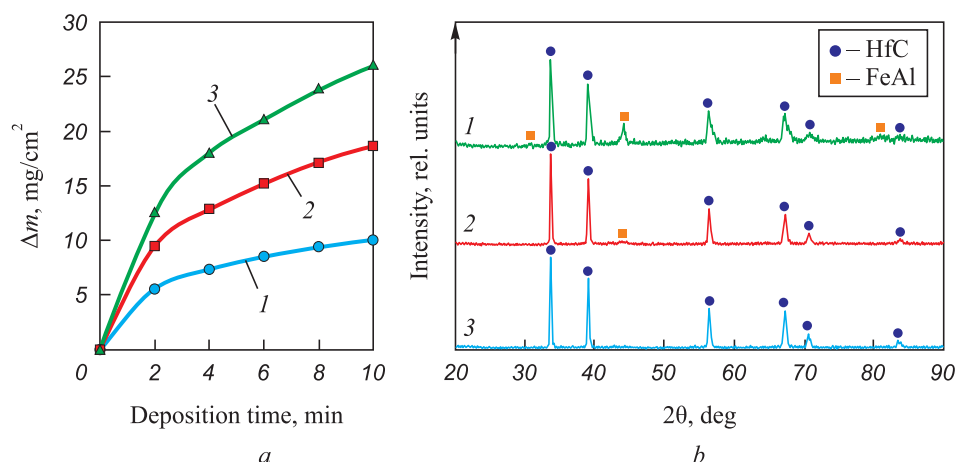


Fig. 2. Cathode gain during electrospray deposition with a non-localized electrode (a) and X-ray diffraction patterns of deposited coatings (b): 1 – Hf4; 2 – Hf8; 3 – Hf12

Рис. 2. Привес катода в процессе ЭИЛНЭ (a) и рентгеновские дифрактограммы осажденных покрытий (b): 1 – Hf4; 2 – Hf8; 3 – Hf12

The coatings are porous. The pore formation during ESD is usually attributed to the evaporation of the electrode material at high temperatures created by the low-voltage electric discharge [24]. Due to the high cooling rate after the discharge, the gas bubble does not have enough time to reach

the surface of the melt. Several studies report that the porosity decreases with the discharge energy increase resulting in a reduced material cooling rate [25; 26]. The average  $R_a$  roughness values are similar for all the coatings and fall in a narrow range from 5.1 to 5.28  $\mu\text{m}$  (Table 2).

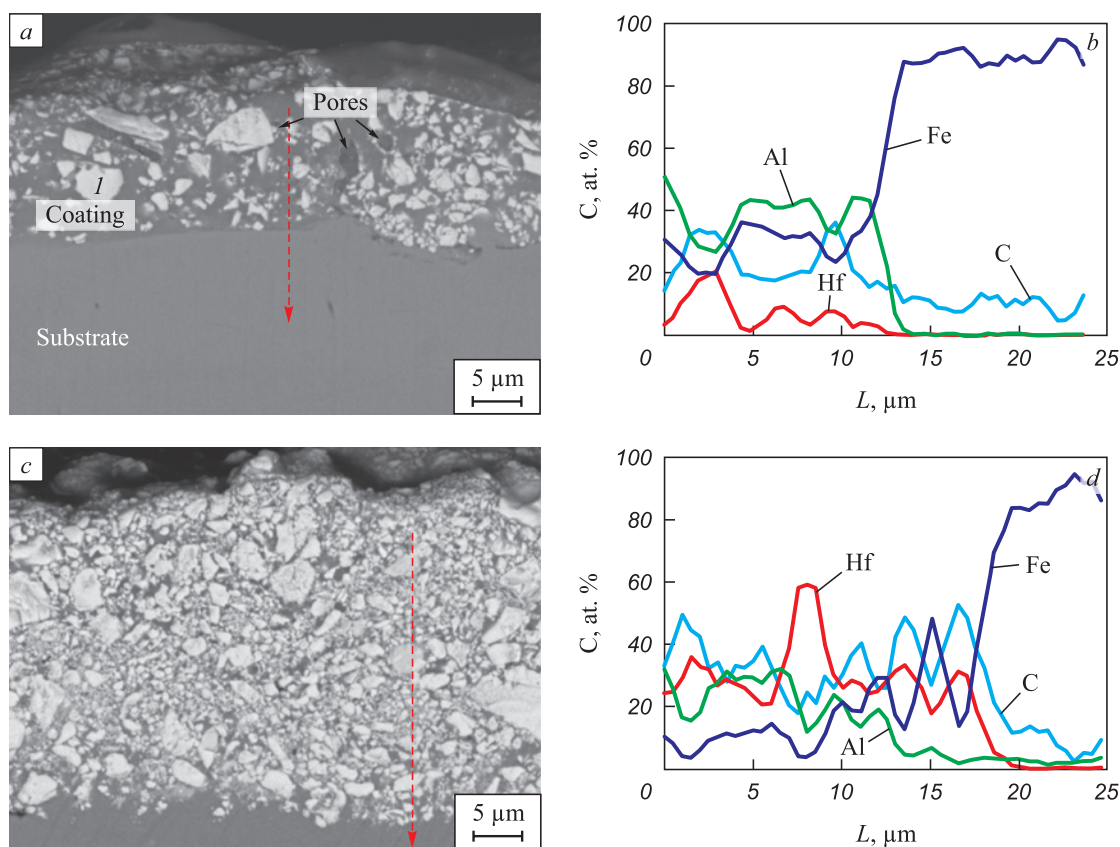


Fig. 3. Typical electron images of the cross section of coatings: Hf4 (a), Hf12 (c) and distribution of elements in the cross section of the corresponding coatings according to EDS analysis (b, d). Dotted line indicates the scanning direction

Рис. 3. Типичные электронные изображения поперечного сечения покрытий: Hf4 (a), Hf12 (c) и распределение элементов в сечении соответствующих покрытий согласно ЭДС анализу (b, d). Пунктирная линия указывает направление сканирования



Table 2

Characteristics of the coatings

Таблица 2. Характеристики покрытий

Samples	Thickness, $\mu\text{m}$	Roughness ( $R_a$ ), $\mu\text{m}$
Hf4	$30.5 \pm 8.3$	$5.28 \pm 0.65$
Hf8	$38.4 \pm 9.7$	$5.26 \pm 0.63$
Hf12	$43.5 \pm 10.6$	$5.10 \pm 0.88$

Fig. 5 shows the average microhardness values of the Fe–Al/HfC coatings. Note that the indentation diagonal at a 0.5 N load is at least 10  $\mu\text{m}$ . This is significantly larger than the diameter of the HfC grains in the coating. The microhardness of the Fe–Al/HfC coatings ranges from 10.9 to 13.5 GPa, which is 400 – 500 % higher than that of steel 1035. Coating hardness varies in a non-linear way with the HfC powder content in the BE. The maximum value is observed in the Hf8 coating. The lower hardness of the Hf4 coating can be explained by its lower content of hafnium carbide (Fig. 2, b). On the other hand, the low hardness of the Hf12 coating can be attributed to the insufficient content of the Fe–Al bonding (Fig. 2, b). As a result, the HfC grains easily shift relative to each other when the diamond indenter is driven in.

Fig. 6, a shows the friction coefficients of the coatings measured by wear tests (dry sliding) under 25 and 50 N loads. The average friction coefficient of the Fe–Al/HfC coatings ranges from 0.51 to 0.85: 6 to 40 % lower than that of steel 1035. Moreover, the wear tests of uncoated steel produced highly irregular friction coefficient curves. This can be explained by the periodic deposition and detachment of the material particles carried between the friction surfaces. Under both loads, the average friction coefficients of the coatings decrease linearly

with the hafnium carbide content increase in the BE material due to the lower concentration of the ductile Fe–Al bond.

Fig. 6, b shows wear resistance test results. Coating wear rate ranges from  $(2.82 - 4.41) \cdot 10^{-5}$  to  $(0.95 - 2.53) \cdot 10^{-7} \text{ mm}^3/(\text{N} \cdot \text{m})$  under 25 and 50 N loads, respectively. The Hf8 coating has the lowest wear rate under both loads. This agrees well with the coating hardness values (Fig. 5) obtained with the Archard wear equation [27]:

$$V_w = k \frac{Pl}{H},$$

where  $V_w$  is the volume of wear debris produced;  $H$  is the material hardness;  $k$  is the wear factor;  $P$  is normal load;  $l$  is the sliding distance.

For the Hf4 sample, the low concentration of HfC grains and high friction coefficient leads to more extensive wear. With regard to the Hf12 coating, the low concentration of metal bonding cannot hold hafnium carbide grains, and the grains fall out. The wear rate of the coatings under a 50 N load is 72 to 89 % lower than that of steel 1035. The average coating wear rate under a 25 N load is slightly lower than that of steel 1035, and almost half as much under a 50 N load. This is probably caused by the steel 1035 surface hardening, when a 25 N friction load is applied. Therefore, the optimum concentration of hafnium carbide powder in the BE material is about 8 vol. %. In general, the wear rate values indicate a relatively low wear resistance of Fe–Al/HfC coatings. Note that our paper on Ti/HfC coatings [14] reports much lower wear rate values. This can be explained by the fact that the wettability of hafnium carbide with FeAl aluminide is lower than that of titanium. On the other hand, the wettability of tungsten carbide with FeAl aluminide is high [28].

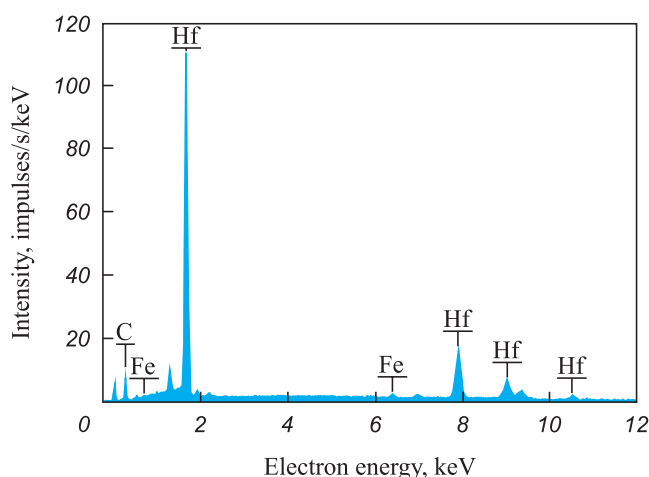


Fig. 4. EDS spectrum of section I at Fig. 3, a

Рис. 4. ЭДС спектр участка I к рис. 3, a

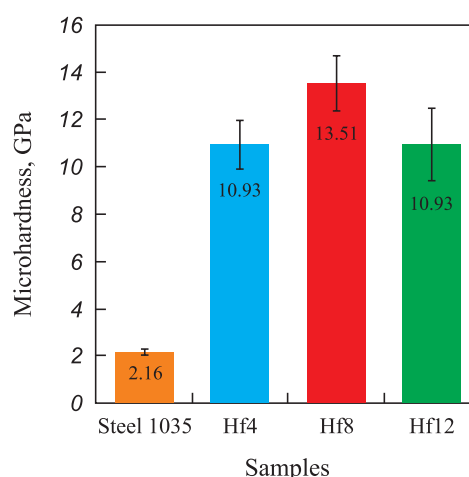


Fig. 5. Microhardness of the coatings and steel 1035

Рис. 5. Микротвердость покрытий и стали 35

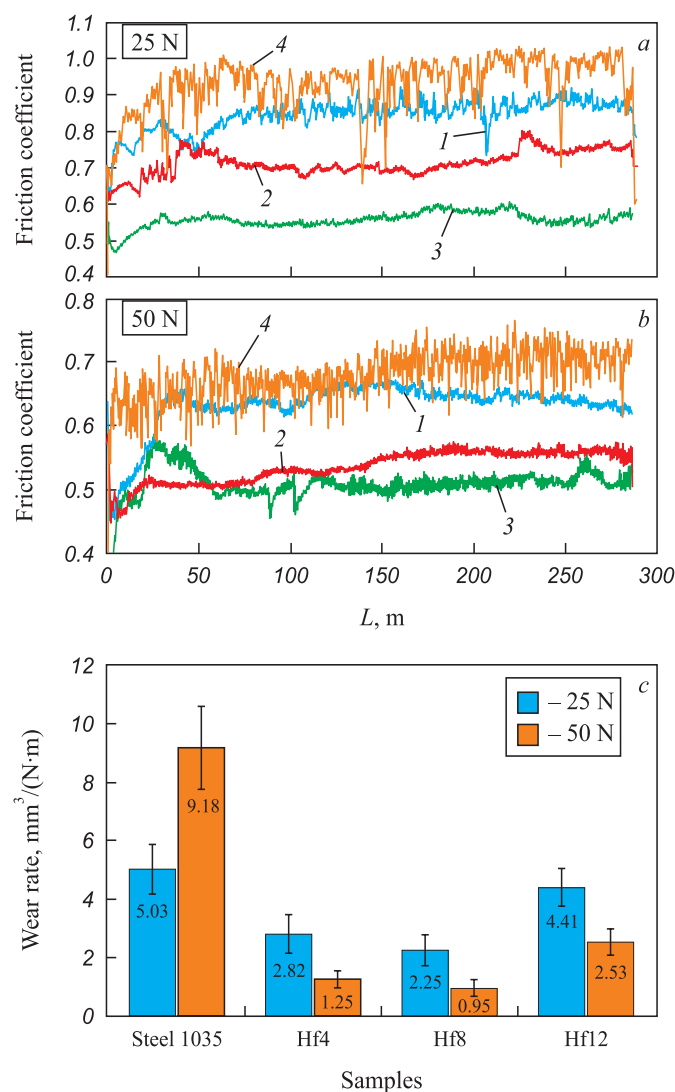


Fig. 6. Friction coefficient (*a, b*) and wear rate (*c*) of the coatings at loads of 25 and 50 N compared to steel 1035: 1 – Hf4; 2 – Hf8; 3 – Hf12; 4 – steel 1035

Рис. 6. Коэффициент трения (*a, b*) и износ (*c*) покрытий при нагрузках 25 и 50 Н по сравнению со сталью 35: 1 – Hf4; 2 – Hf8; 3 – Hf12; 4 – сталь 35

Fig. 7, *a* shows the results of cyclic heat resistance tests of the steel 1035 samples with Fe–Al/HfC coatings at 700 °C. After 100 h, the weight gain of the coated samples ranges from 123 to 164 g/m<sup>2</sup>. The weight gain is caused by oxygen fixation as iron oxide Fe<sub>2</sub>O<sub>3</sub> as the hematite and hafnium dioxide HfO<sub>2</sub> are modified (Fig. 7, *b*). The XRD patterns of the Hf8 and Hf12 coatings feature reflexes of hafnium carbide. It can be attributed to the protective effect of the Fe–Al matrix. However, this is unlikely due to weak Fe–Al to HfC adhesion. Furthermore, Musa C. et al. [29] showed that a compacted hafnium carbide-based material obtained by self-propagating high-temperature synthesis (SHS) followed by spark plasma sintering is resistant to oxidation at temperatures up to 750 – 800 °C. Luo H. et al. [30] reported that PVD coatings (HfC/*a*-C:H) begin to oxidize in

the 500 to 600 °C temperature range. The HfO<sub>2</sub> reflexes shown in Fig. 7, *b* indicate that the hafnium carbide was oxidized at 700 °C. In general, the oxidation start temperature in hafnium carbide-based materials strongly depends on the carbon content in HfC, the presence of impurities, and the share of the amorphous phase. The highest weight gain after 100 h of testing was observed in the Hf12 and

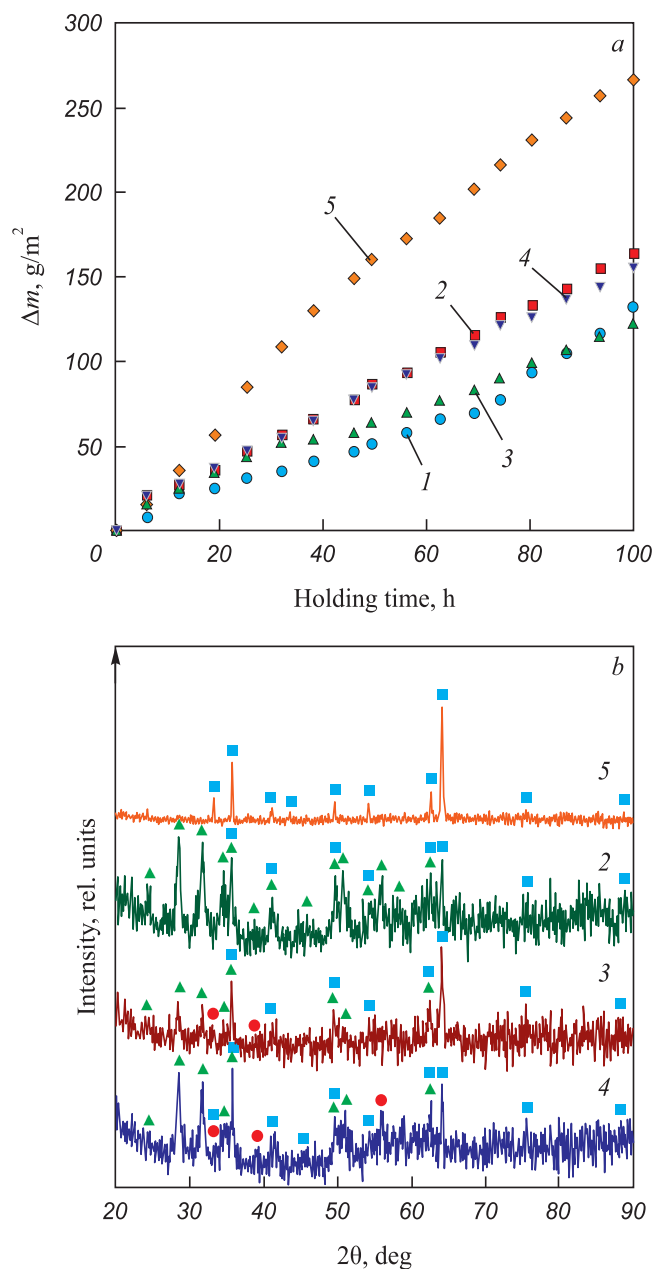


Fig. 7. Oxidation resistance of the samples at a temperature of 700 °C in air (*a*): 1 – FeAl; 2 – Hf4; 3 – Hf8; 4 – Hf12; 5 – steel 1035 and X-ray diffraction patterns of their surface after testing for oxidation resistance compared to steel 1035 (*b*):

● – HfC; ■ – Fe<sub>2</sub>O<sub>3</sub>; ▲ – HfO<sub>2</sub>

Рис. 7. Жаростойкость образцов при температуре 700 °C на воздухе (*a*): 1 – FeAl; 2 – Hf4; 3 – Hf8; 4 – Hf12; 5 – сталь 35 и рентгеновские дифрактограммы их поверхности после испытания на жаростойкость по сравнению со сталью 35 (*b*):

● – HfC; ■ – Fe<sub>2</sub>O<sub>3</sub>; ▲ – HfO<sub>2</sub>

Hf4 samples with the highest and lowest hafnium carbide contents, while the lowest gain was found in the Hf8 sample with an intermediate hafnium carbide content. For comparison, we tested a sample with Fe–Al, hafnium carbide-free coating. The weight gain was slightly higher than for the Hf8 sample. Reinforcing a Fe–Al matrix with hafnium carbide does not increase the heat resistance at 700 °C. The comparison of the sample weight gains in the samples indicates that electrospark deposition of Fe–Al/HfC coatings improves the heat resistance of steel 1035 at 700 °C by 70 – 120 %.

## CONCLUSION

As the concentration of HfC powder in the anode material increases, the cathode weight gain and coating thickness increase in a linear way. The coating structure is a FeAl intermetallide matrix reinforced with hafnium carbide grains (a metal-ceramic composite). The hafnium carbide content in the coating increases with the HfC powder content in the anode material. The average friction coefficient values of Fe–Al/HfC coatings range from 0.51 to 0.85: 6 to 40 % lower than that of steel 1035. The dry sliding wear resistance of the coatings under a 50 N load is 260 – 860 % higher than that of steel 1035. Electrospark deposition of Fe–Al/HfC coatings improves the heat resistance of steel 1035 at 700 °C by 70 – 120 %. The decrease in hardness, wear, and heat resistance with the increase of HfC content in the anode material above 8 vol. % indicates low wettability and weak adhesion of Fe–Al to hafnium carbide.

## REFERENCES / СПИСОК ЛИТЕРАТУРЫ

1. Zang K., Chen W., Liang W., Miao Q., Yao W., Li J., Ma Y. Tribological behaviors of HfC coating prepared on 45 steel via double glow plasma surface metallurgy technique. *Industrial Lubrication and Tribology*. 2022;74(2):228–236. <https://doi.org/10.1108/ILT-09-2021-0378>
2. Gao W., Wang S.C., Hu K.K., Jiang X.Z., Yu H.Y., Sun D.B. Effect of laser cladding speed on microstructure and properties of titanium alloy coating on low carbon steel. *Surface and Coatings Technology*. 2022;451:129029. <https://doi.org/10.1016/j.surfcoat.2022.129029>
3. Bazhin P.M., Titov N.V., Zhidovich A.O., Avdeeva V., Kolomeichenko A.V., Stolin A.M. Features of the carbo-vibroarc surfacing in the development of multicomponent cermet wear-resistant coatings. *Surface and Coatings Technology*. 2022;429:127952. <https://doi.org/10.1016/j.surfcoat.2021.127952>
4. Kumar A., Nayak S.K., Laha T. Comparative study on wear and corrosion behavior of plasma sprayed  $\text{Fe}_{73}\text{Cr}_2\text{Si}_{11}\text{B}_{11}\text{C}_3$  and  $\text{Fe}_{63}\text{Cr}_9\text{P}_5\text{B}_{16}\text{C}_7$  metallic glass composite coatings. *Journal of Thermal Spray Technology*. 2022;32:1302–1316. <https://doi.org/10.1007/s11666-021-01280-1>
5. Wang Y., Gao W. Microstructure and performance of Ni/TiN coatings deposited by laser melting deposition on 40Cr substrates. *Coatings*. 2022;12(3):367. <https://doi.org/10.3390/coatings12030367>
6. Torabinejad V., Rouhaghdam A.S., Aliofkhaezrai M., Allahyazadeh M.H. Ni–Fe– $\text{Al}_2\text{O}_3$  electrodeposited nanocomposite coating with functionally graded microstructure. *Bulletin of Materials Science*. 2016;39:857–864. <https://doi.org/10.1007/s12034-016-1211-1>
7. Burkov A.A., Bytsura A.Yu. Corrosion properties and tribological behavior of tungsten carbide coatings with aluminide matrix on SS AISI304. *Fundamental'nye problemy sovremennoy materialovedeniya*. 2022;4(19):509–519. (In Russ.). <https://doi.org/10.25712/ASTU.1811-1416.2022.04.010>
- Бурков А.А., Быцур А.Ю. Коррозионные свойства и трибологическое поведение покрытий из карбида вольфрама с алюминидной матрицей на нержавеющей стали AISI304. *Фундаментальные проблемы современного материаловедения*. 2022;19(4):509–519. <https://doi.org/10.25712/ASTU.1811-1416.2022.04.010>
8. Deevi S.C. Advanced intermetallic iron aluminide coatings for high temperature applications. *Progress in Materials Science*. 2021;118:100769. <https://doi.org/10.1016/j.pmatsci.2020.100769>
9. Yürektürk Y., Baydoğan M. Effect of aluminizing and austempering processes on structural, mechanical and wear properties of a SSF ductile iron. *Materials Research Express*. 2018;6(1):016550. <https://doi.org/10.1088/2053-1591/aae804>
10. Palm M., Stein F., Dehm G. Iron aluminides. *Annual Review of Materials Research*. 2019;49:297–326. <https://doi.org/10.1146/annurev-matsci-070218-125911>
11. Toth L.E. *Transition Metal Carbides and Nitrides. Refractory Materials Series. Vol. 7*. New York, London: Academic Press; 1971:91.
12. Hans K., Latha S., Bera P., Barshilia H.C. Hafnium carbide based solar absorber coatings with high spectral selectivity. *Solar Energy Materials and Solar Cells*. 2018;185:1–7. <https://doi.org/10.1016/j.solmat.2018.05.005>
13. Sciti D., Guicciardi S., Nygren M. Densification and mechanical behavior of HfC and HfB<sub>2</sub> fabricated by spark plasma sintering. *Journal of the American Ceramic Society*. 2008;91(5):1433–1440. <https://doi.org/10.1111/j.1551-2916.2007.02248.x>
14. Burkov A.A. Improvement of Ti6Al4V-alloy wear resistance by electric-spark hafnium carbide coatings. *Journal of Friction and Wear*. 2020;41(6):543–548. <https://doi.org/10.3103/S1068366620060045>
- Бурков А.А. Улучшение износостойкости сплава Ti6Al4V электроискровыми покрытиями из карбида гафния. *Трение и износ*. 2020;41(6):731–737.
15. Shimada S., Inagaki M., Matsui K. Oxidation kinetics of hafnium carbide in the temperature range of 480° to 600 °C. *Journal of the American Ceramic Society*. 1992;75(10):2671–2678. <https://doi.org/10.1111/j.1151-2916.1992.tb05487.x>
16. Kudryashov A.E., Kiryukhantsev-Korneev P.V., Mukanov S.K., Petrzhik M.I., Levashov E.A. The effect of electrospark deposition using zirconium electrodes on structure and properties of nickel-containing alloy obtained selective laser melting. *Powder Metallurgy and Functional Coatings*. 2022;(3):63–77. (In Russ.). <https://doi.org/10.17073/1997-308X-2022-3-63-77>

- Кудряшов А.Е., Кирюханцев-Корнеев Ф.В., Муканов С.К., Петржик М.И., Левашов Е.А. Влияние электроискровой обработки электродами из циркония на структуру и свойства никельсодержащего сплава, полученного селективным лазерным сплавлением. *Известия вузов. Порошковая металлургия и функциональные покрытия*. 2022;(3):63–77.  
<https://doi.org/10.17073/1997-308X-2022-3-63-77>
17. Burkov A.A., Pyachin S.A. Formation of WC–Co coating by a novel technique of electrospark granules deposition. *Materials & Design*. 2015;80:109–115.  
<https://doi.org/10.1016/j.matdes.2015.05.008>
  18. Nikolenko S.V., Syui N.A. Investigation of coatings produced by the electrospark machining method of steel 45 with electrodes based on carbides of tungsten and titanium. *Protection of Metals and Physical Chemistry of Surfaces*. 2017;53:889–894.  
<https://doi.org/10.1134/S207020511705015X>
  19. Burkov A.A., Kulik M.A. Wear-resistant and anticorrosive coatings based on chrome carbide  $\text{Cr}_7\text{C}_3$  obtained by electric spark deposition. *Protection of Metals and Physical Chemistry of Surfaces*. 2020;56:1217–1221.  
<https://doi.org/10.1134/S2070205120060064>  
Бурков А.А., Кулик М.А. Износостойкие и антикоррозионные покрытия на основе карбида хрома  $\text{Cr}_7\text{C}_3$ , полученные электроискровым осаждением. *Физикохимия поверхности и защита материалов*. 2020;56(6):667–672.
  20. Burkov A.A., Krutikova V.O. Deposition of titanium silicide on stainless AI SI304 surface. *Metal Working and Material Science*. 2022;24(4):127–137. (In Russ.).  
<https://doi.org/10.17212/1994-6309-2022-24.4-127-137>  
Бурков А.А., Крутикова В.О. Осаждение силицида титана на нержавеющую сталь AISI304. *Обработка металлов (технология, оборудование, инструменты)*. 2022;24(4):127–137.  
<https://doi.org/10.17212/1994-6309-2022-24.4-127-137>
  21. Burkov A.A., Kulik M.A., Krutikova V.O. Electrospark deposition of tungsten carbide powder on titanium alloy Ti6Al4V. *Letters on Materials*. 2021;11(2):175–180. (In Russ.).  
<https://doi.org/10.22226/2410-3535-2021-2-175-180>  
Бурков А.А., Кулик М.А., Крутикова В.О. Электроискровое нанесение порошка карбида вольфрама на титановый сплав Ti6Al4V. *Письма о материалах*. 2021; 11(2):175–180.  
<https://doi.org/10.22226/2410-3535-2021-2-175-180>
  22. Burkov A.A., Kulik M.A., Krutikova V.O. Characteristics of Ti–Si coatings on Ti6Al4V alloy subjected to electrospark granules. *Tsvetnye Metally*. 2019;4:54. (In Russ.).  
<https://doi.org/10.17580/tsm.2019.04.07>  
Бурков А.А., Кулик М.А., Крутикова В.О. Характеристика Ti–Si-покрытий на сплаве Ti6Al4V, осажденных электроискровой обработкой в среде гранул. *Цветные металлы*. 2019;4:54. <https://doi.org/10.17580/tsm.2019.04.07>
  23. Nurminen J., Näkki J., Vuoristo P. Microstructure and properties of hard and wear resistant MMC coatings deposited by laser cladding. *International Journal of Refractory Metals and Hard Materials*. 2009;27(2):472–478.  
<https://doi.org/10.1016/J.IJRMHM.2008.10.008>
  24. Liu J., Wang R., Qian Y. The formation of a single-pulse electrospark deposition spot. *Surface and Coatings Technology*. 2005;200(7):2433–2437.  
<https://doi.org/10.1016/j.surfcoat.2004.07.104>
  25. Shafeyi H., Salehi M., Bahrami A. Fabrication, microstructural characterization and mechanical properties evaluation of Ti/TiB/TiB<sub>2</sub> composite coatings deposited on Ti6Al4V alloy by electro-spark deposition method. *Ceramics International*. 2020;46(10A):15276–15284.  
<https://doi.org/10.1016/j.ceramint.2020.03.068>
  26. Wang D., Deng S., Chen H., Chi C., Hu D., Wang W., He W., Liu X. Microstructure and properties of TiC particles planted on single crystal superalloy by electrospark discharging. *Surface and Coatings Technology*. 2023;461:129438.  
<https://doi.org/10.1016/j.surfcoat.2023.129438>
  27. Greer A.L., Rutherford K.L., Hutchings I.M. Wear resistance of amorphous alloys and related materials. *International Materials Reviews*. 2002;47:87–112.  
<https://doi.org/10.1179/095066001225001067>
  28. Karimi H., Hadi M. Effect of sintering techniques on the structure and dry sliding wear behavior of WC–FeAl composite. *Ceramics International*. 2020;46(11B):18487–18497. <https://doi.org/10.1016/j.ceramint.2020.04.154>
  29. Musa C., Licheri R., Orrù R., Cao G., Balbo A., Zanutto F., Sani E. Optical characterization of hafnium boride and hafnium carbide-based ceramics for solar energy receivers. *Solar Energy*. 2018;169:111–119.  
<https://doi.org/10.1016/j.solener.2018.04.036>
  30. Luo H., Sun H., Gao F., Billard A. Mechanical properties, thermal stability and oxidation resistance of HfC/a-C:H films deposited by HiPIMS. *Journal of Alloys and Compounds*. 2020;847:156538.  
<https://doi.org/10.1016/j.jallcom.2020.156538>

## Information about the Authors

## Сведения об авторах

**Aleksandr A. Burkov**, Cand. Sci. (Phys.-Math.), Senior Researcher, Head of the Laboratory of Physical and Chemical Foundations of Materials Technology, Institute of Materials Science of the Khabarovsk Federal Research Center, Far-Eastern Branch of the Russian Academy of Sciences

ORCID: 0000-0002-5636-4669

E-mail: burkovalex@mail.ru

**Mariya A. Kulik**, Junior Researcher, Institute of Materials Science of the Khabarovsk Federal Research Center, Far-Eastern Branch of the Russian Academy of Sciences

ORCID: 0000-0002-4857-1887

E-mail: marijka80@mail.ru

**Александр Анатольевич Бурков**, к.ф.-м.н., старший научный сотрудник, заведующий лабораторией физико-химических основ технологии материалов, Институт материаловедения Хабаровского Федерального исследовательского центра Дальневосточного отделения РАН

ORCID: 0000-0002-5636-4669

E-mail: burkovalex@mail.ru

**Мария Андреевна Кулик**, младший научный сотрудник, Институт материаловедения Хабаровского Федерального исследовательского центра Дальневосточного отделения РАН

ORCID: 0000-0002-4857-1887

E-mail: marijka80@mail.ru



## Contribution of the Authors

## Вклад авторов

**A. A. Burkov** – formation of the idea, literature review, conducting the experiment, data processing and analysis, writing the text.

**M. A. Kulik** – study of microhardness and structure of the samples, search and analysis of literary data, article design.

**А. А. Бурков** – идея статьи, литературный обзор, проведение эксперимента, обработка и анализ данных, написание статьи.

**М. А. Кулик** – исследование микротвердости и структуры образцов, поиск и анализ литературных данных, оформление статьи.

Received 06.04.2023

Revised 16.04.2023

Accepted 26.04.2023

Поступила в редакцию 06.04.2023

После доработки 16.04.2023

Принята к публикации 26.04.2023



УДК 620.186:620.178.74:539.42

DOI 10.17073/0368-0797-2023-3-311-319



Оригинальная статья

Original article

## ВЛИЯНИЕ УСКОРЕННОГО ОХЛАЖДЕНИЯ ПОСЛЕ ПОПЕРЕЧНО-ВИНТОВОЙ ПРОКАТКИ НА ФОРМИРОВАНИЕ СТРУКТУРЫ И НИЗКОТЕМПЕРАТУРНУЮ ВЯЗКОСТЬ РАЗРУШЕНИЯ НИЗКОУГЛЕРОДИСТОЙ СТАЛИ

А. И. Гордиенко<sup>✉</sup>, И. В. Власов, Ю. И. Почивалов

Институт физики прочности и материаловедения Сибирского отделения РАН (Россия, 634055, Томск, пр. Академический 2/4)

✉ mirantil@ispms.ru

**Аннотация.** Исследуется влияние ускоренного охлаждения после поперечно-винтовой прокатки низкоуглеродистой стали класса прочности К60 на формирование структуры и механические свойства при статическом растяжении и ударном изгибе. Показано, что использование прерванного ускоренного охлаждения стали после прокатки с выдержкой при 530 °С (режим *I*) и непрерывного ускоренного охлаждения (режим *II*) приводит к формированию разного типа и соотношения количества структур в стали. После прокатки по режиму *I* структура характеризуется присутствием феррита, троостита, гранулярного бейнита и мелкодисперсных карбидов Fe<sub>3</sub>C. После прокатки по режиму *II* структура отличается наличием реечного бейнита и крупных участков мартенситно-аустенитной (МА) составляющей размерами до 1 – 2 мкм. Уменьшение дисперсности ферритных зерен в стали после прокатки по режимам *I* и *II* с 12 до 4,6 – 4,3 мкм, формирование бейнитной фазы и упрочнение матрицы карбидами приводит к повышению пределов текучести стали до 440 и 490 МПа и пределов прочности до 760 и 880 МПа. Проведение поперечно-винтовой прокатки по режиму *I* позволяет существенно увеличить низкотемпературную вязкость разрушения стали (160 Дж/см<sup>2</sup>) по сравнению с горячекатаным состоянием (11 Дж/см<sup>2</sup>) и снизить хладноломкость стали в область температур ниже –50 °С. Применение непрерывного ускоренного охлаждения (режим *II*) не позволяет повысить хладостойкость стали вследствие формирования структуры реечного бейнита и крупных областей МА составляющей.

**Ключевые слова:** низкоуглеродистая сталь, поперечно-винтовая прокатка, ускоренное охлаждение, микроструктура, прочность, вязкость разрушения

**Благодарности:** Работа выполнена в рамках государственного задания Института физики прочности и материаловедения Сибирского отделения РАН, проект FWRW- 2021-0009.

Авторы благодарят И.П. Мишина и Е.Е. Найденкина за содействие в проведении поперечно-винтовой прокатки стали.

Микроструктурные исследования проведены с помощью оборудования ЦКП «Нанотех» Института физики прочности и материаловедения Сибирского отделения РАН (Centre “Nanotech” of the ISPMS SB RAS).

**Для цитирования:** Гордиенко А.И., Власов И.В., Почивалов Ю.И. Влияние ускоренного охлаждения после поперечно-винтовой прокатки на формирование структуры и низкотемпературную вязкость разрушения низкоуглеродистой стали. *Известия вузов. Черная металлургия.* 2023;66(3):311–319. <https://doi.org/10.17073/0368-0797-2023-3-311-319>

## EFFECT OF ACCELERATED COOLING AFTER CROSS-HELICAL ROLLING ON FORMATION OF STRUCTURE AND LOW-TEMPERATURE FRACTURE TOUGHNESS OF LOW-CARBON STEEL

А. И. Gordienko<sup>✉</sup>, I. V. Vlasov, Yu. I. Pochivalov

Institute of Strength Physics and Materials Science, Siberian Branch of the Russian Academy of Sciences (2/4 Akademicheskii Ave., Tomsk 634055, Russian Federation)

✉ mirantil@ispms.ru

**Abstract.** The effect of accelerated cooling after cross-helical rolling of X70 low-carbon steel on the formation of structures and mechanical properties under static tension and impact bending was investigated. The use of interrupted accelerated cooling of steel after cross-helical rolling with exposure at 530 °C (mode *I*) and continuous accelerated cooling (mode *II*) leads to the formation of different types and ratios of structures in steel. After

rolling according to mode *I*, the structure is characterized by the presence of ferrite, troostite, granular bainite, and fine  $\text{Fe}_3\text{C}$  carbides. After rolling according to mode *II*, the structure is characterized by the formation of lath bainite and large sections of the martensitic-austenitic (MA) component up to 1–2  $\mu\text{m}$  in size. It is shown that a decrease in the fineness of ferrite grains in steel after cross-helical rolling in modes *I* and *II* from 12 to 4.6–4.3  $\mu\text{m}$ , the formation of a bainitic phase, and hardening of the matrix with carbides led to an increase in the yield strength of steel up to 440 and 490 MPa and tensile strength up to 760 and 880 MPa. Carrying out helical rolling according to mode *I* makes it possible to significantly increase the low-temperature fracture toughness of steel ( $\text{KCV}^{-70^\circ\text{C}} = 160 \text{ J/cm}^2$ ) compared to the hot-rolled state ( $\text{KCV}^{-70^\circ\text{C}} = 11 \text{ J/cm}^2$ ) and reduce the cold brittleness of steel to the temperatures below  $-50^\circ\text{C}$ . The use of continuous accelerated cooling (mode *II*) does not allow increasing the cold resistance of steel due to the formation of the lath bainite structure and large areas of the MA component.

**Keywords:** low-carbon steel, cross-helical rolling, accelerated cooling, microstructure, strength, fracture toughness

**Acknowledgements:** The work was performed within the framework of the state task of the Institute of Strength Physics and Materials Science, Siberian Branch of Russian Academy of Sciences, project FWRW- 2021-0009.

The authors express their gratitude to Mishin I.P. and Naydenkin E.E. for their assistance in carrying out steel cross-helical rolling.

Microstructural studies were carried out using the equipment of the Centre “Nanotech” of the Institute of Strength Physics and Materials Science, Siberian Branch of Russian Academy of Sciences.

**For citation:** Gordienko A.I., Vlasov I.V., Pochivalov Yu.I. Effect of accelerated cooling after cross-helical rolling on formation of structure and low-temperature fracture toughness of low-carbon steel. *Izvestiya. Ferrous Metallurgy*. 2023;66(3):311–319.

<https://doi.org/10.17073/0368-0797-2023-3-311-319>

## INTRODUCTION

Low-carbon low alloy steels are extensively utilized in various industries. The enhancement of mechanical properties of steels is accomplished through integrated micro-doping and different modes of thermomechanical processing [1–11]. However, the improvement in strength is often accompanied by a decrease in plastic properties and fracture toughness, particularly under low temperatures [1; 2]. Thus, the primary objective is to increase the low-temperature fracture toughness of such steels. Factors that contribute to its increase include grain refinement [3–6], reduction in the fraction and grain size of pearlite [5; 6] and the martensite-austenite (MA) constituent [7]. Additionally, a more uniform alternation of ferrite and pearlite [5; 8; 9], as well as the absence of a predominant orientation of planes  $\{001\}$  [3], promote increased fracture toughness. Another factor that improves the cold resistance of steel is the utilization of accelerated cooling (with cooling rates  $V_{\text{cool}}$ , ranging from 5 to 30  $^\circ\text{C/s}$ ) after rolling, leading to the formation of ferrite-bainite structures. Depending on the temperature range of rolling, start and finish temperatures of accelerated cooling, cooling rates, and holding time, different types of bainite structures can be formed, achieving varying levels of strength and fracture toughness [8–10]. In most studies [2–4; 7–10], the structure and mechanical properties of steels were examined after conventional longitudinal rolling. In contrast to the longitudinal process, cross-helical rolling involves a rotating reciprocal motion of ingots, resulting in a higher fraction of shift deformation component. This facilitates more efficient refinement of the granular structure in a lower number of passes, promoting the formation of a homogeneous structure and simultaneous increase in strength and low-temperature fracture toughness [5; 6; 11].

The objective of this study is to analyze the impact of accelerated cooling following cross-helical rolling of low-carbon X70 steel on the formation of its structure.

Additionally, the investigation aims to examine the mechanical properties and micromechanisms of steel fracture under static tension and impact bending conditions.

## EXPERIMENTAL

The study focused on low-carbon low alloy steel, specifically grade X70, which was in the state after hot rolling. The chemical composition of the steel (wt. %) was as follows: C 0.13; Mn 1.6; V 0.05; Nb 0.04; Si 0.4; Ti 0.05; Cu 0.3; Al 0.03; P 0.013; S 0.01. The ingots used for cross-helical rolling were obtained by cutting a hot-rolled steel sheet with a thickness of 56 mm. The initial diameter of the ingot before rolling was 40 mm. Cross-helical rolling was conducted using an RSP 14-40 three roll mill in six passes, gradually reducing the diameter. Previous research [11] demonstrated that rolling this steel at 850  $^\circ\text{C}$  in the region where  $(\gamma + \alpha)$  phases exist in the phase diagram, following by air cooling, resulted in higher fracture toughness compared to rolling at 1000, 920 and 810  $^\circ\text{C}$ . In this study, the rolling process was performed at 850  $^\circ\text{C}$ . After rolling, accelerated cooling was applied using a water sprayer at a rate of 6  $^\circ\text{C/s}$  until reaching 530  $^\circ\text{C}$ , followed by a three-minute hold and subsequent cooling at a rate of 6  $^\circ\text{C/s}$  to 200  $^\circ\text{C}$  (mode *I*). In the second case, the ingot was cooled at a rate of 6  $^\circ\text{C/s}$  to 200  $^\circ\text{C}$  (mode *II*). Cumulative degree of deformation  $\varepsilon = \ln\left(\frac{S_0}{S_f}\right)$

(where  $S_0$  and  $S_f$  represent the initial and final surface areas of the transversal cross sections of the rods), after six rolling passes in both cases, was approximately 1.6. The final diameter of the rods after rolling was 17 mm.

Microstructural studies were conducted using a scanning electron microscope (LEO EVO 50). To prepare the samples for structural analysis, their surfaces were sequentially polished using emery paper with gradually decreasing abrasive grain sizes. Subsequently, the samples were polished on cloth using diamond paste.

In order to reveal grain boundaries, the polished surfaces were etched in a 3 % alcohol solution of  $\text{HNO}_3$ . Vickers microhardness measurements were performed using a PMT-3 hardness meter with a load of 0.49 N. For static tension tests, samples with a working area size of  $15 \times 3 \times 1$  mm were used. Impact tests were carried out on samples with dimensions of  $10 \times 10 \times 55$  mm, which featured a *V*-notch. An INSTRON MPX 450 impact machine was used for these tests within a temperature range  $T_{\text{test}}$  from +20 to  $-70$  °C. By measuring the surface areas under the load-deflection curves, the work of crack nucleation (the surface area under the loading curve until reaching the maximum load  $F_{\text{max}}$ ) and crack propagation (the surface area under the loading curve after reaching  $F_{\text{max}}$ ) were determined. The stages of crack propagation and the micromechanisms of fracture at each stage were analyzed by examining the surfaces of the fractured samples using a scanning electron microscope (LEO EVO 50). The fracture surfaces were examined to identify regions exhibiting brittle fracture and shear lips. Shear lips refer to segments of ductile fracture adjacent to the lateral sides of the sample and are typically oriented at an angle of approximately  $45^\circ$  to them. The fractions of these regions were calculated as the ratio of their surface areas to the surface area of the cross section of the sample under the notch after fracture. The temperature of the viscous brittle transition,  $T_{50}$  (or  $\text{FATT}_{50}$  [12]), was determined based on the fraction of the brittle region observed on the fracture surface.  $T_{50}$  corresponded to the temperature at which 50 % of the fracture surface exhibited brittle fracture.

## RESULTS

In the hot rolled state, X70 steel exhibits a ferrite-sorbite structure (Fig. 1, *a*). The average size ( $d_F$ ) of ferrite grains is  $12 \mu\text{m}$ . The volumetric fraction of sorbite (dispersed pearlite) is 20 %, and the interplanar distance in sorbite is  $0.25 \mu\text{m}$ . The microhardness of the ferrite regions is measured at  $165 \text{HV}_{50}$ .

After cross-helical rolling of the steel, the structure becomes refined and shows a more homogeneous distribution of structural constituents (Fig. 1, *b*, *d*). In the case of processing according to mode *I*, the cooling rate is insufficient to suppress diffusion decomposition of austenite. As a result, additional holding during cooling creates conditions for carbon diffusion.

In the steel structure after processing according to mode *I*, in addition to ferrite, there are regions of bainite with a granular morphology (Fig. 1, *b*), troostite (Fig. 1, *c*) and dispersed  $\text{Fe}_3\text{C}$  carbide particles ( $d_{\text{Fe}_3\text{C}} = 50 \div 250 \text{ nm}$ ) located within and at the boundaries of ferrite and bainite grains (Fig. 1, *c*). Coarser carbide particles up to  $1 \mu\text{m}$  in size are also present. The average grain size of ferrite  $d_F$  decreased to  $4.6 \mu\text{m}$ ,

while the average grain size of bainite ( $d_B$ ) is  $2.5 \mu\text{m}$ . The fraction of troostite segments decreased to 10.5 % and the interplanar distance in troostite is  $0.17 \mu\text{m}$  (Fig. 1, *c*). The high dispersity of troostite is a result of accelerated cooling.

In the steel samples processed according to mode *II*, the structure consists of regions of ferrite, troostite, granulated and lath bainite, as well as the segments of the MA constituent and  $\text{Fe}_3\text{C}$  carbide particles (Fig. 1, *d*–*f*). The average size of ferrite grains decreased to  $4.3 \mu\text{m}$ , and the sizes of the MA constituent ranges from 1 to  $2 \mu\text{m}$ . The structure also contains coarse particles of  $\text{Fe}_3\text{C}$  carbide (up to  $1 \mu\text{m}$ ), although the fraction of finely dispersed carbides is lower compared to processing according to mode *I*. The fraction of troostite grains decreased to 7.5 %. In the case of processing according to mode *II*, the fraction of the bainite phase is higher.

The microhardness of the ferrite matrix increased to  $205 \text{HV}_{50}$  after steel cooling according to mode *I* and to  $225 \text{HV}_{50}$  after steel cooling according to mode *II*. Similarly, the microhardness of the bainite regions increased to  $320 \text{HV}_{50}$  and  $335 \text{HV}_{50}$ , respectively (refer to Table, where  $\text{HV}_F$  is the microhardness of ferrite;  $\text{HV}_B$  is the microhardness of bainite;  $\sigma_{0.2}$  is the yield stress;  $\sigma_u$  is the ultimate tensile strength;  $\varepsilon$  is the plasticity; KCV is the impact toughness at various test temperatures).

The yield stress of the steel increased by 20 and 35 % after cross-helical rolling according to modes *I* and *II*, respectively. Additionally, the ultimate tensile strength increased by 20 and 75 % in the respective modes. However, there was only a slight decrease in plasticity. The higher level of strength properties observed after cooling according to mode *II* can be attributed to the formation of a higher fraction of the bainite phase, as well as the formation of lath bainite and segments of the MA phase.

During impact bending tests, it was observed that the steel samples in the hot rolled state exhibited higher fracture energy at ambient temperature (refer to Table; Fig. 2, *a*). However, as the test temperature decreased to  $-40$  and  $-70$  °C, the fracture toughness sharply decreased. All impact loading diagrams of the steel showed segments of sharp load decrease (indicated by arrow in Fig. 2, *a*). At negative test temperatures, a sharp decrease in the curves was observed immediately after reaching the maximum load. This form of load–deflection curves indicates the occurrence of avalanche crack propagations, which is characteristic of brittle fracture.

The fracture of the samples at low temperatures occurs through the mechanism of transcrystalline cleavage, as depicted in Fig. 3, *a* and *b*. Even at  $-40$  °C, the fraction of brittle fracture is almost 100 %, as shown in Fig. 4, *a*.

In the temperature range of  $-40 \div -70$  °C, the fracture surfaces exhibit a lack of tightening of the lateral faces and shear lips (represented as  $\lambda$  in Fig. 3, *d*), which are



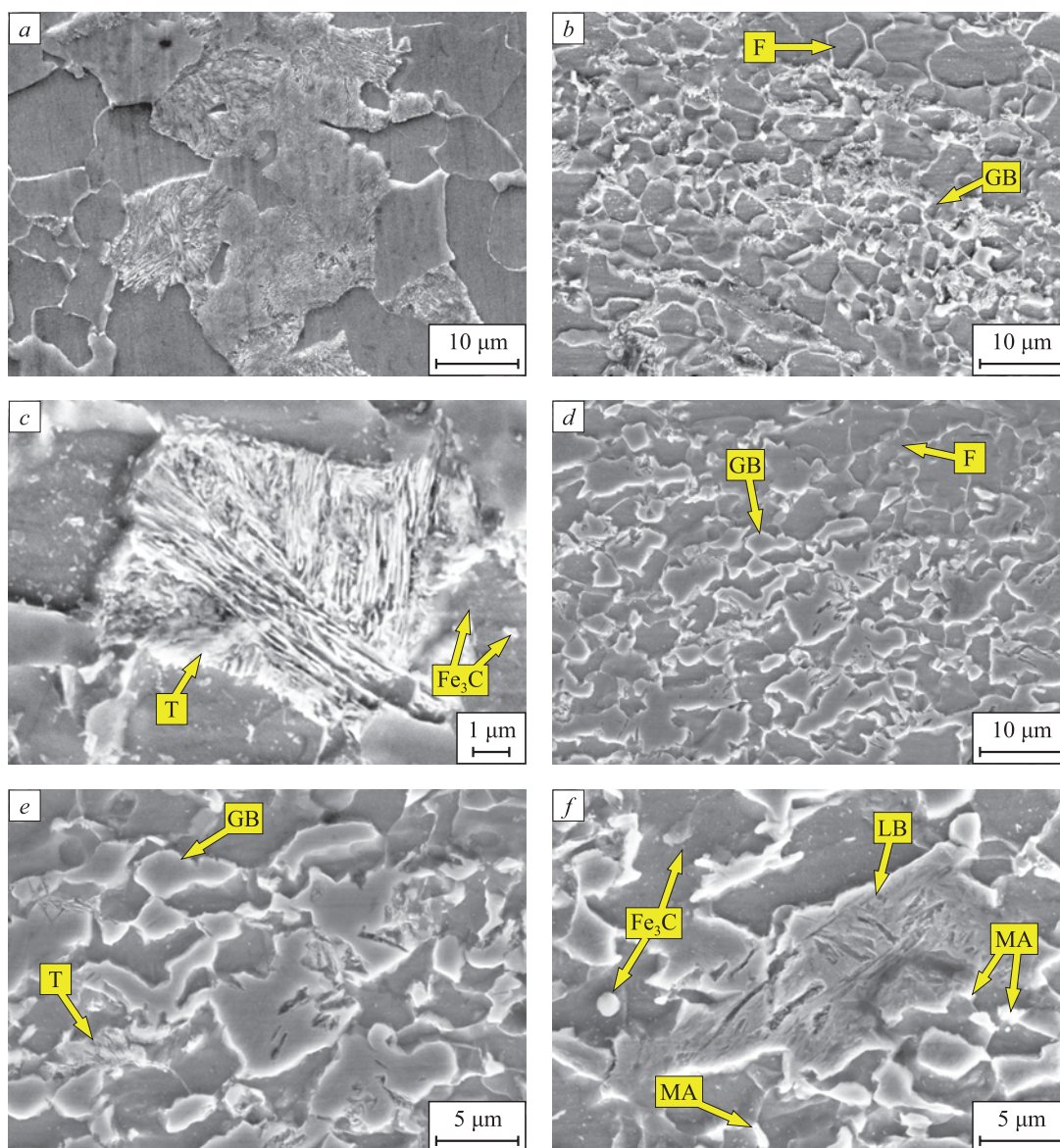


Fig. 1. SEM images of steel structures in hot-rolled state (a), after cross-helical rolling using mode I (b, c) and mode II (d–f) (F – ferrite; GB – granular bainite; LB – lath bainite; T – troostite; MA – MA component)

Рис. 1. РЭМ-изображения структур стали в горячекатаном состоянии (a), после поперечно-винтовой прокатки по режимам I (b, c) и II (d–f) (F – феррит; GB – гранулярный бейнит; LB – реечный бейнит; T – троостит; MA – MA составляющая)

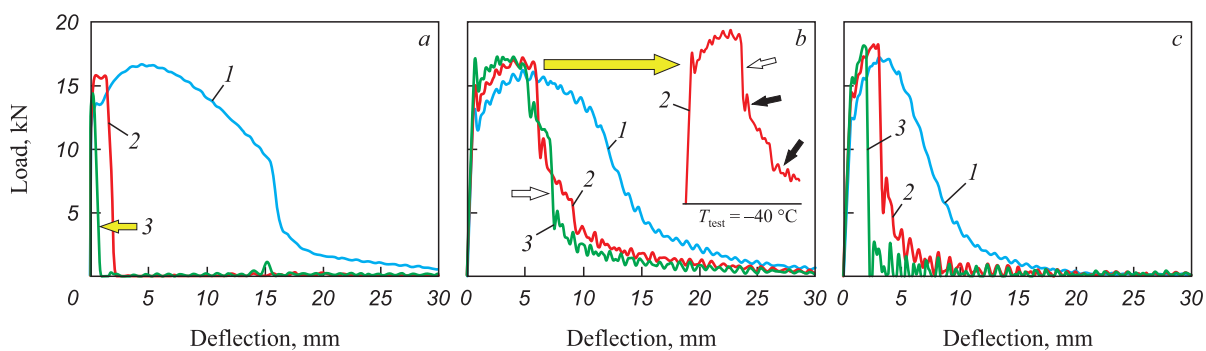


Fig. 2. Curves of impact loading of steel in the hot-rolled state (a), after treatments using mode I (b) and mode II (c):  
1 –  $T_{\text{test}} = +20\text{ }^{\circ}\text{C}$ ; 2 –  $T_{\text{test}} = -40\text{ }^{\circ}\text{C}$ ; 3 –  $T_{\text{test}} = -70\text{ }^{\circ}\text{C}$

Рис. 2. Кривые ударного нагружения стали в горячекатаном состоянии (a), после обработок по режимам I (b) и II (c):  
1 –  $T_{\text{test}} = +20\text{ }^{\circ}\text{C}$ ; 2 –  $T_{\text{test}} = -40\text{ }^{\circ}\text{C}$ ; 3 –  $T_{\text{test}} = -70\text{ }^{\circ}\text{C}$

# Mechanical properties of X70 steel

## Механические свойства стали категории прочности K60

State	HV <sub>50</sub>	$\sigma_{0.2}$ , MPa	$\sigma_u$ , MPa	$\epsilon$ , %	KCV <sup>+20</sup> , J/cm <sup>2</sup>	KCV <sup>-40</sup> , J/cm <sup>2</sup>	KCV <sup>-70</sup> , J/cm <sup>2</sup>
Hot rolled	HV <sub>F</sub> = 165	360	650	23.0	250	23	11
Processing according to mode I	HV <sub>F</sub> = 205	440	760	20.5	245	185	160
	HV <sub>B</sub> = 320						
Processing according to mode II	HV <sub>F</sub> = 225	490	880	20.0	160	85	45
	HV <sub>B</sub> = 335						

characteristic of macroplastic deformation (Fig. 3, a; Fig. 4, b). The temperature at which the steel undergoes a transition from a viscous to a brittle fracture mode, known as  $T_{50}$ , is  $-30\text{ }^{\circ}\text{C}$ .

After cross-helical rolling of steel according to mode I, the fracture toughness of the samples at ambient temperature remains at a similar level to that of the hot rolled state (refer to Table). The loading diagram of these samples

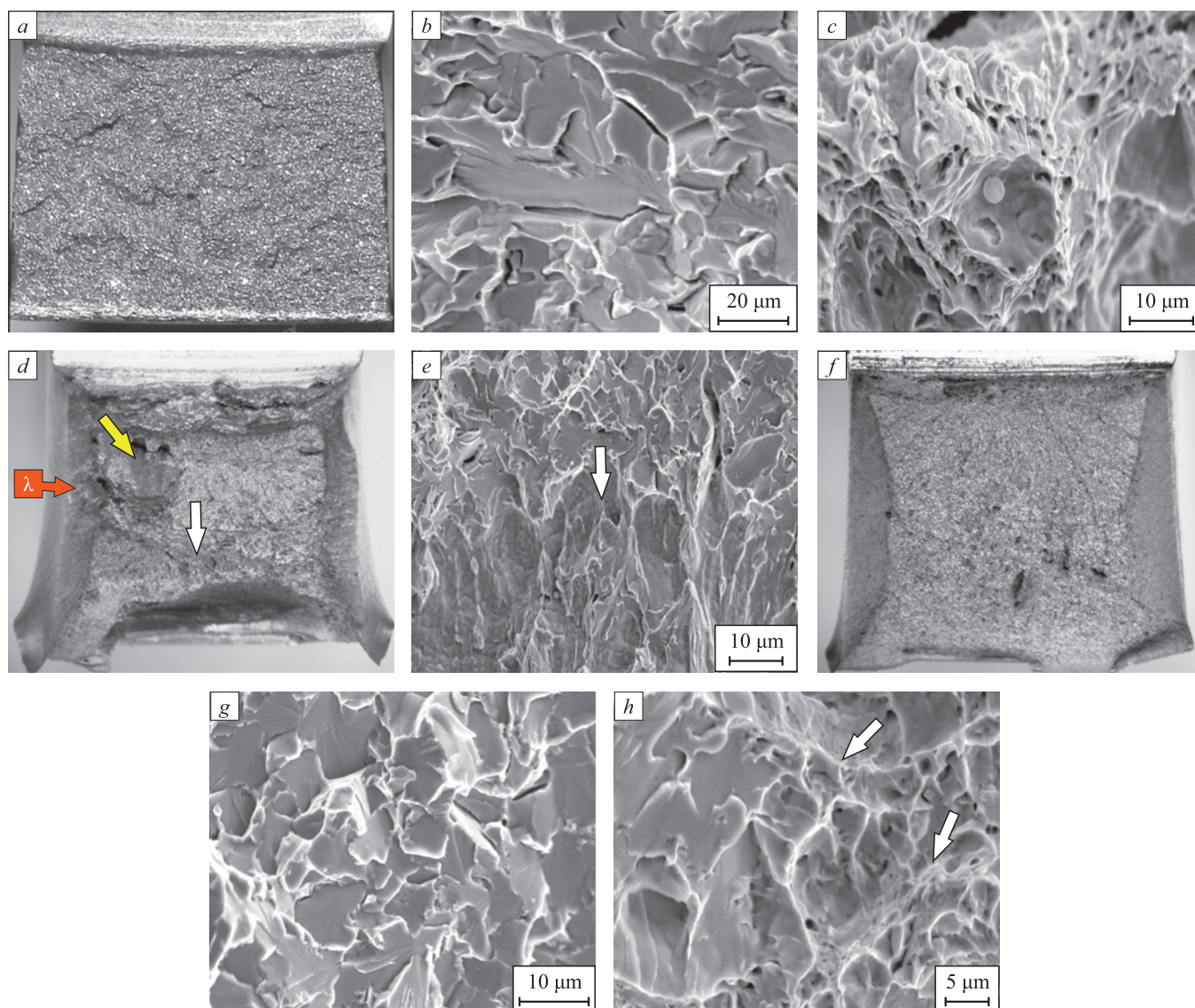


Fig. 3. Fracture surfaces of the impacted samples of steel in hot-rolled state at  $T_{\text{test}} = -40\text{ }^{\circ}\text{C}$  (a, b), after treatment using mode I at  $T_{\text{test}} = +20\text{ }^{\circ}\text{C}$  (c) and  $T_{\text{test}} = -40\text{ }^{\circ}\text{C}$  (d, e) and using mode II at  $T_{\text{test}} = -40\text{ }^{\circ}\text{C}$  (f–h)

Рис. 3. Поверхности разрушения ударных образцов стали в горячекатаном состоянии при  $T_{\text{test}} = -40\text{ }^{\circ}\text{C}$  (a, b), после обработки по режиму I при  $T_{\text{test}} = +20\text{ }^{\circ}\text{C}$  (c) и  $T_{\text{test}} = -40\text{ }^{\circ}\text{C}$  (d, e) и по режиму II при  $T_{\text{test}} = -40\text{ }^{\circ}\text{C}$  (f–h)



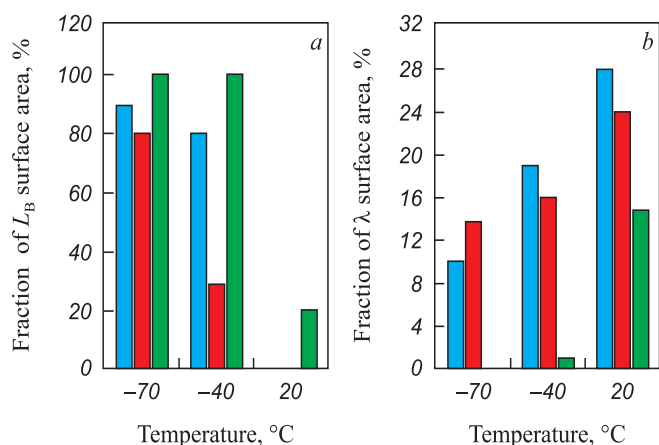


Fig. 4. Bar graphs of the area fractions of brittle fracture zones  $L_B$  (a) and shear lips (b) on steel fractures after hot rolling (green) and after treatment using modes I and II (red and blue)

Рис. 4. Гистограммы долей площади зон хрупкого разрушения  $L_B$  (a) и губ среза (b) на изломах стали после горячей прокатки (зеленый) и после обработки по режимам I и II (красный и синий)

does not exhibit linear segments of load drop (Fig. 2, b, curve 1). Instead, oscillations of the load are detected, which are characteristic of high ductile steels and typical for fracture toughness analysis [13]. The nucleation and propagation of crack at all stages of fracture occur through the formation, growth and coalescence of pores (Fig. 3, c). Coarse carbide particles are present within the dimples observed on the fracture surface.

As the test temperature decreases, the fracture toughness, work of crack nucleation, and work of crack propagation in the steel processed according to mode I decrease (refer to Table and Fig. 2, b). However, these properties remain at a higher level compared to the hot rolled state. In the loading curves, segments of sharp load decrease were observed (Fig. 2, b; curves 2 and 3, indicated by white arrow). However, after the avalanche propagation of the crack, there is a “blunting” of the crack. Further crack propagation is accompanied by plastic deformation (Fig. 2, b; black arrows). On the fracture surfaces of the destroyed samples, a clear transition from brittle to viscous fracture is observed (Fig. 3, d, e; indicated by white arrow). Additionally, the fracture surfaces exhibit segments of splitting (Fig. 3, d; indicated by yellow arrow), which contribute to an increase in fracture toughness by increasing the surface area upon crack formation [14]. Consequently, the energy required for crack development is higher, and the fraction of the brittle constituent in the fracture is lower (Fig. 4, a). At temperatures of  $-40$  and  $-70$  °C, the fraction of the brittle constituent in the fracture is 29 and 80 %, respectively. The presence of significant tightening on the lateral faces (Fig. 3, d), wide lips (Fig. 4, b), and rupture area (Fig. 3, d) down to  $-70$  °C indicates a high degree of plastic deformation during crack propagation. This confirms higher resistance to fracture of the steel after processing according

to mode I. The temperature of the viscous brittle transition,  $T_{50}$ , decreases to  $-55$  °C.

In the case of continuous accelerated cooling after cross-helical rolling (mode II), the fracture toughness at ambient temperature is lower compared to all considered states of the steel (refer to Table). At negative test temperatures, the work of crack nucleation and propagation is higher compared to the hot rolled state but lower than after processing according to mode I (Fig. 2, c). The sample exhibits a higher degree of macroplastic deformation compared to the hot rolled state, as evidenced by the presence of tightening on the lateral faces (Fig. 3, f) and shear lips (Fig. 4, b) even at temperatures as low as  $-70$  °C. Oscillations are observed in the loading-deflection curves until reaching the maximum load. The highest load, at which the main crack begins to develop, is observed in the case of processing according to mode II. This results in the highest concentration of stresses near the crack tip. After reaching the maximum load, there is a sharp drop in the curve along a straight path. This stage corresponds to the brittle propagation of the crack through the mechanism of transcrystalline cleavage (Fig. 3, g). However, the fracture exhibits a mixed pattern, as it contains both cleavage facets and dimples on the fracture surface (Fig. 3, h – indicated by white arrows), indicating a certain degree of plastic deformation during the propagation of the main crack. The temperature of the viscous brittle transition,  $T_{50}$ , for the steel after processing according to mode II is  $-35$  °C.

## DISCUSSION

The application of cross-helical rolling according to mode I offers a significant increase in the low temperature fracture toughness of X70 steel. This improvement is attributed to several factors, including the refinement of ferrite grain size (from 12 to  $4.6 \mu\text{m}$ ), a reduction in the size and fraction of the more brittle troostite phase, and a more homogeneous distribution of structural constituents (ferrite, troostite, bainite). These conclusions align with the experimental findings reported in references [3 – 6; 8]. During low temperature impact loading, there is an incompatibility of plastic deformation between the “soft” ferrite and the brittle troostite regions. The presence of larger troostite regions increases the likelihood of brittle cleavage crack development. By implementing accelerated cooling according to mode I, the formation of granular bainite occurs, and the structure releases finely dispersed carbides due to the holding at  $530$  °C. As a result, the fraction of troostite decreases to 10.5 %. Consequently, the propensity for brittle fracture during low temperature tests is reduced.

The absence of holding and continuous cooling in mode II restricts the release of carbides. As a result, the fraction of finely dispersed carbides in the ferrite matrix

after cooling according to mode *II* is lower compared to processing according to mode *I*. This leads to a higher carbon concentration in austenite and an increase in its stability [15]. Consequently, the subsequent decomposition of austenite occurs at lower temperatures, resulting in the formation of lath bainite and the presence of segments of the MA phase (Fig. 1, *f*). As a consequence, the fracture toughness of the steel after processing according to mode *II* is lower than after processing according to mode *I*. In the available literature [3; 16 – 19] focusing on the study of bainite structures, there is no consensus on which type of bainite phase provides higher fracture toughness for steel. Some studies have shown that the structure of acicular ferrite leads to higher fracture energies and a lower temperature of viscous brittle transition [16; 17]. On the other hand, the formation of granular bainite has been associated with lower fracture energies due to coarser grains and larger segments of the MA phase. However, other researchers [3; 18; 19] have mentioned that the structure of granular bainite offers higher fracture toughness compared to lath bainite and pearlite. These differing conclusions can be attributed to variations in carbon content and micro-dopants (such as niobium, vanadium, molybdenum, titanium, etc.) in the steels, as well as differences in the rolling temperature modes that influence the conditions of bainite phase formation. In the studied case with a carbon content of 0.13 wt. %, rolling in the ( $\gamma + \alpha$ ) region results in significantly enriched overcooled austenite. Subsequent accelerated cooling leads to the formation of lath bainite and large segments of the MA constituent. This aligns with the higher strength observed in the bainite structure (335 HV<sub>50</sub>). However, the more strained structure of lath bainite does not allow for sufficient fracture toughness to be achieved after processing according to mode *II*.

It is important to note that fracture toughness is not solely controlled by the properties of the more brittle phase, but also by the properties of the surrounding matrix [20]. Microregions with higher fracture toughness can inhibit the propagation of brittle fracture originating from adjacent regions with lower fracture toughness. This explains the higher low temperature fracture toughness observed in the steel with a dispersed structure after rolling according to mode *II*, in comparison to the hot rolled state. Additionally, the mixed viscous brittle pattern of fracture, with the presence of blunting of the brittle crack and alternating cleavage facets and dimple relief in the fractures (Fig. 3, *h*), further supports this observation.

Based on the experimental results, it can be assumed that for this specific X70 steel, the favorable type of bainite phase is granular rather than lath bainite. In order to achieve a higher increase in fracture toughness through accelerated cooling, it may be necessary to decrease the carbon content in the steel.

## CONCLUSIONS

Cross-helical rolling combined with accelerated cooling and holding at 530 °C (mode *I*) enables the refinement of the granular structure of X70 steel from 12 to 4.6 μm. The resulting structure consists of ferrite, troostite, granular bainite and finely dispersed carbides Fe<sub>3</sub>C. Continuous accelerated cooling after cross-helical rolling (mode *II*) leads to the presence of grains of ferrite, troostite, granular and lath bainite, as well as segments of the martensite-austenite phase and Fe<sub>3</sub>C particles. Compared to the hot rolled state, both modes *I* and *II* result in a more homogeneous distribution of structural constituents (ferrite, troostite, bainite) and a lower fraction of troostite in the structure (10.5 and 7.5 %, respectively).

As a result of the refinement of the granular structure, formation of the bainite phase, and matrix hardening by carbides, the microhardness of the ferrite matrix in the steel increases to 205 and 225 HV<sub>50</sub> in modes *I* and *II*, respectively, compared to the hot rolled state. In the bainite regions, the microhardness reaches 320 and 335 HV<sub>50</sub>. The yield stress of the steel increases to 440 and 490 MPa, and the ultimate strength increases to 760 and 880 MPa in modes *I* and *II*, respectively.

After cross-helical rolling according to mode *I*, the fracture toughness at negative temperatures significantly increases (KCV<sup>-70 °C</sup> = 160 J/cm<sup>2</sup>) compared to the hot rolled state (KCV<sup>-70 °C</sup> = 11 J/cm<sup>2</sup>). The presence of significant tightening on the lateral faces and wide shear lips up to -70 °C indicates a high degree of plastic deformation during crack propagation. The temperature of the viscous brittle transition, *T*<sub>50</sub>, decreased to -55 °C for the steel after rolling according to mode *I*.

## REFERENCES / СПИСОК ЛИТЕРАТУРЫ

1. Efron L.I. *Metal Science in "Big" Metallurgy. Pipe Steels*. Moscow: Metallurgizdat; 2012:696. (In Russ.).  
Эфрон Л.И. *Металловедение в «большой» металлургии. Трубные стали*. Москва: Металлургиздат; 2012:696.
2. Ali M., Porter D., Kömi J., Eissa M., Faramawy H.E., Mattar T. Effect of cooling rate and composition on microstructure and mechanical properties of ultrahigh-strength steels. *Journal of Iron and Steel Research International*. 2019;26:1350–1365. <https://doi.org/10.1007/s42243-019-00276-0>
3. Jia T., Zhou Y., Jia X., Wang Z. Effects of microstructure on CVN impact toughness in thermomechanically processed high strength microalloyed steel. *Metallurgical and Materials Transactions A*. 2017;48:685–696. <https://doi.org/10.1007/s11661-016-3893-9>
4. Li X.C., Zhao J.X., Jia S.J., Lu G.Y., Misra R.D.K., Liu Q.Y., Li B. Ultrafine microstructure design of high strength pipeline steel for low temperature service: The significant impact on toughness. *Materials Letters*. 2021;303:130429. <https://doi.org/10.1016/j.matlet.2021.130429>
5. Derevyagina L.S., Gordienko A.I., Pochivalov Yu.I., Smirnova A.S. Modification of the structure of low-car-



- bon pipe steel by helical rolling, and the increase in its strength and cold resistance. *Physics of Metal and Metallography*. 2018;119(1):83–91.  
<https://doi.org/10.1134/S0031918X18010076>
6. Surikova N.S., Vlasov I.V., Derevyagina L.S., Gordienko A.I., Narkevich N.A. Influence of cross-screw rolling modes on mechanical properties and fracture toughness of pipe steel. *Izvestiya. Ferrous Metallurgy*. 2021;64(1):28–37. (In Russ.). <https://doi.org/10.17073/0368-0797-2021-1-28-37>  
Сурикова Н.С., Власов И.В., Деревягина Л.С., Гордиенко А.И., Наркевич Н.А. Влияние режимов поперечно-винтовой прокатки на механические свойства и вязкость разрушения трубной стали. *Известия вузов. Черная металлургия*. 2021;64(1):28–37.  
<https://doi.org/10.17073/0368-0797-2021-1-28-37>
  7. Huda N., Midawi A.R.H., Gianetto J., Lazor R., Gerlich A.P. Influence of martensite-austenite (MA) on impact toughness of X80 line pipe steels. *Materials Science and Engineering: A*. 2016;662:481–491.  
<https://doi.org/10.1016/j.msea.2016.03.095>
  8. Kang N., Lee Y., Byun S., Kim K., Kim K., Chung J., Cho K. Quantitative analysis of microstructural and mechanical behavior for Fe–0.1C–(V, Nb) steels as a function of the final rolling temperature. *Materials Science and Engineering: A*. 2009;499(1–2):157–161.  
<https://doi.org/10.1016/j.msea.2007.11.145>
  9. Rybin V.V., Malyshevskii V.A., Khlusova E.I. Structure and the properties of cold-resistant steels for the constructions of Northern design. *Voprosy materialovedeniya*. 2006;1(45):24–44. (In Russ.).  
Рыбин В.В., Малышевский В.А., Хлусова Е.И. Структура и свойства хладостойких сталей для конструкций северного исполнения. *Вопросы материаловедения*. 2006;1(45):24–44.
  10. Hwang B., Lee C.G., Kim S.-J. Low-temperature toughening mechanism in thermomechanically processed high-strength low-alloy steels. *Metallurgical and Materials Transactions A*. 2011;42(3):717–728.  
<https://doi.org/10.1007/s11661-010-0448-3>
  11. Derevyagina L.S., Gordienko A.I., Surikova N.S., Volochaev M.N. Effect of helical rolling on the bainitic microstructure and impact toughness of the low-carbon microalloyed steel. *Materials Science and Engineering: A*. 2021;816:141275. <https://doi.org/10.1016/j.msea.2021.141275>
  12. Pallaspuro S., Kajjalainen A., Mehtonen S., Kömi J., Zhang Z., Porter D. Effect of microstructure on the impact toughness transition temperature of direct-quenched steels. *Materials Science and Engineering: A*. 2018;712:671–680.  
<https://doi.org/10.1016/j.msea.2017.12.037>
  13. Khotinov V.A., Farber V.M., Morozova A.N. Evaluating the toughness of pipe steels by impact fracture curves. *Diagnostics, Resource and Mechanics of materials and structures*. 2015;(2):57–66.  
<https://doi.org/10.17804/2410-9908.2015.2.057-066>
  14. Morozova A.N., Schapov G.V., Khotinov V.A., Farber V.M., Selivanova O.V. Influence of the direction of propagation of the main crack on the fracture mechanism upon impact bending of samples of high-viscous steel with a filamentary structure. Tensile Region. *Physics of Metals and Metallography*. 2019;120(9):919–924.  
<https://doi.org/10.1134/S0031918X19070068>
  15. Wang J., Van Der Wolk P.J., Van Der Zwaag S. On the influence of alloying elements on the bainite reaction in low alloy steels during continuous cooling. *Journal of Materials Science*. 2000;35:4393–4404.  
<https://doi.org/10.1023/A:1004865209116>
  16. Ghosh S., Mula S. Thermomechanical processing of low carbon Nb–Ti stabilized microalloyed steel: Microstructure and mechanical properties. *Materials Science and Engineering: A*. 2015;646:218–233.  
<https://doi.org/10.1016/j.msea.2015.08.072>
  17. Lan H.F., Du L.X., Misra R.D.K. Effect of microstructural constituents on strength–toughness combination in a low carbon bainitic steel. *Materials Science and Engineering: A*. 2014;611:194–200.  
<https://doi.org/10.1016/j.msea.2014.05.084>
  18. Hwang B., Lee C.G., Lee T.-H. Correlation of microstructure and mechanical properties of thermomechanically processed low-carbon steels containing boron and copper. *Metallurgical and Materials Transactions A*. 2010;41(1):85–96.  
<https://doi.org/10.1007/s11661-009-0070-4>
  19. Jia S.-J., Li B., Liu Q.-Y., Ren Y., Zhang S., Gao H. Effects of continuous cooling rate on morphology of granular bainite in pipeline steels. *Journal of Iron and Steel Research International*. 2020;27(7):681–690.  
<https://doi.org/10.1007/s42243-019-00346-3>
  20. Luo X., Chen X., Wang T., Pan S., Wang Z. Effect of morphologies of martensite–austenite constituents on impact toughness in intercritically reheated coarse-grained heat-affected zone of HSLA steel. *Materials Science and Engineering A*. 2018;710:192–199.  
<http://dx.doi.org/10.1016/j.msea.2017.10.079>

## Information about the Authors

## Сведения об авторах

**Antonina I. Gordienko**, Cand. Sci. (Eng.), Research Associate of the Laboratory of Physical Mesomechanics and Non-Destructive Control Methods, Institute of Strength Physics and Materials Science, Siberian Branch of Russian Academy of Sciences

ORCID: 0000-0002-4361-8906

E-mail: mirantil@ispms.ru

**Ilya V. Vlasov**, Cand. Sci. (Eng.), Research Associate of the Laboratory of Physical Mesomechanics and Non-Destructive Control Methods, Institute of Strength Physics and Materials Science, Siberian Branch of Russian Academy of Sciences

ORCID: 0000-0001-9110-8313

E-mail: viv@ispms.ru

**Антонина Ильдаровна Гордиенко**, к.т.н., научный сотрудник лаборатории физической мезомеханики и неразрушающих методов контроля, Институт физики прочности и материаловедения Сибирского отделения РАН

ORCID: 0000-0002-4361-8906

E-mail: mirantil@ispms.ru

**Илья Викторович Власов**, к.т.н., научный сотрудник лаборатории физической мезомеханики и неразрушающих методов контроля, Институт физики прочности и материаловедения Сибирского отделения РАН

ORCID: 0000-0001-9110-8313

E-mail: viv@ispms.ru

**Yurii I. Pochivalov**, *Cand. Sci. (Phys.-Math.), Leading Researcher of the Laboratory of Physical Mesomechanics and Non-Destructive Control Methods*, Institute of Strength Physics and Materials Science, Siberian Branch of Russian Academy of Sciences

**ORCID:** 0000-0003-0236-816X

**E-mail:** pochiv@ispms.ru

**Юрий Иванович Почивалов**, *к.ф.-м.н., ведущий научный сотрудник физической мезомеханики и неразрушающих методов контроля*, Институт физики прочности и материаловедения Сибирского отделения РАН

**ORCID:** 0000-0003-0236-816X

**E-mail:** pochiv@ispms.ru

## Contribution of the Authors

**A. I. Gordienko** – formation of the basic concept, goals and objectives of research; writing the text; reviewing publications on the article topic; analysis of experimental data.

**I. V. Vlasov** – conducting experimental studies; processing results and data analysis; revision of the text.

**Yu. I. Pochivalov** – conducting experimental studies; processing results and data analysis.

## Вклад авторов

**А. И. Гордиенко** – формирование основной концепции, цели и задач исследования; написание текста рукописи; литературный обзор публикаций по теме статьи; анализ экспериментальных данных.

**И. В. Власов** – проведение экспериментальных исследований; обработка результатов и анализ данных; доработка текста.

**Ю. И. Почивалов** – проведение экспериментальных исследований; обработка результатов и анализ данных.

Received 02.09.2022

Revised 16.11.2022

Accepted 29.11.2022

Поступила в редакцию 02.09.2022

После доработки 16.11.2022

Принята к публикации 29.11.2022



UDC 669:539.381.296

DOI 10.17073/0368-0797-2023-3-320-326



Original article

Оригинальная статья

## PATTERNS OF LOCALIZED DEFORMATION AT PRE-FRACTURE STAGE IN CARBON STEEL – STAINLESS STEEL BIMETAL

S. A. Barannikova<sup>✉</sup>, Yu. V. Li

Institute of Strength Physics and Materials Science, Siberian Branch of the Russian Academy of Sciences (2/4 Akademicheskii Ave., Tomsk 634055, Russian Federation)

✉ bsa@ispms.ru

**Abstract.** The work is devoted to the study of strain localization at macroscale level during parabolic mechanical hardening and pre-fracture under quasi-static loading of a carbon steel – stainless steel bimetal. The problem of estimating the scale of the phenomena that determine plasticity is decisive in the development of any theories of plastic deformation, in particular, dislocation theories. The main difficulty in constructing such theories is the reconciling the dislocation scales, characteristic for most deformation and mechanical hardening mechanisms, with macroscopic parameters of deformation processes. In the framework of the autowave model of localized plastic deformation, this problem can be reduced to the possibility of obtaining parameters from the results of macroscale observations of localized plastic flow development. During the experiments, it was confirmed that in a bimetal at any forming stage, a specific pattern of localization centers distribution is spontaneously generated - a pattern of localized plastic flow. The shape of such patterns is determined by the law of mechanical hardening acting in the material. It is shown that the observed localization patterns can be used as an informative feature in predicting the plasticity margin. In the process of uniaxial tension at the stage of parabolic mechanical hardening of the bimetal, the deformation mode is realized with the formation of several potential fracture centers. It was established that at the pre-fracture stage, during the time evolution of the wave pattern of deformation localization, the zone of active plastic deformation narrows, but the number of centers in it either remains the same with a decrease in the distance between them, or even increases. The result of this process is the formation of a macroscopic neck, and then fracture. At the pre-fracture stage, the collapse point indicates the place of future fracture and signals the need to stop the deformation process in order to avoid the fracture of the bimetallic material. Thus, the well-known manifestation of deformation macroscopic localization – formation of a neck – is preceded by complex phenomena of mutually coordinated motion of localized plasticity centers at the pre-fracture stage.

**Keywords:** plastic deformation, localization, bimetal, low carbon steel, stainless steel

**Acknowledgements:** The work was performed within the framework of the state task of the Institute of Strength Physics and Materials Science, Siberian Branch of Russian Academy of Sciences, project No. FWRW-2021-0011.

**For citation:** Barannikova S.A., Li Yu.V. Patterns of localized deformation at pre-fracture stage in carbon steel – stainless steel bimetal. *Izvestiya. Ferrous Metallurgy*. 2023;66(3):320–326. <https://doi.org/10.17073/0368-0797-2023-3-320-326>

## КАРТИНЫ ЛОКАЛИЗАЦИИ ДЕФОРМАЦИИ НА СТАДИИ ПРЕДРАЗРУШЕНИЯ В БИМЕТАЛЛЕ УГЛЕРОДИСТАЯ СТАЛЬ – НЕРЖАВЕЮЩАЯ СТАЛЬ

С. А. Баранникова<sup>✉</sup>, Ю. В. Ли

Институт физики прочности и материаловедения Сибирского отделения РАН (Россия, 634055, Томск, пр. Академический 2/4)

✉ bsa@ispms.ru

**Аннотация.** В работе проведено исследование локализации деформации на макромасштабном уровне на стадиях параболического деформационного упрочнения и предразрушения в условиях квазистатического нагружения биметалла углеродистая сталь – нержавеющая сталь. Проблема оценки масштабов явлений, определяющих пластичность, является решающей при разработке любых теорий пластической деформации, в частности, дислокационных. Основной сложностью при построении таких теорий является трудность согласования дислокационных масштабов, характерных для большинства механизмов деформации и деформационного упрочнения, с макроскопическими параметрами деформационных процессов. В рамках автоволновой модели локализованной пластической деформации эта задача может быть сведена к возможности получения параметров из результатов макронаблюдений развития локализованного пластического течения. В ходе экспериментов подтверждается, что в биметалле на любой стадии процесса

формоизменения самопроизвольно генерируется специфическая картина распределения очагов локализации – паттерн локализованного пластического течения. Форма таких паттернов определяется действующим в материале законом деформационного упрочнения. Наблюдаемые паттерны локализации могут быть использованы в качестве информативного признака при прогнозировании запаса пластичности. В процессе одноосного растяжения на стадии параболического деформационного упрочнения биметалла реализуется режим деформирования с образованием нескольких потенциальных очагов разрушения. Установлено, что на стадии предразрушения в ходе временной эволюции волновой картины локализации деформации зона активной пластической деформации сужается, но количество очагов в ней сохраняется при уменьшении расстояния между ними или даже возрастает. Результатом этого процесса является образование макроскопической шейки, а затем разрушение. На стадии предразрушения точка коллапса указывает на место будущего разрушения и сигнализирует о необходимости остановки процесса деформирования во избежание разрушения биметаллического материала. Таким образом, общеизвестное проявление макроскопической локализации деформации – образование шейки – предворяется сложными явлениями взаимосогласованного движения очагов локализованной пластичности на стадии предразрушения в биметаллах.

**Ключевые слова:** пластическая деформация, локализация, биметаллы, низкоуглеродистая сталь, нержавеющая сталь

**Благодарности:** Работа выполнена в рамках государственного задания Института физики прочности и материаловедения Сибирского отделения РАН, тема № FWRW-2021-0011.

**Для цитирования:** Баранникова С.А., Ли Ю.В. Картины локализации деформации на стадии предразрушения в биметалле углеродистая сталь – нержавеющая сталь. *Известия вузов. Черная металлургия*. 2023;66(3):320–326.  
<https://doi.org/10.17073/0368-0797-2023-3-320-326>

## INTRODUCTION

In physical description of plastic flow still poses an unsolved issue concerning the reasons and essence of changes in the pattern of macroscopic localization and deformational hardening during the transition from one stage of the process to another. While the mechanisms of deformational hardening at specific stages of deformation have been extensively studied at the microscopic level [1], the main problem remains unresolved: understanding exhaustion of one mechanism and the initiation of another. Consequently, there are gaps in the macroscopic description of the plasticity phenomenon. On the one hand, this hinders a complete comprehension of material hardening, and on the other hand, it impedes the development of technological procedures for material processing such as rolling, forging, stamping, and drawing, which involve significant plastic deformations [2]. Therefore, there is a need to expand and clarify the model and mechanism of metals' response to external mechanical impacts. This will facilitate the development of a modern variant of plasticity theory, which takes into account the physical, mechanical, and materials science aspects of the bimetal materials problem [3]. Bimetal materials find wide applications in various technological fields due to their ability to provide not only qualitatively new product properties but also significant savings in expensive materials. During the combined rolling of workpieces composed of dissimilar metal components, the complex development patterns of their plastic flow along the length of the deformation center determine the intricate formation of the junction zone [4].

Extensive research has been conducted over several decades to investigate the structure and mechanical properties of bimetal materials [5 – 7]. As a result, issues related to their production technology have been resolved, methods to enhance the mechanical properties of finished products have been identified, and a significant amount of experimental data has been collected, shedding

light on various aspects of their structure and property control [8 – 11]. However, the existing theoretical concepts fail to provide adequate predictions for the failure of bimetals in the form of lamination during plastic forming processes. Although the application of layered composite materials mechanics approaches [12; 13] has allowed for the prediction of lamination in bimetal materials under small elastic-plastic deformations [14; 15], which are typical for operational loads, forecasting such processes under high plastic deformations remains challenging.

Studies conducted in [16; 17] have demonstrated that the patterns of plastic deformation localization in tensioned bimetal samples exhibit autowave characteristics [18 – 21]. During the elastic-plastic transition, localized plastic deformation zones originate in the regions of the bimetal junction and propagate as Lueders fronts. Initially, they occur in the main layer of low carbon steel and subsequently in the cladding layers of stainless steel [16; 17]. This research provides data on the distribution of local deformations in the main and cladding layers of bimetal materials at advanced stages of plastic flow and fracture. Furthermore, it enables a comparison of the localized deformation patterns observed in different bimetal components deformed under identical conditions.

## EXPERIMENTAL

A corrosion resistant bimetal consisting of low carbon steel St3sp and stainless steel 12Kh18N9T was chosen for the study.

The bimetal was obtained by pouring and subsequently rolling into a sheet 8 mm thick sheet.

The method involved preparing two or multilayer ingots by pouring one or more layers onto a solid layer of a different composition [3]. The main layer, with a thickness of approximately 6.7 mm, consisted of low



carbon steel St3sp. The upper and lower cladding layers, with a thickness of approximately 0.75 mm, were made of stainless steel 12Kh18N9T. Flat samples, measuring 42×8×2 mm, were cut from sheets of three-layer metal in such a way that the working surface (observation surface) was perpendicular to the sheet rolling direction.

The microstructure and elemental composition of the bimetal junction zone have been extensively discussed in [16; 17]. The structure of the base metal St3sp is typical of low carbon steels, with a ferrite matrix containing a small amount of pearlite. The structure of the cladding metal 12Kh18N9T is characteristic of stainless steels, consisting of elongated austenite grains aligned along the rolling axis. The formation of  $\alpha'$  martensite deformation in the cladding layer of stainless steel 12Kh18N9T, resulting from the tension of the 12Kh18N9T + St3sp bimetal, was determined through X-ray diffraction analysis. X-ray diffraction patterns were obtained using monochromatized  $\text{CuK}_\alpha$  radiation with a DRON3 facility. Analysis of the X-ray diffraction patterns of the bimetal's surface layer revealed that the initial state consisted solely of austenite ( $\gamma$  phase) with a lattice parameter of  $a = 3.5999 \text{ \AA}$ . Upon tensile deformation of the bimetal samples, a deformation-induced  $\gamma - \alpha'$  phase transformation occurred in the surface layers of stainless steel 12Kh18N9T [9], resulting in a two-phase structure with varying ratios of  $\alpha$  and  $\gamma$  phases. With a total deformation  $\varepsilon_{\text{tot}} = 15 \%$ , the content of  $\alpha'$  martensite ( $a = 2.8873 \text{ \AA}$ ) was approximately  $52 \pm 4 \%$ , while the remaining phase was austenite ( $\gamma$  phase) with a lattice parameter of  $a = 3.5999 \text{ \AA}$ .

The samples were subjected to stretching using a Walter + Bai LFM125 testing machine at an ambient temperature, with a deformation rate of  $6.67 \cdot 10^{-5} \text{ s}^{-1}$ . To analyze the stages of deformation hardening described by the Ludwik–Hollomon empirical equation  $\sigma = K\varepsilon^n$  (where  $K$  and  $n$  are material constants), the values of  $K$  and  $n$  were determined by plotting the “stress – true deformation” relationship on double logarithmic coordinates  $\ln(s - s_0) = f(\ln \varepsilon)$ .

According to the concept of material failure, considering damage accumulation [13], the damage parameter  $D$  can be calculated as follows [22]:

$$D = -\frac{1}{2} \ln \left( \frac{\tilde{E}_i}{E_0} \right), \quad (1)$$

where  $E_0$  is the elasticity modulus (Young's modulus);  $\tilde{E}_i$  is the secant modulus.

In this study, the secant modulus was determined from the slope of the linear section of the tension diagrams obtained in the cyclic load-unload mode, with an interval of 2.5 % of the total deformation.

To observe the macroscopic localization of plastic deformation, a technique combining mechanical tests for

uniaxial tension with the correlation of digital speckle images was employed. This technique enables the reconstruction of displacement vector fields on the surface of flat samples at different stages of the process and the calculation of the components of the plastic deformation tensor. Further details and the capabilities of this technique are described in [18 – 21] and will not be discussed further in this context.

## RESULTS AND DISCUSSION

Previous research [16] has demonstrated that during the tensioning process of a bimetal specimen composed of low carbon steel St3sp and austenitic stainless steel 12H18N9T, which have different mechanical properties, the initial plastic flow occurs in the softer main layer, while the more resilient cladding stainless steel layer deforms elastically. Both the base layer and the cladding layer undergo plastic deformation in the flow region. Analysis of the distribution patterns of local deformations revealed that, during the early stages of plastic flow in the three-layer bimetal, a single front in the form of the Chernov–Lueders band (CLB) first appears at the interface of the composite in the main layer of low carbon St3sp steel, subsequently initiating the formation of the CLB front in the 12H18N9T steel cladding layer. A single localization front propagates throughout the entire flow region, encompassing both the main and cladding layer.

During the stage of parabolic deformation hardening, a system of stationary areas of plastic deformation localization  $\varepsilon_{xx}$  with a spatial period of  $\lambda = 4 \pm 1 \text{ mm}$  is observed in the main layer of low carbon steel St3sp bimetal (Fig. 1, *a*). It is worth noting that a change in the increments of local strains  $\varepsilon_{xx}(x, t)$  in the main St3sp layer was observed during the transition from the stage of parabolic strain hardening to the stage of pre-fracture of the bimetal (Fig. 1, *b*).

Subsequently, during the pre-fracture stage of the bimetal, the previously immobile centers of plastic deformation localization  $\varepsilon_{xx}$  in the main St3sp layer begin to move coordinately, converging towards a high-amplitude maximum of local deformations. Similar to a monolithic sample of St3sp low carbon steel, the presence of a high-amplitude maximum in the form of localized elongation distributions indicates the formation of a macroscopic neck and future ductile fracture within the main layer of the St3sp bimetal.

To conduct a comprehensive analysis of the evolution of localized elongation distributions  $\varepsilon_{xx}$  during the transition from the parabolic stage of strain hardening to the pre-fracture stage of the bimetal, we examined the changes in the overall values of the  $\varepsilon_{xx}$  component at various points along the tension axis. Specifically, we focused on the main layer of the St3sp steel bimetal (Fig. 2, *a*, points 1 – 4) and the vicinity of the material

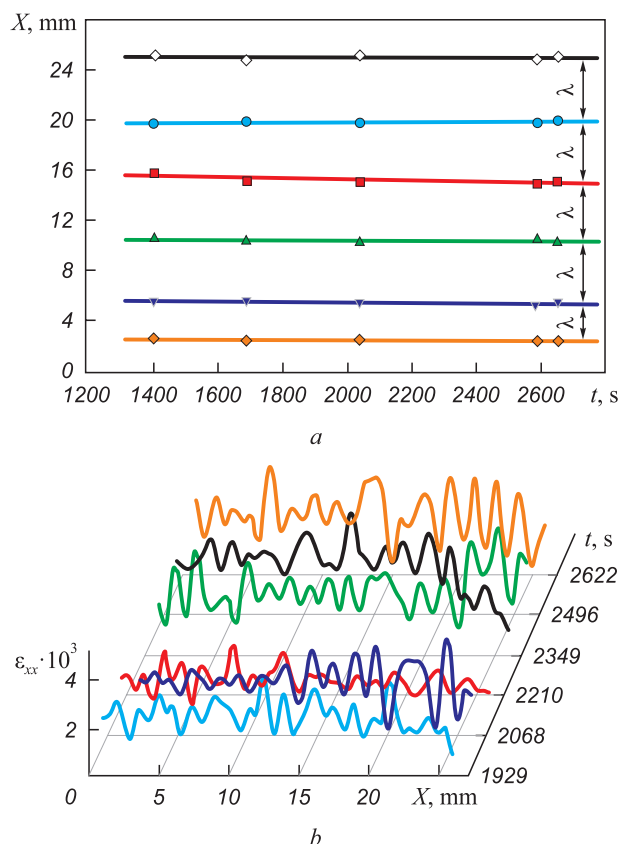


Fig. 1. Kinetic diagrams  $X(t)$  of the positions of localized strain maxima  $\varepsilon_{xx}$  along the tension axis with time  $t$  in the base layer of 12Kh18N9T + St3sp bimetal at parabolic mechanical hardening (a) and distribution of local elongations  $\varepsilon_{xx}(x, t)$  during transition from parabolic mechanical hardening to prefracture (b)

Рис. 1. Кинетические диаграммы  $X(t)$  положений максимумов локализованной деформации  $\varepsilon_{xx}$  вдоль оси растяжения с течением времени  $t$  в основном слое биметалла 12Х18Н9Т + Ст3сп на стадии параболического деформационного упрочнения (a) и распределение приростов локальных удлинений  $\varepsilon_{xx}(x, t)$  при переходе от стадии параболического деформационного упрочнения к предразрушению (b)

junction zone (Fig. 2, a, points 1' – 4') within the time interval of  $t = 1400 \div 3850$  s, corresponding to a total deformation of  $\varepsilon_{tot} = 0.12 \div 0.33$ .

The investigation has revealed that the average total value of localized elongations,  $\varepsilon_{xx}$  remains relatively constant during the parabolic deformation hardening stage. However, it begins to deviate from this constant level at a total strain of  $\varepsilon_{tot} = 0.19 \div 0.25$ , marking the transition from the parabolic strain hardening stage to the pre-fracture stage (Fig. 2, b, curves 1 and 2). In the region of plastic deformation localization (Fig. 2, a, points 4 and 4') both in the main layer of low carbon steel St3sp (Fig. 2, b, curve 2) and near the cladding layer of stainless steel 12Kh18N9T (Fig. 2, b, curve 1) a significant increase in the total values of localized elongations,  $\varepsilon_{xx}$  is observed. This increase corresponds to the transition from the parabolic strain hardening stage to the pre-fracture stage of the bimetal.

By taking the logarithm of the  $\varepsilon_{xx}(\varepsilon/\delta)$  dependences (Fig. 2, b, curves 1 and 2), it was possible to identify linear segments with different slopes. The first point of intersection of these straight lines represents the start of the parabolic deformation hardening stage, while the second point indicates its end and the transition to the pre-fracture stage.

Mathematical analysis of the  $\varepsilon_{xx}(\varepsilon/\delta)$  dependences (Fig. 2, b, curves 1 and 2), which correspond increase in localized elongations in the localization zone of the main and cladding layers of the bimetal during the pre-fracture stage, was performed using the double  $t$ -criterion method [23]. Statistical analysis revealed that the difference in the slope of curves 1 and 2 (Fig. 2, b) for the base and cladding metals is significant, as the double  $t$ -criterion  $|t| = 17.5 > 2.3$ , indicating  $|t| > t_{a,f}$ , where the reference value of the Student's coefficient  $t_{a,f} = 2.3$  [23].

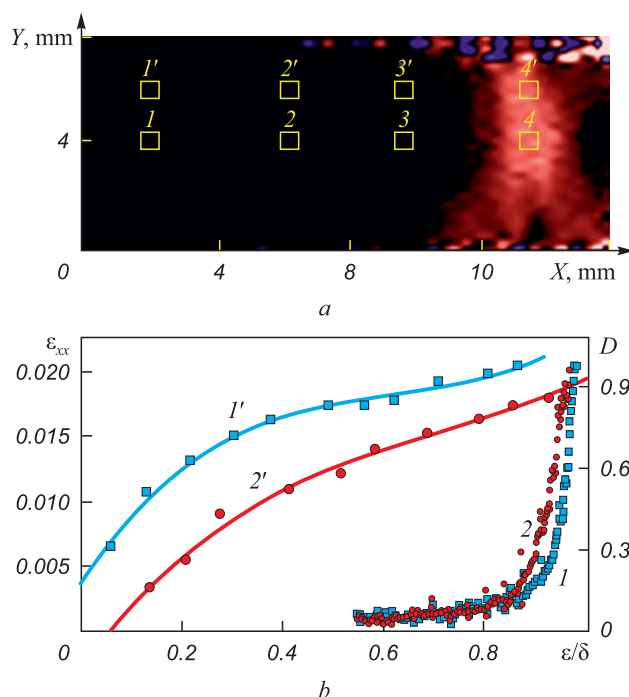


Fig. 2. Areas for analysis of local elongations total values during transition to prefracture in the fracture center in the base and cladding layers of 12Kh18N9T + St3sp bimetal with total deformation  $\varepsilon_{tot} = 0.28$  (a); dependence of distributions of total local elongations  $\varepsilon_{xx}$  (1 – cladding layer 12Kh18N9T; 2 – base layer St3sp) and damage parameter  $D$  (1' – cladding layer 12Kh18N9T; 2' – base layer St3sp) on the bimetal normalized plasticity  $\varepsilon/\delta$  (b)

Рис. 2. Области для анализа суммарных значений локальных удлинений при переходе к стадии предразрушения в очаге разрушения в основном и плакирующем слоях биметалла 12Х18Н9Т + Ст3сп при общей деформации  $\varepsilon_{tot} = 0,28$  (a); зависимости распределений суммарных локальных удлинений  $\varepsilon_{xx}$  (1 – плакирующий слой 12Х18Н9Т; 2 – основной слой Ст3сп) и параметра поврежденности  $D$  (1' – плакирующий слой 12Х18Н9Т; 2' – основной слой Ст3сп) от нормированной пластичности  $\varepsilon/\delta$  биметалла (b)

The results indicate that during the transition from the parabolic stage to the pre-fracture stage of the bimetal, the increment of localized elongations  $\varepsilon_{xx}$  in the localization center (Fig. 2, *a*, points 4 and 4') is greater in the cladding layer of stainless steel 12Kh18N9T (Fig. 2, *b*, curve 1) compared to the main layer of low carbon steel St3sp (Fig. 2, *b*, curve 2). This difference is likely associated with the nature of damage accumulation in the different layers of the bimetal during stretching.

The damage parameter  $D$  was calculated using Equation (1) during the uniaxial tension mechanical tests in the load-unload mode. Analysis of the data revealed an exponential relationship between the damage parameter and the total tensile strain in both individual components and the bimetal specimens. Considering the significant differences in the mechanical properties of the materials in different layers of the bimetal, it is more reasonable to examine the dependence of the damage parameter  $D$  on the normalized total tensile strain  $\varepsilon$ , relative to the elongation at fracture  $\delta$  for each material. From the combined dependencies of total localized elongations  $\varepsilon_{xx}$  and the damage parameter  $D$  on the normalized plasticity  $\varepsilon/\delta$  (Fig. 2, *b*), it can be observed that the accumulation of damage and the increase in localized elongations at the same level of total deformation occur more rapidly in the cladding layer of austenitic stainless steel 12Kh18N9T (curves 1 – 1') compared to the main layer of low carbon steel St3sp (curves 2 – 2') in the bimetal.

It has been determined that the fracture of the bimetal initiates at a total deformation of  $\varepsilon_{\text{tot}} = 0.33$ , where a crack forms in the cladding layer of stainless steel. Subsequently, the crack propagates into the main layer of low carbon steel and divides into several microcracks during its propagation. The primary crack in the main layer follows a stepwise zigzag trajectory. Once the crack traverses the entire cross-section of the samples at a total deformation of  $\varepsilon_{\text{tot}} = 33.5$ , the bimetal experiences complete fracture. The fracture behavior of low carbon steel St3sp and austenitic stainless steel 12Kh18N9T differs significantly. The main component of the bimetal, St3sp steel, exhibits a viscous fracture mechanism, while the cladding layer composed of 12Kh18N9T steel undergoes brittle fracture [24]. These findings substantiate the distinct nature of the damage parameter dependencies in different layers of the bimetal during loading (Fig. 2, *b*).

During uniaxial tension of the bimetal beyond the yield point, the occurrence of microcracks at the interface between the two layers is observed, particularly on the cladding side. This phenomenon can be attributed to the presence of a stress gradient in the junction zone, which arises due to chemical and structural heterogeneities [16; 17]. Although stainless steel 12Kh18N9T possesses high strength and ductility in its monolithic state, the joint deformation of the bimetal, rolled to a thickness of 8 mm, leads to more intense plastic deformation localization and the accumulation of micro-

cracks in the cladding layer compared to the low-strength main layer of low carbon steel.

## CONCLUSIONS

During the analysis of localized deformation patterns in the 12Kh18N9T + St3sp bimetal at advanced stages of plastic flow using speckle image correlation, the following regularities were observed.

In the main layer of low carbon steel (St3sp) bimetal, during the parabolic deformation hardening stage, a stationary system of equidistant areas of deformation localization is formed with a spatial period of approximately  $4 \pm 1$  mm. At the prefracture stage, the fixed centers of plastic deformation localization within the main layer initiate coordinated movement towards the center characterized by high amplitudes of the  $\varepsilon_{xx}$  component of local elongation. This movement eventually leads to the formation of a neck region and subsequent ductile fracture of the specimen.

A significant exponential growth in the cumulative value of localized elongations  $\varepsilon_{xx}$  was observed during the transition from the parabolic deformation hardening stage to the prefracture stage in the region where the neck of the bimetal forms. This growth in elongations was observed in both the main layer of low carbon steel and the cladding layer of stainless steel.

## REFERENCES / СПИСОК ЛИТЕРАТУРЫ

1. Rao S.I., Dimiduk D.M., Tang M., Uchic M.D., Parthasarathy T.A., Woodward C. Estimating the strength of single-ended dislocation sources in micron-sized single crystals. *Philosophical Magazine*. 2007;87(30):4777–4794. <http://dx.doi.org/10.1080/14786430701591513>
2. Gronostajski Z., Pater Z., Madej L., Gontarz A., Lisiecki L., Łukaszek-Solek A., Łuksza J., Mróz S., Muskalski Z., Muzykiewicz W., Pietrzyk M., Śliwa R.E., Tomczak J., Wiewiórowska S., Winiarski G., Zasadziński J., Ziolkiewicz S. Recent development trends in metal forming. *Archives of Civil and Mechanical Engineering*. 2019;19(3):898–941. <http://dx.doi.org/10.1016/j.acme.2019.04.005>
3. Zasukha P.F., Korshchikov V.D., Bukhvalov O.B., Ershov A.A. *Bimetallic Rolled Products*. Moscow: Metallurgiya; 1971:264. (In Russ.).  
*Биметаллический прокат* / П.Ф. Засуха, В.Д. Корщиков, О.Б. Бухвалов, А.А. Ершов. Москва: Металлургия, 1971:264.
4. Li L., Nagai K., Yin F. Progress in cold roll bonding of metals. *Science and Technology of Advanced Materials*. 2008;9(2):023001. <http://dx.doi.org/10.1088/1468-6996/9/2/023001>
5. Deb-Roy T., Wie H.L., Zuback J.S., Mukherjee T., Elmer J.W., Milewski J.O., Beese A.M., Wilson-Heid A., De A., Zhang W. Additive manufacturing of metallic components – Process, structure and properties. *Progress in Materials Science*. 2018;92:112–224. <https://doi.org/10.1016/j.pmatsci.2017.10.001>



6. Hinojos A., Mireles J., Reichardt A., Frigola P., Hosemann P., Murr L.E., Wicker R.B. Joining of Inconel 718 and 316 Stainless Steel using electron beam melting additive manufacturing technology. *Materials and Design*. 2016;94:17–27. <http://dx.doi.org/10.1016/j.matdes.2016.01.041>
7. Hofmann D.C., Roberts S., Otis R., Kolodziejaska J., Dillon R.P., Suh J., Shapiro A.A., Li Z.-K., Borgonia J.-P. Developing gradient metal alloys through radial deposition additive manufacturing. *Scientific Reports*. 2014;4:5357. <http://dx.doi.org/10.1038/srep05357>
8. Li Z., Lin Y.C., Zhang L., Jia F., Jiang Z., Jiao S. Investigation of compact tensile and fracture mechanical properties of a duplex stainless steel bimetal composite with the interfacial zone. *Journal of Materials Research and Technology*. 2022;19:809–820. <https://dx.doi.org/10.1016/j.jmrt.2022.05.085>
9. Li Z., Zhao J., Jia F., Liang X., Zhang Q., Yuan X., Jiao S., Jiang Z. Interfacial characteristics and mechanical properties of duplex stainless steel bimetal composite by heat treatment. *Materials Science and Engineering: A*. 2020;787:139513. <http://dx.doi.org/10.1016/j.msea.2020.139513>
10. Chen N., Ali Khan H., Wan Z., Lippert J., Sun H., Shang S.-L., Liu Z.-K., Li J. Microstructural characteristics and crack formation in additively manufactured bimetal material of 316L stainless steel and Inconel 625. *Additive Manufacturing*. 2020;32:101037. <https://doi.org/10.1016/j.addma.2020.101037>
11. Li Z., Zhao J., Jia F., Lu Y., Liang X., Yuan X., Jiao S., Zhou C., Jiang Z. Hot deformation behaviour and interfacial characteristics of bimetal composite at elevated temperatures. *Intermetallics*. 2020;125:106893. <http://dx.doi.org/10.1016/j.intermet.2020.106893>
12. Fudzii T., Dzako M. *Mechanics of Composite Materials Fracture*. Moscow: Mir; 1982:232. (In Russ.).  
Фудзии Т., Дзак М. *Механика разрушения композиционных материалов*. Москва: Мир; 1982:232.
13. Murakami S. *Continuum Damage Mechanics*. Springer: Netherlands; 2012:402.
14. Gladkovskii S.V., Trunina T.A., Kokovikhin E.A., Vichuzhanin D.I., Golubkova I.A. Formation of structure and properties of lamellar metal compounds. *Zagotovitel'nye proizvodstva v mashinostroenii*. 2010;(4):41–45. (In Russ.).  
Гладковский С.В., Трунина Т.А., Коковихин Е.А., Вичужанин Д.И., Голубкова И.А. Формирование структуры и свойств слоистых соединений металлов. *Заготовительные производства в машиностроении*. 2010;(4):41–45.
15. Smirnov S.V., Golubkova I.A. Simulation of cold rolling of thin strips by finite element method. *Zagotovitel'nye proizvodstva v mashinostroenii*. 2010;(5):27–30. (In Russ.).  
Смирнов С.В., Голубкова И.А. Моделирование процесса холодной прокатки тонких полос методом конечных элементов. *Заготовительные производства в машиностроении*. 2010;(5):27–30.
16. Barannikova S.A., Bochkareva A.V., Li Yu.V., Lunev A.G., Shlyakhova G.V., Zuev L.B. Investigation of localization patterns of plastic deformation and fracture of a two-layer metal material. *Fundamental'nye problemy sovremenogo materialovedeniya*. 2016;13(4):511–516. (In Russ.).  
Баранникова С.А., Бочкарева А.В., Ли Ю.В., Лунев А.Г., Шляхова Г.В., Зуев Л.Б. Исследование картин локализации пластической деформации и разрушения двухслойного металлического материала. *Фундаментальные проблемы современного материаловедения*. 2016;13(4):511–516.
17. Shlyakhova G.V., Barannikova S.A., Bochkareva A.V., Li Yu.V., Zuev L.B. Study of the structure of bimetal construction carbon steel – stainless steel. *Izvestiya. Ferrous Metallurgy*. 2018;61(4):300–305. (In Russ.). <https://doi.org/10.17073/0368-0797-2018-4-300-305>  
Шляхова Г.В., Баранникова С.А., Бочкарева А.В., Ли Ю.В., Зуев Л.Б. Исследование структуры биметалла конструкционная углеродистая сталь – нержавеющая сталь. *Известия вузов. Черная металлургия*. 2018;61(4):300–305. <https://doi.org/10.17073/0368-0797-2018-4-300-305>
18. Zuev L.B. Autowave Mechanics of plastic flow. *Springer Tracts in Mechanical Engineering*. 2021:245–274. [https://doi.org/10.1007/978-3-030-60124-9\\_12](https://doi.org/10.1007/978-3-030-60124-9_12)
19. Zuev L.B., Khon Yu.A. Plastic flow as a process of the formation of spatio-temporal structures. Part I. Qualitative and quantitative patterns. *Fizicheskaya Mezomechanika*. 2021;24(6):5–14. (In Russ.). <https://doi.org/10.24412/1683-805X-2021-6-5-14>  
Зуев Л.Б., Хон Ю.А. Пластическое течение как процесс формирования пространственно-временных структур. Часть I. Качественные и количественные закономерности. *Физическая мезомеханика*. 2021;24(6):5–14. <https://doi.org/10.24412/1683-805X-2021-6-5-14>
20. Barannikova S.A., Kosinov D.A., Zuev L.B., Gromov V.E., Kononov S.V. Hydrogen effect on macrolocalization of plastic deformation of low carbon steel. *Izvestiya. Ferrous Metallurgy*. 2016;59(12):891–895. (In Russ.). <https://doi.org/10.17073/0368-0797-2016-12-891-895>  
Баранникова С.А., Косинов Д.А., Зуев Л.Б., Громов В.Е., Коновалов С.В. Влияние водорода на макролокализацию пластической деформации низкоуглеродистой стали. *Известия вузов. Черная металлургия*. 2016;59(12):891–895. <https://doi.org/10.17073/0368-0797-2016-12-891-895>
21. Danilov V.I., Barannikova S.A., Zuev L.B. Localized strain autowaves at the initial stage of plastic flow in single crystals. *Technical Physics*. 2003;48(11):1429–1435. <https://doi.org/10.1134/1.1626775>  
Данилов В.И., Баранникова С.А., Зуев Л.Б. Автоволны локализованной деформации на начальных стадиях пластического течения монокристаллов. *Журнал технической физики*. 2003;73(11):69–75.
22. Chow C.L., Wang J. An anisotropic theory of continuum damage mechanics for ductile fracture. *Engineering Fracture Mechanics*. 1987;27(5):547–558. [https://doi.org/10.1016/0013-7944\(87\)90108-1](https://doi.org/10.1016/0013-7944(87)90108-1)
23. Mendenhall W.M., Sincich T.L. *Statistics for Engineering and the Sciences*. New York: Chapman and Hall/CRC; 2016:1182. <https://doi.org/10.1201/b19628>
24. Gorkunov E.S., Zadvorkin S.M., Putilova E.A. Magnetic estimation of stresses applied to a two-layer steel ct3-steel 08x18h10t composite material during elastoplastic deformation by uniaxial tension. *Russian Journal of Nondestructive Testing*. 2012;48(8):495–504. <https://doi.org/10.1134/S1061830912080050>  
Горкунов Э.С., Задворкин С.М., Путилова Е.А. Оценка приложенных напряжений при упругопластической деформации одноосным растяжением двухслойного композиционного материала «Сталь Ст3 – Сталь 08Х18Н10Т» магнитными методами. *Дефектоскопия*. 2012;8:64–75.



## Information about the Authors

## Сведения об авторах

**Svetlana A. Barannikova**, Dr. Sci. (Phys.-Math.), Leading Researcher of the Laboratory of Strength Physics, Institute of Strength Physics and Materials Science, Siberian Branch of Russian Academy of Sciences

**ORCID:** 0000-0001-5010-9969

**E-mail:** bsa@ispms.ru

**Yuliya V. Li**, Junior Researcher of the Laboratory of Strength Physics, Institute of Strength Physics and Materials Science, Siberian Branch of Russian Academy of Sciences

**ORCID:** 0000-0003-1759-9606

**E-mail:** lyuv@ispms.ru

**Светлана Александровна Баранникова**, д.ф.-м.н., ведущий научный сотрудник лаборатории физики прочности, Институт физики прочности и материаловедения Сибирского отделения РАН

**ORCID:** 0000-0001-5010-9969

**E-mail:** bsa@ispms.ru

**Юлия Владимировна Ли**, младший научный сотрудник лаборатории физики прочности, Институт физики прочности и материаловедения Сибирского отделения РАН

**ORCID:** 0000-0003-1759-9606

**E-mail:** lyuv@ispms.ru

Received 19.09.2022

Revised 15.11.2022

Accepted 20.12.2022

Поступила в редакцию 19.09.2022

После доработки 15.11.2022

Принята к публикации 20.12.2022



UDC 669.539.382:669.17:669.14.018:539.27

DOI 10.17073/0368-0797-2023-3-327-329



Short report

Краткое сообщение

## EVOLUTION OF STRUCTURAL-PHASE STATE AND PROPERTIES OF HYPEREUTECTOID STEEL RAILS AT LONG-TERM OPERATION

M. A. Porfir'ev, V. E. Gromov , R. E. Kryukov

Siberian State Industrial University (42 Kirova Str., Novokuznetsk, Kemerovo Region – Kuzbass 654007, Russian Federation)

gromov@physics.sibsiu.ru

**Abstract.** The methods of modern physical materials science were used to analyze the evolution of microhardness, tribological properties, dislocation substructure and phase composition of the rails with increased wear resistance and contact endurance of DT 400 IR category after missed tonnage of 187 million gross tons on the experimental ring of Russian Railways. It is shown that extremely long-term operation of the rails is accompanied by a decrease (3.1 times) in wear parameter of the rolling surface and an increase (1.4 times) in microhardness, scalar dislocation density (1.5 times) and  $\text{Fe}_3\text{C}$  carbide content (1.24 times). Operation of the rails led to a decrease in the crystal lattice parameter, which correlates with an increase in the content of iron carbide. We made the assumptions about physical causes of the change in parameters.

**Keywords:** special purpose rails, structure, microhardness, phase composition, tribological properties

**Acknowledgements:** The authors express their gratitude to E.V. Polevoy for the provided samples of rails and Y.F. Ivanov for his help in conducting experiments and discussing the results.

**For citation:** Porfir'ev M.A., Gromov V.E., Kryukov R.E. Evolution of structural-phase state and properties of hypereutectoid steel rails at long-term operation. *Izvestiya. Ferrous Metallurgy*. 2023;66(3):327–329. <https://doi.org/10.17073/0368-0797-2023-3-327-329>

## ЭВОЛЮЦИЯ СТРУКТУРНО-ФАЗОВОГО СОСТОЯНИЯ И СВОЙСТВ РЕЛЬСОВ ИЗ ЗАЭВТЕКТОИДНОЙ СТАЛИ ПРИ ДЛИТЕЛЬНОЙ ЭКСПЛУАТАЦИИ

М. А. Порфирьев, В. Е. Громов , Р. Е. Крюков

Сибирский государственный индустриальный университет (Россия, 654007, Кемеровская область – Кузбасс, Новокузнецк, ул. Кирова, 42)

gromov@physics.sibsiu.ru

**Аннотация.** Методами современного физического материаловедения выполнен анализ эволюции микротвердости, трибологических свойств, дислокационной субструктуры и фазового состава рельсов повышенной износостойкости и контактной выносливости категории ДТ 400 ИК после пропущенного тоннажа 187 млн т брутто на экспериментальном кольце РЖД. Экстремально длительная эксплуатация рельсов сопровождается уменьшением параметра износа поверхности катания (в 3,1 раза), увеличением микротвердости (в 1,4 раза), скалярной плотности дислокаций (в 1,5 раза) и содержания карбида  $\text{Fe}_3\text{C}$  (в 1,24 раза). Эксплуатация рельсов привела к уменьшению параметра кристаллической решетки, что коррелирует с ростом содержания карбида железа. Высказаны предположения о физических причинах изменения параметров.

**Ключевые слова:** рельсы специального назначения, структура, микротвердость, фазовый состав, трибологические свойства

**Благодарности:** Авторы работы выражают благодарность Е.В. Полевому за предоставленные образцы рельсов и Ю.Ф. Иванову за помощь в проведении экспериментов и обсуждении результатов.

**Для цитирования:** Порфирьев М.А., Громов В.Е., Крюков Р.Е. Эволюция структурно-фазового состояния и свойств рельсов из заэвтектоидной стали при длительной эксплуатации. *Известия вузов. Черная металлургия*. 2023;66(3):327–329. <https://doi.org/10.17073/0368-0797-2023-3-327-329>

## INTRODUCTION

The continuous rise in the demand for rail reliability under high axle loads and high speeds necessitates ensuring their operational stability and analyzing potential causes of rail withdrawals [1]. Understanding the patterns in the formation of structural-phase states and the properties of specialized rail types is essential for enhancing production techniques and predicting their performance during operation.

In Russia, the production of differentially hardened special purpose rails with enhanced wear resistance and contact endurance has been ongoing for over three years. These rails, categorized as DT 400 IK, are designed for use on straight track sections with speeds up to 200 km/h and on curved sections without traffic density limitations. The significance of information on the structural-phase state, strength, and tribological properties of these new rail types arises from the profound challenges in physical materials science, as well as the practical importance of the issue [2–4]. As per the development program of Russian Railways, there are plans to increase the service life of rails up to 2.0 billion tons of passed tonnage. According to Russian Railways, up to 75 % of rail withdrawals in 2020 were attributed to reaching the limit state for wear and contact fatigue defects.

The objective of this study is to analyze the change in phase composition, dislocation substructure, and properties of special-purpose rails following long-term operation.

## EXPERIMENTAL

Samples of hypereutectoid steel E90KhAF, which comply with the properties and elemental composition regulated by State Standard GOST 51685–2013 and Specifications TU 24.10.75111-298-05757676.2017 RZhD, were utilized as the material for this study. The analysis was conducted on the rails after undergoing differential hardening and subsequent operation on the experimental track of the Russian Railways, with a total tonnage was 187 million gross tons).

The microhardness of the steel was determined using a PMT-3 instrument, employing the Vickers method with an indenter load of 0.5 N. The tribological properties were evaluated by measuring the wear parameter and friction coefficient. Dry friction conditions were maintained during the tests, employing the Pin-on-Disc and Oscillating layout, with a TRIBotester tribometer (TRIBOtechnic, France). The test parameters included a VK8 hard alloy 6 mm ball, a wear track radius of 2 mm, a 50 m path traveled by the counterbody, a sample rotation speed of 25 mm/s, a 2 N load on the indenter, and ambient temperature. The wear groove profile and its parameters were examined using a contact nanoprofilometer (refer to the figure provided)). The wear parameter  $\kappa$  was calculated using the following equation:

$$\kappa = \frac{2\sigma RA}{FL},$$

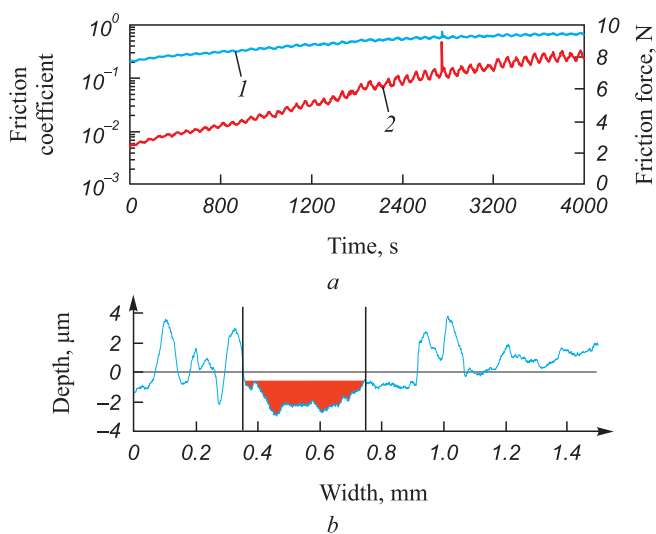
where  $R$  represents the track radius, mm;  $A$  denotes the surface area of the transversal cross-section of the wear tread, mm<sup>2</sup>;  $F$  signifies the applied load, N;  $L$  represents the path passed by the ball counterbody, m [5].

The dislocation substructure was analyzed using transmission electron microscopy (JEOLJEM 2100 F) [6; 7]. The investigation of the phase composition and structural parameters was carried out using an XRD-600 diffractometer with CuK<sub>α</sub> radiation. The RDK 4+ databases and the POWDERCELL 2/4 full-profile analysis program were utilized for the analysis.

## RESULTS AND DISCUSSION

After the operation of DT 400 IK rail, the microhardness of the tread surface increased by 1.4 times, from 5.5 to 7.7 GPa, while the scalar dislocation density increased by 1.5 times, from  $5.0 \cdot 10^{10}$  to  $7.5 \cdot 10^{10}$  cm<sup>-2</sup>. These changes in parameters are attributed to the development of a complex stress-strain state of the rail tread surface during long-term operation [1]. These factors likely contribute to the more than threefold increase in the wear resistance of the tread surface. Initially, the wear parameter was  $7.7 \cdot 10^{-6}$  mm<sup>3</sup>/(N·m), which reduced to  $2.5 \cdot 10^{-6}$  mm<sup>3</sup>/(N·m) after operation. The friction coefficient exhibited a slight decrease from 0.43 to 0.35. However, these results do not provide sufficient grounds for extrapolation wear behavior during subsequent operation. To obtain a comprehensive understanding, additional values of this parameter at different carried tonnage levels, as presented in [1], are required.

X-ray phase analysis of DT 400 IK rails revealed that the primary phases present in the steel are  $\alpha$ -Fe and iron carbide Fe<sub>3</sub>C. In the initial state, the phase content



Dependence of friction coefficient (1) and friction force (2) on time of tribological testing of DT 400 IR rails after missed tonnage of 187 million tons (a) and profile of friction track (b)

Зависимость коэффициента трения (1) и силы трения (2) от времени трибологических испытаний рельсов ДТ 400 ИК после пропущенного тоннажа 187 млн т (a) и профиль дорожки трения (b)

is 95.83 wt. % and 4.17 wt. %, respectively. The crystal lattice constants: for  $\alpha$ -Fe  $a = 2.8736 \text{ \AA}$ , for  $\text{Fe}_3\text{C}$  carbide  $a = 4.7313 \text{ \AA}$ ,  $b = 4.3299 \text{ \AA}$ ,  $c = 2.8330 \text{ \AA}$ .

After the rails have undergone cargo operation, the content of  $\alpha$ -Fe and  $\text{Fe}_3\text{C}$  phases changes to 94.84 wt. % and 5.16 wt. %, respectively. Additionally, the crystal lattice constants become: for  $\alpha$ -Fe  $a = 2.8713 \text{ \AA}$ ; for iron carbide  $a = 4.3057 \text{ \AA}$ ,  $b = 4.3057 \text{ \AA}$ ,  $c = 2.8342 \text{ \AA}$ . These findings indicate that the rails operation resulted in a 1.24-fold increase in the content of  $\text{Fe}_3\text{C}$  carbide, by a factor of, accompanied by changes in its crystal lattice constants, suggesting a potential presence of structural defects. Furthermore, the crystal lattice constant of  $\alpha$ -Fe decreased, which corresponds to the increased content of iron carbide and indicates the release of carbon from the  $\alpha$ -Fe crystal lattice during operation, leading to the formation of a carbide phase.

## CONCLUSIONS

Overall, the operation of DT 400 IK rails contributes to an enhancement in wear resistance, microhardness, scalar dislocation density, and  $\text{Fe}_3\text{C}$  carbide content.

## REFERENCES / СПИСОК ЛИТЕРАТУРЫ

1. Yuriev A.A., Gromov V.E., Ivanov Yu.F., Rubannikova Yu.A., Starostenkov M.D., Tabakov P.Y. *Structure and Properties of*

*Lengthy Rails after Extreme Long Term Operation*. Materials Research Forum LLC, 2021;106:193.

<https://doi.org/10.21741/9781644901472>

2. Ivanov Yu.A., Gromov V.E., Yuriev A.A., Kormyshev V.E., Rubannikova Yu.A., Semin A.P. Deformation strengthening mechanisms of rails in extremely long-term operation. *Journal of Materials Research and Technology*. 2021;11:710–718. <https://doi.org/10.1016/j.jmrt.2020.12.107>
3. Pan R., Ren R., Chen C., Zhao X. Formation of nanocrystalline structure in pearlitic steels by dry sliding wear. *Materials Characterization*. 2017;132:397–404. <https://doi.org/10.1016/j.matchar.2017.05.031>
4. Vinogradov A., Estrin Y. Analytical and numerical approaches to modelling severe plastic deformation. *Progress in Materials Science*. 2018;95:172–242. <https://doi.org/10.1016/j.pmatsci.2018.02.001>
5. *Tribology. Physical Basics, Mechanics and Technical Applications*. Berkovich I.I., Gromakovskii D.G. eds. Samara: SamSU; 2000:268. (In Russ.).  
Беркович И.И., Громаковский Д.Г. Трибология. Физические основы, механика и технические приложения / Под ред. Д.Г. Громаковского. Самара: СамГТУ; 2000:268.
6. Egerton F.R. *Physical Principles of Electron Microscopy*. Basel: Springer International Publishing; 2016:196. <https://doi.org/10.1007/978-3-319-39877-8>
7. Kumar C.S.S.R. *Transmission Electron Microscopy. Characterization of Nanomaterials*. New York: Springer; 2014:717. <https://doi.org/10.1007/978-3-642-38934-4>

## Information about the Authors

**Mikhail A. Porfir'ev**, Research Associate of Department of Scientific Researches, Siberian State Industrial University  
ORCID: 0000-0003-3602-5739  
E-mail: mport372@gmail.com

**Viktor E. Gromov**, Dr. Sci. (Phys.-Math.), Prof., Head of the Chair of Science named after V.M. Finkel', Siberian State Industrial University  
ORCID: 0000-0002-5147-5343  
E-mail: gromov@physics.sibsiu.ru

**Roman E. Kryukov**, Dr. Sci. (Eng.), Assist. Prof. of the Chair of Ferrous Metallurgy, Siberian State Industrial University  
ORCID: 0000-0002-3394-7941  
E-mail: rek\_nzrmk@mail.ru

## Сведения об авторах

**Михаил Анатольевич Порфирьев**, научный сотрудник Управления научных исследований, Сибирский государственный индустриальный университет  
ORCID: 0000-0003-3602-5739  
E-mail: mport372@gmail.com

**Виктор Евгеньевич Громов**, д.ф.-м.н., профессор, заведующий кафедрой естественнонаучных дисциплин им. профессора В.М. Финкеля, Сибирский государственный индустриальный университет  
ORCID: 0000-0002-5147-5343  
E-mail: gromov@physics.sibsiu.ru

**Роман Евгеньевич Крюков**, д.т.н., доцент кафедры металлургии черных металлов, Сибирский государственный индустриальный университет  
ORCID: 0000-0002-3394-7941  
E-mail: rek\_nzrmk@mail.ru

## Contribution of the Authors

**M. A. Porfir'ev** – conducting experiments, writing the text.

**V. E. Gromov** – formation of the work concept, editing the text.

**R. E. Kryukov** – preparation of the samples, discussion of the results, literature review.

## Вклад авторов

**М. А. Порфирьев** – проведение экспериментов, составление текста.

**В. Е. Громов** – формирование концепции работы, редактирование текста.

**Р. Е. Крюков** – подготовка образцов, обсуждение результатов, обзор литературы.

Received 10.01.2023  
Revised 25.01.2023  
Accepted 31.01.2023

Поступила в редакцию 10.01.2023  
После доработки 25.01.2023  
Принята к публикации 31.01.2023





UDC 669.15:546.17:(546.11+546.77):546.74

DOI 10.17073/0368-0797-2023-3-330-336



Original article

Оригинальная статья

# WAGNER INTERACTION COEFFICIENTS OF NITROGEN WITH CHROMIUM AND MOLIBDENUM IN LIQUID NICKEL-BASED ALLOYS

L. A. Bol'shov, S. K. Korneichuk<sup>✉</sup>, E. L. Bol'shova

Vologda State University (15 Lenina Str., Vologda 16000, Russian Federation)

✉ korn62@mail.ru

**Abstract.** The authors propose a simple theory of thermodynamic properties of liquid nitrogen solutions in alloys of the Fe–Ni–Cr and Fe–Ni–Mo systems. This theory is analogous to the theory for liquid nitrogen solutions in binary alloys of the Fe–Cr and Fe–Ni systems proposed previously by the authors in 2019 and 2021. The theory is based on lattice model of ternary liquid solutions of the Fe–Ni–Cr and Fe–Ni–Mo systems. The model assumes a FCC lattice. Atoms of Fe, Ni, Cr and Mo are deposited in the sites of the lattice. Nitrogen atoms are located in octahedral interstices. The nitrogen atom interacts only with the metal atoms located in the lattice sites neighboring to it. This interaction is pairwise. It is assumed that the energy of this interaction depends neither on composition nor on temperature. It is supposed that the liquid solutions in the Fe–Ni–Cr and Fe–Ni–Mo systems are perfect. Within the framework of the proposed theory, the relation is obtained that expresses the Wagner interaction coefficient between nitrogen and chromium in liquid nickel-based alloys  $\varepsilon_N^{\text{Cr}}(\text{Ni})$ . The right-hand part of the appropriate formula is a function of the Wagner interaction coefficients between nitrogen and chromium  $\varepsilon_N^{\text{Cr}}(\text{Fe})$  and between nitrogen and nickel  $\varepsilon_N^{\text{Ni}}(\text{Fe})$  in liquid iron-based alloys. A similar relation is obtained for the Wagner interaction coefficient between nitrogen and molybdenum in liquid nickel-based alloys  $\varepsilon_N^{\text{Mo}}(\text{Ni})$ . According to the first of these formulas, the value  $\varepsilon_N^{\text{Cr}}(\text{Ni}) = -21,9$  at a temperature of 1873 K is calculated. This corresponds to the value of the Langenberg interaction coefficient  $e_N^{\text{Cr}}(\text{Ni}) = -0,108$ , which coincides with experimental estimate. According to the second formula, the value  $\varepsilon_N^{\text{Mo}}(\text{Ni}) = -14,3$  is calculated at a temperature 1873 K. This corresponds to the value of the Langenberg interaction coefficient  $e_N^{\text{Cr}}(\text{Ni}) = -0,036$ , which is in satisfactory agreement with the experimental estimate  $\varepsilon_N^{\text{Mo}}(\text{Ni}) = -15,1$ ;  $e_N^{\text{Cr}}(\text{Ni}) = -0,038$ .

**Keywords:** thermodynamics, solutions, nitrogen, iron, nickel, chromium, molybdenum, activity coefficient, Wagner interaction coefficient, Langenberg interaction coefficient

**For citation:** Bol'shov L.A., Korneichuk S.K., Bol'shova E.L. Wagner interaction coefficients of nitrogen with chromium and molybdenum in liquid nickel-based alloys. *Izvestiya. Ferrous Metallurgy*. 2023;66(3):330–336. <https://doi.org/10.17073/0368-0797-2023-3-330-336>

# ВАГНЕРОВСКИЕ ПАРАМЕТРЫ ВЗАИМОДЕЙСТВИЯ АЗОТА С ХРОМОМ И МОЛИБДЕНОМ В ЖИДКИХ СПЛАВАХ НА ОСНОВЕ НИКЕЛЯ

Л. А. Большов, С. К. Корнейчук<sup>✉</sup>, Э. Л. Большова

Вологодский государственный университет (Россия, 160000, Вологда, ул. Ленина, 15)

✉ korn62@mail.ru

**Аннотация.** Предложена простая теория термодинамических свойств жидких растворов азота в сплавах систем Fe–Ni–Cr и Fe–Ni–Mo, которая аналогична теории для жидких растворов азота в бинарных сплавах систем Fe–Cr и Fe–Ni, представленной авторами ранее (2019 – 2021). Теория основана на решеточной модели трехкомпонентных жидких растворов Fe–Ni–Cr и Fe–Ni–Mo. Предполагается модельная решетка типа ГЦК. В узлах этой решетки располагаются атомы железа, хрома, никеля и молибдена. Атомы азота располагаются в октаэдрических междоузлиях. Атом азота взаимодействует лишь с атомами металлов, находящимися в соседних с этим атомом узлах решетки. Это взаимодействие парное. Предполагается, что энергия этого взаимодействия не зависит ни от состава сплавов, ни от температуры, и что жидкие растворы систем Fe–Ni–Cr и Fe–Ni–Mo являются совершенными. В рамках предложенной теории представлено выражение для вагнеровского параметра взаимодействия азота с хромом в жидких сплавах на основе никеля  $\varepsilon_N^{\text{Cr}}(\text{Ni})$ . Правая часть соответствующей формулы является функцией вагнеровских параметров взаимодействия азота с хромом  $\varepsilon_N^{\text{Cr}}(\text{Fe})$  и азота с никелем  $\varepsilon_N^{\text{Ni}}(\text{Fe})$  в жидких сплавах на основе железа. Аналогичное выражение получено для вагнеровского параметра взаимодействия азота с молибденом в жидких сплавах на основе никеля  $\varepsilon_N^{\text{Mo}}(\text{Ni})$ . По первой из этих формул рассчитано значение  $\varepsilon_N^{\text{Cr}}(\text{Ni}) = -21,9$  при температуре 1873 К. Этому соответствует значение лангенберговского параметра взаимодействия  $e_N^{\text{Cr}}(\text{Ni}) = -0,108$ , что совпадает

с экспериментальной оценкой. По второй из формул рассчитано значение  $\varepsilon_N^{\text{Mo}}(\text{Ni}) = -14,3$  при температуре 1873 К. Этому соответствует значение лангенберговского параметра взаимодействия  $e_N^{\text{Cr}}(\text{Ni}) = -0,036$ , что удовлетворительно согласуется с экспериментальной оценкой  $\varepsilon_N^{\text{Mo}}(\text{Ni}) = -15,1$ ;  $e_N^{\text{Cr}}(\text{Ni}) = -0,038$ .

**Ключевые слова:** термодинамика, растворы, азот, железо, никель, хром, молибден, коэффициент активности, вагнеровские параметры взаимодействия, лангенберговские параметры взаимодействия

**Для цитирования:** Большов Л.А., Корнейчук С.К., Большова Э.Л. Вагнеровские параметры взаимодействия азота с хромом и молибденом в жидких сплавах на основе никеля. *Известия вузов. Черная металлургия*. 2023;66(3):331–336.

<https://doi.org/10.17073/0368-0797-2023-3-330-336>

Nichrome, the heat-resistant alloy, and chromium stainless steel were invented at the beginning of the 20<sup>th</sup> century, signifying that the addition of chromium as an alloying element in substantial concentrations to iron and nickel passivates the surface of the resulting alloy at normal and high temperatures. Industrial-scale production of nickel-based heat-resistant alloys commenced in the mid-20<sup>th</sup> century. These alloys are composed of several alloying elements, with chromium being the primary one. Additionally, these alloys typically have a molybdenum content of a few percent.

Molybdenum plays a vital role in the production of corrosion-resistant, nickel-based alloys. Roughly a century ago, corrosion-resistant alloys like Hastelloy A (Ni – 20 % Mo) and Hastelloy B (Ni – 30 % Mo) were developed, with modern grades of Hastelloy featuring up to 30 % Mo. The nitrogen content has a significant impact on the properties of heat-resistant and corrosion-resistant nickel-based alloys.

More than 60 years ago, Schenck H. et al. [1] and Humbert J. et al. [2] conducted experiments to examine the solubility of nitrogen in liquid nickel and its alloys. Ongoing research [3] continues to explore similar studies, necessitating a theoretical explanation based on thermodynamic theory. Such an explanation is vital for estimating the solubility of nitrogen in liquid nickel-based alloys and assessing the potential formation of nitrides in these alloys. This study specifically focuses on the thermodynamics of nitrogen solutions in Fe–Ni–Cr and Fe–Ni–Mo liquid alloys, aiming to determine Wagner interaction coefficients between nitrogen and chromium and nitrogen and molybdenum in nickel-based liquid alloys based on these coefficients in iron-based liquid alloys.

A. Stomakhin was among the pioneering Soviet researchers who investigated the solubility of nitrogen in liquid nickel and nickel-based alloys. This paper is dedicated to honoring the memory of this exceptional researcher and educator.

We start with the Fe–Ni–Cr alloy and denote the concentrations of the solution components Fe–Ni–Cr–N, as  $c_{\text{Fe}}$ ,  $c_{\text{Ni}}$ ,  $c_{\text{Cr}}$  and  $c_{\text{N}}$ , respectively, using mole fractions. The fundamental concept explored in this study is the thermodynamic activity of nitrogen within the solution, denoted as  $a_{\text{N}}$ . The notion of thermodynamic activity was first intro-

duced by Lewis in 1907. In the context of nitrogen solutions, the Lewis definition implies the following equation:

$$a_{\text{N}} = \exp\left(\frac{\mu_{\text{N}} - \mu_{\text{N}}^{\circ}}{RT}\right),$$

where  $T$  represents the absolute temperature,  $R$  is the universal gas constant,  $\mu_{\text{N}}$  signifies the chemical potential of nitrogen in the solution,  $\mu_{\text{N}}^{\circ}$  denotes the chemical potential of nitrogen at the standard state and temperature  $T$ . The standard state chosen to align with the unit of measurement (UoM) employed for expressing the nitrogen concentration in the solution. For this study, the  $\mu_{\text{N}}^{\circ}$  value is assumed to be constant. The simplest approach is to assume  $\mu_{\text{N}}^{\circ} = 0$ , leading to the following definition:

$$a_{\text{N}} = \exp\left(\frac{\mu_{\text{N}}}{RT}\right). \quad (1)$$

This definition, introduced by Guggenheim in the 1930s [4], represent the absolute activity (1). The absolute activity, when  $T = \text{const}$ , is a dimensionless function depending on the composition of the solution. Its accuracy extends to a certain number of decimal places, determined by an arbitrary constant. Importantly, it remains unaffected by the representation of solution component concentrations and the choice of the standard state. In this study, the activity of nitrogen is determined according to equation (1).

The activity coefficient of nitrogen is determined using the standard equation  $\gamma_{\text{N}} = \frac{a_{\text{N}}}{c_{\text{N}}}$ . These coefficients were referred to as “rational activity coefficients” by Robinson R. et al. [5]. Considering that  $\gamma_{\text{N}} \rightarrow \gamma_{\text{N}}^{\circ}$  at  $c_{\text{N}} \rightarrow 0$ ,  $\gamma_{\text{N}}^{\circ}$  represents the rational activity coefficient of nitrogen in an infinitely dilute solution. For Fe–Ni–Cr–N alloys, where  $c_{\text{Fe}} \rightarrow 1$  and  $T = \text{const}$ , it is more convenient to express the coefficient  $\gamma_{\text{N}}^{\circ}$  as a function of  $c_{\text{Ni}}$  and  $c_{\text{Cr}}$ :  $\gamma_{\text{N}}^{\circ} = \gamma_{\text{N}}^{\circ}(c_{\text{Ni}}, c_{\text{Cr}})$ . Let us determine the Wagner interaction coefficients [6] that describe the interaction between nitrogen and alloying elements in iron-based liquid alloys:

$$\varepsilon_{\text{N}}^{\text{Ni}}(\text{Fe}) = \frac{\partial \ln \gamma_{\text{N}}^{\circ}(c_{\text{Ni}}; c_{\text{Cr}})}{\partial c_{\text{Ni}}} \text{ at } c_{\text{Fe}} \rightarrow 1;$$

$$\varepsilon_{\text{N}}^{\text{Cr}}(\text{Fe}) = \frac{\partial \ln \gamma_{\text{N}}^{\circ}(c_{\text{Ni}}; c_{\text{Cr}})}{\partial c_{\text{Cr}}} \text{ at } c_{\text{Fe}} \rightarrow 1.$$

Fe–Ni–Cr–N alloys at  $c_{\text{Ni}} \rightarrow 1$  and  $T = \text{const}$  it is more convenient to express the coefficient  $\gamma_{\text{N}}^{\circ}$  as a function of  $c_{\text{Fe}}$  and  $c_{\text{Cr}}$ :  $\gamma_{\text{N}}^{\circ} = \gamma_{\text{N}}^{\circ}(c_{\text{Fe}}, c_{\text{Cr}})$ . Then the Ni–Cr Wagner interaction coefficient in nickel-based liquid alloys is defined as

$$\varepsilon_{\text{N}}^{\text{Cr}}(\text{Ni}) = \frac{\partial \ln \widetilde{\gamma}_{\text{N}}^{\circ}(c_{\text{Fe}}; c_{\text{Cr}})}{\partial c_{\text{Cr}}} \text{ at } c_{\text{Ni}} \rightarrow 1$$

or

$$\varepsilon_{\text{N}}^{\text{Ni}}(\text{Fe}) = \frac{\partial \ln \widetilde{\gamma}_{\text{N}}^{\circ}(1 - c_{\text{Fe}} - c_{\text{Cr}}; c_{\text{Cr}})}{\partial c_{\text{Cr}}} \text{ at } c_{\text{Ni}} \rightarrow 1. \quad (2)$$

In practical metallurgical production, the concentrations of solution components are commonly expressed as wt. %. Therefore, we denote the concentrations of the Fe–Ni–Cr–N solution components as [% Fe], [% Ni], [% Cr] and [% N], respectively. In this context, we will refer to the activity coefficient of nitrogen in the liquid solution  $f_{\text{N}} = \frac{a_{\text{N}}}{[\% \text{ N}]}$  “the wt. % activity coefficient”. Let

$\gamma_{\text{N}} \rightarrow f_{\text{N}}^{\circ}$  at  $[\% \text{ N}] \rightarrow 0$ .  $f_{\text{N}}^{\circ}$  is the wt. % the activity coefficient of nitrogen in an infinitely dilute nitrogen solution. Our objective now is to determine the Langenberg interaction coefficient for the nitrogen and alloying elements interaction in iron-based liquid alloys [7]:

$$e_{\text{N}}^{\text{Ni}}(\text{Fe}) = \frac{\partial \lg f_{\text{N}}^{\circ}([\% \text{ Ni}]; [\% \text{ Cr}])}{\partial [\% \text{ Ni}]} \text{ at } [\% \text{ Fe}] \rightarrow 100;$$

$$e_{\text{N}}^{\text{Cr}}(\text{Fe}) = \frac{\partial \lg f_{\text{N}}^{\circ}([\% \text{ Ni}]; [\% \text{ Cr}])}{\partial [\% \text{ Cr}]} \text{ at } [\% \text{ Fe}] \rightarrow 100.$$

For Fe–Ni–Cr–N alloys at  $[\% \text{ N}] \rightarrow 100$  and  $T = \text{const}$ , it is more convenient to express the coefficient  $f_{\text{N}}^{\circ}$  as a function of [% Fe] and [% Cr]:  $f_{\text{N}}^{\circ} = \widetilde{f}_{\text{N}}^{\circ}([\% \text{ Fe}], [\% \text{ Cr}])$ . The N–Cr Langenberg interaction coefficient in nickel-based liquid alloys is defined as follows:

$$e_{\text{N}}^{\text{Cr}}(\text{Ni}) = \frac{\partial \lg \widetilde{f}_{\text{N}}^{\circ}([\% \text{ Fe}]; [\% \text{ Cr}])}{\partial [\% \text{ Cr}]} \text{ at } [\% \text{ Ni}] \rightarrow 100.$$

We will examine the relationship between the Wagner  $\varepsilon_i^j(k)$  and Langenberg  $e_i^j(k)$  interaction coefficients in alloys based on the  $k$  component, where  $i, j$  represent the dissolved components. Lupis C. et al. [8] derived the exact ratio, considering the differential invariance of the logarithm of the solution component activity concerning different representations of the concentrations. The ratio is given by:

$$\varepsilon_i^j(k) = 230,3 \frac{A_j}{A_k} e_i^j(k) + \frac{A_k - A_j}{A_k}, \quad (3)$$

where  $A_j$  represents the atomic mass of the alloying component  $j$  and  $A_k$  represents the atomic mass of the base metal.

In the context of this study, component  $i$  refers to nitrogen, component  $j$  represents chromium or molybdenum, and component  $k$  pertains to iron or nickel. The inverse relationship to relation (3) is expressed as [9]:

$$e_i^j(k) = \frac{1}{230,3} \frac{A_k}{A_j} \left[ \varepsilon_i^j(k) + \frac{A_k - A_j}{A_k} \right]. \quad (4)$$

The primary objective of this study is to establish analytical relationships between the interaction coefficient  $\varepsilon_{\text{N}}^{\text{Cr}}(\text{Ni})$  and the  $\varepsilon_{\text{N}}^{\text{Cr}}(\text{Fe})$  and  $\varepsilon_{\text{N}}^{\text{Ni}}(\text{Fe})$  coefficients and between the interaction coefficient  $\varepsilon_{\text{N}}^{\text{Mo}}(\text{Ni})$  with the  $\varepsilon_{\text{N}}^{\text{Mo}}(\text{Fe})$  and  $\varepsilon_{\text{N}}^{\text{Ni}}(\text{Fe})$  interaction coefficients. To achieve this, we propose a straightforward model for nitrogen solutions in Fe–Ni–Cr and Fe–Ni–Mo liquid alloys, which serves as a generalization of the model for nitrogen solutions in binary Fe–Cr alloys presented in [10]. The theoretical framework employed in this study utilizes the lattice model of Fe–Ni–Cr and Fe–Ni–Mo solutions, where the lattice structure adheres to the face-centered cubic (FCC) arrangement. Iron, nickel, chromium, and molybdenum atoms are situated at the lattice sites, while nitrogen atoms occupy the octahedral interstices. The interaction between nitrogen and metal atoms occurs exclusively with the neighboring lattice sites, constituting a pair interaction. It is assumed that this interaction energy remains invariant with respect to alloy composition or temperature. Furthermore, the Fe–Ni–Cr and Fe–Ni–Mo liquid solutions are considered to be ideal ternary solutions. We assume that the contribution of positional entropy to the partial entropy of the solution does not rely on the alloy composition or temperature.

A similar model, based on classical statistical mechanics principles, is presented in [11; 12]. The model as applied to the Fe–Cr–Ni–N system is reduced to

$$\gamma_{\text{N}}^{\circ} = \left\{ 1 - \frac{1}{\delta} \left[ \varepsilon_{\text{N}}^{\text{Ni}}(\text{Fe}) c_{\text{Ni}} + \varepsilon_{\text{N}}^{\text{Cr}}(\text{Fe}) c_{\text{Cr}} \right] \right\}^{-\delta},$$

where  $\delta$  represents the number of FCC lattice sites adjacent to the octahedral interstices ( $\delta = 6$ );  $\gamma_{\text{N}}^{\circ}$  is the nitrogen activity coefficient in an infinitely diluted nitrogen solution normalized as follows:  $\gamma_{\text{N}}^{\circ} = 1$  at  $c_{\text{Fe}} \rightarrow 1$ . Therefore

$$\ln \gamma_{\text{N}}^{\circ}(1 - c_{\text{Fe}} - c_{\text{Cr}}, c_{\text{Cr}}) = -\delta \ln \left\{ 1 - \frac{1}{\delta} \left[ \varepsilon_{\text{N}}^{\text{Ni}}(\text{Fe}) (1 - c_{\text{Fe}} - c_{\text{Cr}}) + \varepsilon_{\text{N}}^{\text{Cr}}(\text{Fe}) c_{\text{Cr}} \right] \right\}. \quad (5)$$

It follows from (2) and (5):

$$\varepsilon_{\text{N}}^{\text{Cr}}(\text{Ni}) = \delta \frac{\varepsilon_{\text{N}}^{\text{Cr}}(\text{Fe}) - \varepsilon_{\text{N}}^{\text{Ni}}(\text{Fe})}{\delta - \varepsilon_{\text{N}}^{\text{Ni}}(\text{Fe})}.$$

The final equation is:

$$\varepsilon_N^{\text{Cr}}(\text{Ni}) = 6 \frac{\varepsilon_N^{\text{Cr}}(\text{Fe}) - \varepsilon_N^{\text{Ni}}(\text{Fe})}{6 - \varepsilon_N^{\text{Ni}}(\text{Fe})}. \quad (6)$$

The definitions and models for the Fe–Ni–Mo–N system are similar, leading to a final equation that is also similar to equation (6):

$$\varepsilon_N^{\text{Mo}}(\text{Ni}) = 6 \frac{\varepsilon_N^{\text{Mo}}(\text{Fe}) - \varepsilon_N^{\text{Ni}}(\text{Fe})}{6 - \varepsilon_N^{\text{Ni}}(\text{Fe})}. \quad (7)$$

To utilize equation (6), we also require the Wagner interaction coefficients  $\varepsilon_N^{\text{Cr}}(\text{Fe})$  and  $\varepsilon_N^{\text{Ni}}(\text{Fe})$  in iron-based alloys. We have considered the most reliable experimental studies on nitrogen solubility in Fe–Cr liquid alloys that estimate of the Langenberg interaction coefficient at  $T = 1873$  K:  $e_N^{\text{Cr}}(\text{Fe}) = -0.045$  [13] and  $e_N^{\text{Cr}}(\text{Fe}) = -0.047$  [14]. Another recommended value is  $e_N^{\text{Cr}}(\text{Fe}) = -0.046$  as suggested by Linchevsky B. et al. [15]. According to equation (3), this corresponds to the Wagner interaction coefficient  $\varepsilon_N^{\text{Cr}}(\text{Fe}) = -9.8$ .

Papers [14; 16] report the Langenberg interaction coefficient  $e_N^{\text{Ni}}(\text{Fe}) = 0.011$ . According to equation (3), this value corresponds to  $\varepsilon_N^{\text{Ni}}(\text{Fe}) = 2.6$ .

By substituting  $\varepsilon_N^{\text{Cr}}(\text{Fe}) = -9.8$  and  $\varepsilon_N^{\text{Ni}}(\text{Fe}) = 2.6$ , into the right-hand side of equation (6), we can obtain the analytical value of the N–Cr Wagner interaction coefficient in liquid nickel-based alloys  $\varepsilon_N^{\text{Cr}}(\text{Ni}) = -21.9$  at  $T = 1873$  K. According to equation (4), this value corresponds to the Langenberg interaction coefficient  $e_N^{\text{Cr}}(\text{Ni}) = -0.108$ . This result is consistent with the experimental values reported by Surovoy Yu. et al. [16].

Estimating the true interaction coefficient  $e_N^{\text{Cr}}(\text{Ni})$  poses significant challenges. Here are some experimental values of this coefficient at  $T = 1873$  K obtained from nitrogen solubility measurements in Ni–Cr melts:  $-0.13$  [2];  $-0.11$  (at  $T = 1823$  K) [17];  $-0.098$  [18];  $-0.108$  [16];  $-0.093$  [19];  $-0.0766$  [20];  $-0.0952$  (at  $T = 1823$  K) [21]. The arithmetic mean of these values is  $e_N^{\text{Cr}}(\text{Ni}) = -0.102$ . Monographs [15; 22] suggest  $\varepsilon_N^{\text{Cr}}(\text{Ni}) = -0.1$  at  $T = 1873$  K.

Previously, we presented an alternative theory [9] to estimate the  $\varepsilon_N^{\text{Cr}}(\text{Ni})$  Wagner interaction coefficient. Let us express Sievert's law [23] for the solubility of nitrogen in Fe–Cr liquid alloys as follows:

$$[\% \text{ N}]^* = K'_N \sqrt{\frac{P_{\text{N}_2}}{P_0}},$$

where  $P_{\text{N}_2}$  represents the partial pressure of the nitrogen gas phase;  $P_0$  is the standard pressure ( $P_0 = 1 \text{ atm} \approx 0.101 \text{ MPa}$ );  $K'_N$  is Sievert's law constant for the solubility of nitrogen in Ni–Cr liquid alloys. Let  $K'_N(\text{Ni})$  at  $c_{\text{Ni}} = 1$

and  $K'_N = K'_N(\text{Cr})$  at  $c_{\text{Cr}} = 1$ . According to the theory presented in [9]

$$\varepsilon_N^{\text{Cr}}(\text{Ni}) = 6 \left( 1 - \sqrt{\frac{A_{\text{Cr}} K'_N(\text{Cr})}{A_{\text{Ni}} K'_N(\text{Ni})}} \right). \quad (8)$$

As mentioned in [9], equations (8) and (4) yield the following N–Cr Langenberg interaction coefficient in liquid nickel alloys  $e_N^{\text{Cr}}(\text{Ni}) = -0.105$  at  $T = 1873$  K.

Therefore, according to [9], the interaction coefficient  $e_N^{\text{Cr}}(\text{Ni})$  at  $T = 1873$  K is  $-0.105$ , and according to the theory proposed in this paper,  $e_N^{\text{Cr}}(\text{Ni}) = -0.108$ . These values are very close, considering the experimental uncertainty. A similar conclusion is reached when comparing this result with the averaged experimental value  $e_N^{\text{Cr}}(\text{Ni}) = -0.102$ .

It should be noted that theory [9] and equation (8) cannot estimate the N–Mo Wagner interaction coefficients in liquid nickel-based alloys due to the high melting point of molybdenum (approximately 2888 K [24]).

To use equation (7) for estimating the  $\varepsilon_N^{\text{Mo}}(\text{Ni})$  coefficient, we need to know the Wagner interaction coefficient  $\varepsilon_N^{\text{Mo}}(\text{Fe})$  in iron-based alloys. Here are the Langenberg interaction coefficient values at  $T = 1873$  K, reported in reputable studies on nitrogen solubility in Fe–Mo liquid alloys:  $e_N^{\text{Mo}}(\text{Fe}) = -0.011$  [13] and  $e_N^{\text{Mo}}(\text{Fe}) = -0.013$  [25]. The arithmetic mean of these values is  $e_N^{\text{Mo}}(\text{Fe}) = -0.012$ . According to equation (3), this value corresponds to the Wagner interaction coefficient  $\varepsilon_N^{\text{Mo}}(\text{Fe}) = -5.5$ .

Let us substitute  $\varepsilon_N^{\text{Mo}}(\text{Fe}) = -5.5$  and  $\varepsilon_N^{\text{Ni}}(\text{Fe}) = 2.6$  in equation (7). Then we obtain the analytical N–Mo interaction Wagner interaction coefficient in liquid nickel-based alloys at  $T = 1873$  K:  $\varepsilon_N^{\text{Mo}}(\text{Ni}) = -14.3$ . Equation (4) yields the theoretical value of the Langenberg interaction coefficient  $e_N^{\text{Mo}}(\text{Ni}) = -0.036$ .

Let us consider the  $e_N^{\text{Mo}}(\text{Ni})$  and  $\varepsilon_N^{\text{Mo}}(\text{Ni})$  interaction coefficients at  $T = 1873$  K. Stomakhin A. et al. [17] applied the Sievert method [23] to study the solubility of nitrogen in Ni–Mo liquid alloys at  $T = 1823$  K. They reported the experimental value of the Langenberg interaction coefficient  $e_N^{\text{Mo}}(\text{Ni}) = -0.04$ . According to equation (3), the Wagner interaction coefficient  $\varepsilon_N^{\text{Mo}}(\text{Ni}) = -15.9$  at  $T = 1823$  K.

In the study [9], we proposed an analytical equation to convert the Wagner interaction coefficient for the interaction between nitrogen and alloying metal from temperature  $T_0$  to temperature  $T$ . For the  $\varepsilon_N^{\text{Mo}}$  interaction coefficient and  $\delta = 6$ , this equation can be expressed as:

$$\varepsilon_N^{\text{Mo}}(T) = 6 \left\{ 1 - \left[ 1 - \frac{1}{6} \varepsilon_N^{\text{Mo}}(T_0) \right]^{\frac{T_0}{T}} \right\}. \quad (9)$$



By substituting the values  $T_0 = 1823$  K,  $T = 1873$  K,  $\varepsilon_N^{\text{Mo}}(1823) = -15.9$  into equation (9), we obtain  $\varepsilon_N^{\text{Mo}}(\text{Ni}) = -15.1$  at  $T = 1873$  K. It corresponds to the N–Mo Langenberg interaction coefficient in nickel-based liquid alloys  $e_N^{\text{Mo}}(\text{Ni}) = -0.038$  (equation (4)). The theoretical value  $e_N^{\text{Mo}}(\text{Ni}) = -0.036$ , (equation (7)) agrees well with the experimental value [17].

With these analytical results, we can verify the experiments. The most plausible N–Cr interaction coefficient in liquid nickel-based alloys is  $e_N^{\text{Cr}}(\text{Ni}) = -0.108$  at  $T = 1873$  K. This value was obtained by Surovoy Yu. et al. [16] who measured the nitrogen solubility using the Sievers method. This coincides with the conclusions presented in [9].

The most plausible N–Mo interaction coefficient in liquid nickel-based alloys is  $e_N^{\text{Mo}}(\text{Ni}) = 0.04$  at  $T = 1823$  K. It was obtained by Stomakhin A. et al. [17] who measured the nitrogen solubility using the Sievers method. If we convert this value by equation (9) to  $T = 1873$  K, the result is  $e_N^{\text{Mo}}(\text{Ni}) = -0.038$ .

The most plausible experimental values of the Wagner interaction coefficients for nitrogen in liquid nickel at  $T = 1873$  K seem to be  $\varepsilon_N^{\text{Cr}}(\text{Ni}) = -21.9$ ;  $\varepsilon_N^{\text{Mo}}(\text{Ni}) = -15.1$ . The analytical values of these parameters are  $\varepsilon_N^{\text{Cr}}(\text{Ni}) = -21.9$ ;  $\varepsilon_N^{\text{Mo}}(\text{Ni}) = -14.3$ .

It is indeed noteworthy that both chromium and molybdenum belong to the same group in the Periodic Table, specifically group VI (chromium subgroup). Molybdenum serves as the closest chemical analog to chromium. This helps explain the applicability of the theoretical model to both Fe–Ni–Cr–N and Fe–Ni–Mo–N systems.

Furthermore, it is important to highlight the continued interest and research in the thermodynamics of nitrogen solutions in pure Cr, Mn, Fe, and Ni metals and alloys (refer to [3; 20; 21; 26–30]).

## CONCLUSIONS

In our proposed analytical model of the structure and interatomic interaction for nitrogen solutions in Fe–Ni–Cr and Fe–Ni–Mo liquid alloys, we have developed equations (6) and (7) to calculate the Wagner interaction coefficients  $\varepsilon_N^{\text{Cr}}(\text{Ni})$  and  $\varepsilon_N^{\text{Mo}}(\text{Ni})$  for nitrogen in nickel-based liquid alloys based on the corresponding  $\varepsilon_N^{\text{Cr}}(\text{Fe})$  and  $\varepsilon_N^{\text{Mo}}(\text{Fe})$  coefficients in iron-based liquid alloys.

We obtained analytical values for the nitrogen interaction coefficients in liquid nickel-based alloys at  $T = 1873$  K:  $\varepsilon_N^{\text{Cr}}(\text{Ni}) = -21.9$ ;  $\varepsilon_N^{\text{Mo}}(\text{Ni}) = -14.3$ ;  $e_N^{\text{Cr}}(\text{Ni}) = -0.108$ ;  $e_N^{\text{Mo}}(\text{Ni}) = -0.036$ .

The most plausible experimental values for the nitrogen interaction coefficients in liquid nickel-based alloys

at  $T = 1873$  K are:  $e_N^{\text{Cr}}(\text{Ni}) = -0.108$ ;  $e_N^{\text{Mo}}(\text{Ni}) = -0.038$ ;  $\varepsilon_N^{\text{Cr}}(\text{Ni}) = -21.9$ ;  $\varepsilon_N^{\text{Mo}}(\text{Ni}) = -15.1$ .

## REFERENCES / СПИСОК ЛИТЕРАТУРЫ

1. Schenck H., Froberg M.G., Graf H. Untersuchungen über die Beeinflussung der Gleichgewichte von Stickstoff mit flüssigen Eisenlösungen durch den Zusatz weiterer Elemente (II). *Archiv für das Eisenhüttenwesen*. 1959;30(9):533–537.
2. Humbert J.C., Elliott J.F. The solubility of nitrogen in liquid Fe–Cr–Ni alloys. *Transactions of the Metallurgical Society of AIME*. 1960;218(10):1076–1088.
3. Qian K., Chen B., Zhao P., Zhang M., Liu K. Solubility of nitrogen in liquid Ni, Ni–Nb, Ni–Cr–Nb, Ni–Fe–Nb and Ni–Cr–Fe–Nb systems. *ISIJ International*. 2019;59(12):2220–2227.  
<https://doi.org/10.2355/isijinternational.ISIJINT-2019-187>
4. Fowler R.H., Guggenheim E.A. *Statistical Thermodynamics*. Cambridge: Addison-Wesley Press; 1939:693.  
Фаулер Р., Гуттенгейм Э. *Статистическая термодинамика*. Москва: Издательство иностранной литературы; 1949:612.
5. Робинсон Р., Стокс Р. *Растворы электролитов*. Москва: Издательство иностранной литературы; 1963:647.  
Robinson R.A., Stokes R.H. *Electrolyte Solutions*. London: Butterworths Scientific Publications; 1959:559.
6. Wagner C. *Thermodynamics of Alloys*. Cambridge: Addison-Wesley Press; 1952:162.  
Вагнер К. *Термодинамика сплавов*. Москва: Металлургиздат; 1957:179.
7. Langenberg F.C. Predicting solubility of nitrogen in molten steel. *JOM*. 1956;8(8):1099–1101.  
<https://doi.org/10.1007/BF03377828>
8. Lupis C.H.P., Elliott J.F. The relation between interaction coefficients  $\varepsilon$  and  $e$ . *Transactions of the Metallurgical Society of AIME*. 1965;233(1):257–258.
9. Bol'shov L.A., Korneichuk S.K., Bol'shova E.L. Wagner interaction coefficient between nitrogen and chromium in liquid nickel-based alloys. *Izvestiya. Ferrous Metallurgy*. 2021;64(9):693–697. (In Russ.).  
<https://doi.org/10.17073/0368-0797-2021-9-693-697>
10. Bol'shov L.A., Korneichuk S.K. Thermodynamics of liquid nitrogen solutions in chromium. *Izvestiya. Ferrous Metallurgy*. 2019;62(5):387–393. (In Russ.).  
<https://doi.org/10.17073/0368-0797-2019-5-387-393>
11. Bol'shov L.A., Korneichuk S.K. Термодинамика жидких растворов азота в хроме. *Известия вузов. Черная металлургия*. 2019;62(5):387–393.  
<https://doi.org/10.17073/0368-0797-2019-5-387-393>
11. Bol'shov L.A. On solubility of nitrogen in liquid multicomponent iron alloys with transition metals. *Izvestiya. Ferrous Metallurgy*. 1982;25(1):8–10. (In Russ.).

- Большов Л.А. О растворимости азота в жидких многокомпонентных сплавах железа с переходными металлами. *Известия вузов. Черная металлургия*. 1982;25(1):8–10.
12. Большов Л.А. *Статистическая теория многокомпонентных и малокоцентрированных сплавов*. Дисс... докт. физ.-мат. наук. Москва: МГУ; 1991:496.  
Bol'shov L.A. *Statistical theory of multicomponent and low-concentration alloys: Dr. Phys.-Math. Sci. Diss.* Moscow: 1991:496. (In Russ.).
13. Pehlke R.D., Elliott J.F. Solubility of nitrogen in liquid iron alloys. I. Thermodynamics. *Transactions of the Metallurgical Society of AIME*. 1960;218(6):1088–1101.
14. Turnock R.H., Pehlke R.D. The solubility of nitrogen in multicomponent liquid iron alloys. *Transactions of the Metallurgical Society of AIME*. 1966;236(11):1540–1547.
15. Linchevskii B.V. *Thermodynamics and Kinetics of Interaction of Gases with Liquid Metals*. Moscow: Metallurgiya; 1986:224. (In Russ.).  
Линчевский Б.В. *Термодинамика и кинетика взаимодействия газов с жидкими металлами*. Москва: Металлургия; 1986:224.
16. Surovoi Yu.N., Okorokov G.N., Nefedova S.A. Solubility of nitrogen in iron-nickel melts with chromium. In: *Reports of Soviet Scientists in the 3<sup>rd</sup> Soviet-Japanese Symp. on Physico-Chemical Fundamentals of Metallurgical Processes, September 27–29, 1971*. Moscow: Institut metallurgii im. A.A. Baikova; 1971. (In Russ.).  
Суровой Ю.Н., Окороков Г.Н., Нефедова С.А. Растворимость азота в расплавах железа и никеля с хромом: *Сборник «Доклады советских ученых на III советско-японском симпозиуме по физико-химическим основам металлургических процессов», 27–29 сентября 1971 г.* Москва: Институт металлургии им. А.А. Байкова; 1971.
17. Stomakhin A.Ya., Baier P., Polyakov A.Yu. Solubility of nitrogen in liquid nickel and nickel alloys with chromium, molybdenum and tungsten. *Izvestiya AN SSSR. Metall.* 1965;(4):37–45. (In Russ.).  
Стомахин А.Я., Байер П., Поляков А.Ю. Растворимость азота в жидком никеле и в сплавах никеля с хромом, молибденом и вольфрамом. *Известия АН СССР. Металлы*. 1965;(4):37–45.
18. Fedorchenko V.I., Averin V.V., Samarin A.M. Solubility of nitrogen in liquid nickel and Ni–Cr, Ni–Mo and Ni–W melts. *Doklady Akademii nauk SSSR*. 1968;183(4):894–896. (In Russ.).  
Федорченко В.И., Аверин В.В., Самарин А.М. Растворимость азота в жидком никеле и расплавах Ni–Cr, Ni–Mo и Ni–W. *Доклады Академии наук СССР*. 1968;183(4):894–896.
19. Butskii E.V., Grigoryan V.A., Filippov A.F., Topilin V.V., Krasnova I.A. Solubility of nitrogen in multicomponent nickel-based alloys. *Izvestiya. Ferrous Metallurgy*. 1975; 18(1):47–51. (In Russ.).  
Бутский Е.В., Григорян В.А., Филиппов А.Ф., Топилин В.В., Краснова И.А. Растворимость азота в многокомпонентных сплавах на основе никеля. *Известия вузов. Черная металлургия*. 1975;18(1):47–51.
20. Abdulrahman R.F., Hendry A. Solubility of nitrogen in liquid nickel-based alloys. *Metallurgical and Materials Transactions B*. 2001;32(6):1103–1112.  
<https://doi.org/10.1007/s11663-001-0098-3>
21. Kowanda C., Speidel M.O. Solubility of nitrogen in liquid nickel and binary Ni–X<sub>i</sub> alloys (X<sub>i</sub> = Cr, Mo, W, Mn, Fe, Co) under elevated pressure. *Scripta Materialia*. 2003;48(8): 1073–1078.  
[http://doi.org/10.1016/S1359-6462\(02\)00628-0](http://doi.org/10.1016/S1359-6462(02)00628-0)
22. Grigoryan V.A., Belyanchikov L.N., Stomakhin A.Ya. *Theoretical Fundamentals of Electric Steelmaking Processes*. Moscow: Metallurgiya; 1987:272. (In Russ.).  
Григорян В.А., Белянчиков Л.Н., Стомахин А.Я. *Теоретические основы электросталеплавильных процессов*. Москва: Металлургия; 1987:272.
23. Sieverts A. Zur Kenntnis der Okklusion und Diffusion von Gasen durch Metallen. *Zeitschrift für physikalische Chemie*. 1907;60(2):129–201.  
<https://doi.org/10.1515/zpch-1907-6009>
24. Nekrasov B.V. *Fundamentals of General Chemistry. Vol. 1*. Moscow: Khimiya; 1973:636. (In Russ.).  
Некрасов Б.В. *Основы общей химии. Том 1*. Москва: Химия; 1973:636.
25. Maekawa S., Nakagawa Y. Effect of nickel, cobalt, molybdenum, chromium and vanadium on the solubility in liquid iron: Solubility of nitrogen in liquid iron and iron alloys – II. *Tetsu-to-Hagane*. 1960;46(9):972–976.  
[https://doi.org/10.2355/tetsutohagane1955.46.9\\_972](https://doi.org/10.2355/tetsutohagane1955.46.9_972)
26. Siwka J. Solubility of nitrogen in liquid chromium. *Archives of Metallurgy*. 1998;43(1):67–82.
27. Kim E.-J., Pak J.-J., You B.-D. Nitrogen solubility in liquid manganese and ferromanganese alloys. *Metallurgical and Materials Transactions B*. 2001;32(4):659–668.  
<https://doi.org/10.1007/s11663-001-0120-9>
28. Shin J., Lee J., Min D.J., Park J. Solubility of nitrogen in high manganese steel (HMnS) melts. Interaction parameter between Mn and N. *Metallurgical and Materials Transactions B*. 2011;42(6):1081–1085.  
<https://doi.org/10.1007/s11663-011-9582-6>
29. Grigoryan V.A., Stomakhin A.Ya., Utochkin Yu.I., Ponomarenko A.G., Belyanchikov L.N., Kotelnikov G.I., Ostrovskii O.I. *Physico-Chemical Calculations of Electric Steelmaking Processes*. Moscow: MISIS; 2007:318. (In Russ.).  
Григорян В.А., Стомахин А.Я., Уточкин Ю.И., Пономаренко А.Г., Белянчиков Л.Н., Котельников Г.И., Островский О.И. *Физико-химические расчеты электросталеплавильных процессов*. Москва: МИСиС; 2007:318.
30. Lysenkova E.V. Improving accuracy of calculations of solubility of nitrogen and titanium nitride in iron-based melts. Application to nitrogen and titanium alloyed steel: Cand. Tech. Sci. Diss. Moscow: MISIS; 2015:75. (In Russ.).  
Лысенкова Е.В. *Повышение точности расчетов растворимости азота и нитрида титана в сплавах на основе железа. Применение к сталям, легированным азотом и титаном: Дисс.... канд. техн. наук*. Москва: МИСиС; 2015:75.

## Сведения об авторах

## Information about the Authors

**Леонид Абрамович Большов**, д.ф.-м.н., профессор кафедры математики и информатики, Вологодский государственный университет

**E-mail:** labolshov@mail.ru

**Светлана Константиновна Корнейчук**, к.ф.-м.н., доцент кафедры физики, Вологодский государственный университет

**E-mail:** korn62@mail.ru

**Элина Леонидовна Большова**, доцент кафедры английского языка, Вологодский государственный университет

**E-mail:** labolshov@mail.ru

**Leonid A. Bol'shov**, Dr. Sci. (Phys.–Math.), Prof. of the Chair of Mathematics and Informatics, Vologda State University

**E-mail:** labolshov@mail.ru

**Svetlana K. Korneichuk**, Cand. Sci. (Phys.–Math.), Assist. Prof. of the Chair of Physics, Vologda State University

**E-mail:** korn62@mail.ru

**Elina L. Bol'shova**, Assist. Prof. of the Chair of English, Vologda State University

**E-mail:** labolshov@mail.ru

## Вклад авторов

## Contribution of the Authors

**Л. А. Большов** – идея и текст статьи.

**С. К. Корнейчук** – анализ метода и результатов, оформление текста и сопровождающих документов.

**Э. Л. Большова** – перевод на русский язык англоязычных статей, перевод на английский язык аннотации и библиографического списка.

**L. A. Bol'shov** – formation of the article idea, writing the text.

**S. K. Korneichuk** – analysis of the method and results, preparation of the text and accompanying documents.

**E. L. Bol'shova** – translation of English articles, translation into English of the abstract and references.

Поступила в редакцию 30.12.2022

После доработки 05.03.2023

Принята к публикации 11.03.2023

Received 30.12.2022

Revised 05.03.2023

Accepted 11.03.2023

Materials of the Conference  
«PHYSICO-CHEMICAL FOUNDATIONS  
OF METALLURGICAL PROCESSES»  
named after Academician A.M. Samarin – 2022

По материалам конференции  
«ФИЗИКО-ХИМИЧЕСКИЕ ОСНОВЫ  
МЕТАЛЛУРГИЧЕСКИХ ПРОЦЕССОВ»  
им. академика А.М. Самарина – 2022



UDC 669.046.558.6

DOI 10.17073/0368-0797-2023-3-337-343



Original article

Оригинальная статья

## USING CALCIUM-CONTAINING INJECTION WIRE FILLED WITH ELECTROLYTIC CALCIUM IN STEEL LADLE TREATMENT

A. D. Khoroshilov<sup>1</sup>, S. A. Somov<sup>2</sup>, V. D. Katolikov<sup>1</sup>, V. A. Murysev<sup>2</sup>,  
R. E. Bocherikov<sup>3</sup>, M. R. Yarmukhametov<sup>2</sup>

<sup>1</sup> LLC “Rusatom MetalTech” (49 Kashirskoe Route, Moscow 115409, Russian Federation)

<sup>2</sup> JSC “Vyksa Metallurgical Plant” (45 Br. Batashevskiy Str., Vyksa, Nizhny Novgorod Region 607060, Russian Federation)

<sup>3</sup> National University of Science and Technology “MISIS” (4 Leninskii Ave., Moscow 119049, Russian Federation)

✉ vdkatolikov@yandex.ru

**Abstract.** Aluminum is one of the most common deoxidizers; when it is used in the melt, refractory inclusions of alumina are formed. The presence of these non-metallic inclusions negatively affects the purity of liquid steel, mechanical properties, makes casting difficult due to tightening of the steel-pouring fittings. The modification of alumina inclusions with calcium promotes the formation of liquid calcium aluminates, which leads to an acceleration of their removal from the metal due to a higher ascent rate. Having a high affinity for sulfur, calcium reduces its harmful effect by binding it with the formation of calcium sulfides, reducing the anisotropy of steel properties during further rolling. For steel treatment with calcium, injection wires with a calcium-containing filler are used. As a filler can be used: electrolytic calcium, silicocalcium, aluminum-tremic calcium, or ferrocalcium. The paper describes results of the tests carried out on a calcium-containing wire filled with electrolytic calcium and silicocalcium. It is shown that the consumption of calcium when using silicocalcium wire is on average 35 % higher in comparison with calcium injection wire filled with electrolytic calcium. The calcium recovery rate for different steel grades was evaluated using calcium-containing wires of different designs and filler. In this work, the steel pourability was analyzed. As a determining parameter, dependence of change in position of the tundish stopper rod on calcium content in the metal was considered in the sample from CCM. It was established that a wire filled with electrolytic calcium shows a more effective result in comparison with a silicocalcium wire.

**Keywords:** steel ladle treatment, calcium-containing injection wire calcium, electrolytic calcium, silicocalcium

**For citation:** Khoroshilov A.D., Somov S.A., Katolikov V.D., Murysev V.A., Bocherikov R.E., Yarmukhametov M.R. Using calcium-containing injection wire filled with electrolytic calcium in steel ladle treatment. *Izvestiya. Ferrous Metallurgy*. 2023;66(3):337–343.  
<https://doi.org/10.17073/0368-0797-2023-3-337-343>

## ОПЫТ ПРИМЕНЕНИЯ КАЛЬЦИЙСОДЕРЖАЩЕЙ ИНЖЕКЦИОННОЙ ПРОВОЛОКИ С НАПОЛНИТЕЛЕМ ИЗ ЭЛЕКТРОЛИТИЧЕСКОГО КАЛЬЦИЯ НА ЭТАПЕ ВНЕПЕЧНОЙ ОБРАБОТКИ СТАЛИ

А. Д. Хорошилов<sup>1</sup>, С. А. Сомов<sup>2</sup>, В. Д. Католиков<sup>1</sup>, В. А. Мурысев<sup>2</sup>,  
Р. Е. Бочерилов<sup>3</sup>, М. Р. Ярмухаметов<sup>2</sup>

<sup>1</sup> ООО «Русатом МеталлТех» (Россия, 115409, Москва, Каширское шоссе, 49)

<sup>2</sup> АО «Выксунский металлургический завод» (Россия, 607060, Нижегородская обл., Выкса, ул. Бр. Баташевых, 45)

<sup>3</sup> Национальный исследовательский технологический университет «МИСИС» (Россия, 119049, Москва, Ленинский пр., 4)

✉ vdkatolikov@yandex.ru

**Аннотация.** Алюминий является одним из наиболее распространенных раскислителей, при его использовании в расплаве образуются тугоплавкие включения глинозема. Присутствие данных неметаллических включений негативно влияет на чистоту жидкой стали,



механические свойства, затрудняет разливку вследствие затягивания сталеразливочной фурнитуры. Модифицирование включений оксида алюминия кальцием способствует образованию жидких алюминатов кальция, что приводит к ускорению их удаления из металла ввиду более высокой скорости всплытия. Обладая высоким сродством к сере, кальций связывает ее, образуя сульфиды, тем самым уменьшая вредное влияние серы и снижая анизотропию свойств стали при дальнейшей прокатке. Для обработки стали кальцием используют инъекционные проволоки с кальцийсодержащим наполнителем. В качестве наполнителя могут быть использованы электролитический кальций, силикокальций, алюмотермический кальций, феррокальций. В данной работе описаны результаты проведенных испытаний кальцийсодержащей проволоки с наполнителем из электролитического кальция и силикокальция. Показано, что расход кальция при использовании силикокальциевой проволоки в среднем на 35 % выше в сравнении с кальциевой инъекционной проволокой с наполнителем из электролитического кальция. Проведена оценка коэффициента усвоения кальция для различных сортов сталей при использовании кальцийсодержащих проволок разных дизайнов и наполнителя. Выполнен анализ разливаемости стали, где в качестве определяющего параметра рассмотрена зависимость изменения положения штока стопора промежуточного ковша от содержания кальция в металле по пробе с установки непрерывной разливки стали. Установлено, что проволока с наполнителем из электролитического кальция показывает более эффективный результат в сравнении с силикокальциевой проволокой.

**Ключевые слова:** внепечная обработка стали, кальцийсодержащая инъекционная проволока, кальций, электролитический кальций, силикокальций

**Для цитирования:** Хорошилов А.Д., Сомов С.А., Католиков В.Д., Мурысев В.А., Бочериков Р.Е., Ярмухаметов М.Р. Опыт применения кальцийсодержащей инъекционной проволоки с наполнителем из электролитического кальция на этапе внепечной обработки стали. *Известия вузов. Черная металлургия.* 2023;66(3):337–343. <https://doi.org/10.17073/0368-0797-2023-3-337-343>

## INTRODUCTION

The properties of rolled steel products largely are significantly influenced by the presence of impurities such as sulfur, phosphorus, nitrogen, hydrogen, and others, as well as the content of non-metallic inclusions (NMI) that enter the metal during melting process. The chemical composition, quantity, distribution pattern, and morphology of MNIs have a profound impact on the quality and properties of steel.

In contemporary practice, aluminum is commonly added to steel for the purpose of final deoxidation. However, the deoxidation product ( $\text{Al}_2\text{O}_3$ ), known as alumina, can form irregular shaped inclusions that tend to cluster together, as reported by Wasai K. et al. [1]. These inclusions have the potential to cause surface defects in rolled steel (Zaitsev A. et al. [2]) and adhere to casting equipment [3 – 5].

In order to mitigate these negative effects, the composition of NMI can be efficiently modified. Calcium is extensively employed as an additive through the use of calcium-containing cored wires [6 – 9]. The addition of calcium to steel enables control over the chemical and phase composition of NMI, making the steel more suitable for deep drawing operations and reducing the occurrence of hydrogen-induced cracking [10 – 13].

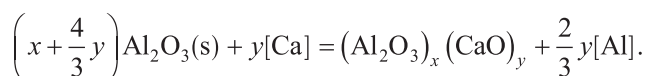
When calcium is added to the liquid metal, it dissolves throughout the entire volume. This leads to a reaction with  $\text{Al}_2\text{O}_3$  inclusions [14; 15], resulting in their conversion to a liquid phase [16]. As a result, the refining rate is accelerated, with the liquid inclusions rising to the surface more rapidly. Lind M. [17] and Yang J. et al. [18] have documented the reaction responsible for the formation of calcium aluminates

Calcium, known for its strong affinity for sulfur, forms sulfide and oxysulfide NMI (also at the crystallization front). Insufficient level of calcium accumulation along the centerline of the continuous casting billet can result in the elongated manganese sulfide inclusions. This centerline region may contain NMI and micro-discontinuities, leading to the rejection of rolled sheets during ultrasonic inspection or an increased susceptibility to hydrogen-induced cracking in corrosive environments [19].

The modification of NMI with calcium is a complex process. One key challenge involves maintaining the optimal range of calcium concentration within the melt, as well as ensuring the stable assimilation of calcium. Calcium has a high vapor pressure and its addition can induce intense boiling, which may cause liquid metal ejection from the ladle. Therefore, the method by which calcium is added to the liquid metal is crucial. Calcium should be introduced to the depth of the melt, where the ferrostatic pressure balances the pressure of the calcium vapor [20]. The effectiveness of a calcium-containing wire depends on multiple factors, including the steel and slag composition, steel temperature [21] weight, wire insertion rate, as well as wire design and a filler composition.

The filler is enclosed in a steel outer layer [22; 23], which serves the following functions:

- protecting the filler during shipping and storage by preventing contact with air and moisture;
- preventing the filler oxidation by acting as a barrier as the wire passes through the slag layer on the metal's surface;
- providing rigidity to the wire, enabling it to pass the slag layer;
- facilitating controlled wire introduction depth by preventing direct contact between the core and liquid metal; this can be achieved by adjusting the wire feed rate and the thickness of the outer layer;



– the key design features of the wire include the outer diameter, calcium-containing filler diameter, steel outer layer thickness, outer layer joint type.

In current practice, calcium can be used as a filler material in both powdered and solid forms. The different types of calcium fillers include:

- electrolytic calcium;
- aluminothermic calcium;
- ferrocacium;
- silicocalcium.

Each of these fillers possesses distinct characteristics, such as variations in the content of metallic calcium, impurity elements, and consequently, the assimilation rate. These differences in wire properties contribute to inconsistencies in the calcium addition process.

The objective of this study is to compare the performance of different calcium-containing wires using pure electrolytic calcium filler and silicocalcium filler.

## MATERIALS AND METHODS

We conducted tests on a ladle-furnace line using calcium-containing wires. The filler material used was pure electrolytic calcium. The wire designs were as follows:

- outer diameter: 10 mm; outer layer thickness: 0.8 mm (10×0.8);
- outer diameter: 11 mm; outer layer thickness: 0.8 mm (11×0.8);
- outer diameter: 10 mm; outer layer thickness: 1.0 mm (10×1.0).

For each wire design, the wire feed rate was adjusted accordingly, ranging from 120 to 180 m/min.

The composition of the wire filler is listed below (in %):

Ca	Al	Si	Mg	K + Na
99.300	<0.001	<0.010	0.010	<0.010

The table presents the physical characteristics of the calcium-containing wire.

### Physical characteristics of the wire

#### Физические характеристики используемой проволоки

Property	Wire design, mm		
	10×0.8	11×0.8	10×1.0
Weight of the filler, kg	675	666	598
Fill factor, %	25	27	21
Rated filler content per 1 m of wire, g	74	94	67
Rated weight of 1 m of wire, g	295	342	323
Calcium consumption, g/ton	95	99	113

The wire was utilized in 43 melts, comprising 51 % medium-carbon (0.14 to 0.22 % carbon content), 37 % low-carbon (carbon content <0.14 %) and 12 % low-carbon, low-silicon steel products. A wire-feeding machine introduces the wire into the ladle with the molten metal. No instance of wire breakage were observed. We conducted a comparative analysis of the results obtained from this wire and the CK40 powder-cored wire.

## RESULTS AND DISCUSSION

Initially, we compared the average consumption per melt and the calcium consumption (Fig. 1, 2). It is evident that the CK40 wire demonstrate a higher average consumption compared to the calcium-containing wire with an electrolytic calcium filler, ranging from 30 to 45 %. The calcium consumption is higher by 30 to 40 %.

In addition, we conducted an analysis of the steel pourability to evaluate the impact of introducing calcium wire on pourability, while avoiding any obstruction to the casting equipment with with NMI). In order to achieve this, we recorded the positions of the intermediate tundish stopper rod during the steel casting process (Fig. 3). Positive values of this property may indicate the initiation of the NMI deposition, while negative values suggest erosion of refractory steel components. Our findings revealed that the stopper rod positions for calcium-containing wire sizes 10×1.0 and 11×0.8 are negative. This implies that the consumption of these wire sizes can be reduced in comparison to wires sizes 10×0.8 and CK40.

Fig. 4 illustrates the relationship between steel pourability and calcium content for the calcium-containing wire designs tested. It is evident that wire grades 10×1.0 and 11×0.8 exhibit the following trend: as the calcium content increases, the displacement of the intermediate tundish stopper rod shifts towards negative values. The obtained result aligns perfectly with Fig. 3. However, it is important to acknowledge that the variance in the displacement of the stopper rod is relatively high, indicating the presence of additional factors.

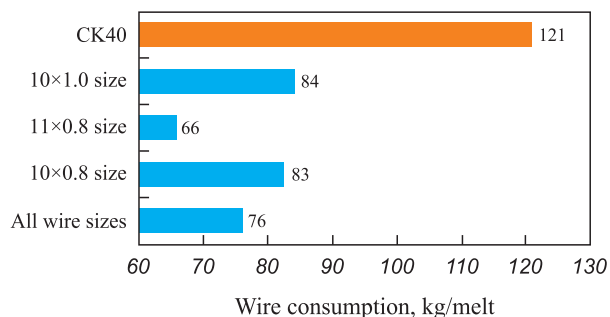


Fig. 1. Consumption of calcium-containing wire for melting

Рис. 1. Расход кальцийсодержащей проволоки на плавку

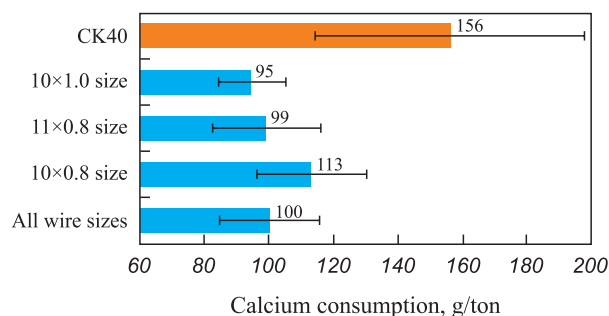


Fig. 2. Calcium consumption for melting

Рис. 2. Расход кальция на плавку

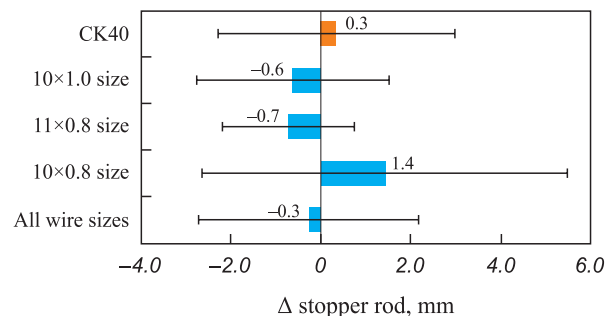


Fig. 3. Changing the tundish stopper position

Рис. 3. Изменение положения штока стопора промежуточного ковша

We thoroughly examined Fig. 3 and 4 and determined the optimal calcium content in the liquid metal that ensures consistent steel pourability for the tested wire grades. The results are depicted in Fig. 5.

Fig. 6 displays the estimated calcium assimilation factors for each wire size tested, categorized by steel grade. The findings indicate that the 11x0.8 wire exhibits the highest assimilation factor for low-carbon and carbon steel grades, whereas the 10x1.0 wire yields the best results for low-silicon steel grades. On average, wires with electrolytic calcium cores demonstrate assimilation factors that are 35 to 45 % higher compared to the CK40 wire.

Furthermore, it is important to emphasize that the primary objective of adding calcium to steel is to enhance the pourability and quality of rolled products. The calcium assimilation factor serves as a valuable tool for

estimating the process variables required to achieve the desired calcium content in the melt under specific casting conditions.

## CONCLUSIONS

We conducted a performance comparison between calcium injection wire filled with electrolytic calcium and the calcium-containing CK40 wire. Our findings reveal that, on average, the former wire exhibits a 30 to 45 % lower consumption (depending on the wire design) compared to the CK40 wire. To assess the steel pourability, we measured the position of the intermediate tundish stopper rod. Through our analysis, we determined that a minimum calcium content of 10 to 12 ppm in the metal guarantees consistent steel pourability. It is evident that expressing steel pourability in terms of the position of the interme-

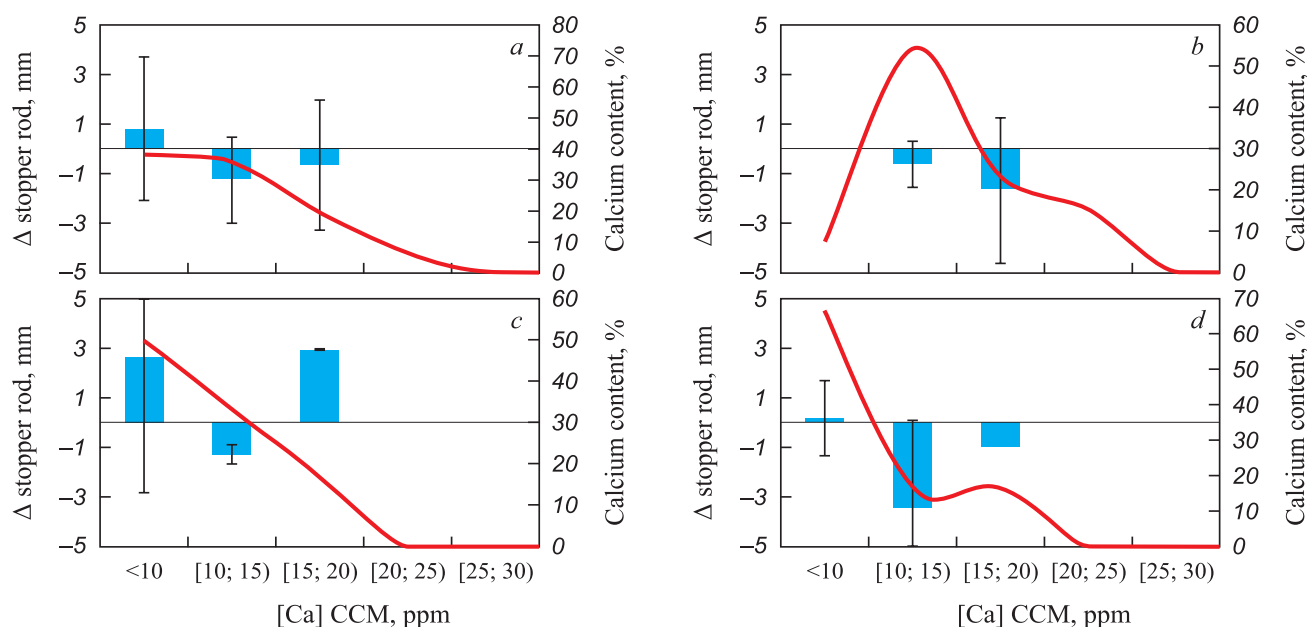


Fig. 4. Dependence of the tundish stopper rod from calcium according to the certification piece: a – all calcium injection wires (CIW); b – 11.5x0.8; c – 10x0.8; d – 10x1.0; ■ – Δ ram, mm; — data, %

Рис. 4. Зависимость положения штока стопора промежуточного ковша от содержания кальция по данным аттестационной пробы: a – все КИП; b – 11,5x0,8; c – 10x0,8; d – 10x1,0; ■ – Δ штока, мм; — данные, %

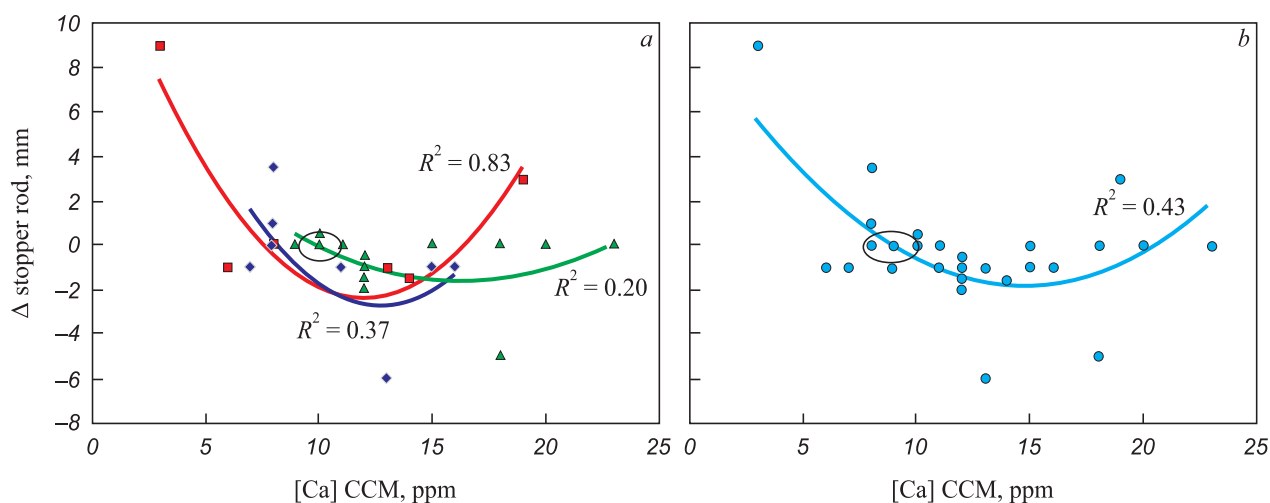


Fig. 5. Optimal calcium content in the metal:

■ – CIW 10×0.8, ◆ – CIW 10×1.0, ▲ – CIW 11×0.8 (a); ● – all CIWs (b)

Рис. 5. Оптимальное содержание кальция в металле:

■ – КИП 10×0,8, ◆ – КИП 10×1,0, ▲ – КИП 11×0,8 (a); ● – все КИП (b)

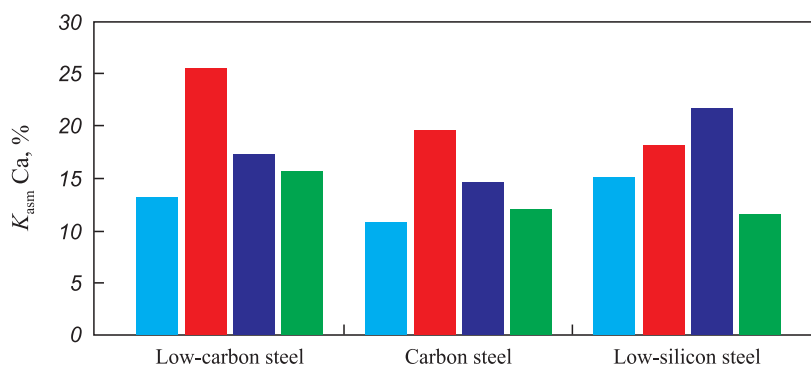


Fig. 6. Calcium recovery rate for various calcium-containing wires:

■ – 10×0.8; ■ – 11×0.8; ■ – 10×1.0; ■ – SK40

Рис. 6. Коэффициент усвоения кальция для различных кальцийсодержащих проволок:

■ – 10×0,8; ■ – 11×0,8; ■ – 10×1,0; ■ – СК40

diate tundish stopper rod serves as a convenient metric for evaluating the calcium-containing wire performance.

## REFERENCES / СПИСОК ЛИТЕРАТУРЫ

- Wasai K., Mukai K., Miyanaga A. Observation of inclusion in aluminum deoxidized iron. *ISIJ International*. 2002;42(5):459–466. <https://doi.org/10.2355/isijinternational.42.459>
- Zaitsev A.I., Rodionova I.G., Khoroshilov A.D., Mezin F.I., Semernin G.V., Mishnei P.A., Zhironkin M.V., Bikin K.B. Analysis of surface defects occurrence in cold-rolled products from IF-steels. *Elektrometallurgiya*. 2012;(7):36–40. (In Russ.).  
Зайцев А.И., Родионова И.Г., Хорошилов А.Д., Мезин Ф.И., Семернин Г.В., Мишней П.А., Жиронкин М.В., Бикин К.Б. Анализ природы возникновения поверхностных дефектов холоднокатаного проката из ИФ-сталей. *Электromеталлургия*. 2012;(7):36–40.
- Deng Z., Zhu M., Zhong B., Sichen D. Attachment of liquid calcium aluminate inclusions on inner wall of submerged entry nozzle during continuous casting of calcium-treated steel. *ISIJ International*. 2014;54(12):2813–2820. <https://doi.org/10.2355/isijinternational.54.2813>
- Zhang L., Thomas B.G. State of the art in the control of inclusions during steel ingot casting. *Metallurgical and Materials Transactions B*. 2006;37:733–761. <https://doi.org/10.1007/s11663-006-0057-0>
- Agarkov A.Yu., Rutsii D.V., Zyuban N.A., Babin G.V., Kirilichev M.V., Morozov V.V. Identification of nature of the formed “growths” on inner wall of the nozzle during continuous casting of C45E steel. *Teoriya i tekhnologiya metallurgicheskogo proizvodstva*. 2020;(1):11–17. (In Russ.).  
Агарков А.Ю., Руцкий Д.В., Зюбан Н.А., Бабин Г.В., Кириличев М.В., Морозов В.В. Выявление природы образующихся «наростов» на внутренней стенке разливочного стакана при непрерывной разливке стали марки С45Е. *Теория и технология металлургического производства*. 2020;(1):11–17.



6. Yang W., Zhang L., Wang X., Ren Y., Liu X., Shan Q. Characteristics of inclusions in low carbon Al-killed steel during ladle furnace refining and calcium treatment. *ISIJ International*. 2013;53(8):1401–1410. <https://doi.org/10.2355/isijinternational.53.1401>
7. Higuchi Y., Numata M., Fukagawa S., Shinme K. Effect of method of calcium treatment on composition and shape of non-metallic inclusions. *Tetsu-to-Hagane*. 1996;82(8):671–676. [https://doi.org/10.2355/tetsutohagane1955.82.8\\_671](https://doi.org/10.2355/tetsutohagane1955.82.8_671)
8. Ren Y., Zhang L., Li S. Transient evolution of inclusions during calcium modification in linepipe steels. *ISIJ International*. 2014;54(12):2772–2779. <https://doi.org/10.2355/isijinternational.54.2772>
9. Kushnerev I.V., Serov G.V., Tikhonov S.M., Kuznetsov D.V., Aksel'rod L.M. The non-metallic inclusion's composition and quantity's prediction in the low-alloyed tube steel production. *Novye огнеупоры*. 2017;(12):36–41. (In Russ.). <https://doi.org/10.17073/1683-4518-2017-12-36-41>  
Кушнерев И.В., Серов Г.В., Тихонов С.М., Кузнецов Д.В., Аксельрод Л.М. Прогнозирование состава и количества неметаллических включений при производстве низколегируемых трубных сталей. *Новые огнеупоры*. 2017;(12): 36–41. <https://doi.org/10.17073/1683-4518-2017-12-36-41>
10. Choudhary S.K., Ghosh A. Thermodynamic evaluation of formation of oxide-sulfide duplex inclusions in steel. *ISIJ International*. 2008;48(11):1552–1559. <https://doi.org/10.2355/isijinternational.48.1552>
11. Takahashi A., Ogawa H. Influence of microhardness and inclusion on stress oriented hydrogen induced cracking of line pipe steels. *ISIJ International*. 1996;36(3):334–340. <https://doi.org/10.2355/isijinternational.36.334>
12. Brown A., Jones C.L. Hydrogen induced cracking in pipeline steels. *Corrosion*. 1984;40(7):330–336. <https://doi.org/10.5006/1.3593931>
13. Moon J., Kim S.-J., Lee C. Role of Ca treatment in hydrogen induced cracking of hot rolled API pipeline steel in acid sour media. *Metals and Materials International*. 2013;19(1): 45–48. <https://doi.org/10.1007/s12540-013-1008-3>
14. Varma N., Pistorius P.C., Fruehan R.J., Potter M., Lind M., Story S. Transient inclusion evolution during modification of alumina inclusions by calcium in Liquid steel: Part I. Background, experimental techniques and analysis methods. *Metallurgical and Materials Transactions B*. 2011;42:711–719. <https://doi.org/10.1007/s11663-011-9516-3>
15. Varma N., Pistorius P.C., Fruehan R.J., Potter M., Lind M., Story S. Transient inclusion evolution during modification of alumina inclusions by calcium in Liquid steel: Part II. Results and discussion. *Metallurgical and Materials Transactions B*. 2011;42:720–729. <https://doi.org/10.1007/s11663-011-9517-2>
16. Guo J., Cheng S.-s., Guo H.-j., Mei Y.-g. Novel mechanism for the modification of  $Al_2O_3$  – based inclusions in ultra-low carbon Al-killed steel considering the effects of magnesium and calcium. *International Journal of Minerals, Metallurgy and Materials*. 2018;25(3):280–287. <https://doi.org/10.1007/s12613-018-1571-1>
17. Lind M. *Mechanism and kinetics of transformation of alumina inclusions in steel by calcium treatment: Doctoral Thesis*. Helsinki: Helsinki University of Technology Publications in Materials Science and Engineering; 2006:89.
18. Yang J., Wang X.-h., Jiang M., Wang W.-j. Effect of calcium treatment on non-metallic inclusions in ultra-low oxygen steel refined by high basicity high  $Al_2O_3$  slag. *Journal of Iron and Steel Research International*. 2011;(18):8–14. [https://doi.org/10.1016/S1006-706X\(11\)60083-6](https://doi.org/10.1016/S1006-706X(11)60083-6)
19. Khoroshilov A.D., Salikhanov P.A., Byzov D.P., Zhironkin M.V., Bikin K.B. Experience of application of calcium-containing cored wire with various fillers at steel ladle treatment. *Ferrous Metallurgy. Bulletin of Scientific, Technical and Economic Information*. 2021;77(4):432–444. (In Russ.). <https://doi.org/10.32339/0135-5910-2021-4-432-444>  
Хорошилов А.Д., Салиханов П.А., Бызов Д.П., Жиронкин М.В., Бикин К.Б. Опыт применения кальцийсодержащей инъекционной проволоки с различными наполнителями при внепечной обработке стали. *Черная металлургия. Бюллетень научно-технической и экономической информации*. 2021;77(4):432–444. <https://doi.org/10.32339/0135-5910-2021-4-432-444>
20. Krupennikov S.A., Filimonov Yu.P., Kuz'menko A.G., Mazurov E.F. Determination of optimal input speed of flux-cored wire with silicocalcium filler in a ladle with liquid steel. *Elektrometallurgiya*. 2000;(11):15–22. (In Russ.).  
Крупенников С.А., Филимонов Ю.П., Кузьменко А.Г., Мазуров Е.Ф. Определение оптимальной скорости ввода порошковой проволоки с силикокальциевым наполнителем в ковш с жидкой сталью. *Электromеталлургия*. 2000;(11):15–22.
21. Lind M., Holappa L. Transformation of alumina inclusions by calcium treatment. *Metallurgical and Materials Transactions B*. 2010;41:359–366. <https://doi.org/10.1007/s11663-009-9337-9>
22. Kablukovskii A.F., etc. *Steel Ladle Treatment with Flux-Cored Wire*. Moscow: Metallurgizdat; 2006:288. (In Russ.).  
Каблуковский А.Ф. и др. *Внепечная обработка стали порошковой проволокой*. Москва: Metallurgizdat; 2006: 288.
23. Shalimov A.G., Semin A.E., Galkin M.P., Kosyrev K.L. *Innovative Development of Electric Steelmaking*. Moscow: Metallurgizdat; 2014:308. (In Russ.).  
Шалимов А.Г., Семин А.Е., Галкин М.П., Косырев К.Л. *Инновационное развитие электросталеплавильного производства*. Москва: Metallurgizdat; 2014:308.

## Information about the Authors

## Сведения об авторах

**Andrei D. Khoroshilov**, Chief Expert on the Product “Calcium Injection Wire and Alloying Elements”, LLC Rusatom MetalTech  
E-mail: [khoroshilovad@gmail.com](mailto:khoroshilovad@gmail.com)

**Sergei A. Somov**, Head of the Department, JSC “Vyksa Metallurgical Plant”  
E-mail: [Somov\\_sa@vsw.ru](mailto:Somov_sa@vsw.ru)

**Андрей Дмитриевич Хорошилов**, главный эксперт по продукту «КИП и легирующие элементы», ООО «Русатом МеталлТех»  
E-mail: [khoroshilovad@gmail.com](mailto:khoroshilovad@gmail.com)

**Сергей Александрович Сомов**, начальник отдела, АО «Выксунский металлургический завод»  
E-mail: [Somov\\_sa@vsw.ru](mailto:Somov_sa@vsw.ru)

**Vladimir D. Katolikov**, Chief Expert on the Product “Calcium Injection Wire and Alloying Elements”, LLC Rusatom MetalTech  
**ORCID:** 0000-0001-7554-1467  
**E-mail:** vdkatolikov@yandex.ru

**Vladimir A. Murysev**, Chief Specialist, JSC “Vyksa Metallurgical Plant”  
**E-mail:** Murysev\_va@vsw.ru

**Roman E. Bocherikov**, Postgraduate of the Chair “Energy-Efficient and Resource-Saving Industrial Technologies”, National University of Science and Technology “MISIS”  
**ORCID:** 0000-0002-7315-3222  
**E-mail:** Romann961@gmail.com

**Marat R. Yarmukhametov**, Technologist, JSC “Vyksa Metallurgical Plant”  
**E-mail:** Jarmukhametov\_mr@vsw.ru

**Владимир Дмитриевич Католиков**, главный эксперт по продукту «КИП и легирующие элементы», ООО «Русатом МеталлТех»  
**ORCID:** 0000-0001-7554-1467  
**E-mail:** vdkatolikov@yandex.ru

**Владимир Александрович Мurysev**, главный специалист, АО «Выксунский металлургический завод»  
**E-mail:** Murysev\_va@vsw.ru

**Роман Евгеньевич Бочерилов**, аспирант кафедры энергоэффективных и ресурсосберегающих промышленных технологий, Национальный исследовательский технологический университет «МИСИС»  
**ORCID:** 0000-0002-7315-3222  
**E-mail:** Romann961@gmail.com

**Марат Рафхатович Ярмухаметов**, технолог, АО «Выксунский металлургический завод»  
**E-mail:** Jarmukhametov\_mr@vsw.ru

## Contribution of the Authors

## Вклад авторов

**A. D. Khoroshilov** – formation of the main concept of the article, setting the goal of the work, calculations, finalizing the text, correcting the conclusions.

**S. A. Somov** – guidelines for industrial melting, revision of the text, discussion of the results.

**V. D. Katolikov** – generalization and interpretation of the research results, calculations, formation of the conclusions.

**V. A. Murysev** – analysis and systematization of industrial data, revision of the text, discussion of the results.

**R. E. Bocherikov** – selection, analysis and generalization of literature data, discussion of the results.

**M. R. Yarmukhametov** – conducting industrial melting, discussion of the results.

**А. Д. Хорошилов** – формирование основной концепции работы, постановка цели работы, проведение расчетов, доработка текста, корректировка выводов.

**С. А. Сомов** – руководство при проведении промышленных плавок, доработка текста, обсуждение результатов.

**В. Д. Католиков** – обобщение результатов исследований, проведение расчетов, интерпретация результатов, формирование выводов.

**В. А. Мurysev** – анализ и систематизация промышленных данных, доработка текста, обсуждение результатов.

**Р. Е. Бочерилов** – подбор, анализ и обобщение литературных данных, обсуждение результатов.

**М. Р. Ярмухаметов** – проведение промышленных плавок, обсуждение результатов.

Received 15.02.2023

Revised 20.02.2023

Accepted 11.04.2023

Поступила в редакцию 15.02.2023

После доработки 20.02.2023

Принята к публикации 11.04.2023

Materials of the Conference  
«PHYSICO-CHEMICAL FOUNDATIONS  
OF METALLURGICAL PROCESSES»  
named after Academician A.M. Samarin – 2022

По материалам конференции  
«ФИЗИКО-ХИМИЧЕСКИЕ ОСНОВЫ  
МЕТАЛЛУРГИЧЕСКИХ ПРОЦЕССОВ»  
им. академика А.М. Самарина – 2022



UDC 669.187.2: 628.511/.512: 504.05

DOI 10.17073/0368-0797-2023-3-344-355



Original article

Оригинальная статья

## LEAD AND ZINC SELECTIVE EXTRACTION FROM EAF DUST WHILE HEATING IN RESISTANCE FURNACE WITH FLOWING ARGON

N. V. Podusovskaya<sup>1,2</sup>, O. A. Komolova<sup>1,2</sup>, K. V. Grigorovich<sup>1,2</sup>,  
A. V. Pavlov<sup>2</sup>, V. V. Aksenova<sup>2</sup>, B. A. Rumyantsev<sup>1</sup>, M. V. Zheleznyi<sup>1,2</sup>

<sup>1</sup> Baikov Institute of Metallurgy and Materials Science, Russian Academy of Sciences (49 Leninskii Ave., Moscow 119991, Russian Federation)

<sup>2</sup> National University of Science and Technology “MISIS” (4 Leninskii Ave., Moscow 119049, Russian Federation)

✉ ndemidova\_n@mail.ru

**Abstract.** The elemental and phase compositions of electric arc furnace (EAF) dust from PJSC Severstal were studied. We carried out the thermodynamic modeling of zinc and lead selective extraction process and determined its possible mechanisms. EAF dust was heated in the temperature range of 20 – 1300 °C in vacuum resistance furnace and the Tamman furnace with flowing argon. Experiments in the vacuum resistance furnace with linear heating showed that lead and zinc removal from the sample occurs in the temperature range of 800 – 1200 °C, with higher lead removal rate. Intensive lead removal was observed at temperature above 1000 °C, while intensive zinc removal occurs at temperature above 1200 °C. Clarifying isothermal experiments performed in the Tamman furnace showed that lead complete transition to the gas phase was achieved at a temperature of 1100 °C (holding time – 12 min) and at a temperature of 1200 °C (holding time – 6 min or more). At the same time, zinc removal was observed in the amount of 14.4 % ratio and 32.2 % ratio, respectively, which allows us to conclude that it is possible to consistently obtain two products: lead and zinc mixture and zinc not contaminated with lead. When comparing experimental and thermodynamic modeling data, the reactions that are most likely to occur during the carbon reduction of lead- and zinc-containing phases were determined.

**Keywords:** ferrous metallurgy, non-ferrous metals, steel dust, electric-arc furnace dust, EAF-dust, carbon-free process, selective extraction, evaporation, zinc, lead, iron, secondary resources, resource saving

**For citation:** Podusovskaya N.V., Komolova O.A., Grigorovich K.V., Pavlov A.V., Aksenova V.V., Rumyantsev B.A., Zheleznyi M.V. Lead and zinc selective extraction from EAF dust while heating in resistance furnace with flowing argon. *Izvestiya. Ferrous Metallurgy*. 2023;66(3):344–355. <https://doi.org/10.17073/0368-0797-2023-3-344-355>

## ИЗУЧЕНИЕ СЕЛЕКТИВНОГО ИЗВЛЕЧЕНИЯ СВИНЦА И ЦИНКА ИЗ ПЫЛИ ДСП ПРИ НАГРЕВЕ В ПЕЧАХ СОПРОТИВЛЕНИЯ В ТОКЕ АРГОНА

Н. В. Подусовская<sup>1,2</sup>, О. А. Комолова<sup>1,2</sup>, К. В. Григорович<sup>1,2</sup>,  
А. В. Павлов<sup>2</sup>, В. В. Аксенова<sup>2</sup>, Б. А. Румянцев<sup>1</sup>, М. В. Железный<sup>1,2</sup>

<sup>1</sup> Институт металлургии и материаловедения им. А.А. Байкова РАН (Россия, 119991, Москва, Ленинский пр., 49)

<sup>2</sup> Национальный исследовательский технологический университет «МИСИС» (Россия, 119049, Москва, Ленинский пр., 4)

✉ ndemidova\_n@mail.ru

**Аннотация.** Изучены элементный и фазовый составы пыли дуговой сталеплавильной печи ПАО «Северсталь», проведено термодинамическое моделирование процесса селективного извлечения цинка и свинца из пыли. Определены возможные механизмы его протекания. Выполнен нагрев электросталеплавильной пыли в диапазоне температур 20 – 1300 °C в вакуумной печи сопротивления и печи Таммана в токе аргона.

Эксперименты в вакуумной печи сопротивления с линейным нагревом показали, что удаление свинца и цинка из образца протекало в интервале температур 800 – 1200 °С. При этом скорость удаления свинца была выше. Интенсивное удаление свинца наблюдали при температурах свыше 1000 °С, а интенсивное удаление цинка при температурах свыше 1200 °С. Уточняющие изотермические эксперименты, выполненные в печи Таммана, показали, что полный переход свинца в газовую фазу достигался при температуре 1100 °С (время выдержки 12 мин) и при температуре 1200 °С (время выдержки 6 мин и более). Параллельно с этим наблюдали удаление цинка в количестве 14,4 и 32,2 % (отн.) соответственно, что позволило сделать вывод о возможности последовательного получения двух продуктов: смеси свинца с цинком и цинка, не загрязненного свинцом. При сопоставлении экспериментальных данных и данных термодинамического моделирования определены реакции, протекание которых наиболее вероятно при восстановлении свинец- и цинксодержащих фаз углеродом.

**Ключевые слова:** черная металлургия, цветные металлы, сталеплавильная пыль, пыль ДСП, безуглеродный процесс, селективное извлечение, испарение, цинк, свинец, железо, вторичные ресурсы, ресурсосбережение

**Для цитирования:** Подусовская Н.В., Комолова О.А., Григорович К.В., Павлов А.В., Аксенова В.В., Румянцев Б.А., Железный М.В. Изучение селективного извлечения свинца и цинка из пыли ДСП при нагреве в печах сопротивления в токе аргона. *Известия вузов. Черная металлургия*. 2023;66(3):344–355. <https://doi.org/10.17073/0368-0797-2023-3-344-355>

## INTRODUCTION

The accumulation of electric arc furnace (EAF) dust in the dumps of metallurgical companies contains significant amounts of zinc (typically 15 – 25 %) and lead (up to 3 %). Given the limited reserves of zinc and lead ores<sup>1</sup>, as well as the low content of these metals in the dust, it has become crucial to develop technologies for the selective extraction of non-ferrous metals from EAF dust. Reprocessing this dust would not only allow for the recovery of zinc, lead, and iron for metallurgical production but also address the issue of toxic waste occupying substantial areas [1].

In general, zinc and lead in the EAF dust are present in the form of oxides due to the oxidizing nature of the steel-making process. However, in the gas flow, there is a high probability of the formation of complex oxides, such as zinc ferrite  $ZnFe_2O_4$  [2 – 4]. Moreover, the diverse chemical composition of materials processed in the EAF leads to variations in both the chemical and phase compositions of the EAF dust. This necessitates continuous monitoring when disposing of metallurgical dust and complicates EAF dust disposal procedure [5].

Currently, selective extraction of lead and zinc from the EAF dust is primarily carried out using hydrometallurgical methods [6; 7] or integrated pyro-hydrometallurgical methods [4; 8; 9]. However, the hydrometallurgical process is highly complex and involves multiple technological stages that require large amounts of chemical reagents, overheated vapor, hot water, and energy-intensive equipment. This poses environmental risks as numerous production sites are associated with poorly regulated or unregulated emissions of spent reagents, heat, energy carriers, production wastes and by-products [10; 11]. Therefore, it appears advisable to explore pyrometallurgical methods for the reprocessing of EAF dust to achieve selective extraction of lead and zinc.

An overview of studies on the disposal of toxic EAF dust reveals that the majority of efforts are focused on con-

ventional approaches that utilize excessive amounts of reducing agents, such as carbon, to lower the starting temperature of zinc and other metals recovery. However, this hampers the selective extraction of these metals during the recovery process.

Furthermore, the reduction of industrial carbon consumption to mitigate CO<sub>2</sub> emissions has become a key objective for BRICS countries [12]. In Russia, specifically, government measures have been planned to address greenhouse gas emissions according to sources<sup>2, 3</sup>. These measures include:

- implementation of mandatory carbon accounting;
- establishment of performance targets for companies;
- implementation of fees or fines for excessive emissions;
- introduction of carbon emission trading;
- technological upgrades in production process.

These governmental actions impose restrictions on metallurgical technologies that are associated with significant greenhouse gas emissions. As a result, there is a need to develop methods for the selective extraction of lead and zinc from the EAF dust that do not rely on the use of additional reducing agent.

## OBJECT OF RESEARCH

The research focuses on the EAF dust from PJSC Severstal, which exhibits the following element composition (wt. %): 41.4 Fe; 14.5 Zn; 6.2 Ca; 2.5 Mn; 1.7 Cl; 1.74 C; 1.3 Si; 1.0 K; 1.0 Pb; 0.74 S; 0.2 Cr; 0.2 Cu; 0.1 Ti; with the remaining portion likely being oxygen. The determination of element content ranging from Na to U was performed using the MAX-GVM wave-dispersion X-ray fluorescent spectroscopy specimen (MAX-GVM). This method involves exposing the sample to pri-

<sup>1</sup> Governmental report "On conditions and usage of raw mineral resources in the Russian Federation in 2020". URL: [https://www.mnr.gov.ru/upload/iblock/74a/GD\\_msb-2020.pdf](https://www.mnr.gov.ru/upload/iblock/74a/GD_msb-2020.pdf) (access date 11.05.2023).

<sup>2</sup> Federal Law dated 02.07.2021 No. 296-ФЗ "On restriction of emissions of greenhouse gases". URL: <http://publication.pravo.gov.ru/Document/View/0001202107020031> (access date 11.05.2023).

<sup>3</sup> Governmental decree of the Russian Federation dated October 29, 2021 No. № 3052-p. URL: <http://publication.pravo.gov.ru/Document/View/00012021101010022> (access date 11.05.2023).



mary radiation from an X-ray tube, measuring the intensity of secondary fluorescent irradiation at wavelengths corresponding to the elements of interest, and subsequently calculating the weight fraction of these elements using fundamental parameter methods. Sample preparation involved milling and averaging loose samples, mixing them with a binder (polyacrylamide) at a concentration of 0.2 wt. % above the sample, wetting, forming the mixture into moderate-height cylinders ( $D = 7$  mm,  $h = 2 - 3$  mm), and drying. For solid samples, polished cross-sections were prepared.

The carbon and sulfur content was determined using a Leco CS 600 instrument through high temperature extraction in a carrier gas. The determination of carbon and sulfur involved combusting the sample in an oxygen flow (99.998 %) in the presence of special fluxes, followed by the measurement of the formed carbon dioxide ( $\text{CO}_2$ ) and sulfur dioxide ( $\text{SO}_2$ ).

The phase composition of the EAF dust was determined using X-ray diffraction (XRD). The phase content (wt. %) was found to be as follows: 78.2  $\text{Fe}_3\text{O}_4$ ; 4.4 (Zn, Mn, Fe) $_3\text{O}_4$ ; 6.0 ZnO; 4.5  $\text{Ca}_2\text{Fe}_2\text{O}_5$ ; 3.0  $\text{MnO}_2$ ; 2.7  $\text{Pb}_2\text{O}_3$ ; 1.2  $\text{SiO}_2$ . It should be noted that since the structures of magnetite and spinel are essentially identical, they can be considered as a combined phase.

## THEORETICAL OBJECTIVES

Previous studies have suggested that selective reduction of lead from the EAF dust can be achieved with an insufficient amount of reducing agent. For example, it was demonstrated in [13] that during the reducing melting of lead agglomerate, selective reduction of lead can be achieved with a limited amount of carbon monoxide as a reducing agent (CO content not exceeding 60 %). Similar effects of solid carbon on the reduction of lead-containing industrial wastes were also considered in [14; 15]. It was observed that when the carbon content exceeded 3 %, combined reduction of lead and zinc from EAF dust occurred. Furthermore, when the carbon content exceeded 3.7 %, the selectivity of lead reduction from copper melting dust became more complex.

In order to determine the conditions necessary for the selective extraction of zinc and lead from EAF dust, it is crucial to identify the temperatures at which the zinc and lead compounds in the dust transition into the gas phase.

According to [16], HSC Chemistry 6 software has been successfully utilized to evaluate thermodynamic parameters, and the simulated results have shown good comparability with experimental data. The software employs calculating modules that rely on a comprehensive thermochemical database encompassing enthalpy ( $H$ ), entropies ( $S$ ), and reaction heat capacitances ( $C_p$ ). By calculating changes in Gibbs energies, thermodynamic

temperatures of reactions ( $\Delta G < 0$ ) can be determined. The thermodynamic simulation considered reactions involving the reduction, thermal dissociation, and evaporation of detected lead and zinc-containing phases, as well as the reduction of iron and manganese oxides.

Table 1 summarizes the reduction of lead oxide (III) and the subsequent transition of lead and its compounds into the gas phase. The thermodynamic simulation assumed a carbon monoxide pressure of 1 atm.

From Table 1, it can be observed that the reduction of lead oxide (III) and the transition of lead into the gas phase begin at temperature not exceeding 877 °C.

Table 2 summarizes the reduction of zinc oxide and the accompanying transition of zinc into the gas phase.

According to Table 2, the reduction of zinc oxide with consideration for thermodynamics starts from the temperature exceeding 958 °C. However, it has been demonstrated in [17 – 19] that zinc reduction from EAF dust can occur successfully in the temperature range of 925 – 1300 °C with an excessive amount of reducing agent.

Reduction of complex spinel (Zn, Mn, Fe) $_3\text{O}_4$ , specifically zinc ferrite  $\text{ZnFe}_2\text{O}_4$  (franklinite), by carbon and carbon monoxide upon heating is investigated. The reactions of franklinite reduction which begin in the temperature range of 0 – 1326 °C are shown in Table 3.

Reactions 4 – 7, 10 – 12 in Table 3 exhibit similar starting temperatures for the reduction of lead and zinc-containing phases, emphasizing the need for accurate selection of temperature and composition of the gas phase to enable selective extraction of lead and zinc from EAF dust.

Since the spinel (Zn, Mn, Fe) $_3\text{O}_4$ , detected in the EAF dust is not included in the HSC Chemistry 6 database,

Table 1

**Lead (III) oxide reduction chemical reactions with their course temperatures, resulting in lead and its compounds transition into the gas phase**

*Таблица 1. Химические реакции восстановления оксида свинца (III), сопровождающиеся переходом свинца и его соединений в газовую фазу, и температуры их протекания*

No.	Reaction	Reaction temperature, °C
1	$\text{Pb}_2\text{O}_3 + 3\text{C} = 2\text{Pb}_{(\text{g})} + 3\text{CO}_{(\text{g})}$	>449
2	$\text{Pb}_2\text{O}_3 + 1.5\text{C} = 2\text{Pb}_{(\text{g})} + 1.5\text{CO}_{2(\text{g})}$	>295
3	$\text{Pb}_2\text{O}_3 + 3\text{CO}_{(\text{g})} = 2\text{Pb}_{(\text{g})} + 3\text{CO}_{2(\text{g})}$	0 – 2000
4	$\text{Pb}_2\text{O}_3 + \text{C} = 2\text{PbO}_{(\text{g})} + \text{CO}_{(\text{g})}$	>809
5	$2\text{Pb}_2\text{O}_3 + \text{C} = 4\text{PbO}_{(\text{g})} + \text{CO}_{2(\text{g})}$	>835
6	$\text{Pb}_2\text{O}_3 + \text{CO}_{(\text{g})} = 2\text{PbO}_{(\text{g})} + \text{CO}_{2(\text{g})}$	>877

**Zinc oxide reduction chemical reactions  
with their course temperatures, resulting  
in zinc transition into the gas phase**

*Таблица 2. Химические реакции восстановления оксида цинка, сопровождающиеся переходом цинка в газовую фазу, и температуры их протекания*

No.	Reaction	Reaction temperature, °C
7	$\text{ZnO} + \text{C} = \text{Zn}_{(\text{g})} + \text{CO}_{(\text{g})}$	>958
8	$2\text{ZnO} + \text{C} = 2\text{Zn}_{(\text{g})} + \text{CO}_{2(\text{g})}$	>1064
9	$\text{ZnO} + \text{CO}_{(\text{g})} = \text{Zn}_{(\text{g})} + \text{CO}_{2(\text{g})}$	>1326

possible reduction reactions were considered for the compounds iron or manganese oxides ( $\text{Fe}_3\text{O}_4$  and  $\text{Mn}_3\text{O}_4$ ). The reactions, which occur in the temperature range of 295 – 1400 °C, are summarized in Table 4.

In accordance with Table 4, reactions 15 – 25 can occur simultaneously with the reduction of lead oxide (III).

Since the transition of zinc-containing phases into gas phase will occur after the reduction of lead (and possibly other components of EAF dust), it is likely that the carbon present in the dust will be fully consumed for other components. Therefore, without an additional reducing agent, the mechanism for the transition of zinc into the gas phase will be the thermal dissociation of zinc oxide (as shown in Table 5).

The temperature required for reaction 26 is too high for industrial conditions. The starting temperature of thermal dissociation can be reduced by decreasing the partial pressure of the resulting gases through the addition of argon. In order to confirm this, a thermodynamical simulation of the equilibrium composition was performed for the reaction of thermal decomposition of zinc oxide

Table 2

using Terra software [20]. The temperature of reaction  $\text{ZnO} = \text{Zn}_{(\text{g})} + \text{O}_{2(\text{g})}$  as a function of the partial pressure of  $\text{Zn}_{(\text{g})}$  is illustrated in Fig. 1.

From Fig. 1, it can be observed that a decrease in the partial pressure of  $\text{Zn}_{(\text{g})}$  (by argon addition) would allow for a reduction in the temperature range of thermal decomposition of zinc oxide from 1970 to 1300 °C.

Theoretically, a similar approach can be applied to reduce the starting temperature of the reduction of lead oxide (III) in order to expand the range of selective extraction of lead and zinc-containing phases.

It has been determined that selective extraction of lead and zinc from EAF dust is possible using two methods (temperatures provided without considering the addition of inert gas to the system):

– consecutive reduction of lead containing phases (295 – 877 °C) and zinc containing phases (794 – 1326 °C) by carbon or carbon monoxide;

– reduction of lead-containing phases (295 – 877 °C) by carbon or carbon monoxide, followed by the thermal dissociation of zinc-containing phases (1970 °C).

The need to investigate the mechanism of consecutive reduction of lead-containing phases and zinc-containing phases from EAF dust is driven by the preference for operating the process at lower temperatures. This would result in reduced energy consumption and the ability to carry out the process without the formation of a melt.

However, the temperatures in the actual process may deviate significantly from the calculated values. In order to determine the actual temperatures for the selective extraction of lead and zinc from EAF dust, an experimental study was conducted.

## EXPERIMENTAL

The experimental study involved heating EAF dust in the temperature range of 20 – 1300 °C using a vacuum

### Franklinite reduction chemical reactions and their course temperatures

*Таблица 3. Химические реакции восстановления франклинита и температуры их протекания*

No.	Reaction	Reaction temperature, °C
10	$\text{ZnFe}_2\text{O}_4 + \text{CO}_{(\text{g})} = \text{ZnO} + 2\text{FeO} + \text{CO}_{2(\text{g})}$	>838
11	$\text{ZnFe}_2\text{O}_4 + 4\text{C} = \text{Zn}_{(\text{g})} + 2\text{Fe} + 4\text{CO}_{(\text{g})}$	>794
12	$\text{ZnFe}_2\text{O}_4 + 2\text{C} = \text{Zn}_{(\text{g})} + 2\text{Fe} + 2\text{CO}_{2(\text{g})}$	>863
13	$\text{ZnFe}_2\text{O}_4 + 3\text{CO}_{(\text{g})} = \text{ZnO} + 2\text{Fe} + 3\text{CO}_{2(\text{g})} + \text{ZnO} + \text{CO}_{(\text{g})} = \text{Zn}_{(\text{g})} + \text{CO}_{2(\text{g})} =$ $= \sum \text{ZnFe}_2\text{O}_4 + 2\text{CO}_{(\text{g})} = \text{Zn}_{(\text{g})} + 2\text{FeO} + 2\text{CO}_{2(\text{g})}$	>1126
14	$\text{ZnFe}_2\text{O}_4 + \text{CO}_{(\text{g})} = \text{ZnO} + 2\text{FeO} + \text{CO}_{2(\text{g})} + \text{ZnO} + \text{C} = \text{Zn}_{(\text{g})} + \text{CO}_{(\text{g})} =$ $= \sum \text{ZnFe}_2\text{O}_4 + \text{C} = \text{Zn}_{(\text{g})} + 2\text{FeO} + \text{CO}_{2(\text{g})}$	>905

Table 3

Table 4

**Fe<sub>3</sub>O<sub>4</sub> and Mn<sub>3</sub>O<sub>4</sub> reduction chemical reactions and their course temperatures**

Таблица 4. Химические реакции восстановления оксидов Fe<sub>3</sub>O<sub>4</sub> и Mn<sub>3</sub>O<sub>4</sub> и температуры их протекания

No.	Reaction	Reaction temperature, °C
15	Fe <sub>3</sub> O <sub>4</sub> + C = 3FeO + CO <sub>(g)</sub>	>700
16	2Fe <sub>3</sub> O <sub>4</sub> + C = 6FeO + CO <sub>2(g)</sub>	>694
17	Fe <sub>3</sub> O <sub>4</sub> + CO <sub>(g)</sub> = 3FeO + CO <sub>2(g)</sub>	>514
18	FeO + C = Fe + CO <sub>(g)</sub>	>725
19	2FeO + C = 2Fe + CO <sub>2(g)</sub>	>751
20	FeO + CO <sub>(g)</sub> = Fe + CO <sub>2(g)</sub>	<579
21	Fe <sub>3</sub> O <sub>4</sub> + C = Fe <sub>2</sub> O <sub>3</sub> + Fe + CO <sub>(g)</sub>	>941
22	Mn <sub>3</sub> O <sub>4</sub> + C = 3MnO + CO <sub>(g)</sub>	>277
23	2Mn <sub>3</sub> O <sub>4</sub> + C = 6MnO + CO <sub>2(g)</sub>	0 – 2000
24	Mn <sub>3</sub> O <sub>4</sub> + CO <sub>(g)</sub> = 3MnO + CO <sub>2(g)</sub>	0 – 2000
25	MnO + C = Mn + CO <sub>(g)</sub>	>1397

Table 5

**Zinc oxide thermal dissociation chemical reaction and its course temperature**

Таблица 5. Химическая реакция термической диссоциации оксида цинка и температура ее протекания

No.	Reaction	Reaction temperature, °C
26	2ZnO = 2Zn <sub>(g)</sub> + O <sub>2(g)</sub>	>2118

resistance furnace with constant heating rate and a Tamman furnace under isothermal conditions with argon flow. Prior to the study, a blank test was conducted to ensure that the weight loss of the crucible did not affect the measurements of the sample weight.

The temperature in the furnace was monitored using BP(A) 5/20 thermocouple placed in the isothermal area of the furnace, inside an empty crucible.

After the samples were cooled, they were weighed and subjected to chemical composition analysis.

The carbon and sulfur content in the samples was determined using a Leco CS 600 instrument through high temperature extraction in a gas carrier. The element content from Na to U was determined using a MAX-GVM wave-dispersion X-ray fluorescent spectroscan (MAX-GVM).

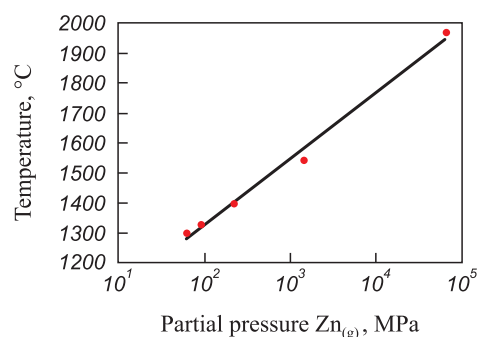


Fig. 1. Dependence of ZnO = Zn<sub>(g)</sub> + O<sub>2(g)</sub> reaction temperature on Zn<sub>(g)</sub> partial pressure

Рис. 1. Зависимость температуры протекания реакции ZnO = Zn<sub>(r)</sub> + O<sub>2(r)</sub> от парциального давления Zn<sub>(r)</sub>

**EXPERIMENTS IN A VACUUM RESISTANCE FURNACE**

EAF dust from bag filters was subjected to processing in a vacuum resistance furnace (Fig. 2) equipped with a graphite heater ( $D = 65$  mm,  $L = 300$  mm) in the temperature range of 20 – 1300 °C. The furnace specification are as follows:  $P = 20$  kW;  $U = 10$  V;  $I = 2000$  A;  $f = 50$  Hz. The furnace is equipped with a water cooling system.

A total of 3 g of the dust was placed in a thin-walled alundum crucible ( $D = 19$  mm,  $d = 18$  mm,  $H = 40$  mm,  $h = 38.5$  mm). The layer height was maintained at 1.25 – 1.5 cm. Seven crucibles, weighting a dust total of 21 g, were placed in the isothermal area of the furnace. From the furnace chamber was evacuated air using a vacuum pump to reach a residual pressure of  $10^{-1}$  Pa, after which it was filled with high-purity argon.

Subsequently, the gas was discharged into the atmosphere and the argon flow rate was set to 0.5 l/min. The furnace was heated at a rate of 15 °C/min, with the temperature reaching 100 °C in ~7 min. Once the desired temperature (800, 1000, 1100, 1200, 1300 °C) was reached, one to two crucibles containing the melted products were removed from the furnace and cooled in ambient air.

The appearance of the samples before and after processing in the furnace is depicted in Fig. 3. After heating, the samples exhibited a darkened color, likely due to partial reduction of magnetite. The samples processed at 800 and 1000 °C crumbled under light pressure, while those processed at 1100 and 1200 °C were easily milled in mortar. Heating to 1300 °C resulted in the formation of a melt.

After cooling, the samples were analyzed to determine their chemical composition. The actual weight loss of the samples after heating is presented in Table 6, showing a significant increase in weight loss at 1200 °C and higher temperatures.

The contents of lead, zinc (determined using a MAX-GVM wave-dispersion X-ray fluorescent spectroscan), and car-

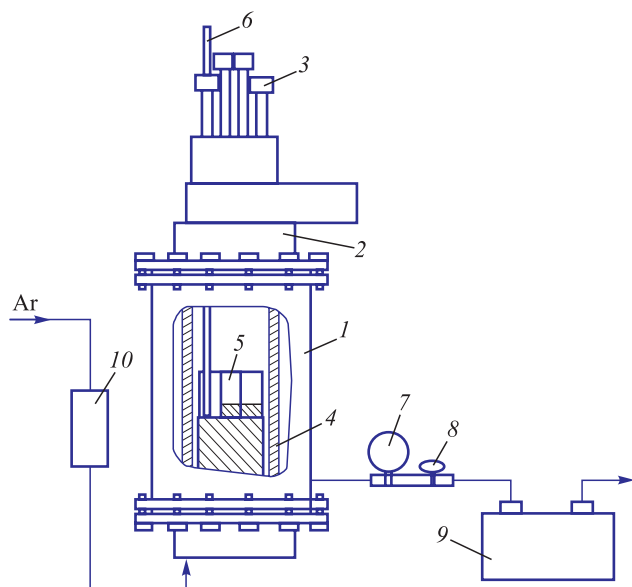


Fig. 2. Scheme of vacuum resistance furnace:

1 – furnace body; 2 – furnace lid; 3 – observation hole;  
4 – graphite heater; 5 – working alumina crucibles; 6 – BP 5/20  
thermocouple; 7 – monometer; 8 – vacuum system valve;  
9 – vacuum pump; 10 – rotameter

Рис. 2. Схема вакуумной печи сопротивления:

1 – корпус печи; 2 – крышка печи; 3 – смотровое окно;  
4 – графитовый нагреватель; 5 – рабочие алундовые тигли;  
6 – термопара BP 5/20; 7 – манометр; 8 – вентиль вакуумной системы; 9 – вакуумный насос; 10 – ротаметр

bon (determined using a Leco CS 600 instrument by high temperature extraction in a carrier gas) in the EAF dust after heating in vacuum resistance furnace in argon flow are summarized in Table 7. The extraction rate of elements as a function of processing temperature of EAF dust in the vacuum resistance furnace is illustrated in Fig. 4.

According to Fig. 4, heating the EAF dust with a constant rate at flowing argon resulted in a significant decrease in carbon, zinc, and lead content. The removal of lead and

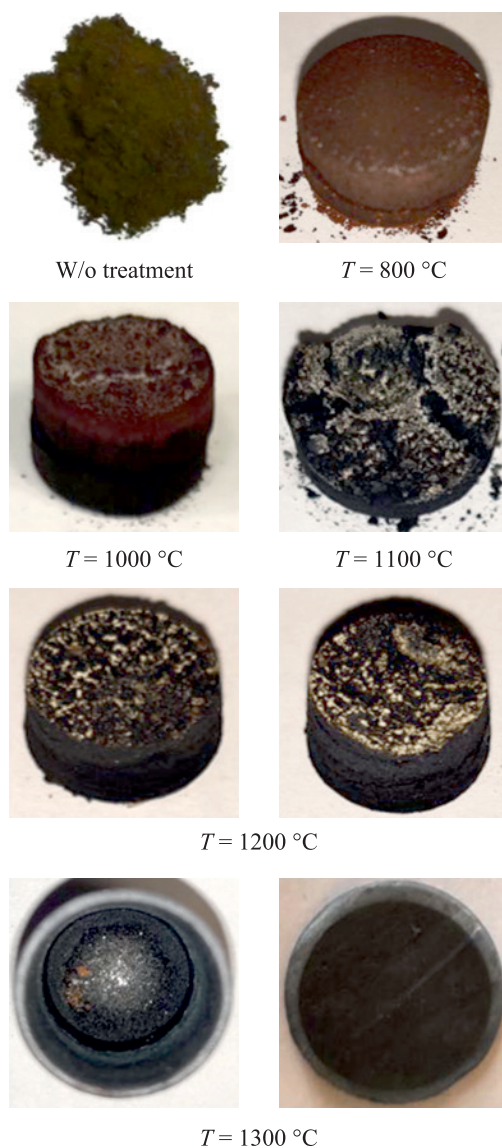


Fig. 3. Appearance of the samples before and after treatment in the vacuum resistance furnace

Рис. 3. Внешний вид образцов до и после обработки в вакуумной печи сопротивления

Table 6

**Actual EAF dust mass decrease after heating in the vacuum resistance furnace with flowing argon**

Таблица 6. Фактическая убыль массы навески пыли ДСП после нагрева в вакуумной печи сопротивления в токе аргона

Holding temperature, °C	Actual mass decrease, rel. %
800	2.32
1000	3.64
1100	4.28
1200	10.04*
1300	21.49*

\* Averaged by two samples.

zinc from the sample occurred in the temperature range of 800 – 1200 °C, with a higher extraction rate observed for lead. The intensive removal of lead occurred at temperatures above 1000 °C, while the intensive removal of zinc started at the temperatures above 1100 °C. To further investigate the possibility of selectively removing lead and zinc from EAF dust, their behavior in the temperature range of 800 – 1200 °C needs to be studied under isothermal conditions using the Tamman furnace, allowing for similar experiments to be conducted.

#### EXPERIMENTS IN A TAMMAN FURNACE

EAF dust from bag filters of the gas scrubbing system was subjected to processing in a Tamman furnace with a graphite heater ( $D = 80$  mm,  $L = 400$  mm) in the tem-



Table 7

**Lead, zinc and carbon content in EAF dust before and after heating in the vacuum resistance furnace with flowing argon**

**Таблица 7. Содержание свинца, цинка и углерода в пыли ДСП до и после нагрева в вакуумной печи сопротивления в токе аргона**

Element	Initial composition	Content of elements (wt. %) at the temperature of treatment, °C						
		800	1000	1100	1200		1300	
C	1.74	1.29	0.92	0.40	0.06	0.06	n.a.	n.a.
Zn	14.50	14.70	14.80	14.70	9.40	9.70	7.90	8.40
Pb	1.00	1.00	0.70	0.60	0	0	0	0

Remark: n.a. – not available.

perature range of 800 – 1200 °C, with holding time: 3, 6, 9, 12 min. The furnace specifications are as follows:  $P = 40$  kW;  $f = 50$  Hz. The flowing argon rate (high purity) was set to 1 l/min. The furnace is equipped with a water cooling system.

A total of 3 g of EAF dust was placed in a thin-walled alund crucible ( $D = 19$  mm,  $d = 18$  mm,  $H = 40$  mm,  $h = 38.5$  mm), with a layer height of 1.25 – 1.50 cm.

Once the preset temperature in the furnace chamber was reached (800, 900, 1000, 1100, 1200 °C), four samples arranged in a cartridge were simultaneously placed into the furnace. The time of sample placement into the furnace was considered as the starting time of the experiment. The samples at each temperature were held for 3, 6, 9, 12 min.

As the furnace temperature and holding time increased, the color of samples varies from brown, dark brown and dark grey to black, which is likely attributed to the partial reduction of magnetite. The samples held at 800, 900, 1000 and 1100 °C (for no longer than for three minutes) retained their shapes but crumbled under light pressure. The samples held at 1100 °C for three minutes,

upon extraction from the crucible, retained their shape under pressure, but could be easily milled in a mortar. The samples held at 1200 °C required considerable force to be milled in a mortar. Meanwhile, the samples held at 1200 °C for more than 6 min were difficult to extract from the crucible.

After cooling in ambient air, the samples were weighed, and their chemical composition was analyzed by the aforementioned methods. The actual weight loss of the samples after heating in the amman furnace with flowing argon is presented in Table 8, with a significantly higher weight loss observed at 1200 °C.

The contents of lead, zinc (determined using a MAX-GVM wave-dispersion  $X$ -ray fluorescent spectroscan), and carbon (determined using a Leco CS 600 instrument by high temperature extraction in a carrier gas) in the EAF dust after heating in the Tamman furnace with flowing argon are summarized in Table 9.

The extraction rates of carbon, zinc, and lead from EAF dust as a function of holding time during heating in the Tamman furnace (800 – 200 °C) with flowing argon are illustrated in Figs. 5 – 7.

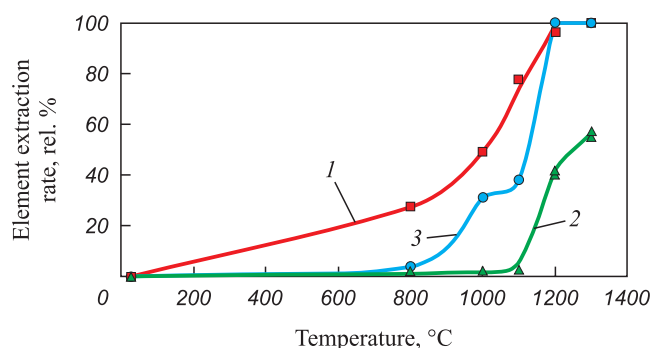


Fig. 4. Dependence of the element extraction rate on the temperature of EAF dust treatment in vacuum resistance furnace:  
1 – C; 2 – Zn; 3 – Pb

Рис. 4. Зависимость степени извлечения элемента от температуры обработки пыли ДСП в вакуумной печи сопротивления:  
1 – C; 2 – Zn; 3 – Pb

Table 8

**Actual EAF dust mass decrease after heating and holding in the Tamman furnace with flowing argon**

**Таблица 8. Фактическая убыль массы навески пыли ДСП после нагрева и выдержки в печи Таммана в токе аргона**

Holding temperature of samples, °C	Actual mass decrease, rel. %, at holding time, min			
	3	6	9	12
800	0.67	1.67	2.67	4.00
900	1.00	2.33	3.33	4.33
1000	1.67	2.67	4.00	5.33
1100	2.33	3.67	5.67	6.67
1200	8.67	10.33	12.33	14.00

According to Figs. 5 – 7, during the isothermal heating of EAF dust in an inert environment, the concentrations of lead, zinc and carbon underwent changes.

Complete transition of lead into the gas phase during the experiments was achieved at 1100 °C (holding time: 12 min) and at 1200 °C (holding time: 6 min and higher). However, at 900 and 1000 °C, increasing the holding time from 9 to 12 min did not result in an increased extraction rate of lead when carbon was present in the samples. This suggests that there may be a combined process involving multiple reactions of  $Pb_2O_3$  reduction within the temperature range of 800 – 1200 °C.

Simultaneously with the transition of lead into the gas phase, there was an extraction of zinc, amounting of 14.4 % (relative) ( $t = 1100$  °C, holding time: 12 min) and 32.2 % (relative) ( $t = 1200$  °C, holding time: 6 min and longer), respectively. This indicates a failure to achieve selective

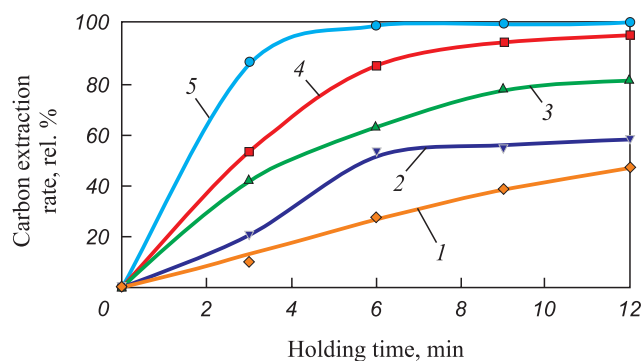


Fig. 5. Dependence of the extraction rate of carbon from EAF dust on the holding time during heating in the Tamman furnace with flowing argon at, °C: 1 – 800; 2 – 900; 3 – 1000; 4 – 1100; 5 – 1200

Рис. 5. Зависимость степени извлечения углерода из пыли ДСП от времени выдержки при нагреве в печи Таммана в токе аргона, °C: 1 – 800; 2 – 900; 3 – 1000; 4 – 1100; 5 – 1200

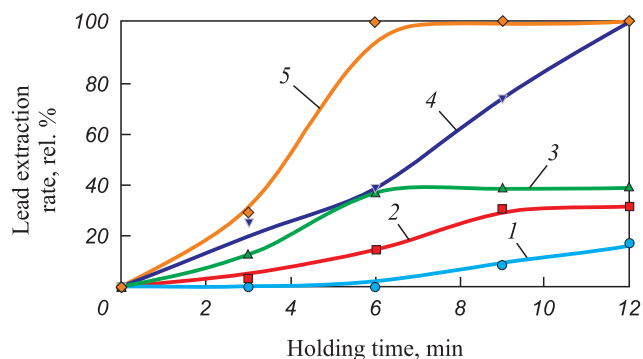


Fig. 6. Dependence of the extraction rate of lead from EAF dust on the holding time during heating in the Tamman furnace with flowing argon at, °C: 1 – 800; 2 – 900; 3 – 1000; 4 – 1100; 5 – 1200

Рис. 6. Зависимость степени извлечения свинца из пыли ДСП от времени выдержки при нагреве в печи Таммана в токе аргона, °C: 1 – 800; 2 – 900; 3 – 1000; 4 – 1100; 5 – 1200

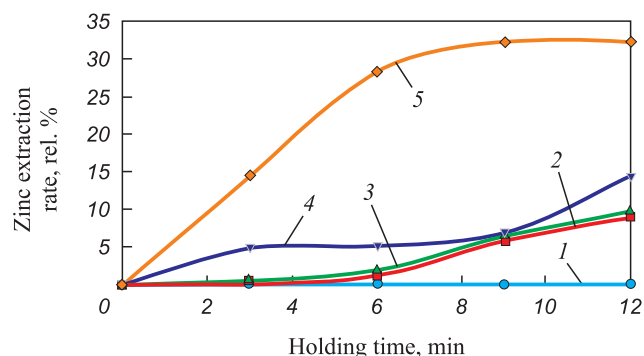


Fig. 7. Dependence of the extraction rate of zinc from EAF dust on the holding time during heating in the Tamman furnace with flowing argon at, °C:

1 – 800; 2 – 900; 3 – 1000; 4 – 1100; 5 – 1200

Рис. 7. Зависимость степени извлечения цинка из пыли ДСП от времени выдержки при нагреве в печи Таммана в токе аргона, °C: 1 – 800; 2 – 900; 3 – 1000; 4 – 1100; 5 – 1200

extraction of lead during the heating of EAF dust under the experimental conditions. Further heating of the EAF dust would likely lead to selective extraction of zinc, as it appears that lead was completely removed from the EAF dust during the experiment. It is possible to achieve higher selectivity in the extraction of zinc and lead by adjusting the process temperatures for specific dust compositions. At 1200 °C, the extraction rate of zinc reaches a plateau, while the carbon content in the EAF dust decreases to zero. This suggests that the reduction reactions of zinc-containing phases ceased due to an insufficient amount of reducing agent.

Comparison of the experimental data with the results of thermodynamical simulation in HSC Chemistry 6 software confirmed that the transition of lead-containing phases of EAF dust into the gas state can occur according to reactions 1 – 6 (see Table 1). Furthermore, the transition of zinc-containing phases of EAF dust into the gas state most likely occurs through reactions 7 – 8 (see Table 2) and 12 – 14 (see Table 3).

The carbon content present in the EAF dust was not sufficient for the complete recovery of zinc from its compounds, particularly due to the presence of manganese and iron in the complex spinel composition  $(Zn, Mn, Fe)_3O_4$ . In order to achieve the full recovery of zinc-containing phases in the dust sample, the addition of a reducing agent in the form of carbon or CO is required. Since an additional reducing agent is needed after the recovery of the lead-containing phase, the most effective approach appears to be the intensification of zinc recovery from the electric arc furnace dust by CO purging. Increasing the flow rate of the reducing agent allows for a reduction in the recovery temperature of zinc [21]. For example, increasing the CO concentration from 75 to 85 % at 1200 °C results in four-five times increase in the intensity of zinc removal to the gas phase [13].

Table 9

**Lead, zinc and carbon content change in EAF dust after heating and holding in the Tamman furnace with flowing argon**

**Таблица 9. Изменение содержания свинца, цинка и углерода в пыли ДСП после нагрева и выдержки в печи Таммана в токе аргона**

Element	Temperature of treatment, °C	Initial composition, wt. %	Chemical composition of dust, wt. % at holding time, min			
			3	6	9	12
C	800	1.74	1.59	1.31	1.13	1.00
Zn		14.50	14.60	14.70	14.90	15.00
Pb		1.00	1.00	1.00	0.90	0.90
C	900	1.74	1.41	0.87	0.86	0.81
Zn		14.50	14.60	14.70	14.20	13.80
Pb		1.00	1.00	0.90	0.70	0.70
C	1000	1.74	1.06	0.71	0.47	0.41
Zn		14.50	14.70	14.60	14.10	13.80
Pb		1.00	0.90	0.60	0.60	0.60
C	1100	1.74	0.88	0.30	0.15	0.10
Zn		14.50	14.10	14.30	14.30	13.30
Pb		1.00	0.70	0.60	0.30	0
C	1200	1.74	0.29	0.04	0.02	0.01
Zn		14.50	13.60	11.60	11.20	11.40
Pb		1.00	0.80	0	0	0

Researchers [22] have conducted studies on the recovery of zinc and iron from EAF dust using carbon monoxide as a reducing agent at various temperatures within the pyrometallurgical process. The optimal working temperature was found to be 950 °C. However, they also observed the negative influence of other impurities such as alkali-metal chlorides (NaCl, KCl) and lead compounds. The impact of these impurities can be mitigated by implementing a selective extraction process for lead and zinc from the EAF dust.

## CONCLUSIONS

Thermodynamic simulation was performed to investigate the selective extraction of zinc and lead from EAF dust. Two methods were determined to achieve selective extraction (the temperatures are given without accounting for addition of an inert gas into the system):

- consecutive recovery of lead-containing (295 – 877 °C) and zinc-containing (794 – 1326 °C) phases using carbon or carbon monoxide;
- recovery of lead-containing phases (295 – 877 °C) using carbon or carbon monoxide, followed by thermal dissociation of zinc-containing phases (1970 °C).

Experimental studies conducted in the vacuum resistance furnace with linear heating revealed that the removal of lead and zinc occurred within the temperature range

of 800 – 1200 °C. The rate of lead removal was higher, with intensive removal observed at temperature above 1000 °C, while zinc removal was more pronounced at temperature above 1200 °C.

Additional corrective isothermal experiments carried out in the Tamman furnace showed that complete transfer of lead into the gas phase was achieved at 1100 °C (holding time: 12 min) and at 1200 °C (holding time: 6 min and longer). However, during this transition, the extraction of lead was only 14.4 and 32.2 rel. %, respectively, indicating a failure to achieve selective lead extraction during the heating of EAF dust in the experiments. It is expected that further heating of the EAF dust would lead to selective zinc extraction, as the lead has been completely removed.

A comparison between the experimental data and the results of thermodynamic simulation allowed the identification of the most probable reactions involved in the recovery of lead and zinc containing phases.

## REFERENCES / СПИСОК ЛИТЕРАТУРЫ

1. Patrushov A.E. Technical and economic efficiency evaluation of pyrometallurgical technology for processing dust from electric steel production. *iPolytech Journal*. 2020;24(3): 672–683. (In Russ.).  
<https://doi.org/10.21285/1814-3520-2020-3-672-683>

- Патрушов А.Е. Оценка технико-экономической эффективности пирометаллургической технологии переработки пылей электросталеплавильного производства. *Вестник Иркутского государственного технического университета*. 2020;24(3):672–683.  
<http://dx.doi.org/10.21285/1814-3520-2020-3-672-683>
2. Tyushnyakov S.N., Selivanov E.N., Pankratov A.A. Forms of zinc found in electric steel smelting furnace gas cleaning dust. *Metallurgist*. 2018;62(5-6):485–492.  
<https://doi.org/10.1007/s11015-018-0685-z>  
Тюшняков С.Н., Селиванов Е.Н., Панкратов А.А. Формы нахождения цинка в пыли газоочистки электросталеплавильных печей. *Металлург*. 2018;(6):8–13.
  3. Da Silva Machado J.G.M., Brehm F.A., Moraes C.A.M., dos Santos C.A., Vilela A.C.F. Characterization study of electric arc furnace dust phases. *Materials Research*. 2006;9(1):30–36.  
<https://doi.org/10.1590/S1516-14392006000100009>
  4. Ahmad S., Sajal W.R., Gulshan F., Hasan M., Rhamdhani M.A. Thermodynamic analysis of caustic-roasting of electric arc furnace dust. *Heliyon*. 2022;8(10):e11031.  
<https://doi.org/10.1016/j.heliyon.2022.e11031>
  5. Omran M., Fabritius T. Effect of steelmaking dust characteristics on suitable recycling process determining: Ferrochrome converter (CRC) and electric arc furnace (EAF) dusts. *Powder Technology*. 2017;308:47–60.  
<http://dx.doi.org/10.1016/j.powtec.2016.11.049>
  6. Halli P., Agarwal V., Partinen J., Lundström M. Recovery of Pb and Zn from a citrate leach liquor of a roasted EAF dust using precipitation and solvent extraction. *Separation and Purification Technology*. 2020;236:116264.  
<https://doi.org/10.1016/j.seppur.2019.116264>
  7. Leclerc N., Meux E., Lecuire J.-M. Hydrometallurgical recovery of zinc and lead from electric arc furnace dust using mononitritotriacetate anion and hexahydrated ferric chloride. *Journal of Hazardous Materials*. 2001;91(1-3):257–270.  
[https://doi.org/10.1016/S0304-3894\(01\)00394-6](https://doi.org/10.1016/S0304-3894(01)00394-6)
  8. Antuñano N., Cambra J.F., Arias P.L. Hydrometallurgical processes for Waelz oxide valorisation – An overview. *Process Safety and Environmental Protection*. 2019;129:308–320.  
<https://doi.org/10.1016/j.psep.2019.06.028>
  9. Al-Harashsheh M., Altarawneh S., Al-Omari M. Selective dissolution of zinc and lead from electric arc furnace dust via oxidative thermolysis with polyvinyl chloride and water-leaching process. *Hydrometallurgy*. 2022;212:105898.  
<https://doi.org/10.1016/j.hydromet.2022.105898>
  10. Razinkova O.A. Sources of environmental pollution in hydrometallurgical production and ways of their use. *Nauchnyi potentsial regionov na sluzhbu modernizatsii*. 2013;(1):25–29. (In Russ.).  
Разинкова О.А. Источники загрязнения окружающей среды в гидрометаллургическом производстве и пути их использования. *Научный потенциал регионов на службу модернизации*. 2013;(1):25–29.
  11. Wang L., Peng Z., Lin X., Ye Q., Ye L., Zhang J., Liu Y., Liu M., Rao M., Li G., Jiang T. Microwave-intensified treatment of low-zinc EAF dust: A route toward high-grade metallized product with a focus on multiple elements. *Powder Technology*. 2021;383:509–521.  
<https://doi.org/10.1016/j.powtec.2021.01.047>
  12. Adedoyin F.F., Gumedé M.I., Bekum F.V., Etokakpan M.U., Balsalobre-Lorente D. Modelling coal rent, economic growth and CO<sub>2</sub> emissions: Does regulatory quality matter in BRICS economies? *Science of the Total Environment*. 2020;710:136284.  
<https://doi.org/10.1016/j.scitotenv.2019.136284>
  13. Marchenko N.V., Vershinina E.P., Gil'debrandt E.M. *Metalurgy of Heavy Non-Ferrous Metals*. Available at URL: <https://c-metal.ru/image/catalog/books/Marchenko.pdf> (Accessed 11.05.2023). (In Russ.).  
Марченко Н.В., Вершинина Е.П., Гильдебрандт Э.М. *Металлургия тяжелых цветных металлов: Электронное учебное пособие* [Электронный ресурс]. Красноярск: ИПК СФУ, 2009. URL: <https://c-metal.ru/image/catalog/books/Marchenko.pdf> (дата обращения 11.05.2023).
  14. Simonyan L.M., Demidova N.V. Selective extraction of carbon-free zinc and lead from EAF-dust. *Izvestiya. Ferrous Metallurgy*. 2020;63(8):631–638. (In Russ.).  
<https://doi.org/10.17073/0368-0797-2020-8-631-638>  
Симонян Л.М., Демидова Н.В. Исследование процесса безуглеродного селективного извлечения цинка и свинца из пыли ДСП. *Известия вузов. Черная металлургия*. 2020;63(8):631–638.  
<https://doi.org/10.17073/0368-0797-2020-8-631-638>
  15. Grudinsky P.I., Dyubonov V.G., Kozlov P.A. Distillation separation of the copper-smelting dusts with primary recovery of lead. *Russian Metallurgy (Metally)*. 2018;2018(1):7–13.  
<https://doi.org/10.1134/S003602951801007X>  
Грудинский П.И., Дюбанов В.Г., Козлов П.А. Исследование процессов дистилляционного разделения пыли плавки меди с первичным извлечением свинца. *Металлы*. 2018;(1):9–16.
  16. Jabbour K., El Hassan N. Optimized conditions for reduction of iron (III) oxide into metallic form under hydrogen atmosphere: A thermodynamic approach. *Chemical Engineering Science*. 2022;252:117297.  
<https://doi.org/10.1016/j.ces.2021.117297>
  17. Kleonovskii M.V., Sheshukov O.Yu., Mikheenkova M.A., Lozovaya E.Yu. Thermodynamic modeling of zinc recovery from ferrous metallurgy sludge. *Izvestiya. Ferrous Metallurgy*. 2022;65(3):170–178. (In Russ.).  
<https://doi.org/10.17073/0368-0797-2022-3-170-178>  
Клеоновский М.В., Шешуков О.Ю., Михеенков М.А., Лозовая Е.Ю. Термодинамическое моделирование восстановления цинка из шламов черной металлургии. *Известия вузов. Черная металлургия*. 2022;65(3):170–178.  
<https://doi.org/10.17073/0368-0797-2022-3-170-178>
  18. Omran M., Fabritius T. Utilization of blast furnace sludge for the removal of zinc from steelmaking dusts using microwave heating. *Separation and Purification Technology*. 2019;210:867–884.  
<https://doi.org/10.1016/j.seppur.2018.09.010>
  19. Li C., Liu W., Jiao F., Yang C., Li G., Liu S., Qin W. Separation and recovery of zinc, lead and iron from electric arc furnace dust by low temperature smelting. *Separation and Purification Technology*. 2023;312:123355.  
<https://doi.org/10.1016/j.seppur.2023.123355>
  20. Trusov B.G. TERRA software system for modeling phase and chemical equilibria. In: *Abstracts of the XIV Int. Conf. on Chemical Thermodynamics*. St. Petersburg: NII Khimii SpbSU; 2002:483. (In Russ.).



Трусов Б.Г. Программная система TERRA для моделирования фазовых и химических равновесий. *Тезисы докладов XIV Международной конференции по химической термодинамике*. СПб: НИИ Химии СПбГУ; 2002:483.

21. Vusikhis A.S., Selivanov E.N., Leont'ev L.I., Tyushnyakov S.N. Thermodynamic simulation of metal reduction from  $B_2O_3$ –CaO–FeO–ZnO melts by hydrogen and carbon monoxide. *Russian Metallurgy (Metally)*. 2022;2022(5): 475–480. <https://doi.org/10.1134/S0036029522050111>

Вусихис А.С., Селиванов Е.Н., Леонтьев Л.И., Тюшняков С.Н. Термодинамическое моделирование процессов восстановления металлов из расплавов  $B_2O_3$ –CaO–FeO–ZnO. *Металлы*. 2022;(3):17–23.

22. Wu C.-C., Chang F.-C., Chen W.-S., Tsay M.-S., Wang Y.-N. Reduction behavior of zinc ferrite in EAF-dust recycling with CO gas as a reducing agent. *Journal of Environmental Management*. 2014;143:208–213. <https://doi.org/10.1016/j.jenvman.2014.04.005>

## Information about the Authors

## Сведения об авторах

**Nadezhda V. Podusovskaya**, Junior Researcher of the Laboratory of Materials Diagnostics, Baikov Institute of Metallurgy and Materials Science, Russian Academy of Sciences; Postgraduate of the Chair of Metallurgy of Steel, New Production Technologies and Metal Protection, National University of Science and Technology "MISIS"

ORCID: 0000-0002-4124-0444

E-mail: ndemidova\_n@mail.ru

**Ol'ga A. Komolova**, Cand. Sci. (Eng.), Senior Researcher of the Laboratory of Materials Diagnostics, Baikov Institute of Metallurgy and Materials Science, Russian Academy of Sciences; Assist. Prof. of the Chair of Metallurgy of Steel, New Production Technologies and Metal Protection, National University of Science and Technology "MISIS"

ORCID: 0000-0001-9517-8263

E-mail: o.a.komolova@gmail.com

**Konstantin V. Grigorovich**, Academician, Dr. Sci. (Eng.), Head of the Laboratory of Materials Diagnostics, Baikov Institute of Metallurgy and Materials Science, Russian Academy of Sciences; Prof. of the Chair of Metallurgy of Steel, New Production Technologies and Metal Protection, National University of Science and Technology "MISIS"

ORCID: 0000-0002-5669-4262

E-mail: grigorov@imet.ac.ru

**Aleksandr V. Pavlov**, Dr. Sci. (Eng.), Prof. of the Chair of Metallurgy of Steel, New Production Technologies and Metal Protection, National University of Science and Technology "MISIS"

ORCID: 0000-0003-3773-9469

E-mail: pav-gnts@isis.ru

**Viktoriya V. Aksenova**, Postgraduate of the Chair of Metallurgy of Steel, New Production Technologies and Metal Protection, National University of Science and Technology "MISIS"

E-mail: axenovaviki@gmail.com

**Boris A. Rumyantsev**, Cand. Sci. (Eng.), Research Associate of the Laboratory of Materials Diagnostics, Baikov Institute of Metallurgy and Materials Science, Russian Academy of Sciences

ORCID: 0000-0001-8250-3565

E-mail: brumyantsev@imet.ac.ru

**Mark V. Zheleznyi**, Junior Researcher of the Laboratory of Materials Diagnostics, Baikov Institute of Metallurgy and Materials Science, Russian Academy of Sciences; Assistant of the Chair of Physical Materials, National University of Science and Technology "MISIS"

ORCID: 0000-0003-3821-6790

E-mail: markiron@mail.ru

**Надежда Владимировна Подусовская**, младший научный сотрудник лаборатории диагностики материалов, Институт металлургии и материаловедения им. А.А. Байкова РАН; аспирант кафедры металлургии стали, новых производственных технологий и защиты металлов, Национальный исследовательский технологический университет «МИСИС»

ORCID: 0000-0002-4124-0444

E-mail: ndemidova\_n@mail.ru

**Ольга Александровна Комолова**, к.т.н., старший научный сотрудник лаборатории диагностики материалов, Институт металлургии и материаловедения им. А.А. Байкова РАН; доцент кафедры металлургии стали, новых производственных технологий и защиты металлов, Национальный исследовательский технологический университет «МИСИС»

ORCID: 0000-0001-9517-8263

E-mail: o.a.komolova@gmail.com

**Константин Всеволодович Григорович**, академик РАН, д.т.н., заведующий лабораторией диагностики материалов, Институт металлургии и материаловедения им. А.А. Байкова РАН; профессор кафедры металлургии стали, новых производственных технологий и защиты металлов, Национальный исследовательский технологический университет «МИСИС»

ORCID: 0000-0002-5669-4262

E-mail: grigorov@imet.ac.ru

**Александр Васильевич Павлов**, д.т.н., профессор кафедры металлургии стали, новых производственных технологий и защиты металлов, Национальный исследовательский технологический университет «МИСИС»

ORCID: 0000-0003-3773-9469

E-mail: pav-gnts@isis.ru

**Виктория Владимировна Аксенова**, аспирант кафедры металлургии стали, новых производственных технологий и защиты металлов, Национальный исследовательский технологический университет «МИСИС»

E-mail: axenovaviki@gmail.com

**Борис Алексеевич Румянцев**, к.т.н., научный сотрудник лаборатории диагностики материалов, Институт металлургии и материаловедения им. А.А. Байкова РАН

ORCID: 0000-0001-8250-3565

E-mail: brumyantsev@imet.ac.ru

**Марк Владимирович Железный**, младший научный сотрудник лаборатории диагностики материалов, Институт металлургии и материаловедения им. А.А. Байкова РАН; ассистент кафедры физического материаловедения, Национальный исследовательский технологический университет «МИСИС»

ORCID: 0000-0003-3821-6790

E-mail: markiron@mail.ru

## Contribution of the Authors

## Вклад авторов

**N. V. Podusovskaya** – conducting thermodynamic calculations, planning and conducting experiments, processing of the obtained experimental data, writing the text.

**O. A. Komolova** – setting the research goal, experiments planning, discussion of the results and conclusions.

**K. V. Grigorovich** – setting the research goal, formation of the article main concept, discussion of the results and conclusions.

**A. V. Pavlov** – planning and organization of experiments.

**V. V. Aksenova** – samples chemical composition determination by wave-dispersive X-ray fluorescence spectroscopy (MAX-GVM).

**B. A. Rumyantsev** – determination of S and C content by high-temperature extraction in a carrier gas (Leco CS 600).

**M. V. Zheleznyi** – X-ray diffraction analysis (XRD) of initial dust composition.

**Н. В. Подусовская** – проведение термодинамических расчетов, планирование и проведение экспериментов, обработка полученных экспериментальных данных, подготовка текста статьи.

**О. А. Комолова** – определение цели работы, планирование экспериментов, обсуждение результатов и выводов.

**К. В. Григорович** – определение цели работы и общей концепции статьи, обсуждение результатов и выводов.

**А. В. Павлов** – планирование и организация экспериментов.

**В. В. Аксенова** – определение химического состава образцов методом волно-дисперсионной рентгенофлуоресцентной спектроскопии (МАКС-GVM).

**Б. А. Румянцев** – определение содержания в образцах серы и углерода методом высокотемпературной экстракции в несущем газе (Leco CS 600).

**М. В. Железный** – проведение рентгенодифракционного анализа (XRD) исходного состава пыли.

Received 03.05.2023

Revised 05.05.2023

Accepted 05.05.2023

Поступила в редакцию 03.05.2023

После доработки 05.05.2023

Принята к публикации 05.05.2023



UDC 669.15-194.2:620.186

DOI 10.17073/0368-0797-2023-3-356-366



Original article

Оригинальная статья

## STRUCTURE AND PROPERTIES OF STEELS FOR MANUFACTURE OF CORE CATCHER VESSEL OF NUCLEAR REACTOR

S. A. Nikulin<sup>1</sup>, S. O. Rogachev<sup>1,2</sup>, V. A. Belov<sup>1</sup>, N. V. Shplis<sup>1</sup>,  
A. A. Komissarov<sup>1</sup>, V. Yu. Turilina<sup>1</sup>, Yu. A. Nikolaev<sup>3</sup>

<sup>1</sup> National University of Science and Technology “MISIS” (4 Leninskii Ave., Moscow 119049, Russian Federation)

<sup>2</sup> Baikov Institute of Metallurgy and Materials Science, Russian Academy of Sciences (49 Leninskii Ave., Moscow 119991, Russian Federation)

<sup>3</sup> National Research Center “Kurchatov Institute” (1 Akademika Kurchatova Sqr., Moscow 123182, Russian Federation)

✉ csaap@mail.ru

**Abstract.** The Russian new nuclear reactors are provided with a special core catcher vessel device (cc-vessel) designed to minimize the consequences of a severe beyond design basis accident at a nuclear power plant, when the reactor pressure vessel collapses and the core melts. For manufacture of the cc-vessel structural elements, low-carbon unalloyed or low-alloyed steels are used. When a severe beyond design basis accident develops, the cc-vessel's body is subjected to extreme temperature and force loads, which can lead to degradation of the structure, loss of strength and failure of the entire cc-vessel. To calculate the strength characteristics of the cc-vessel, which ensure its safe and reliable operation, the detailed data are required on the structure and mechanical properties of low-carbon steels at high temperatures and after extreme thermal actions simulating the development of a severe beyond design basis accident. The paper analyzes data on the structure and mechanical properties (tensile strength, crack resistance, toughness and cyclic strength) of a number of low-carbon steels under extreme temperature and force actions, including conditions simulating the development of a severe beyond design basis accident at a nuclear power plant, in order to select the material for the design of cc-vessel of nuclear reactor. New data on the structure, mechanical properties, and thermal diffusivity in a wide temperature range of a Cr–Mo steel (Russian Standard – 15KhM) as a candidate structural material for the manufacture of the cc-vessel body are presented. The low content of manganese and alloying with molybdenum and vanadium in 15KhM steel provides a finer grained structure and eliminates the steel's tendency to temper brittleness.

**Keywords:** low carbon steel, core catcher vessel, strength, impact strength, thermal diffusivity, microstructure, austenite, high temperature exposure

**Acknowledgements:** The structure was studied using the equipment of the Center for Collective Use “Materials Science and Metallurgy” with the financial support of the Ministry of Science and Higher Education of the Russian Federation (agreement No. 075-15-2021-696). The authors express their gratitude to engineer A.A. Tokar', postgraduate D.V. Ten and master student F.A. Salenkov for their help in sample preparation and testing.

**For citation:** Nikulin S.A., Rogachev S.O., Belov V.A., Shplis N.V., Komissarov A.A., Turilina V.Yu., Nikolaev Yu.A. Structure and properties of steels for manufacture of core catcher vessel of nuclear reactor. *Izvestiya. Ferrous Metallurgy*. 2023;66(3):356–366.  
<https://doi.org/10.17073/0368-0797-2023-3-356-366>

## СТРУКТУРА И СВОЙСТВА СТАЛЕЙ ДЛЯ КОНСТРУКЦИИ УСТРОЙСТВА ЛОКАЛИЗАЦИИ РАСПЛАВА АТОМНЫХ РЕАКТОРОВ

С. А. Никулин<sup>1</sup>, С. О. Рогачев<sup>1,2</sup>, В. А. Белов<sup>1</sup>, Н. В. Шплис<sup>1</sup>,  
А. А. Комиссаров<sup>1</sup>, В. Ю. Турилина<sup>1</sup>, Ю. А. Николаев<sup>3</sup>

<sup>1</sup> Национальный исследовательский технологический университет «МИСИС» (Россия, 119049, Москва, Ленинский пр., 4)

<sup>2</sup> Институт металлургии и материаловедения им. А.А. Байкова РАН (Россия, 119991, Москва, Ленинский пр., 49)

<sup>3</sup> НИЦ «Курчатовский институт» (Россия, 123182, Москва, пл. Академика Курчатова, 1)

✉ csaap@mail.ru

**Аннотация.** В российских атомных реакторах нового поколения предусмотрено специальное устройство локализации расплава (корнума), предназначенное для минимизации последствий тяжелой запроектной аварии на атомной электростанции с разрушением корпуса

реактора и расплавлением активной зоны. Для изготовления конструктивных элементов устройства локализации расплава используются низкоуглеродистые нелегированные и низколегированные стали. При развитии тяжелой запроектной аварии корпус устройства локализации расплава подвергается экстремальным температурно-силовым нагрузкам, что может привести к деградации структуры, потере прочности и разрушению всей конструкции. Для расчета характеристик прочности конструкции устройства локализации расплава, обеспечивающих его безопасную и надежную работу, необходимы детальные данные о структуре и механических свойствах низкоуглеродистых сталей при высоких температурах и после экстремальных термических воздействий, имитирующих условия развития тяжелой запроектной аварии. В статье анализируются данные по структуре и механическим свойствам (статическому растяжению, трещиностойкости, ударной вязкости и циклической прочности) ряда низкоуглеродистых сталей при экстремальных температурно-силовых воздействиях. В том числе рассматриваются условия, имитирующие развитие тяжелой запроектной аварии на атомной электростанции с целью определения материала для конструкции устройства локализации расплава атомных реакторов. Представлены новые данные по структуре, механическим свойствам и температуропроводности в широком диапазоне температур стали 15XM, как конструкционного материала для изготовления корпуса устройства локализации расплава. Пониженное содержание марганца, легирование молибденом и ванадием стали 15XM обеспечивают более мелкозернистую структуру и устраняют склонность стали к отпускной хрупкости.

**Ключевые слова:** низкоуглеродистая сталь, устройство локализации расплава, прочность, ударная вязкость, температуропроводность, микроструктура, аустенит, высокотемпературное воздействие

**Благодарности:** Исследование структуры выполнено с использованием оборудования ЦКП «Материаловедение и металлургия» при финансовой поддержке Министерства науки и высшего образования РФ (соглашение № 075-15-2021-696). Благодарим инженера А.А. Токаря, аспиранта Д.В. Тена и магистра Ф.А. Саленкова за помощь в подготовке образцов и проведении испытаний.

**Для цитирования:** Никулин С.А., Рогачев С.О., Белов В.А., Шплис Н.В., Комиссаров А.А., Турилина В.Ю., Николаев Ю.А. Структура и свойства сталей для конструкции устройства локализации расплава атомных реакторов. *Известия вузов. Черная металлургия*. 2023;66(3):357–366. <https://doi.org/10.17073/0368-0797-2023-3-356-366>

## INTRODUCTION

In order to minimize consequences of beyond the design accident (BDB) at NPS, involving destruction of reactor vessel, Russian new generation WWR reactors are equipped with special core catcher vessels (cc-vessel) [1; 2]. This device is a large structure with diameters up to 6 m and the height up to 12 m, and a vessel thickness of up to 60 mm. Low carbon non-alloy and low alloy steels are used for manufacture of cc-vessel structural elements [3]. At present only Russian NPS with new generation reactors are equipped with a cc-vessel. Their structural elements, vessel and support plate, are manufactured from 22K and 09G2S steels, respectively.

In the course of BDB, the cc-vessel is exposed simultaneously to long-term thermal impact, as well as high static and impact loads [4 – 6]. The temperature of corium entering cc-vessel during BDB exceeds several thousand degrees. According to calculations the cc-vessel during localization and cooling of molten corium is heated to 1200 °C. Corium cooling takes up to 10 – 12 months [7]. Long term thermal impact can significantly change the structural state and, as a consequence, induce degradation of the mechanical properties of the vessel material. This leads to strength loss and increase in destruction of cc-vessel [8; 9]. Calculations of the strength properties of the cc-vessel, providing for its safe and reliable operation, require for detailed data on the structure and mechanical properties of low carbon steels at high temperatures and after extreme thermal impacts. It is important to account for the possible heterogeneity of the structure and mechanical properties of the material [10]. For the reliable operation of the cc-vessel, it is also important to retain high impact strength and resistance against the low cycle

fatigue of vessel material after corium cooling, mostly for NPS in areas with higher seismic hazard.

The issue of selecting the optimum material for the manufacture of cc-vessel structural elements, capable of providing the required level of strength and impact strength under BDB conditions, has not been discussed. This is partially due to insufficient data on the mechanical properties and resistance against destruction of low carbon steels under extreme temperature and load conditions.

In the past decade, studies have been carried out aimed at detailed analysis of changes in structure and mechanical properties of low carbon steels under extreme temperature and load conditions, including those simulating BDB [11 – 22]. In particular, the changes in structural state were studied. The mechanical properties were established, and the mechanical behavior of 22K and 09G2S steels was analyzed at the temperatures from ambient to 1200 °C. Resistance against destruction before and after extreme impact peculiar for BDB [11; 12] was also analyzed. Embrittlement was studied upon temperature impacts in the range of temper brittleness of 22K and 09G2S steels under BDB conditions [14 – 16]. The influence of thermal impact on low cycle fatigue of 22K steel was determined [17]. The advantages and disadvantages of 22K and 09G2S steels are described for their use in the cc-vessel. It was demonstrated that 22K and 09G2S steels are characterized by the following disadvantages: a tendency to increase in austenite grain and decrease in strength at high temperatures due to relatively high manganese content; absence of carbide forming elements in the steels, as well as tendency to temper brittleness in certain temperature range and occurrence of brittle intergranular failure (for 22K steel). In order to eliminate the existing uncertainties in the cc-vessel



Table 1

Chemical composition of low-carbon steels, wt. %

Таблица 1. Химический состав низкоуглеродистых сталей, % (по массе)

Steel	Fe	C	Si	Mn	P	S	Cr	Mo	Ni	Al	Cu
22K [13]	basis	0.24	0.26	0.75	0.013	0.001	0.04	–	0.03	–	0.05
09G2S [12]	basis	0.13	0.58	1.54	0.014	0.003	0.04	–	0.04	0.04	0.09
SA533-B1 [29]	basis	0.21	0.22	1.28	<0.020	0.006	–	0.52	0.61	0.01	0.03

and to improve competitiveness of Russian NPS at global market new material for cc-vessels based on modification of the alloying system needs to be selected. Studies of its high temperature properties under BDB conditions also need to be carried out.

This work analyzes previously available and new data on the structure and mechanical properties of some low carbon steels under conditions simulating BDB at NPS, aimed at selecting optimum material of cc-vessel for nuclear reactors.

# STRUCTURE AND MECHANICAL PROPERTIES OF 22K, 09G2S AND SA533-B1 LOW CARBON STEELS UNDER CONDITIONS SIMULATING BEYOND THE DESIGN BASIS ACCIDENT

Low carbon steels, such as 22K and 09G2S (foreign analogs: 20Mn5 in Germany or AISI 1022 in USA and 13Mn6 in Germany, respectively) are usually applied as structural materials for items operating at moderate mechanical loads and temperatures not higher than 350 – 450 °C. This is related with a significant decrease in their strength properties (especially yield stress) upon heating to higher temperatures [23 – 25]. An important advantage of low carbon steels is their weldability and high thermal diffusivity [26 – 28]. Little research has been done on the high-temperature mechanical properties of such steels. Published results are as yet unavailable. As of the present moment, the behavior of low carbon steels under BDB conditions were not carried out. Only few foreign studies of high temperature properties are available (including creeping) of low carbon steel with the addition of molybdenum and nickel SA533-B1 [18; 19] to be used in cc-vessel [3]. Table 1 presents the chemical composition of SA533-B1 steel in comparison with 22K and 09G2S steels. The work [18] presents only ultimate strength of SA533-B1 steel as a function of temperature, determined in tensile tests (according to ASTM). According to this data, sharp drop of ultimate strength from 380 to 150 MPa occurs in the temperature range from 527 to 727 °C (Fig. 1). In addition, interest is attracted to data on thermal diffusivity

of SA533-B1 steel. The thermal diffusivity of SA533-B1 steel in the range from 77 to 907 °C decreases from 12.1 to 4.7 mm<sup>2</sup>/s, and with temperature increase to 1340 °C, it increases to 5.5 mm<sup>2</sup>/s [18].

Other experimental results of the high temperature mechanical properties of SA533-B1 steel were limited by analysis of the influence of strain rate (0.050 – 0.007 min<sup>-1</sup>) on the strength and plasticity in the temperature range from 650 to 1200 °C [18].

Numerous recent works devoted to studies of the behavior of low carbon steels under extreme temperature and load conditions have been carried out for 22K and 09G2S steels [11 – 17; 30]. Three modes of thermal impact simulating BDB conditions were used in these works [7].

Mode 1: heating to 1000 °C at the rate of 225 °C/h; cooling to 900 °C at the rate of 6 °C/h; cooling to 840 °C at the rate of 1 °C/h; holding at 840 °C in 39.2 h; cooling to 750 °C at the rate of 2 °C/h; cooling to 700 °C at the rate of 2 °C/h; cooling in furnace to ambient temperature.

Mode 2: heating to 650 °C at the rate of 200 °C/h; cooling to 480 °C at the rate of 1 °C/h; cooling in furnace to ambient temperature.

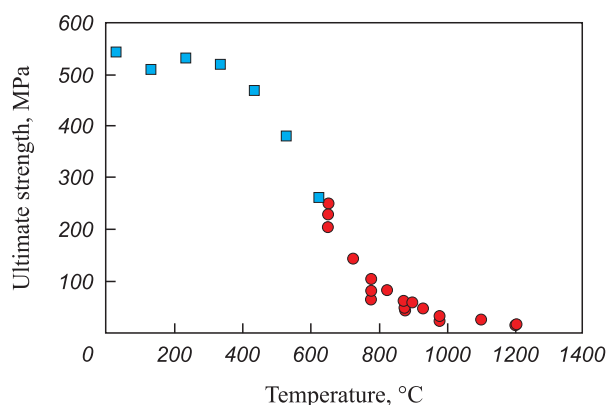


Fig. 1. Temperature dependence of tensile strength of SA533-B1 steel [18]:  
■ – literary data; ● – INL laboratory

Рис. 1. Температурная зависимость предела прочности стали SA533-B1 [18]:  
■ – литературные данные; ● – лаборатория INL

Mode 3: heating to 1200 °C at the rate of 225 °C/h; holding in 3.7 h; cooling in furnace to ambient temperature.

The following main procedures were applied by the authors to establish the mechanical properties of steels.

- Tensile tests in the temperature range from 23 to 1050 °C were pursuant to State standards GOST 1497–84 and GOST 9651–84 using a Zwick/Roell machine, and at 1200°C in the chamber of Gleeble 3800 testing machine. The temperature maintenance accuracy was  $\pm 5$  °C and  $\pm 1$  °C, respectively, and the deformation rate:  $0.004 \text{ s}^{-1}$ . The tests were performed in a vacuum. Three samples in each state were tested.

- Impact bending tests of samples with the size of  $10 \times 10 \times 55$  mm with *V*-notch were carried out at temperatures ranging from 200 to  $-50$  °C using an Instron SI-1M impact tester with maximum impact work of 300 J at the pendulum speed upon impact equaling to  $5 \pm 0.5$  m/s. The samples were heated to the test temperature in an electric furnace, and cooled in a LAUDA Proline RP890 climatic chamber. 18 samples were tested, in order to plot each serial curve.

- Static crack resistance tests of rectangular samples with notch were carried out at ambient temperature according to three-point bending using an Instron 5569 machine. The parameter of non-linear fracture mechanics was used as the property of crack resistance: critical *J*-integral (*JC*). This in the physical sense is the energy in the region of crack apex normalized per unit displacement of crack *dl*. The *J*-integral was determined using the experimental Begley–Landes method [31].

The strength properties of 22K (in normalized state) and 09G2S (after quenching and tempering) steels were determined in the range of test temperatures from 23 to 1200 °C [11; 12]. It was demonstrated that the most significant decrease of strength of 22K steel is observed in the range of 400 – 650 °C, and of 09G2S steel in the range of 600 – 750 °C. Upon a further decrease in the temperature, the unstrengthening rate decreases. At 1200 °C, the yield stress and ultimate strength of both steels are the same equaling to 12 and 21 – 22 MPa, respectively. The strain curves of 22K and 09G2S steels at the temperatures above 600 and 800 °C, respectively, have a wavelike nature. This can be attributed to strengthening–unstrengthening due to dynamic recrystallization. Thermal impact according to mode 1 decreases the yield stress of 22K steel by 7 – 22 % in the range of tests temperatures from 23 to 300 °C. This also increases the yield stress and ultimate strength by 12 – 50 and 10 – 32 %, respectively, in the temperature range from 400 to 700 °C. At higher temperatures, the effect of thermal impact on 22K steel is less pronounced in the form of moderate decrease in yield stress.

Metallographic studies have demonstrated that in both steels, 22K and 09G2S, in the case of a temperature dwell time above 1000 °C, intensive grain growth is observed. Grain size non-homogeneity becomes more pronounced. It was demonstrated that 09G2S steel is more prone to grain growth upon heating to such high temperature than 22K steel [11; 12].

22K steel in initial state is characterized by a high resistance against low cycle bending fatigue: limited fatigue endurance at lifetime of  $N = 3.5 \cdot 10^4$  cycles was 360 MPa [17]. Thermal impact according to modes 2 or 3 leads to insignificant decrease in the resistance to low cycle fatigue: limited fatigue endurance decreases by 9 %.

Static crack resistance tests demonstrated that in the initial state, the parameter *JC* equals to  $118 \pm 8 \text{ kJ/m}^2$ . Thermal impact according to modes 1 and 2 decreases *JC* by 23 and 30 %, respectively, in comparison with the initial state [30].

The highest negative influence of thermal impact is on impact strength of 22K steel [14; 15]. Consecutive thermal impact according to modes 1 and 2 leads to an increase in the temperature of viscous brittle transition by  $\sim 100$  °C (from 23 to 125 °C). The impact strength *KCV* decreases from 180 – 208 to 150 J/cm<sup>2</sup> already at the test temperature of 75 °C, and the fractures contain about 40 % of brittle constituent. On the contrary, for 09G2S steel even long-term overheating according to mode 3 exerts weak influence of impact strength [16]. Viscous brittle transition in 09G2S steel both in initial state and after heating occurs in the region of low temperatures ( $-40$  and  $-30$  °C, respectively) at an impact strength of 285 – 300 J/cm<sup>2</sup>, which is several times higher than for 22K steel.

## EXPERIMENTAL

Low carbon low alloyed 15KhM steel can be considered as an alternative to 22K and 09G2S steels. Alloying with carbide forming elements (Mo and V) and lower manganese content suppress the tendency of the steel to grain growth and temper brittleness.

10 kg ingots were exposed to hot rolling with a reduction rate of 25 % and subsequent air cooling from the rolling temperature. The chemical composition of steel determined by optical emission method is summarized in Table 2.

The modes of thermal impact simulating BDB conditions were the same as in [11 – 17; 30] (see previous section).

The tension tests were carried out according to previously described procedure [11; 12].

Table 2

RESULTS AND DISCUSSION

Chemical composition of 15KhM steel, wt. %

Таблица 2. Химический состав стали 15ХМ, % (по массе)

Fe	C	Si	Mn	P	S	Cr	Mo	Ni	Al
basis	0.14	0.41	0.61	0.01	0.01	0.64	0.50	0.01	0.01

The impact bending tests were carried out according to the procedure described in [14 – 16]. The macrogeometry of fractures after tests was determined according to [32].

The metallographic analysis was carried out using a NIM-100 microscope at magnifications of 100 – 500 $\times$ . In order to reveal grain structure, 5 % aqueous solution of nitric acid was used. In order to identify former austenitic grain, a warm solution of picric acid was used.

Thermal diffusivity was measured by laser flash using a NETZSCH LFA 457 MicroFlash (Germany). The instrument is equipped with IR sensor on the basis of InSb. The following instrument settings were used:

- laser voltage varied in the range of 1730 – 2114 V;
- threshold stability of basic line: 1.0 V/10 s.

The measurements are comprised of two stages:

– recording of the temperature increase of the rear side of a plane-parallel sample as a function of time after irradiation of its front side by short pulse of infrared laser radiation 1.064  $\mu\text{m}$  using a precision infrared sensor;

– calculation of thermal diffusivity using the selected mathematical model.

The measurements were carried out in argon 6.0, at a purge rate of 60 ml/min. The samples were coated with thin graphite layer («GRAPHITE 33» spray, Kontakt Chemie). The thermal diffusivity was calculated using mathematical model “Cape-Lehmann + pulse correction”. This model takes into account frontal and radial heat losses and is usually suitable for most materials.

In initial state, 15KhM had hypopearlitic structure with the recrystallization degree of about 85 % (Fig. 2). Predominant ferrite and pearlite grain size was 15 – 25  $\mu\text{m}$ . This is slightly lower than in 22K steel [17]. After thermal impact according to mode 1 the austenite grain grows by 55 %: from  $23.5 \pm 9.1 \mu\text{m}$  to  $36.5 \pm 14.9 \mu\text{m}$  (Fig. 3). The hypopearlitic structure is enlarged and grain size nonhomogeneity becomes more pronounced (Fig. 4). After thermal impact according to mode 2, the predominant grain size of hypopearlitic structure is the same, and the recrystallization degree increases to 99 % (Fig. 5).

The mechanical properties of 15KhM steel are summarized in Table 3, and the stress–strain curves in Fig. 6. In the temperature range of 700 – 900  $^{\circ}\text{C}$ , the yield stress  $\sigma_{0.2}$  in initial state changes in average from 161 to 37 MPa, and the ultimate strength  $\sigma_u$  from 180 to 70 MPa. Thermal impact according to mode 1 results in a decrease in the yield stress by 27 %, and the ultimate strength by 7 % at the test temperature of 700  $^{\circ}\text{C}$  without significant statistical influence on the strength at 900  $^{\circ}\text{C}$ . After the thermal impact according to mode 1, the yield stress and ultimate strength at 23  $^{\circ}\text{C}$  equaled in average 222 and 436 MPa, and at 1200  $^{\circ}\text{C}$ , 15 and 25 MPa, respectively.

Therefore, at 700  $^{\circ}\text{C}$  the strength of 15KhM steel in initial state is 2 – 4 times higher in comparison with 22K steel [13]. After thermal impact, the strength of 15KhM steel at all considered temperatures in the range from 23 to 1200  $^{\circ}\text{C}$  is higher when compared to 22K steel. In addition, at 700  $^{\circ}\text{C}$  the strength of 15KhM steel in initial state is by 1.5 times higher when compared to 09G2S steel and is comparable with that of SA533-B1 steel. At 900  $^{\circ}\text{C}$  the strength of 15KhM steel in initial state is comparable to that of SA533-B1 steel, and higher in comparison to 09G2S steel.

According to the results of impact bending test (Table 4, Fig. 7), in the fractures of steel in initial state,

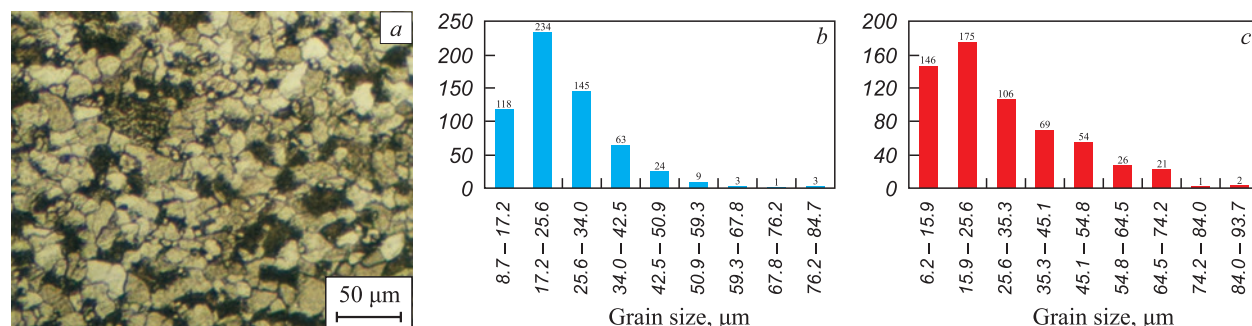


Fig. 2. Microstructure (a) and ferrite (b) and pearlite (c) grain distribution histograms for 15KhM steel in initial state

Рис. 2. Микроструктура (a) и гистограммы распределения зерен феррита (b) и перлита (c) в стали 15ХМ в исходном состоянии



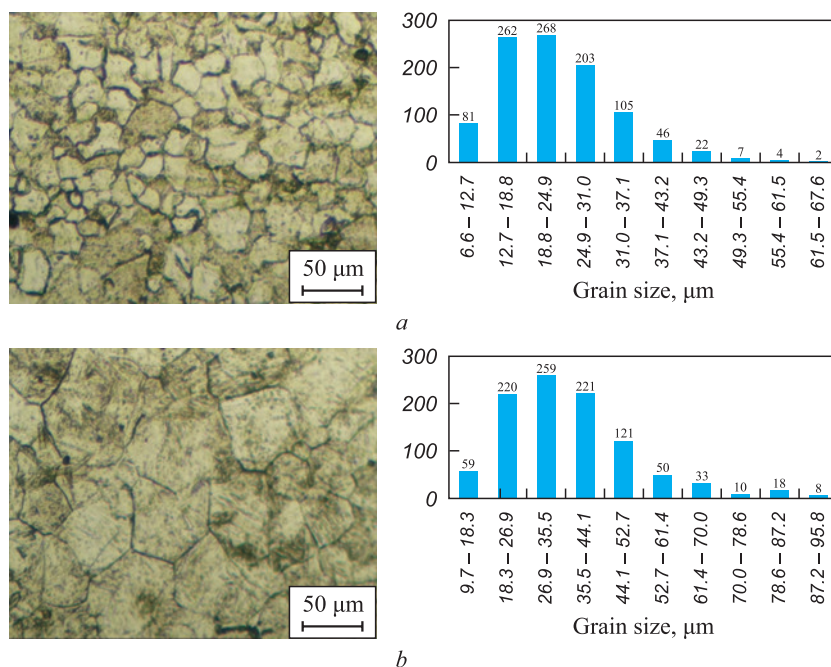


Fig. 3. Microstructure and former austenite grain distribution histograms for 15KhM steel before (a) and after (b) thermal exposure according to mode I

Рис. 3. Микроструктура и гистограммы распределения зерен бывшего аустенита в стали 15ХМ до (a) и после (b) термического воздействия по режиму I

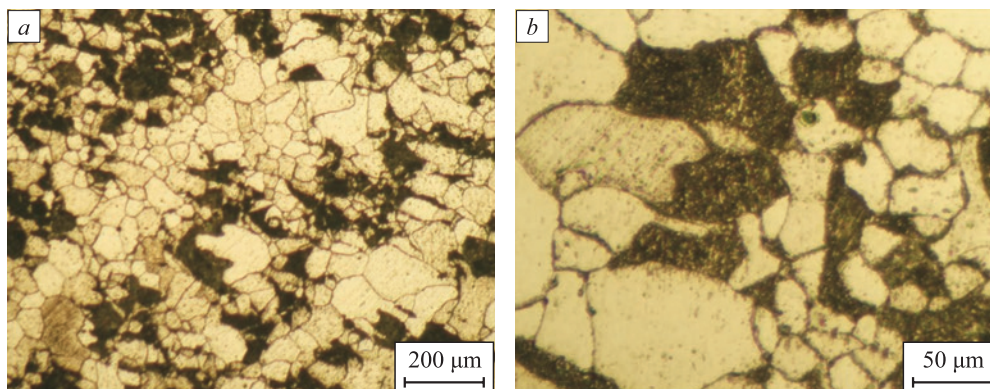


Fig. 4. Microstructure of 15KhM steel after thermal exposure according to mode I

Рис. 4. Микроструктура стали 15ХМ после термического воздействия по режиму I

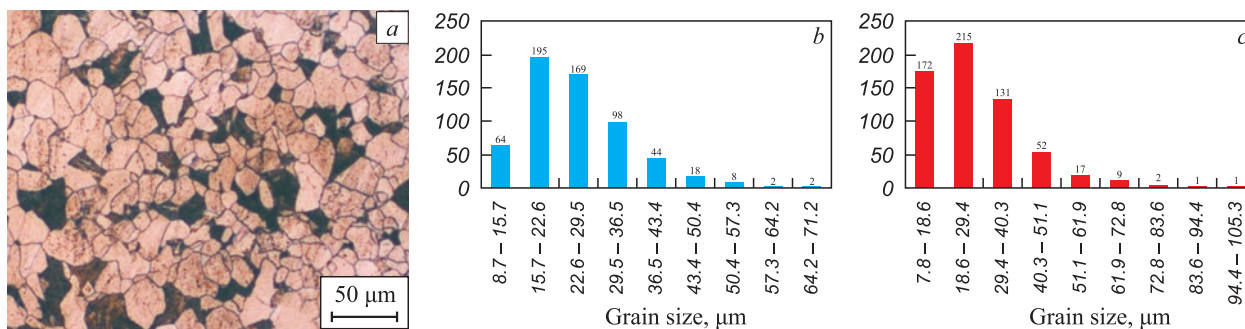


Fig. 5. Microstructure (a) and ferrite (b) and pearlite (c) grain distribution histograms for 15KhM steel after thermal exposure according to mode 2

Рис. 5. Микроструктура (a) и гистограммы распределения зерен феррита (b) и перлита (c) в стали 15ХМ после термического воздействия по режиму 2



Table 3

**Mechanical properties of 15KhM steel before and after thermal exposure according to mode 1**

Таблица 3. Механические свойства стали 15ХМ до и после термического воздействия по режиму 1

Test temperature, °C	$\sigma_{0.2}$ , MPa	$\sigma_u$ , MPa	$\delta$ , %
in initial state			
700	$161 \pm 2$	$180 \pm 2$	$66.7 \pm 1.8$
900	$37 \pm 1$	$70 \pm 2$	$82.9 \pm 2.4$
after thermal exposure			
23	$222 \pm 2$	$436 \pm 3$	$30.8 \pm 0.7$
700	$118 \pm 2$	$167 \pm 2$	$51.4 \pm 2.2$
900	$34 \pm 1$	$69 \pm 2$	$88.0 \pm 2.8$
1200	$15 \pm 1$	$25 \pm 1$	$35.0 \pm 2.5$

the brittle constituent ( $X$ ) to an amount of 30 – 90 % occurs at ambient temperature. At the temperatures from 60 to 0 °C, the impact strength  $KCV$  drops sharply from 171 to 43 J/cm<sup>2</sup>. During a further temperature increase to minus 20 °C, the impact strength consistently decreases to 20 J/cm<sup>2</sup>.

After thermal impact according to mode 2, the brittle constituent in the fracture surface in amount of 30 % occurs at 0 °C. The impact strength does not decrease significantly remaining at the level of 216 J/cm<sup>2</sup>. Total brittle fracture is observed at 0 °C for steel in initial state, and after thermal impact at –50 °C. Therefore, as a consequence of thermal impact, the starting temperature

Table 4

**Results of impact bending tests of 15KhM steel before and after thermal exposure according to mode 2**

Таблица 4. Результаты испытаний на ударный изгиб стали 15ХМ до и после термического воздействия по режиму 2

Temperature, °C	$KCV$ , J/cm <sup>2</sup>		$X$ , %	
	before	after	before	after
200	$184 \pm 3$	$245 \pm 2$	0	0
150	$186 \pm 4$	$237 \pm 3$	0	0
125	$181 \pm 3$	–	0	–
60	$171 \pm 4$	–	0	–
23	$116 \pm 25$	$214 \pm 3$	30 – 90	0
0	$43 \pm 5$	$216 \pm 4$	100	30
–20	$27 \pm 2$	$146 \pm 6$	100	80
–30	$20 \pm 2$	$176 \pm 7$	100	50
–50	–	$22 \pm 2$	–	100

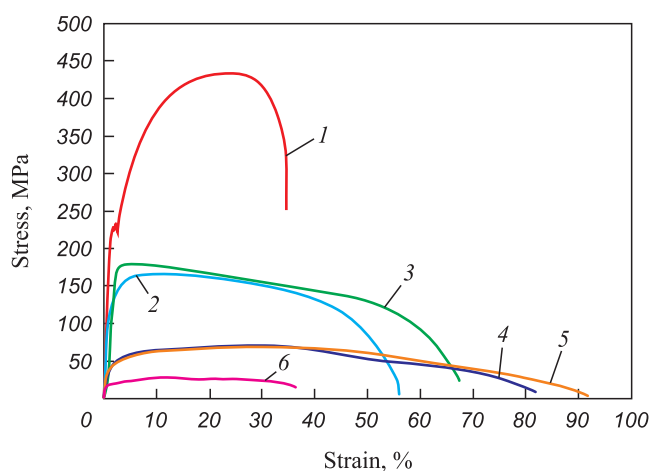


Fig. 6. Stress-strain curves of 15KhM steel at different temperatures in initial state and after thermal exposure according to mode 1: 1 – 23 °C, after thermal exposure; 2 – 700 °C, after thermal exposure; 3 – 700 °C, initial state; 4 – 900 °C, initial state; 5 – 900 °C, after thermal exposure; 6 – 1200 °C, after thermal exposure

Рис. 6. Кривые растяжения стали 15ХМ при различных температурах в исходном состоянии и после термического воздействия по режиму 1: 1 – 23 °C, после термического воздействия; 2 – 700 °C, после термического воздействия; 3 – 700 °C, исходное состояние; 4 – 900 °C, исходное состояние; 5 – 900 °C, после термического воздействия; 6 – 1200 °C, после термического воздействия

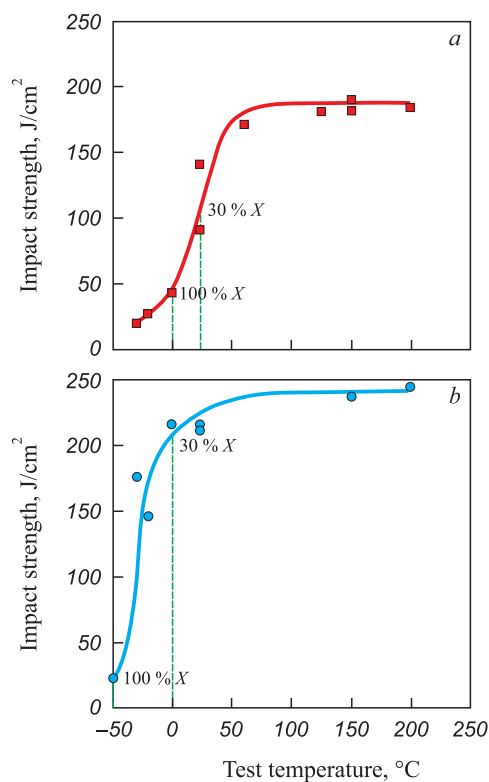


Fig. 7. Impact strength curves of 15KhM steel samples (a) in initial state and (b) after thermal exposure (%  $X$  – fraction of brittle component in the fracture)

Рис. 7. Сериальные кривые ударной вязкости образцов из стали 15ХМ в исходном состоянии (a) и после термического воздействия (b) (%  $X$  – доля хрупкой составляющей в изломе)

of viscous brittle transition of 15KhM steel decreases by 20 – 30 °C. The range of viscous brittle transition is expanded by 25 °C. Increase in the properties of impact strength is related to an increase in the degree of structure recrystallization as well as decrease in residual stresses after hot rolling as a consequence of thermal impact.

According to the measurements of geometry of samples from 15KhM steel after impact tests, it was determined that the samples after thermal impact according to mode 2 were destroyed in a more viscous pattern. They also demonstrated a higher tightening than the samples in initial state in overall range of test temperature (Fig. 8).

The fracture surface of impact samples at temperatures below the start of viscous brittle transition in the region under notch is presented by cleavage facets with river line. The facet size is 10 – 80 μm, and the fracture relief is characterized by a highly non-uniform height of individual elements (Fig. 9).

Thus, the impact strength of 15KhM steel in initial state is inferior to that of 22K and 09G2S steels. However, after thermal impact according to mode 2, the impact strength of 15KhM steel increases and is comparable with that of 22K steel.

The thermal diffusivity of 15KhM steel as a function of temperature in comparison with 22K and 09G2S steels is illustrated in Fig. 10. In addition, the data for SA533-B1 steel are also presented [18]. As can be seen in the plot, the thermal diffusivity for 22K, 09G2S and 15KhM steels as a function of temperature, is characterized by inflection at the temperature above 700 °C. This is related to  $\alpha \rightarrow \gamma$  transformation occurring in steels at these temperatures. At ambient temperature, the ther-

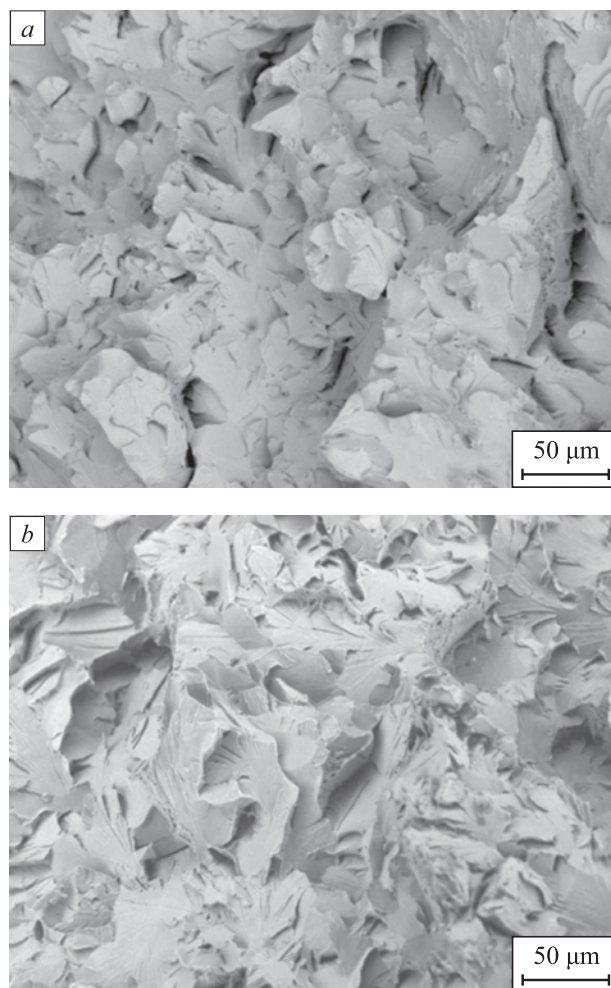


Fig. 9. Fracture surfaces of impact samples at room temperature in initial state (a) and at –30 °C after thermal exposure according to mode 2 (b)

Рис. 9. Изломы ударных образцов при комнатной температуре в исходном состоянии (a) и при –30 °C после термического воздействия по режиму 2 (b)

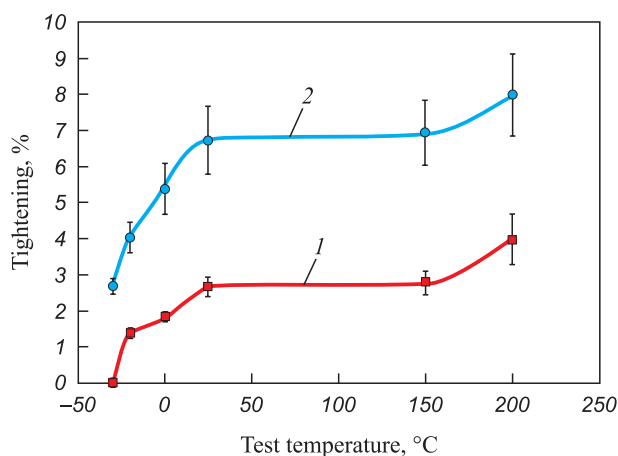


Fig. 8. Dependence of reduction of 15KhM steel samples on the impact test temperature:

1 – initial state; 2 – after thermal exposure according to mode 2

Рис. 8. Зависимость утяжки образцов из стали 15ХМ от температуры ударных испытаний:

1 – исходное состояние; 2 – после термического воздействия по режиму 2

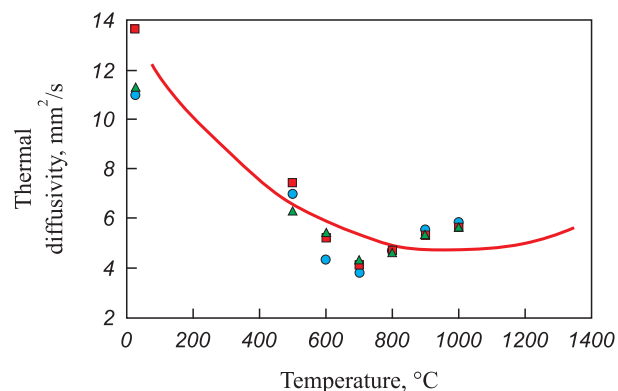


Fig. 10. Temperature dependence of thermal diffusivity of low-carbon steels:

● – 09G2S; ■ – 22K; ▲ – 15KhM; solid line – SA533-B1 steel [18]

Рис. 10. Температурная зависимость температуропроводности низкоуглеродистых сталей:

● – 09Г2С; ■ – 22К; ▲ – 15ХМ; сплошная линия – данные для стали SA533-B1 [18]

mal diffusivity of 15KhM and 09G2S steels is the equal to 11.0 – 11.2 mm<sup>2</sup>/s, while that of 22K is slightly higher: 13.7 mm<sup>2</sup>/s. At 500 °C the lowest thermal diffusivity is demonstrated by 15KhM steel: 6.3 mm<sup>2</sup>/s, while the highest by 22K steel: 7.4 mm<sup>2</sup>/s. At 600 °C lowest thermal diffusivity is demonstrated by 09G2S steel: 4.3 mm<sup>2</sup>/s, while the highest by 22K and 15KhM steels: 5.3 mm<sup>2</sup>/s. In the range from 700 to 100 °C the thermal diffusivity of steel slightly increases, while the temperature dependence of thermal diffusivity for all three steels in this range does not differ statistically. This data differs from that of SA533-B1 steel, for which the inflection in the curve was recorded at a higher temperature: 900 °C.

## CONCLUSIONS

It was demonstrated that low carbon low alloy 15KhM steel is an alternative material to 22K and 09G2S steels as structural material for cc-vessels in nuclear reactors. This steel is characterized by a relatively high level of thermal diffusivity and good weldability. Alloying with molybdenum and vanadium, as well as low manganese content, provides finer grain structure in comparison with 22K and 09G2S steels and eliminates tendency to temper brittleness. This has a positive influence on strength and impact strength of cc-vessel in overall temperature range in the event of BDB. Integrated studies under BDB simulating conditions are required for the experimental establishment of an overall set of physicochemical properties of 15KhM steel and its application as a material of cc-vessel.

## REFERENCES / СПИСОК ЛИТЕРАТУРЫ

1. Artamonov N.V., Sidorov A.S. Nuclear safety of melt localizer device for NPP with WWER reactor model. *Izvestia vuzov. Yadernaya energetika*. 2012;(3):23–31. (In Russ.)  
Артамонов Н.В., Сидоров А.С. Обоснование ядерной безопасности устройства локализации расплава для АЭС с реакторами типа ВВЭР. *Известия вузов. Ядерная энергетика*. 2012;(3):23–31.
2. Sidorov A.S. Core catcher vessel for nuclear power plants with VVER-1000 reactors. In: *7<sup>th</sup> Int. Sci. and Tech. Conf. "Ensuring the Safety of Nuclear Power Plants with VVER"*. Podolsk: OKB Gidropress: 2011. (In Russ.)  
Сидоров А.С. Устройство локализации расплава для АЭС с реакторами ВВЭР-1000. В сборнике: *7-я международная научно-техническая конференция «Обеспечение безопасности АЭС с ВВЭР»*. Подольск: ОКБ «Гидропресс»; 2011.
3. Rempe J.L., Knudson D.L., Condie K.G., Suh K.Y., Cheung F.-B., Kim S.-B. Conceptual design of an in-vessel core catcher. *Nuclear Engineering and Design*. 2004;230(1–3): 311–325.  
<https://doi.org/10.1016/j.nucengdes.2003.11.030>
4. Sultan T., Sapra M.K., Kundu S., Kadam A.V., Kulkarni P.P., Rao A.R. Experimental & analytical study of passive thermal sensing system developed for cooling water injection into AHWR core catcher. *Nuclear Engineering and Design*. 2017;322:81–91.  
<https://doi.org/10.1016/j.nucengdes.2017.06.021>
5. Rempe J.L., Knudson D.L., Condie K.G., Suh K.Y., Cheung F.-B., Kim S.-B. Corium retention for high power reactors by an in-vessel core catcher in combination with external reactor vessel cooling. *Nuclear Engineering and Design*. 2004;230(1–3):293–309.  
<https://doi.org/10.1016/j.nucengdes.2003.11.031>
6. Fischer M. The severe accident mitigation concept and the design measures for core melt retention of the European Pressurized Reactor (EPR). *Nuclear Engineering and Design*. 2004;230(1–3):169–180.  
<https://doi.org/10.1016/j.nucengdes.2003.11.034>
7. Development of a program of heat treatment and mechanical testing for experimental assessment of degradation degree of the welded joints mechanical properties in material of cc-vessel casing and guide plate. Report of the National Research Center "Kurchatov Institute", RPR.0131.10UJA. JKM.BN.DD0001, No. 110.10-49/1-138-118, 2018. (In Russ.)  
*Разработка программы термообработки и механических испытаний для экспериментальной оценки степени деградации механических свойств сварных соединений материала корпуса УЛР и направляющей плиты*. Отчет НИЦ «Курчатовский институт», RPR.0131.10UJA. JKM. BN.DD0001, Инв. № 110.10-49/1-138-118, 2018.
8. Odesskii P.D., Egorova A.A. Strength of steel for unique engineering structures. *Russian Metallurgy (Metally)*. 2012;2012(10):911–918.  
<https://doi.org/10.1134/S0036029512100151>
9. Odesskii P.D., Vedyakov I.I. *Steel in Building Metal Structures*. Moscow: Metallurgizdat; 2018:906. (In Russ.)  
Одесский П.Д., Ведяков И.И. *Сталь в строительных металлических конструкциях*. Москва: Металлургиздат; 2018:906.
10. Kudrya A.V., Sokolovskaya E.A., Trachenko V.A., Ning Le Hai, Skorodumov S.V., Papina K.B. Measurement of nonuniformity of fracture in structural steels with heterogeneous structure. *Metal Science and Heat Treatment*. 2015;57(3–4): 190–196. <https://doi.org/10.1007/s11041-015-9860-z>  
Кудря А.В., Соколовская Э.А., Траченко В.А., Нинь Ле Хай, Скородумов С.В., Папина К.Б. Измерение неоднородности разрушения в конструкционных сталях с разнородной структурой. *Металловедение и термическая обработка металлов*. 2015;(4):12–18.
11. Nikulin S.A., Rogachev S.O., Nikolaev Yu.A., Vasiliev S.G., Belov V.A., Turilina V.Yu. High-temperature mechanical properties of low-carbon steel used for the manufacture of core catcher vessel. *Progress in Nuclear Energy*. 2021;142:104015.  
<https://doi.org/10.1016/j.pnucene.2021.104015>
12. Nikulin S.A., Rogachev S.O., Vasil'ev S.G., Belov V.A., Nikolaev Yu.A. Effect of high temperatures on the mechanical properties of 09G2S steel. *Russian Metallurgy (Metally)*. 2021;2021(4):160–163.  
<https://doi.org/10.1134/S003602952104025X>  
Никулин С.А., Рогачев С.О., Васильев С.Г., Белов В.А., Николаев Ю.А. Влияние высоких температур на механические свойства стали 09Г2С. *Деформация и разрушение*



- материалов. 2020;(7):35–35.  
<https://doi.org/10.31044/1814-4632-2020-7-32-35>
13. Nikulin S.A., Rogachev S.O., Belov V.A., Turilina V.Yu., Shplis N.V. Effect of high temperatures on the mechanical properties of the weld metal in the welded joint of low-carbon low-alloy steel. *Russian Metallurgy (Metally)*. 2021;2021(10):1314–1319.  
<https://doi.org/10.1134/S0036029521100256>  
 Никулин С.А., Рогачев С.О., Белов В.А., Турилина В.Ю., Шплис Н.В. Влияние высоких температур на механические свойства металла шва сварного соединения малоуглеродистой низколегированной стали. *Деформация и разрушение материалов*. 2021;(4):33–38.  
<https://doi.org/10.31044/1814-4632-2021-4-33-38>
  14. Nikulin S.A., Rogachev S.O., Vasil'ev S.G., Belov V.A., Komissarov A.A. Effect of long-term annealing on the impact toughness of 22K steel. *Russian Metallurgy (Metally)*. 2021;2021(4):149–153.  
<https://doi.org/10.1134/S0036029521040248>  
 Никулин С.А., Рогачев С.О., Васильев С.Г., Белов В.А., Комиссаров А.А. Влияние длительного отжига на ударную вязкость стали 22К. *Деформация и разрушение материалов*. 2020;(11):36–40.  
<https://doi.org/10.31044/1814-4632-2020-11-36-40>
  15. Nikulin S.A., Rogachev S.O., Belov V.A., Komissarov A.A., Turilina V.Yu., Shplis N.V., Nikolaev Yu.A. Influence of long-term high-temperature action on impact toughness of base metal and weld metal of 22K steel welded joint. *Izvestiya. Ferrous Metallurgy*. 2021;64(7):498–509. (In Russ.).  
<https://doi.org/10.17073/0368-0797-2021-7-498-509>  
 Никулин С.А., Рогачев С.О., Белов В.А., Комиссаров А.А., Турилина В.Ю., Шплис Н.В., Николаев Ю.А. Влияние длительного высокотемпературного воздействия на ударную вязкость основного металла и металла шва сварного соединения стали 22К. *Известия вузов. Черная металлургия*. 2021;64(7):498–509.  
<https://doi.org/10.17073/0368-0797-2021-7-498-509>
  16. Nikulin S.A., Rogachev S.O., Belov V.A., Komissarov A.A., Turilina V.Yu., Shplis N.V., Nikolaev Yu.A. Impact strength of low-carbon steel 09G2S welded joint metal. *Metallurgist*. 2022;65(8):1391–1400.  
<https://doi.org/10.1007/s11015-022-01286-2>  
 Никулин С.А., Рогачев С.О., Белов В.А., Комиссаров А.А., Турилина В.Ю., Шплис Н.В., Николаев Ю.А. Ударная вязкость металла шва сварного соединения низкоуглеродистой стали 09Г2С. *Металлург*. 2021;(12):39–46. [https://doi.org/10.52351/00260827\\_2021\\_12\\_39](https://doi.org/10.52351/00260827_2021_12_39)
  17. Nikulin S.A., Rogachev S.O., Belov V.A., Zadorozhnyy M.Yu., Shplis N.V., Skripalenko M.M. Effect of prolonged thermal exposure on low-cycle bending fatigue resistance of low-carbon steel. *Metals*. 2022;12(2):281.  
<https://doi.org/10.3390/met12020281>
  18. Rempe J.L., Knudson D.L. High temperature thermal and structural material properties for metals used in LWR vessels. In: *Proceedings of ICAPP '08, Anaheim, CA USA*, 2008:8220.
  19. Thinnies G.L., Korth G.E., Chavez S.A., Walker T.J. High-temperature creep and tensile data for pressure vessel steels SA533B1 and SA508-CL2. *Nuclear Engineering and Design*. 1994;148(1–3):343–350.  
[https://doi.org/10.1016/0029-5493\(94\)90119-8](https://doi.org/10.1016/0029-5493(94)90119-8)
  20. Loktionov V., Lyubashevskaya I., Sosnin O., Terentyev E. Short-term strength properties and features of high-temperature deformation of VVER reactor pressure vessel steel 15Kh2NMFA-A within the temperature range 20–1200 °C. *Nuclear Engineering and Design*. 2019;352:110188.  
<https://doi.org/10.1016/j.nucengdes.2019.110188>
  21. Loktionov V.D., Sosnin O.V., Lyubashevskaya I.V. Strength properties and idiosyncrasies of the deformational behavior of 15Kh2NMFA-A steel at temperatures 20–1100°C. *Atomic Energy*. 2005;99(3):665–669.  
<https://doi.org/10.1007/s10512-005-0263-x>  
 Локтионов В.Д., Соснин О.В., Любашевская И.В. Прочностные свойства и особенности деформационного поведения стали 15Х2НМФА-А в температурном диапазоне 20–1000 °C. *Атомная энергия*. 2005;99(3):229–232.
  22. Belomytsev M.Yu., Mordashov S.V. Regularities of short-term creep of St3 steel. *Izvestiya. Ferrous Metallurgy*. 2015;58(11):798–802. (In Russ.).  
<https://doi.org/10.17073/0368-0797-2015-11-798-802>  
 Беломытцев М.Ю., Мордашов С.В. Закономерности кратковременной ползучести стали Ст3. *Известия вузов. Черная металлургия*. 2015;58(11):798–802.  
<https://doi.org/10.17073/0368-0797-2015-11-798-802>
  23. Yang C.-C., Liu C.-L. Improvement of the mechanical properties of 1022 carbon steel coil by using the Taguchi method to optimize spheroidized annealing conditions. *Materials*. 2016;9(8):693. <https://doi.org/10.3390/ma9080693>
  24. Zubchenko A.S. *Grade Guide of Steels and Alloys*. Moscow: Mashinostroenie; 2003:784. (In Russ.).  
*Марочник сталей и сплавов*. Под общ. ред. А.С. Зубченко. Москва: Машиностроение; 2003:784.
  25. Budynas R.G., Nisbett J.K. *Shigley's Mechanical Engineering Design*. 11<sup>th</sup> ed. New York: McGraw-Hill; 2019:1120.
  26. Saraev Yu.N., Bezborodov V.P., Gladovskii S.V., Golikov N.I. Properties of the welded joints of manganese steel made by low-frequency pulsed arc welding. *Russian Metallurgy (Metally)*. 2017;2017(4):287–292.  
<https://doi.org/10.1134/S0036029517040206>  
 Сараев Ю.Н., Безбородов В.П., Гладковский С.В., Голиков Н.И. Исследование свойств сварных соединений марганцовистой стали, полученных низкочастотной импульсно-дуговой сваркой. *Деформация и разрушение материалов*. 2016;(4):36–41.
  27. Poletaev Yu.V., Poletaev V.Yu. One-pass arc welding under thin slag layer of thick 09G2S steel plate structures. *Vestnik of Don State Technical University*. 2018;18:50–58. (In Russ.).  
<https://doi.org/10.23947/1992-5980-2018-18-1-50-58>  
 Полетаев Ю.В., Полетаев В.Ю. Однопроходная электродуговая сварка под тонким слоем шлака толстолистовых конструкций стали 09Г2С. *Вестник Донского государственного технического университета*. 2018;18(1):50–58.  
<https://doi.org/10.23947/1992-5980-2018-18-1-50-58>
  28. Fetisov G.P., Karpman M.G., Matyunin V.M. *Materials Science and Technology of Metals*. Moscow: Oniks; 2009:624. (In Russ.).  
 Фетисов Г.П., Карпман М.Г., Матюнин В.М. *Материаловедение и технология металлов*. Москва: Оникс; 2009:624.



29. Chen C.Y., Huang J.Y., Yeh J.J., Hwang J.R., Huang J.Y. Microstructural evaluation of fatigue damage in SA533-B1 and type 316L stainless steels. *Journal of Materials Science*. 2003;38(4):817–822. <https://doi.org/10.1023/A:1021817216519>
30. Nikulin S.A., Rogachev S.O., Belov V.A., Ozherelkov D.Yu., Shplis N.V., Fedorenko L.V., Molyarov A.V., Konvalova K.A. Fracture toughness of 22K-type low-carbon steel after extreme thermal exposure. *Journal of Materials Engineering and Performance*. 2023. <https://doi.org/10.1007/s11665-022-07746-9>
31. Begley J.A., Landes J.D. The J-integral as a fracture criterion. In: *Fracture Toughness, Part II*. ASTM STP 514, 1972:1–20.
32. Shtremel M.A. Informativeness of measurements of impact toughness. *Metal Science and Heat Treatment*. 2008;50(11): 11–12. <https://doi.org/10.1007/s11041-009-9099-7>  
Штремель М.А. Информативность измерений ударной вязкости. *Металловедение и термическая обработка металлов*. 2008;(11):37–51.

## Information about the Authors

## Сведения об авторах

**Sergei A. Nikulin**, Dr. Sci. (Eng.), Prof., Head of the Chair “Metallography and Physics of Strength”, National University of Science and Technology “MISIS”

**E-mail:** nikulin@isis.ru

**Stanislav O. Rogachev**, Cand. Sci. (Eng.), Assist. Prof. of the Chair “Metallography and Physics of Strength”, National University of Science and Technology “MISIS”; Research Associate, Baikov Institute of Metallurgy and Materials Science, Russian Academy of Sciences

**ORCID:** 0000-0001-7769-7748

**E-mail:** csaap@mail.ru

**Vladislav A. Belov**, Cand. Sci. (Eng.), Assist. Prof. of the Chair “Metallography and Physics of Strength”, National University of Science and Technology “MISIS”

**E-mail:** vbelov@ymail.com

**Nikolai V. Shplis**, Engineer, National University of Science and Technology “MISIS”

**E-mail:** shplisnikolay@mail.ru

**Aleksandr A. Komissarov**, Cand. Sci. (Eng.), Assist. Prof., Head of the Laboratory “Hybrid Nanostructured Materials”, National University of Science and Technology “MISIS”

**E-mail:** komissarov@isis.ru

**Veronika Yu. Turilina**, Cand. Sci. (Eng.), Assist. Prof. of the Chair “Metallography and Physics of Strength”, National University of Science and Technology “MISIS”

**E-mail:** veronikat77@gmail.com

**Yurii A. Nikolaev**, Dr. Sci. (Eng.), Prof., Leading Researcher, National Research Center “Kurchatov Institute”

**E-mail:** Nikolaev\_YA@nrcki.ru

**Сергей Анатольевич Никулин**, д.т.н, профессор, заведующий кафедрой металлостроения и физики прочности, Национальный исследовательский технологический университет «МИСИС»

**E-mail:** nikulin@isis.ru

**Станислав Олегович Рогачев**, к.т.н., доцент кафедры металлостроения и физики прочности, Национальный исследовательский технологический университет «МИСИС»; научный сотрудник, Институт металлургии и материаловедения им. А.А. Байкова РАН

**ORCID:** 0000-0001-7769-7748

**E-mail:** csaap@mail.ru

**Владислав Алексеевич Белов**, к.т.н., доцент кафедры металлостроения и физики прочности, Национальный исследовательский технологический университет «МИСИС»

**E-mail:** vbelov@ymail.com

**Николай Валерьевич Шплис**, инженер, Национальный исследовательский технологический университет «МИСИС»

**E-mail:** shplisnikolay@mail.ru

**Александр Александрович Комиссаров**, к.т.н., доцент, заведующий лабораторией «Гибридные наноструктурные материалы», Национальный исследовательский технологический университет «МИСИС»

**E-mail:** komissarov@isis.ru

**Вероника Юрьевна Турилина**, к.т.н., доцент кафедры металлостроения и физики прочности, Национальный исследовательский технологический университет «МИСИС»

**E-mail:** veronikat77@gmail.com

**Юрий Анатольевич Николаев**, д.т.н., ведущий научный сотрудник, НИЦ «Курчатовский институт»

**E-mail:** Nikolaev\_YA@nrcki.ru

## Contribution of the Authors

## Вклад авторов

**S. A. Nikulin** – formation of the article main concept, formulation of conclusions.

**S. O. Rogachev** – scientific guidance, writing the text.

**V. A. Belov** – scientific guidance, mechanical testing.

**N. V. Shplis** – structural studies, mechanical testing.

**A. A. Komissarov** – mechanical testing.

**V. Yu. Turilina** – scientific guidance.

**Yu. A. Nikolaev** – formation of the article main concept, revision of the text, correction of conclusions.

**С. А. Никулин** – формирование основной концепции, формулирование выводов.

**С. О. Рогачев** – научное руководство, подготовка текста статьи.

**В. А. Белов** – научное руководство, механические испытания.

**Н. В. Шплис** – структурные исследования, механические испытания.

**А. А. Комиссаров** – механические испытания.

**В. Ю. Турилина** – научное руководство.

**Ю. А. Николаев** – формирование основной концепции, доработка текста, корректировка выводов.

Received 24.12.2022

Revised 22.04.2023

Accepted 24.04.2023

Поступила в редакцию 24.12.2022

После доработки 22.04.2023

Принята к публикации 24.04.2023

INNOVATION IN METALLURGICAL  
INDUSTRIAL AND LABORATORY EQUIPMENT,  
TECHNOLOGIES AND MATERIALSИННОВАЦИИ В МЕТАЛЛУРГИЧЕСКОМ  
ПРОМЫШЛЕННОМ И ЛАБОРАТОРНОМ  
ОБОРУДОВАНИИ, ТЕХНОЛОГИЯХ И МАТЕРИАЛАХ

UDC 620.18

DOI 10.17073/0368-0797-2023-3-367-375



Original article

Оригинальная статья

A METHOD FOR STUDYING THE FREQUENCY STABILITY  
OF MATERIALS DURING TESTS FOR MULTI-CYCLE FATIGUE OF STEELV. V. Myl'nikov<sup>1</sup>, E. A. Dmitriev<sup>2</sup><sup>1</sup> Nizhny Novgorod State University of Architecture, Building and Civil Engineering (65 Il'inskaya Str., Nizhny Novgorod 603950, Russian Federation)<sup>2</sup> Komsomolsk-on-Amur State University (27 Lenina Ave., Komsomolsk-on-Amur, Khabarovsk Territory 681013, Russian Federation)

✉ mrmylnikov@mail.ru

**Abstract.** For trouble-free operation without loss of elastic and inelastic properties of particularly critical elements of electrical-to-mechanical vibration converters during a long period of cyclic operation, it is necessary, in addition to studying the fatigue characteristics of materials used for their manufacture, to study these alloys for frequency stability, since minor deviations in the frequency of natural oscillations lead to unacceptable errors in the operation of such high-precision products. To carry out such studies, we developed and constructed an original installation, in which sinusoidal loading is carried out according to the “soft” scheme of flat samples cantilever bending operating in self-oscillation mode. The frequency of cyclic loading in this installation is generated by current pulses, which are a response to the frequency of the test sample natural oscillations converted using electronics. As a result, frequency equality is achieved in the test process. An algorithm for calculating stresses depending on the loading amplitude of steel samples of different geometric shapes was developed. It is shown that the stress on the sample calculated by the deformation amplitude in all cases is 8 – 10 % higher than the stress calculated by the force, regardless of the shape of the proposed samples. To verify the proposed research method, martensitic-aging steel was tested at loads close to the fatigue limit, since frequency stability in this range is of great interest. We obtained the frequency characteristics in the multi-cycle test area. It was determined that with an operating time of 50 million loading cycles, the frequency change was 0.75 Hz. The dynamics of frequency stability was revealed: the frequency changed most intensively during the first 10 million loading cycles, during this time the frequency changed by 0.54 Hz.

**Keywords:** steel, fatigue, strain amplitude, loading frequency, durability, natural oscillation frequency, cyclic strength, frequency stability

**For citation:** Myl'nikov V.V., Dmitriev E.A. A method for studying the frequency stability of materials during tests for multi-cycle fatigue of steel. *Izvestiya. Ferrous Metallurgy*. 2023;66(3):367–375. <https://doi.org/10.17073/0368-0797-2023-3-367-375>

МЕТОД ИЗУЧЕНИЯ ЧАСТОТНОЙ СТАБИЛЬНОСТИ МАТЕРИАЛОВ  
ПРИ ИСПЫТАНИЯХ НА МНОГОЦИКЛОВУЮ УСТАЛОСТЬ СТАЛИВ. В. Мыльников<sup>1</sup>, Э. А. Дмитриев<sup>2</sup><sup>1</sup> Нижегородский государственный архитектурно-строительный университет (Россия, 603950, Нижний Новгород, ул. Ильинская, 65)<sup>2</sup> Комсомольский-на-Амуре государственный университет (Россия, 681013, Хабаровский край, Комсомольск-на-Амуре, пр. Ленина, 27)

✉ mrmylnikov@mail.ru

**Аннотация.** Для безаварийного функционирования и без потерь упругих и неупругих свойств особо ответственных элементов преобразователей электрических колебаний в механические в течение длительного периода циклической наработки необходимо, кроме исследования усталостных характеристик материалов, применяемых для их изготовления, исследовать эти сплавы и на частотную стабильность. Это связано с тем, что незначительные отклонения частоты собственных колебаний приводят к недопустимым погрешностям в работе такого рода высокоточных изделий. Для проведения исследований разработана и сконструирована оригинальная установка, работающая в режиме автоколебаний, в которой осуществлено синусоидальное нагружение плоских образцов по «мягкой» схеме консольного изгиба. Частота циклического нагружения в установке генерируется импульсами тока, которые являются откликом на частоту собственных колебаний испытываемого образца, преобразованных с помощью электроники. В результате достигается частотное равенство в процессе

испытаний. Разработан алгоритм расчета напряжений в зависимости от амплитуды нагружения образцов из стали разной геометрической формы. Показано, что напряжение на образце, рассчитанное по амплитуде деформации, во всех случаях на 8 – 10 % выше напряжения, рассчитанного по силе вне зависимости от формы образцов. Для верификации предложенного метода исследований проведены испытания мартенситно-старееющей стали на нагрузках, близких к пределу усталости, так как наибольший интерес представляет стабильность частоты в этом диапазоне. Получены частотные характеристики в многоцикловой области испытаний. Определено, что при наработке в 50 млн циклов нагружения изменение частоты составило 0,75 Гц. Выявлена динамика частотной стабильности: наиболее интенсивно частота менялась при первых 10 млн циклов нагружения, за это время она изменилась на 0,54 Гц.

**Ключевые слова:** сталь, усталость, амплитуда деформации, частота нагружения, долговечность, частота собственных колебаний, циклическая прочность, стабильность частоты

**Для цитирования:** Мыльников В.В., Дмитриев Э.А. Метод изучения частотной стабильности материалов при испытаниях на многоцикловую усталость стали. *Известия вузов. Черная металлургия.* 2023;66(3):367–375. <https://doi.org/10.17073/0368-0797-2023-3-367-375>

## INTRODUCTION

Standard fatigue tests serve the purpose of determining the mechanical properties of a material [1]. Engineers rely on these test results for material selection and structural analysis [2].

Several cyclic test procedures exist [3 – 6]. The essential fatigue test properties to accurately simulate the part's operating stress and strain [7 – 10] are as follows:

– loading program determined by the cycle amplitude form (Fig. 1);

– load scheme (Fig. 2);

– testing to a specified stress ( $\sigma$ , MPa) (Fig. 2, *a*) or strain ( $\varepsilon$ , mm) (Fig. 2, *d*).

Mission-critical components undergo validation using dedicated testing machines and specialized testing procedures. For example, materials with low inelastic pro-

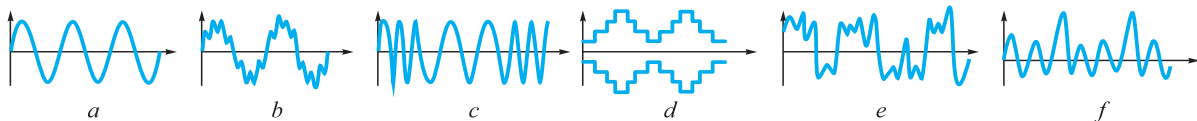


Fig. 1. Varieties of cycle amplitude forms:

*a* – sinusoidal cycle form (harmonic) with constant amplitude values; *b* – biharmonic; *c* – with variable frequency; *d* – programmed block cycle; *e* – with reproduction of the operational spectrum with time variable  $\sigma_a$ , with or without truncation of low  $\sigma_a$ ; *f* – harmonic cycle with single overloads

Рис. 1. Разновидности форм амплитуд циклов:

*a* – синусоидальная форма цикла (гармоническая) с постоянными амплитудными значениями; *b* – бигармоническая; *c* – с переменной частотой; *d* – программированный блочный цикл; *e* – с воспроизведением эксплуатационного спектра с переменной во времени  $\sigma_a$  с усечением низких  $\sigma_a$  или без их усечения; *f* – гармонический цикл с одиночными перегрузками

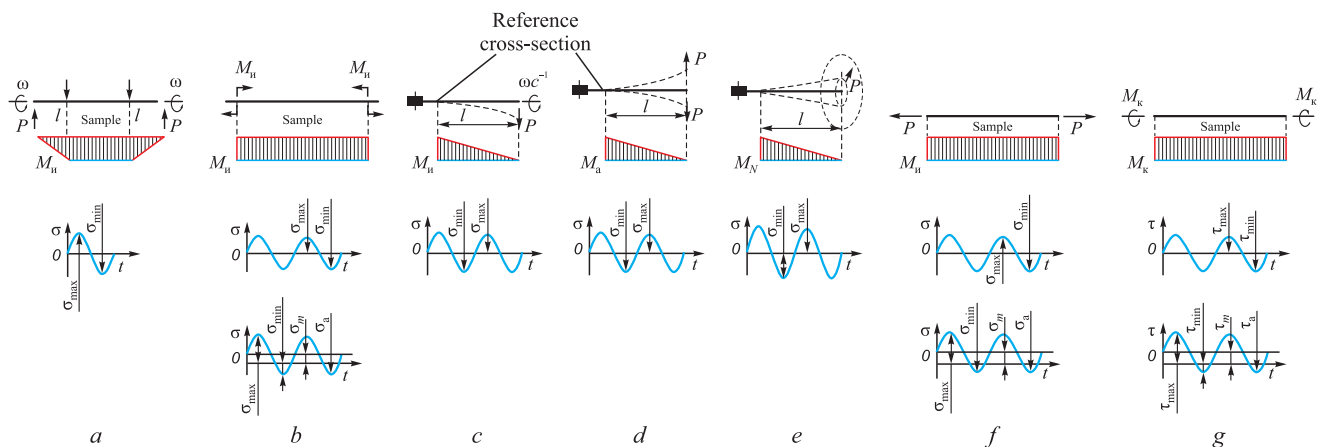


Fig. 2. Loading schemes during fatigue tests:

*a* – pure bending of a rotating cylindrical sample; *b* – pure bending in one plane; *c* – cantilever bending of a rotating cylindrical sample; *d* – cantilever cyclic transverse bending of a flat sample; *e* – transverse bending during rotation of the force plane; *f* – axial stretching along a pulsating cycle; *g* – alternating torsion

Рис. 2. Схемы нагружения при испытаниях на усталость:

*a* – чистый изгиб вращающегося цилиндрического образца; *b* – чистый изгиб в одной плоскости; *c* – консольный изгиб вращающегося цилиндрического образца; *d* – консольный циклический поперечный изгиб плоского образца; *e* – поперечный изгиб при вращении силовой плоскости; *f* – осевое растяжение по пульсирующему циклу; *g* – знакопеременное кручение

properties are required to make parts exposed to complex cyclic loading and dimensionally stable components. The inelastic properties exhibited during cyclic loading can be described as “internal friction”, “imperfect elasticity”, “damping”, “mechanical hysteresis”, or “energy dissipation” [11]. It is commonly assumed in most studies that microplastic deformations under cyclic loading are localized and unevenly distributed due to the heterogeneity of the material’s micro-properties. Another test involves measuring the mechanical properties at different temperatures to determine the elastic limit and activation energy of the micro deformations [12 – 15].

The objective of this study is to develop a testing procedure for estimating the frequency stability in elastic elements used in high-precision oscillators that convert electrical vibrations into mechanical oscillations. Even slight changes in frequency of natural oscillations (eigenfrequencies) caused by variations in the elastic modulus, material inelasticity, and of atomic and lattices vibrations can result in unacceptable errors in electric-to-mechanical oscillation conversion and premature fatigue failure [16 – 19].

## MATERIALS AND METHODS

A frequency stability testing installation was developed as shown in Fig. 3, designed specifically for conducting tests under unique stress conditions. This testing apparatus involved the application of isothermal cyclic loading to a flat cantilever sample, referred to as the “soft

test” [20]. It employed an electromechanical oscillator with mechanical vibration frequency precisely aligned to the sample’s eigenfrequency, facilitating resonance oscillations.

The installation comprised three distinct components arranged separately:

- bed: this component supported both the sample and the electromagnetic exciter;
- power supply and automation unit: responsible for powering the electromagnetic exciter coil, this unit adjusted the amperage and frequency as needed;
- measurement system for monitoring oscillatory parameters.

The bed, a robust L-shaped metal structure, was installed on vibration isolators. It facilitated the transfer of sample oscillations to the piezoelectric accelerometer. The operation of the installation proceeded as follows: the sensor’s signal was transmitted to the power supply and automation unit, which then supplied the electromagnetic exciter coil with a frequency matching the sample’s eigenfrequency. To prevent the overlap of vibrational waves and enhance oscillation transfer, the bed and the coil (assembled with the stator at one end of the electromagnetic exciter armature) were isolated from each other using vibration isolators (antivibration pads).

The electromagnetic exciter coil is energized by current pulses supplied from the power supply (Fig. 3, a). These pulses induce an electromagnetic force that causes

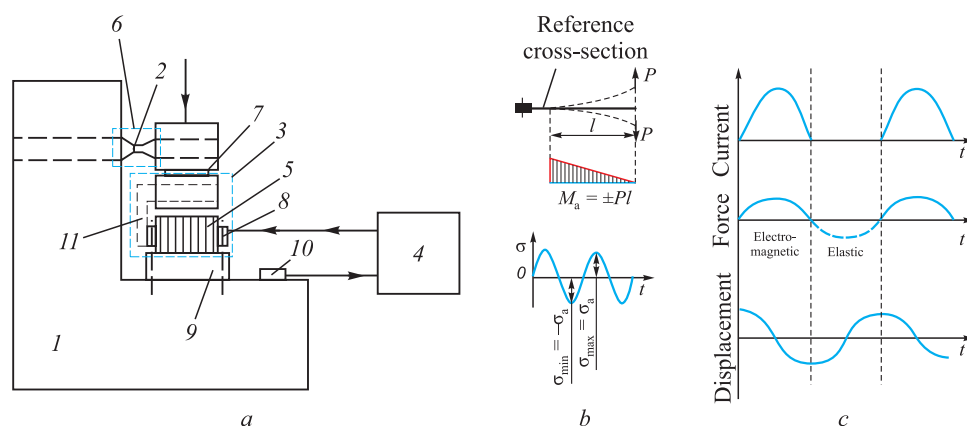


Fig. 3. Diagrams:

- a* – frequency stability testing installations: 1 – bed; 2 – sample; 3 – electromagnetic exciter; 4 – power supply and automation unit; 5 – coil of electromagnetic exciter; 6 – means of measuring parameters of the oscillatory process; 7 – ferromagnetic armature of electromagnetic exciter; 8 – electromagnetic stator exciter; 9 – vibration isolators; 10 – vibration acceleration sensor; 11 – U-shaped ribbon core; *b* – loads during cantilever cyclic transverse bending of a flat sample; *c* – matching current pulses, electromagnetic force and elastic force with movement of the console of the test sample in this installation

Рис. 3. Схемы:

- a* – установки для испытаний на частотную стабильность: 1 – станина; 2 – образец; 3 – электромагнитный возбудитель; 4 – блок питания и автоматики; 5 – катушка электромагнитного возбудителя; 6 – средство измерения параметров колебательного процесса; 7 – ферромагнитный якорь электромагнитного возбудителя; 8 – статор электромагнитного возбудителя; 9 – виброизоляторы; 10 – датчик виброускорения; 11 – П-образный ленточный сердечник; *b* – нагрузки при консольном циклическом поперечном изгибе плоского образца; *c* – согласования импульсов тока, электромагнитной силы и силы упругости с перемещением консоли исследуемого образца в данной установке



the armature, along with the sample, to move downward. When the current is interrupted, the elastic force reinstates the sample to its original position, subjecting it to cyclic loading. The displacement curve of the sample's end is illustrated in Fig. 3, *c*. As fatigue advances, the eigenfrequency of the sample undergoes changes, consequently modifying the frequency of cyclic loading.

Through a series of comprehensive tests, we estimated the fatigue properties, frequency characteristics under cyclic loading, and determined the endurance limit. The frequency characteristics also serve as an indicator of the sample's rate of damage and enables estimation of its remaining lifespan [21].

The following variables were measured in our experiments:

- frequency;
- number of load cycles;
- amplitude of oscillations (measured through an optical sensor);
- amplitude of oscillations (measured via a photoelectric sensor);
- amplitude of oscillations (measured using a piezoelectric accelerometer);
- average current within the exciter coil circuit;
- the waveforms were visualized using an oscilloscope.

The samples illustrated in Fig. 4 were composed of the 03N18K9M5T-EL steel grade. The corresponding Table presents the dimensions of the samples.

We derived the stress within the sample's cross-section from the amplitude of oscillations. In order to gauge the stress, we established a correlation between the force applied to the sample and the displacement of the sample at the point of force application. Subsequently, the stress was calculated based on the force value. We also deduced the analytical relationship between force and displacement for the steady mode. It is assumed that during oscillations, the forces applied to the sample (external force, inertia, elastic force) generate the same maximum stress and maximum displacement (vibration amplitude) as the static force equivalent to the resultant dynamic force.

For the curved axis of a variable cross-section beam, we employed an approximate differential equation:

$$EJ(x) \frac{d^2 y}{dx^2} = M(x), \quad (1)$$

where  $J(x)$  represents the second area moment;  $E$  stands for Young's modulus;  $M(x)$  denotes the bending moment;  $y$  is the coordinate in the force direction;  $x$  is the coordinate along the beam axis.

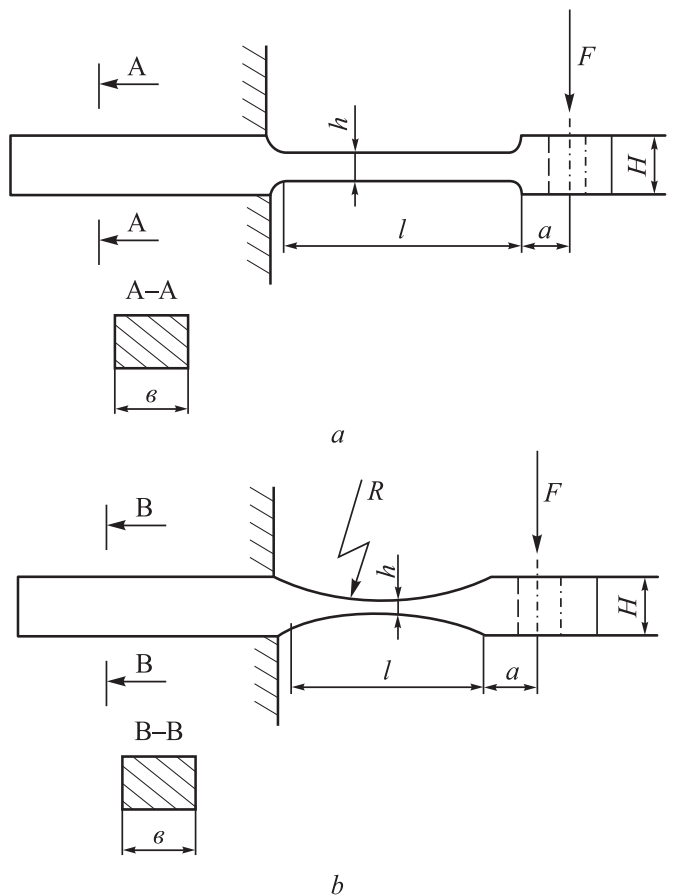


Fig. 4. Sketches of the samples:  
*a* – flat samples; *b* – corset samples

Рис. 4. Эскизы образцов:  
*a* – плоские образцы; *b* – корсетные образцы

#### Dimensions of fatigue test samples, mm

##### Размеры образцов для испытания на усталость, мм

Sample	<i>a</i>	<i>b</i>	<i>l</i>	<i>h</i>	<i>H</i>	<i>R</i>
<i>a</i>	10	22	43	5	13	–
<i>b1</i>	9	20	56	5	13	100
<i>b2</i>	24	20	56	5	13	100

#### STRESS VS. VIBRATION AMPLITUDE IN FLAT SAMPLES

The eference point is located at the sample's restraint point. The bending moment at a distance  $x$  from the restraint point is given by:

$$M = F(l + a - x). \quad (2)$$

The displacement of the sample segment with a height  $h$ :  $\frac{d^2 y}{dx^2} = \frac{F(l + a - x)}{EJ_1}$ , where  $J_1 = \frac{bh^3}{12}$ .

Initial conditions are:  $x = 0$ ;  $y_1 = 0$ ;  $\frac{dy_1}{dx} = 0$ .

A solution for the specified initial conditions is:

$$\begin{cases} \frac{dy_1}{dx} = \frac{F}{EJ_1} x \left( l + a - \frac{x}{2} \right); \\ y_1 = \frac{F}{EJ_1} \frac{x^2}{2} \left( l + a - \frac{x}{3} \right). \end{cases} \quad (3)$$

An equation for the displacement of the sample segment with height  $H$ :  $\frac{d^2 y_2}{dx^2} = \frac{F(l+a-x)}{EJ_2}$ , where  $J_2 = \frac{bH^3}{12}$ .

The solution is:

$$\begin{cases} \frac{dy_2}{dx} = \frac{F}{EJ_2} x \left( l + a - \frac{x}{2} \right) + C_1; \\ Y_2 = \frac{F}{EJ_2} \frac{x^3}{2} \left( l + a - \frac{x}{3} \right) + C_1 x + C_2. \end{cases} \quad (4)$$

Initial conditions are:  $x = l$ ;  $\frac{dy_1}{dx} = \frac{dy_2}{dx}$ ;  $y_1 = y_2$ .

By substituting the values of  $x = l$  into (3) and (4), and solving the equations, we obtain:

$$C_1 = \frac{F}{E} l \left( \frac{l}{2} + a \right) \left( \frac{1}{J_1} - \frac{1}{J_2} \right); \quad C_2 = \frac{F}{E} \frac{l^2}{2} \left( \frac{l}{3} + a \right) \left( \frac{1}{J_1} - \frac{1}{J_2} \right).$$

Using the constants the  $C_1$  and  $C_2$ , along with the equation for  $y_2$  derived from (4), we are able to determine the maximum displacement at the point of force application for  $x = l + a$ :

$$\begin{aligned} A_m = & \frac{F}{EJ_2} \frac{(l+a)^3}{3} + \frac{F}{E} l(l+a) \left( \frac{l}{a} + a \right) \left( \frac{1}{J_1} - \frac{1}{J_2} \right) - \\ & - \frac{F}{E} \frac{l^2}{2} \left( \frac{l}{3} + a \right) \left( \frac{1}{J_1} - \frac{1}{J_2} \right). \end{aligned}$$

Given the provided values of  $h$  and  $H$ , where  $J_2 \gg J_1$  ( $J_1 = 208.3 \text{ mm}^4$ ;  $J_2 = 3662 \text{ mm}^4$ ), taking into account this inequality and disregarding the inherent bending of the heightened sample segment with height  $H$ , we arrive at a more straightforward expression:

$$A_m = \frac{Fl}{EJ_1} \left( a^2 + la + \frac{l^2}{3} \right). \quad (5)$$

The stress at the reference cross-section (the restraint point) is:  $\sigma = \frac{F(l+a)}{W}$ .

By expressing  $F$  from (5) and taking into account that  $\frac{J_1}{W} = \frac{h}{2}$ , we obtain the final expression:

$$\sigma = \frac{1,5h(l+a)}{l(3a^2 + 3la + e^2)} EA_m. \quad (6)$$

For the sample dimensions indicated in Fig. 4,  $a$ , we get:  $\sigma = 26.9 \cdot 10^{-5} EA_m$ .

For the average Young's modulus  $E = 2 \cdot 10^5 \text{ MPa}$ :  $\sigma = 53.8 A_m$ , where  $\sigma$  is measured in MPa,  $A_m$  in mm.

## STRESS VS. VIBRATION AMPLITUDE IN CORSET SAMPLES

We approached the analysis of displacements separately for the curved and thickened segments.

To estimate the displacement of the curved segment, we positioned the origin in the midpoint of this segment (at  $l/2$  from the restraint point). Consequently, the height of the cross-section at a distance  $x$  from the origin is given by:

$$h(x) = h + \left( R - \sqrt{R^2 - x^2} \right). \quad (7)$$

The bending moment at  $x$  is:  $M(x) = F \left( \frac{l}{2} + a - x \right)$ .

The equation for the displacement is derived from equation (1) by substituting  $J_1 = \frac{bh^3(x)}{12}$ . This is further supplemented by  $h(x)$  from equation (7).

The resultant equation is:

$$\frac{d^2 y_1}{dx^2} = \frac{1,5F}{bE} \frac{0,5l + a - x}{\left( 0,5h + R - \sqrt{R^2 - x^2} \right)^3}. \quad (8)$$

The value of  $x$  is in the range:  $-\frac{l}{2} \leq x \leq l_2$ .

A computer-generated solution of differential equation (8) for  $x = 0.5l$ : produces the displacement  $y_{1m}$  and angle  $\theta_{1m} = \frac{dy_1}{dx}$ .

For the estimation of the displacement of the thickened segment, we positioned the origin at a distance  $l$  from the sample's restraint point.

The equation describing the displacement of this segment is:  $\frac{d^2 y_2}{dx^2} = \frac{F(a-x)}{EJ_2}$ , where  $J_2 = \frac{bH^3}{12}$ .

The solution for this equation is:

$$\begin{cases} \frac{dy_2}{dx} = \frac{F}{EJ_2} x \left( a - \frac{x}{2} \right) + C_1; \\ y_2 = \frac{F}{EJ_2} \frac{x^2}{2} \left( a - \frac{x}{3} \right) + C_1 x + C_2, \end{cases} \quad (9)$$

where  $0 \leq x \leq a$ .

Initial conditions are:  $x = 0$ ;  $\theta_{1m} = \frac{dy_2}{dx}$ ;  $y_2 = y_{1m}$ .

Resulting in  $C_1 = \theta_{1m}$ ;  $C_2 = y_{1m}$ .

By substituting  $x = a$  into (9), we find  $y_2$  at the point of force application, which is the amplitude of oscillations:

$$A_m = \frac{F}{EJ_2} \frac{a^3}{2} + \theta_{1m} a + y_{1m}.$$

Due to the substantial value of  $J_2$ , the first term of this expression is significantly smaller compared to the other two and can be disregarded.

Let us denote  $\theta'_{lm}$  and  $Y'_{lm}$  the values derived from equation (9) for  $\frac{1,5F}{bE} = 1$ .

$$\text{Then } \theta_{lm} = \theta'_{lm} \frac{1,5F}{bE}; y_{lm} = y'_{lm} \frac{1,5F}{bE}.$$

The amplitude of oscillations is:

$$A_m = \frac{1,5F}{bE} (\theta'_{lm} a + y'_{lm}). \quad (10)$$

The stress in the sample cross-section at the center of the curved segment:  $\sigma = \frac{F(0,5l + a)}{W}$ .

By expressing  $F$  from equation (10) and considering  $W = \frac{bh^2}{6}$ , we arrive the final expression:

$$\sigma = \frac{2(l + 2a)}{h^2(\theta'_{lm} a + y'_{lm})} EA_m. \quad (11)$$

The problem was addressed through numerical solutions. Computer calculations for the b1 and b2 samples (with dimensions provided in the table and Fig. 4) yielded:

- sample b1:  $\theta'_{lm} = 59.84$ ;  $y'_{lm} = 1853.2$ ;
- sample b2:  $\theta'_{lm} = 84.1$ ;  $y'_{lm} = 2532.4$ .

From equation (11), we obtain:

- sample (b1):  $\sigma = 24.75 \cdot 10^{-3} EA_m$ , MPa;
- sample (b2):  $\sigma = 18.3 \cdot 10^{-3} EA_m$ , MPa.

Considering the average Young's modulus  $E = 2 \cdot 10^5$  MPa:

- $\sigma = 49.5 A_m$  for sample b1;
- $\sigma = 36.6 A_m$  for sample b2.

Here,  $\sigma$  is measured in MPa and  $A_m$  in mm.

#### ERROR ESTIMATION OF THE STRESS VALUE IN THE REFERENCE CROSS-SECTION

If direct measurement errors for variations in Young's modulus and the geometric dimensions of the sample are available, we can estimate the error of the indirectly measured  $\sigma$  as stated in equation (6)

$$\frac{\Delta\sigma}{\sigma} = \delta_A + \delta_E + \delta_e, \quad (12)$$

where  $\delta_E = \frac{\Delta E}{E}$  is the relative error of Young's modulus;

$\delta_A = \frac{\Delta A}{A}$  is the relative error of the amplitude;

$$\delta_e = \frac{\Delta h}{h} + \left[ \frac{1}{a+l} + \frac{1}{l} + \frac{2l+3a}{3\left(a^2+ab+\frac{l^2}{3}\right)} \right] \Delta l + \left( \frac{1}{a+l} + \frac{l+2a}{a^2+al+\frac{l^2}{3}} \right) \Delta a - \quad (13)$$

is the relative error of the sample's dimensions.

The relative error of the amplitude of oscillations has been previously determined as:  $\delta_A = 0.01$  (1 %).

The relative error of the sample's linear dimensions is estimated as (13):

$$\delta_e = 0.0123 \text{ (1.23 \%)}. \quad (14)$$

There is inherent uncertainty in the value of Young's modulus. Available sources specify that for high elastic steels, this value varies from  $1.9 \cdot 10^5$  to  $2.1 \cdot 10^5$  MPa. In this context  $\Delta E = \pm 10^4$  MPa should be considered as the error in Young's modulus:

$$\delta_E = 0.05 \text{ (5 \%)}. \quad (15)$$

The total error of the estimated stress in the reference section is given by:

$$\frac{\Delta\sigma}{\sigma} = 0.0723 \text{ (7.23 \%)}. \quad (16)$$

For validation purposes, we employed static calibration to estimate the stress in the sample. This involved applying static loading to the sample with the force  $F$ , measured using a reference dynamometer. The stress in the sample is then estimated from the force value using equation

$$\sigma = \frac{6F(l+a)}{bh^2}. \quad (17)$$

We simultaneously recorded readings from the reference dynamometer and the linear displacement gauge (which measured strain under load).

The following values were obtained:

$$\left. \begin{aligned} \sigma_A &= 501 A_m \cdot 10^{-6}, \text{ Pa}, \\ \sigma_F &= \frac{6(l+a)}{bh^2} F = 0.596 \cdot 10^{-6} F, \text{ Pa}; \\ &\text{for sample } a \\ \sigma_A &= 485 A_m \cdot 10^{-6}, \text{ Pa}, \\ \sigma_F &= \frac{6(l/2+a)}{bh^2} F = 0.444 \cdot 10^{-6} F, \text{ Pa}. \\ &\text{for sample } b \end{aligned} \right\}$$

This reveals that stress values estimated from strain and measured by the reference dynamometer differ by no more than 10 %.

To assess this outcome, let us calculate the error of the stress value derived from equation (17). It is the sum of the force measurement error  $\sigma_F = \frac{\Delta F}{F}$  and the sample's linear dimension error  $\sigma_E = \frac{\Delta l + \Delta a}{l + a} + \frac{\Delta b}{b} \frac{z \Delta h}{h}$ :

$$\frac{\Delta \sigma}{\sigma} = \delta_F + \delta_e. \quad (18)$$

Given that we measured the sample with a precise micrometer,  $\Delta a = \Delta l = \Delta b = \Delta h = 0.01$  mm and  $\delta_e = 0.00075$  (0.075 %), which is a very low error. The primary contributor to the total error is the force measurement by the reference dynamometer, which is approximately 1 % and corresponds to the instrument's calibration error.

The stress calculated from strain  $\sigma_A$  is 8 – 10 % higher than the stress calculated from the force  $\sigma_F$  for both samples depicted in Fig. 4, *a* and *b*. This divergence can be attributed to several factors: the error in Young's modulus value; the assumptions made when deriving the equations for  $\sigma_A$  and systematic error overlooked during instrument calibration.

## RESULTS AND DISCUSSION

We employed the proposed procedure to conduct a test a sample composed of 03H18K9M5T-EL steel grade (Fig. 4, *a*). The focal point of our investigation lies in the frequency stability when subjected to loads near the fatigue limit. We scrutinized the frequency characteristics of a sample under 670 MPa load applied at ~200 Hz. Notably, the frequency deviation from the initial value displayed an upward trend denoted by positive values and a downward trend with negative values. The sample underwent a total of 50 million loading cycles. The maximum frequency deviation recorded was 0.75 Hz, making it the most stable frequency among all the samples. Interestingly, a significant frequency shift was observed within the initial 10 million load cycles, amounting to 0.54 Hz. The sample underwent continuous testing, with a load cycle of 10 million cycles per day. The frequency of the sample exhibited changes following overnight interruptions. Specifically, after a 10-hour pause, the morning frequency surpassed the frequency recorded the night before.

In Fig. 5, *a*, two envelope curves are depicted. Curve 1 portrays the frequency when the testing installation is operational, while Curve 2 represents the frequency once the testing installation is halted after daily operation. Curve 1 delineates the alteration in the initial frequency (“on” frequency), whereas Curve 2 showcases the modification in the final frequency (“off” frequency). The daily fluctuations in frequency during the cyclic testing period fall within the range delineated by the two curves.

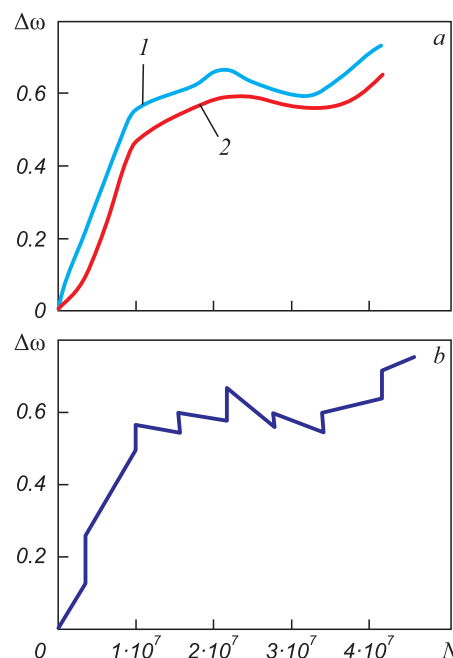


Fig. 5. Frequency characteristics during cyclic loading with interruptions in tests:

1 – frequency at the moment of switching on;  
2 – frequency at the moment of shutdown

Рис. 5. Частотные характеристики при циклическом нагружении с перерывами в испытаниях:

1 – частота в момент включения; 2 – частота в момент отключения

Another frequency response is illustrated in Fig. 5, *b*, represented by a discontinuous line. The vertical steps correspond to frequency shifts following overnight interruptions. The sloped lines indicate daily frequency variations as the number of load cycles increases.

## CONCLUSIONS

We proposed a procedure along with equations to estimate stresses on steel samples of various shapes. This estimation allows us to assess the frequency characteristic alterations during cyclic loading, following the “soft” cantilever bending scheme applied to flat samples with sinusoidal loading. This approach proves to be an effective tool for analyzing the frequency stability and variations in non-continuous fatigue tests. Moreover, it can be employed to gauge material internal friction and energy dissipation, facilitating the determination of damping capacity.

## REFERENCES / СПИСОК ЛИТЕРАТУРЫ

1. Shkol'nik L.M. *Fatigue Testing Methodology. Guide*. Moscow: Metallurgiya; 1978:304. (In Russ.).  
Школьник Л.М. *Методика усталостных испытаний: Справочник*. Москва: Металлургия; 1978:304.
2. Gadolina I.V., Makhutov N.A., Erpalov A.V. Varied approaches to loading assessment in fatigue studies. *International Journal of Fatigue*. 2021;144:106035.  
<https://doi.org/10.1016/j.ijfatigue.2020.106035>



3. Suresh S. *Fatigue of Metals*. Cambridge University Press; 2006:701.
4. Terent'ev V.F., Korableva S.A. *Fatigue of Metals*. Moscow: Nauka; 2015:479. (In Russ.).  
Терентьев В.Ф., Кorableва С.А. *Усталость металлов*. Москва: Наука; 2015:479.
5. Gromov V.E., Ivanov Yu.F., Vorobiev S.V., Konovalov S.V. *Fatigue of Steels Modified by High Intensity Electron Beams*. Cambridge; 2015:272.
6. Mughrabi H., Christ H.-J. Cyclic deformation and fatigue of selected ferritic and austenitic steels; specific aspects. *ISIJ International*. 1997;37(12):1154–1169.  
<https://doi.org/10.2355/isijinternational.37.1154>
7. Gadenin M.M. Study on damaging and fatigue life of constructions under single- and two-frequency loading modes based on deformational and energy approaches. *Inorganic Materials*. 2018;54(15):1543–1550.  
<https://doi.org/10.1134/S0020168518150049>
8. Gadenin M.M. Influence of loading cycle form on resistance to cyclic deformation and destruction of structural materials. *Vestnik nauchno-tekhnicheskogo razvitiya*. 2010;(9(37)):15–19. (In Russ.).  
Гаденин М.М. Влияние формы цикла нагружения на сопротивление циклическому деформированию и разрушению конструкционных материалов. *Вестник научно-технического развития*. 2010;(9(37)):15–19.
9. Myl'nikov V.V., Shetulov D.I., Kondrashkin O.B., Chernyshov E.A., Pronin A.I. Changes in fatigue resistance of structural steels at different loading spectra. *Izvestiya. Ferrous Metallurgy*. 2019;62(10):796–802. (In Russ.).  
<https://doi.org/10.17073/0368-0797-2019-10-796-802>  
Мыльников В.В., Шетулов Д.И., Кондрашкин О.Б., Чернышов Е.А., Пронин А.И. Изменение показателей сопротивления усталости конструкционных сталей при различных спектрах нагружения. *Известия вузов. Черная металлургия*. 2019;62(10):796–802.  
<https://doi.org/10.17073/0368-0797-2019-10-796-802>
10. Gadenin M.M. Calculation-and-experimental estimation of the role of the frequency ratio in changing the endurance at two-frequency deformation modes. *Zavodskaya laboratoriya. Diagnostika materialov*. 2019;85(1-1):64–71. (In Russ.).  
<https://doi.org/10.26896/1028-6861-2019-85-1-1-64-71>  
Гаденин М.М. Расчетно-экспериментальная оценка роли соотношения частот в измерении долговечности при двухчастотных режимах деформирования. *Заводская лаборатория. Диагностика материалов*. 2019; 85(1–1):64–71.  
<https://doi.org/10.26896/1028-6861-2019-85-1-1-64-71>
11. Troshchenko V.T., Khamaza L.A., Pokrovsky V.V., etc. *Cyclic Deformation and Fatigue of Metals*. Bily M. ed. Amsterdam: Elsevier; 1993:500.
12. Golovin S.A., Tikhonova I.V. Temperature dependence of internal friction and properties of deformed low-carbon iron alloys. *Deformatsiya i razrushenie materialov*. 2013;(7):16–21. (In Russ.).  
Головин С.А., Тихонова И.В. Температурная зависимость внутреннего трения и свойства деформированных малоуглеродистых сплавов железа. *Деформация и разрушение материалов*. 2013;(7):16–21.
13. Golovin S.A., Petrushina A.G. Temperature spectrum of internal friction of cast iron. *Izvestiya. Ferrous Metallurgy*. 2009;52(9):51–54. (In Russ.).  
Головин С.А., Петрушина А.Г. Температурный спектр внутреннего трения чугунов. *Известия вузов. Черная металлургия*. 2009;52(9):51–54.
14. McClafflin D., Fatemi A. Torsional deformation and fatigue of hardened steel including mean stress and stress gradient effects. *International Journal of Fatigue*. 2004;26(7):773–784.  
<https://doi.org/10.1016/j.ijfatigue.2003.10.019>
15. Golovin I.S., Bychkov A.S., Mikhailovskaya A.V., Dobatkin S.V. Contributions of phase and structural transformations in multicomponent Al-Mg alloys to the linear and non-linear mechanisms of anelasticity. *The Physics of Metals and Metallography*. 2014;115(2):192–201.  
<https://doi.org/10.1134/S0031918X14020082>  
Головин И.С., Бычков А.С., Михайловская А.В., Добаткин С.В. Вклад фазовых и структурных превращений в многокомпонентных АL-MG сплавах в линейные и нелинейные механизмы неупругости. *Физика металлов и металловедение*. 2014;115(2):204.  
<https://doi.org/10.7868/S0015323014020089>
16. Kardashev B.K., Sapozhnikov K.V., Betekhtin V.I., Kadomtsev A.G., Narykova M.V. Internal friction, Young's modulus, and electrical resistivity of submicrocrystalline titanium. *Physics of the Solid State*. 2017;59(12):2381–2386.  
<https://doi.org/10.1134/S1063783417120204>
17. Blanter M.S., Golovin I.S., Neuhauser H., Sinning H.R. Internal friction in metallic materials. *Springer Series in Materials Science*. 2007;90:1–535.  
<https://doi.org/10.1007/978-3-540-68758-0>
18. Stolyarov V.V. Inelasticity of ultrafine-grained metals. *Izvestiya. Ferrous Metallurgy*. 2010;53(11):51–54. (In Russ.).  
Столяров В.В. Неупругость ультрамелкозернистых металлов. *Известия вузов. Черная металлургия*. 2010;53(11):51–54.
19. Romaniv O.N., Laz'ko L.P., Kry's'kiv A.S. Relationship of internal friction to the fatigue life of patented steel wire. *Soviet Mater Science*. 1984;19:522–527.  
<https://doi.org/10.1007/BF00722120>
20. Myl'nikov V.V., Shetulov D.I. *Installation for fatigue testing*. Patent RF no. 2781466. *Bulleten' izobretenii*. 2022;(29). (In Russ.).  
Пат. 2781466 RU. *Установка для испытаний на усталость* / Мыльников В.В., Шетулов Д.И.; заявл. 14.09.2021; опубл. 12.10.2022. Бюл. № 29.
21. Demidov A.S., Kashelkin V.V. Determination of damage and stress state of beam samples by changing the natural frequency and amplitude of vibrations. *Vestnik Moskovskogo aviatsionnogo instituta*. 2009;16(3):62–64. (In Russ.).  
Демидов А.С., Кашелкин В.В. Определение поврежденности и напряженного состояния балочных образцов по изменению собственной частоты и амплитуды колебаний. *Вестник Московского авиационного института*. 2009;16(3):62–64.

## Information about the Authors

## Сведения об авторах

**Vladimir V. Myl'nikov**, *Cand. Sci. (Eng.), Assist. Prof. of the Chair "Building Technology"*, Nizhny Novgorod State University of Architecture, Building and Civil Engineering

**ORCID:** 0000-0001-5545-4163

**E-mail:** mrmylnikov@mail.ru

**Eduard A. Dmitriev**, *Dr. Sci. (Eng.), Assist. Prof., Rector*, Komsomolsk-on-Amur State University

**ORCID:** 0000-0001-8023-316X

**E-mail:** rector@knastu.ru

**Владимир Викторович Мыльников**, *к.т.н., доцент кафедры «Технологии строительства»*, Нижегородский государственный архитектурно-строительный университет

**ORCID:** 0000-0001-5545-4163

**E-mail:** mrmylnikov@mail.ru

**Эдуард Анатольевич Дмитриев**, *д.т.н., доцент, ректор*, Комсомольский-на-Амуре государственный университет

**ORCID:** 0000-0001-8023-316X

**E-mail:** rector@knastu.ru

Received 12.02.2023

Revised 12.03.2023

Accepted 11.04.2023

Поступила в редакцию 12.02.2023

После доработки 12.03.2023

Принята к публикации 11.04.2023



UDC 621.771.06

DOI 10.17073/0368-0797-2023-3-376-386



Original article

Оригинальная статья

PARAMETRIC MODEL OF A THREE-ROLL UNIT  
OF RADIAL-SHEAR ROLLING MINI-MILLD. V. Troitskii<sup>✉</sup>, Yu. V. Gamin, S. P. Galkin, A. S. Budnikov

National University of Science and Technology “MISIS” (4 Leninskii Ave., Moscow 119049, Russian Federation)

<sup>✉</sup> d.v.troitskiy@gmail.com

**Abstract.** The article discusses the main structural features of radial-shear rolling mini-mills and their most common sizes. A generalized algorithm for designing such mills using modern CAD systems is described. The main approaches to the methodology of software adaptive design of models in engineering are listed with their features and differences. In particular, the methodology of horizontal modeling, explicit modeling methodology, and resilient modeling strategy are considered. The article describes the method of virtual squeezes and presents the main geometric scheme of the spatial position of the rollers of the longitudinal profile. The data obtained as a result of the calculations were encoded and summarized in tables. The formulas presented were used in the parametric design of the roller unit of the three-roller mill 30-70 using Autodesk Inventor software. The obtained parametric model, using classical formulas of the virtual squeezes method, allows for automatic reconstruction of the deformation zone for new initial parameters. The developed model is applicable for three-roller mills with working roll angles  $\delta = 5 - 15^\circ$  and feed angles  $\beta = 18 - 22^\circ$ . The article presents sketches and diagrams of the constructed model for different rolling angles – 5, 10, and  $15^\circ$ . As the rolling angle increases, a noticeable increase in the conicity of the roller is observed. The vector of future research on improving the obtained software model was indicated. Further research on improving the parametric model will include expanding the set of existing parameters to include the frame and full set of roller connections – neck, cover, pressing device, etc.

**Keywords:** helical rolling, radial-shear rolling (RSR), mini-mills, technological squeeze, feed angle, rolling-off, crossing, eccentricity, deformation zone

**For citation:** Troitskii D.V., Gamin Yu.V., Galkin S.P., Budnikov A.S. Parametric model of a three-roll unit of radial-shear rolling mini-mill. *Izvestiya. Ferrous Metallurgy*. 2023;66(3):376–386. <https://doi.org/10.17073/0368-0797-2023-3-376-386>

ПАРАМЕТРИЧЕСКАЯ МОДЕЛЬ ТРЕХВАЛКОВОГО УЗЛА МИНИ-СТАНА  
РАДИАЛЬНО-СДВИГОВОЙ ПРОКАТКИД. В. Троицкий<sup>✉</sup>, Ю. В. Гамин, С. П. Галкин, А. С. Будников

Национальный исследовательский технологический университет «МИСИС» (Россия, 119049, Москва, Ленинский пр., 4)

<sup>✉</sup> d.v.troitskiy@gmail.com

**Аннотация.** В статье рассмотрены основные конструктивные особенности мини-станов радиально-сдвиговой прокатки (РСП), их наиболее распространенные типоразмеры. Описан обобщенный алгоритм проектирования таких станков с применением современных CAD систем. Перечислены основные подходы к методологии программного адаптивного проектирования моделей в инжиниринге, приведены их особенности и различия. В частности, рассмотрены методологии горизонтального моделирования, моделирования с явными ссылками и устойчивого моделирования. Описана методика виртуальных пережимов, приведена основная геометрическая схема пространственного положения валков продольного профиля. Полученные в результате расчетов данные закодированы и сведены в таблицы. Приведенные формулы использованы при параметрическом проектировании валкового узла трехвалкового стана РСП на примере типоразмера «30-70» в программной среде Autodesk Inventor. Полученная параметрическая модель, используя классические формулы методики виртуальных пережимов, позволяет автоматически перестраивать очаг деформации для новых исходных параметров. Разработанная модель применима для трехвалковых станков, имеющих углы раскатки рабочих валков  $\delta = 5 - 15^\circ$  и углы подачи  $\beta = 18 - 22^\circ$ . Приведены эскизы и эпюры построенной модели для различных углов раскатки – 5, 10 и  $15^\circ$ . При увеличении угла раскатки заметно значительное увеличение конусности валка. Обозначен вектор будущих исследований по доработке и совершенствованию полученной программной модели. Дальнейшие исследования по доработке параметрической модели будут включать в себя расширение набора имеющихся параметров для добавления в компьютерную модель станины и валковых узлов, включая опоры, подушки, крышки, нажимное и уравнивающее устройство и т. д.

**Ключевые слова:** винтовая прокатка, радиально-сдвиговая прокатка (РСП), мини-станы, технологический пережим, угол подачи, угол раскатки, угол скрещивания, эксцентриситет, очаг деформации

**Для цитирования:** Троицкий Д.В., Гамин Ю.В., Галкин С.П., Будников А.С. Параметрическая модель трехвалкового узла мини-стана радиально-сдвиговой прокатки. *Известия вузов. Черная металлургия*. 2023;66(3):377–386.  
<https://doi.org/10.17073/0368-0797-2023-3-376-386>

## INTRODUCTION

Modern radial shear rolling (RSR) mini-mills are characterized by a simple design, utilizing optimal feed angles ( $18 - 22^\circ$ ) and rolling angles (not exceeding  $10 - 12^\circ$ ) [1]. Typically, these mills are specifically assembled for the production of particular products, determined by the mill's dimensions and structural features. Despite their compactness and high mobility, these mills offer a wide range of full-scale capabilities. Helical rolling mini-mills align with the requirements of lean production [2] and facilitate the application of innovative RSR methods, which enhance the material properties of long products through intensive plastic deformation [3; 4]. For example, pure magnesium has shown significant improvement in its mechanical properties through three roller helical rolling, attributed to changes in its microstructure [5]. Researchers in [6; 7] have documented the formation of a gradient structure and the improved properties of austenite stainless steel AISI 321. The technological capabilities of RSR mini-mills have been successfully tested using titanium rods in accordance with specific requirements [8].

For example, the «30-80» three-roller piercing mini-mill is specifically designed for hot piercing of ingots into shell with a bottom [9 – 11]. It utilized a wedge lock device as a screw-down mechanism, and the rollers are characterized by pre-feed and rolling angles according to the design. The mini-mill stands out for its mobility, compactness, and the absence of the need for assembly on a power basement.

Furthermore, numerous industrial and research entities have successfully implemented the «14-40» three-roller helical mini-mills [1; 12]. A comprehensive overview of the main designs and specifications of RSR mini-mills can be found in [1]. These new-generation mini-mills exhibit lower metal intensity, reduced energy consumption, and offer simplified operation compared to small section mills using longitudinal rolling techniques. This makes them particularly attractive to small and medium-sized companies operating in the metallurgy and mechanical engineering sectors.

Previously, researchers [13 – 15] developed a systematic approach to the design of mill stand based on the unified “metal deformation–mill design” system, enabling the production of items with predetermined properties.

The new mill stand designs are based on several key principles: the use of a close-top roll housing, positioning the working rollers at consistent angles of feed and rolling, and separation the actuating mechanism of roller

positioning from direct action of the rolling force. These design principles have not only simplified the mini-mill design but also improved its operational conditions.

Typically, the design process for such mills begins with the deformation zone and the predetermined main geometrical profiles of the rollers and rolled ingots. Given the wide range of dimensions for RSR mills and the need to design custom equipment to meet specific customer demands, it is advisable to utilize the parametrization capabilities available in most modern CAD systems during the design process. These capabilities significantly reduce the time required for developing computer models and facilitate subsequent refinement and error elimination.

Modern CAD systems offer parameterization capabilities, allowing for the creation of a wide range of parameters. These parameters can be static (representing a fixed value), calculated (expressed through mathematical equations based on static parameters), or reference (referring to the actual value of existing geometry for use in other geometrical units). CAD systems enable the establishment of semantic connections between constructed geometry and developed parameters of any type, thereby creating associative bonds between different components of the designed equipment.

The choice and implementation of an appropriate design methodology play a crucial role in the design process. A well-defined methodology allows for the development of a unified approach to constructing associative bonds and establishing parametric dependencies between individual units [16]. This formalization of parametric simulation methods brings the design process closer to the original intent of the engineer [17], promotes standardization and internal consistency within the simulated model, reduces development time, and maximizes the potential for reusing previously developed parts and units. Employing an appropriate and well-designed methodology enables faster modifications of models compared to an informal approach [18; 19]. The development of design methods is closely tied to the advancement of CAD systems and their application in engineering design tasks. Ultimately, these methods represent the accumulated engineering experience of researchers aimed at enhancing the flexibility and validity of the designed models [20]. An incorrect or non-formalized methodology can have a negative impact on the overall quality of the model and the time required for the design process [21]. There are documented cases where the correct selection of a methodology, particularly in the context of MDO (*Multidisciplinary design optimization*) tasks, has led to significant achievements in aircraft production [22].



There are three formalized methodologies known for developing computer models, aimed at enhancing model flexibility, reduction development and modification time, and improving overall model stability.

*Horizontal Modeling methodology:* This simulation strategy, patented by Delphi Technologies [23], focuses on reducing critical errors that may arise during model modification by elimination of dependences in the existing geometry and parameters. Traditional CAD systems typically employ a vertical tree structure for elements, which can lead to errors when modifications are made. The Horizontal Modeling Methodology proposes minimizing such dependencies and instead referring to unaffected initial elements, such as basic planes and the center of coordinates. This transforms the vertical tree structure into a horizontal one, reducing the occurrence of errors.

*Explicit Reference Modelling methodology (ERM):* Proposed in [18], ERM aims to minimize the number of dependencies and restrictions related to the current geometry in the model, as it tends to vary with changes in the model. Instead, references are used, which can refer to auxiliary geometric objects. Unlike the Horizontal Modeling Methodology, ERM is focused on maintaining the global concept of parametrical approach.

*Resilient Modeling methodology* [24] was introduced in [25]. This methodology emphasizes the creation of robust models with extensive possibilities for reusing units and elements. It involves optimizing parent-child dependencies and organizing the structure of elements in a more comprehensible manner.

Each of these methodologies has its advantages and disadvantages depending on the pattern of the developed model. The key criterion for the operability of a parametric model is its ability to adapt to changes made to its elements. The operability of these methodologies has been demonstrated in various optimization scenarios, including the automatic generation of numerous geometrical variations and units [26].

This work focuses on the parametric simulation of a roller unit using generalized algorithm for designing of deformation zone of a three-roller RSR mill in Autodesk Inventor software. The model is developed following the recommendations of the Explicit Reference Modelling.

## FORMULATION OF THE PROBLEM AND EXPERIMENTAL METHODS

### Geometry of the spatial position of longitudinal profile rolls

In order to construct and calculate the geometry of the spatial position of longitudinal profile rollers, a procedure known as virtual squeezes is utilized, which

was developed and proposed for calculations of RSR mini-mills [13]. This procedure is based on invariant geometry relations of RSR mills, taking into account changes in virtual angles of feed and rolling along the axis of the deformation zone. It allows for efficient parametrization of roller dimensions and the deformation zone [14]. The procedure is based on the layout depicted in Fig. 1, *a*, where:

– 3 represents the considered cross section of the ingot with radius  $r_p$  and center at  $O$ ;

– B represents the cross section of the roller with radius  $R_p$  and center at  $O_B$ , in contact with the ingot cross section 3 at point  $F$ ;

–  $Ol$  and  $CL$  are the rolling axes for the ingot and the deformation area, respectively;

–  $GG_B$  is the common perpendicular (eccentricate) with length  $E$  to the roller and rolling axes, meaning  $\angle OGG_B = \angle CG_BG = 90^\circ$ ;

–  $OC$  is the line perpendicular to the rolling axis with length  $P$ , intersecting the roller axis, denoted as  $\angle COG = 90^\circ$ . In drum type mills, it is positioned on the drum axis;

–  $\beta, \delta, \gamma$  represent the angles of feed, rolling and cross-ing, respectively.

The set of notions used, such as technological squeeze, geometrical squeeze, and design layout, were introduced in [27; 28]. According to the procedure, the determination of the roller profile is simplified to calculating the radius of the roller's cross section that will come into contact with the ingot's cross section of a known radius  $r_i$ . This contact point is located at a known distance  $\Delta l_i$  along the rolling axis from the technological squeeze (from point  $O$ ) (Fig. 1, *b*).

### Calculation of roll calibration using the deformation center

Now, let us illustrate the calculations based on the procedure by determining the roller radius in extreme cross section of the deformation zone using the initial data for «30-70» mill (Table 1). The roller diameter in the squeeze is chosen to ensure the minimum pass without the roller surface crossing. The maximum feasible roller diameter in the squeeze, taking into account the feed and rolling angles, as well as the gap between rollers, is determined by the equation [29]

$$D_B^{\max} = \frac{d_k^{\min} - \frac{\Delta}{\cos \varphi}}{k}, \quad (1)$$

where  $D_B^{\max}$  is the maximum possible diameter in the squeeze, mm;  $d_k^{\min}$  is the minimum roller pass diameter in the squeeze, mm;  $\Delta$  is the gap between adjacent rollers,

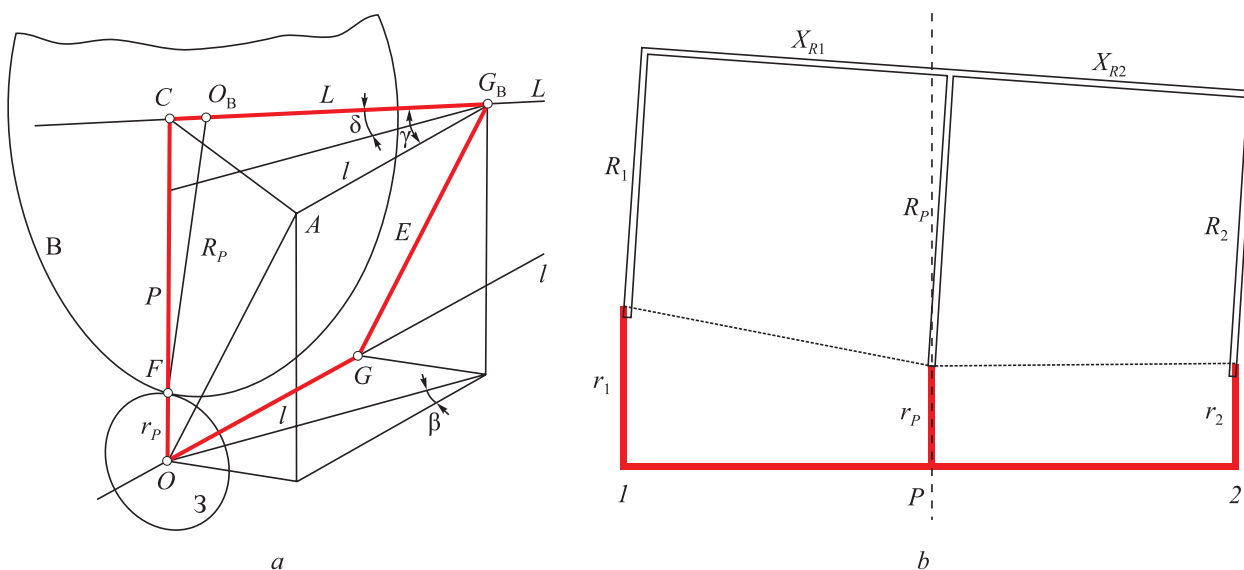


Fig. 1. Diagram of the relative position of the axes of roll  $CL$  and rolling  $Ol$  (a); designations of geometric dimensions of deformation focus and roll (b):

thick red line – deformation focus, double – roll;  $l, 2$  – sections of input and output, respectively;  $P$  – section of technological squeeze

Рис. 1. Схема взаимного расположения осей вала  $CL$  и прокатки  $Ol$  (a) и обозначения геометрических размеров очага деформации и вала (b):

красная толстая линия – очаг деформации; двойная – валок;  $l, 2$  – сечения входа и выхода соответственно;  $P$  – сечение технологического пережима

mm;  $\varphi$  is the inclination angle of the generator of the input roller cone, deg;  $k$  is the coefficient that relates the roller diameter to the pass diameter.

The coefficient  $k$  incorporates parameters such as the feed angle  $\beta$ , rolling angle  $\delta$  and the number of operating rollers, and can be determined using the equation:

$$k = \frac{\cos \delta - 0.87 \sqrt{0.75 \cos^2 \delta + 0.25 \cos^2 \beta}}{\cos \delta \sqrt{0.57 \cos^2 \delta + 0.19 \cos^2 \beta}}. \quad (2)$$

These conditions are subsequently verified by analyzing interference in the CAD system.

Table 1

### Source data for the calculation example

Таблица 1. Исходные данные для примера расчета

Parameter	Notation	Units of measurement	Value
Feed angle	$\beta$	deg	20
Rolling angle	$\delta$	deg	5
Roller radius in squeeze	$R_p$	mm	80
Ingot radius in squeeze	$r_p$	mm	15
Input cross section of deformation zone:			
– radius	$r_1$	mm	25
– distance to squeeze	$\Delta l_1$	mm	80
– roller cross section radius	$R_1$	mm	?
– distance from roller cross section center to roller cross section center in technological squeeze	$X_{R1}$	mm	?
Output cross section of deformation zone:			
– radius	$r_2$	mm	16.5
– distance to squeeze	$\Delta l_2$	mm	–80
– roller radius	$R_2$	mm	?
– distance from roller cross section center to roller cross section center in technological squeeze	$X_{R2}$	mm	?

The calculated data obtained are sufficient for plotting the roller calibration for three cross sections The calculated results are summarized in Table 2.

Similar calculations for roller unit calibration can be based on a higher number of cross sections to achieve greater precision. The calculation process for each cross section is similar to the aforementioned procedure. By using the described algorithm, it is possible to create a table of roller calibration with required step for production using a numerically controlled machine.

## KEY EXPERIMENTAL FINDINGS

The Explicit Reference Modeling methodology was chosen as the foundation for this work. All calculated parameters from Tables 1 and 2 were incorporated as user parameters into the Autodesk Inventor models. These parameters are directly calculated and determined within the Autodesk Inventor software.

To simplify the calculations within Autodesk Inventor, all the parameters are encoded as two-symbol variables (consisting of a Latin letter and a digit). The parameters are categorized as follows:

- parameters  $X$ : these serve as the main initial data for the model calculation;
- parameters  $A$ : these are used to determine the parameters of technological and geometrical squeezes;
- parameters  $B$ : these are used to determine the parameters of the virtual squeeze in cross section 1 of the deformation zone input;
- parameters  $C$ : these are used to determine the parameters of the virtual squeeze in cross section 2 of the deformation zone output.

A comprehensive list of the parameters is provided in Table 3. The accuracy of the constructed model is verified using the parameters  $X1$ ,  $X2$ ,  $A2$ ,  $B5$ ,  $B6$ ,  $C5$  and  $C7$ . The following relationship holds true for these parameters:

Table 2

### Results of calculation of calibration parameters for three sections

Таблица 2. Результаты расчета параметров калибровки по трем сечениям

Cross section	Deformation zone, mm		Roller, mm	
	$\Delta l_i$	$r_i$	$XR_i$	$R_i$
Input 1	80	25	78.001	80.512
Technological squeeze, $P$	0	10	0	80
Output 2	–80	16.5	–80.320	76.034

$$\begin{aligned} \cos X1 \cos X2 &= \cos B5 \cos B6 = \\ &= \cos C5 \cos C7 = \cos A2. \end{aligned} \quad (3)$$

The deformation zone in the model is created using a 3D sketch. The explicit parameters of this sketch are linked to the user-defined parameters. When the dependencies and initial data ( $X$ ) are correctly established, the 3D sketch of the model will have zero degrees of freedom. This means that the constructed geometry variant is the only possible one given the preset parameters. Removing any initial parameter ( $X$ ) will introduce degrees of freedom to the deformation zone model.

The layout of the mutual position of the roller and rolling axes is depicted in Fig. 2.

Fig. 3 illustrates the parameters  $A$ ,  $B$  and  $C$ , which are used to construct the geometrical and technological roller squeezes.

The deformation zone is constructed starting from the technological squeeze on the rolling axis, which serves as the common coordinate center of the model  $O$ . The rolling axis is plotted passing through the coordinate center. The distance  $l$  between technological and

Table 3

### Parameter coding table

Таблица 3. Таблица кодирования параметров

Notation	Parameter	Equation in Autodesk Inventor	Equation
<b>Initial (main) parameters</b>			
$X1$	Feed angle $\beta$ , deg	Explicit value (20)	Explicit value (20)
$X2$	Rolling angle $\delta$ , deg	Explicit value (5)	Explicit value (5)
$X3$	Roller radius in squeeze $R_p$ , mm	Explicit value (80)	Explicit value (80)
$X4$	Ingot radius in squeeze $r_p$ , mm	Explicit value (15)	Explicit value (15)
$X5$	Radius $r_1$ , mm	Explicit value (25)	Explicit value (25)
$X6$	Radius $r_2$ , mm	Explicit value (16.5)	Explicit value (16.5)

Table 3 (Continuation)

Parameter coding table

Таблица 3 (продолжение). Таблица кодирования параметров

Notation	Parameter	Equation in Autodesk Inventor	Equation
<b>Parameters of technological and geometrical squeezes</b>			
A1	Distance $P$ between rolling axis and roller axis in squeeze, mm	$x4 + x3 / \cos(x2)$	$A1 = X4 + \frac{X3}{\cos X2}$
A2	Crossing angle $\gamma$ , deg	$\text{acos}(\cos(x1) * \cos(x2))$	$\cos A2 = \cos X1 \cos X2$
A3	Length of common perpendicular $E$ , mm	$a1 * \sin(x1) * \cos(x2) / \sin(a2)$	$A3 = A1 \frac{\sin X1 \cos X2}{\sin A2}$
A4	Distance $L$ between technological and geometrical squeezes along the rolling axis, mm	$a1 * \sin(x2) / (\sin(a2) * \sin(a2))$	$A4 = A1 \frac{\sin X2}{\sin^2 A2}$
A5	Distance $l$ between technological squeezes along rolling axis, mm	$a4 * \cos(a2)$	$A5 = A4 \cos A2$
A6	Distance $LR$ from roller cross section center to geometrical squeeze, mm	$a4 - x3 * \tan(x2)$	$A6 = A4 - X3 \tan X2$
<b>Parameters of virtual squeeze in cross section 1 of deformation zone input</b>			
B1	Distance $l1$ to geometrical squeeze along rolling axis, mm	$a5 + x3$	$B1 = A5 + X3$
B2	Distance $L1$ to geometrical squeeze along roller axis, mm	$b1 / \cos(a2)$	$B2 = \frac{B1}{\cos A2}$
B3	Distance $P1$ between rolling axis and roller axis in perpendicular to rolling axis, mm	$\text{sqrt}((b1 * \tan(a2)) ^ 2 \text{ 6p} + (a3) ^ 2 \text{ 6p})$	$B3 = \sqrt{(B1 \tan A2)^2 + A3^2}$
B4	Distance $PN1$ between rolling axis and roller axis in perpendicular to roller axis, mm	$\text{sqrt}((b1 * \sin(a2)) ^ 2 \text{ 6p} + (a3) ^ 2 \text{ 6p})$	$B4 = \sqrt{(B1 \sin A2)^2 + A3^2}$
B5	Rolling angle $\delta 1$ , deg	$\text{acos}(b4 / b3)$	$\cos B5 = \frac{B4}{B3}$
B6	Feed angle $\beta 1$ , deg	$\text{atan}(a3 * \tan(a2) / b3)$	$\tan B6 = \frac{A3 \tan A2}{B3}$
B7	Roller radius $R1$ , mm	$\cos(b5) * (b3 - x5)$	$B7 = \cos B5 (B3 - X5)$
B8	Distance $LR1$ from roller cross section center to geometrical squeeze, mm	$b2 - b7 * \tan(b5)$	$B8 = B2 - B7 \tan B5$
B9	Distance $XR1$ from roller cross section center to roller cross section center of technological squeeze, mm	$b8 - a6$	$B9 = B8 - A6$
<b>Parameters of virtual squeeze in cross section 2 of deformation zone output</b>			
C1	Distance $l2$ to geometrical squeeze along rolling axis, mm	$a5 - x3$	$C1 = A5 - X3$
C2	Distance $L2$ to geometrical squeeze along roller axis, mm	$c1 / \cos(a2)$	$C2 = \frac{C1}{\cos A2}$
C3	Distance $P2$ between rolling axis and roller axis perpendicular to rolling axis, mm	$\text{sqrt}((c1 * \tan(a2)) ^ 2 \text{ 6p} + (a3) ^ 2 \text{ 6p})$	$C3 = \sqrt{(C1 \tan A2)^2 + A3^2}$
C4	Distance $PN2$ between rolling axis and roller axis in perpendicular to roller axis, mm	$\text{sqrt}((c1 * \sin(a2)) ^ 2 \text{ 6p} + (a3) ^ 2 \text{ 6p})$	$C4 = \sqrt{(C1 \sin A2)^2 + A3^2}$
C5	Rolling angle $\delta 2$ , deg	$\text{acos}(c4 / c3)$	$\cos C5 = \frac{C4}{C3}$
C6	Feed angle $\beta 2$ , deg	$\text{atan}(a3 * \tan(a2) / c3)$	$\tan C6 = \frac{A3 \tan A2}{C3}$
C7	Roller radius $R2$ , mm	$\cos(c5) * (c3 - x6)$	$C7 = \cos C5 (C3 - X6)$
C8	Distance $XR2$ from roller cross section center to roller center of technological squeeze, mm	$c2 - c7 * \tan(c5)$	$C8 = C2 - C7 \tan C5$
C9	Distance $XR2$ from roller cross section center to roller center of technological squeeze, mm	$c8 - a6$	$C9 = C8 - A6$



geometrical squeezes along the rolling axis (parameter  $A5$ ) is determined to obtain segment  $OG$ . An auxiliary line is drawn from the point  $O$ , perpendicular to segment  $OG$ . Along this line, the rod radius in the squeeze  $r_p$  and the roller radius in the squeeze  $R_p$  are consecutively plotted (parameters  $X4$  and  $X3$ , respectively) to obtain the point  $C$ . The segment  $CG_B$  ( $A4$ ) coincides with the roller axis. Perpendiculars from segment  $OG$  are used to construct the feed angle  $\beta$  (parameter  $X1$ ). Another auxiliary line is drawn from the top of angle  $\beta$ , parallel to segment  $OC$ . Point  $G_B$  is obtained by intersecting this auxiliary line with the perpendicular. The eccentricate  $E$  (parameter  $A3$ ) is plotted from point  $G$  to intersect the auxiliary line. The construction of the other virtual squeezes follows a similar procedure.

Figures 4–6 depict the parametric models of constructed roller-body assemblies for various mill dimensions.

These models can be used to simulate the deformation zone and design roller parts for three-roller mini-mills. The developed parametric model is suitable for three-roller mills with rolling angles of working rollers  $\delta$  ranging from 5 to 15° and feed angles  $\delta$  ranging from 18 to 22°.

Notable features of these models include fast construction and reconstruction of roller joints using parametrization. By employing universal modular joints between individual parameters of each model and mini-mill units, the design time for mills can be significantly reduced.



Fig. 2. Adaptive scheme of relative position of the axes of roll and rolling ( $\beta = 20^\circ$ ,  $\delta = 5^\circ$ )

Рис. 2. Адаптивная схема взаимного положения осей валка и прокатки ( $\beta = 20^\circ$ ,  $\delta = 5^\circ$ )

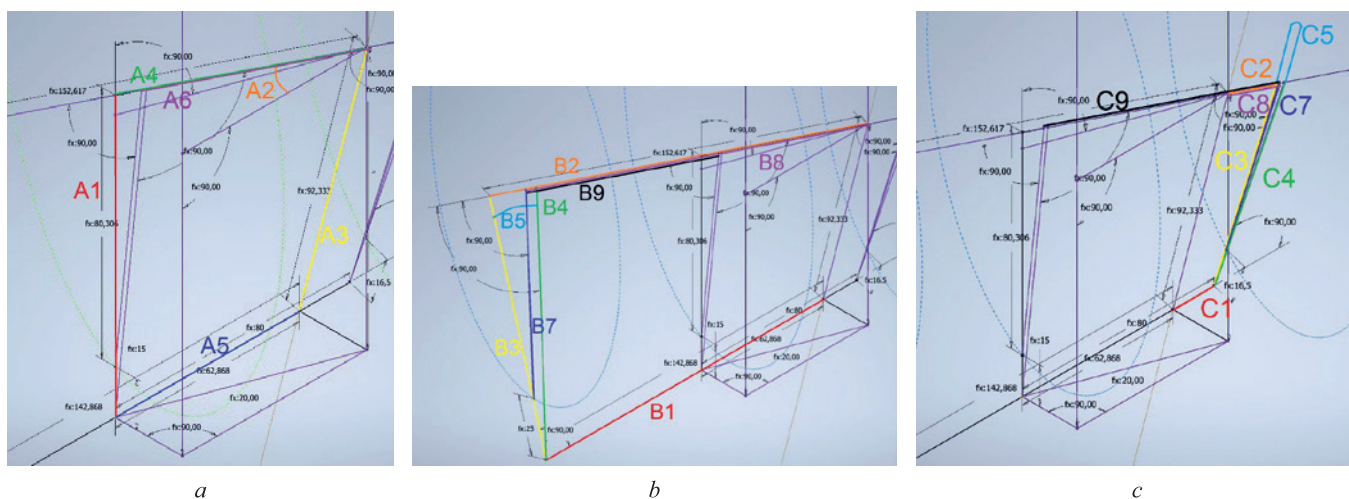


Fig. 3. Parameters used to construct geometric sections:  $A$  (a),  $B$  (b),  $C$  (c)

Рис. 3. Параметры, используемые для построения геометрических пережимов:  $A$  (a);  $B$  (b);  $C$  (c)

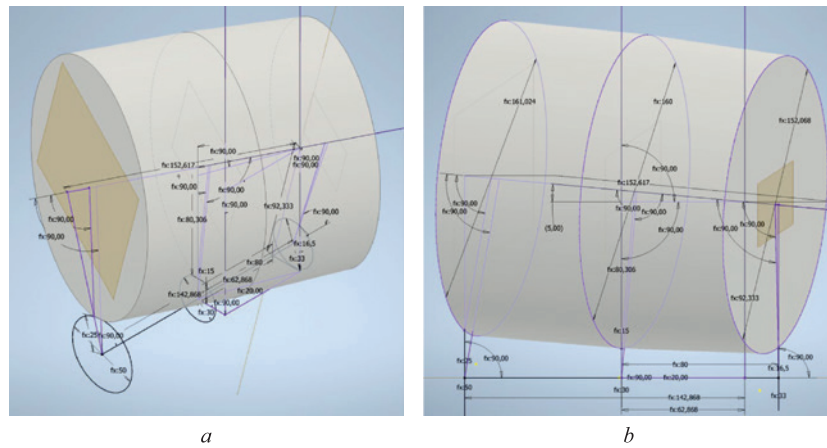


Fig. 4. Adaptive model of the constructed roll-barrel 30-70 with a rolling angle  $\delta = 5^\circ$ : axonometry (a); side view (b)

Рис. 4. Адаптивная модель построенного валька-бочки типоразмера «30-70» с углом раскатки  $\delta = 5^\circ$ : аксонометрия (a); вид сбоку (b)

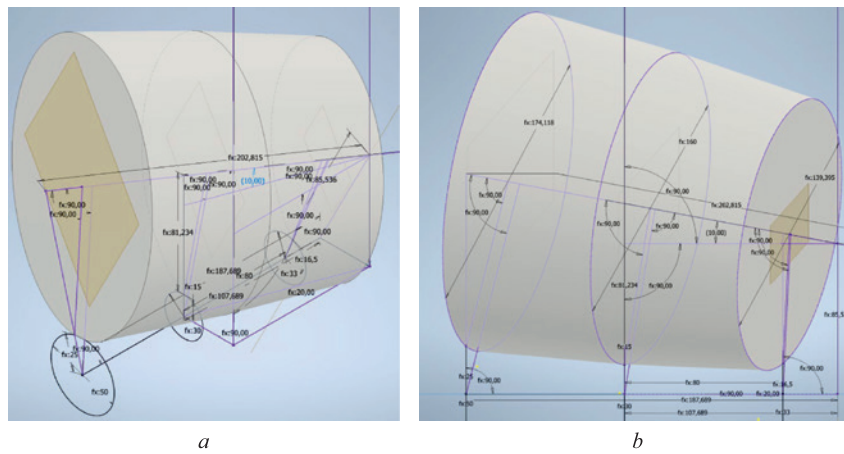


Fig. 5. Adaptive model of the constructed roll-barrel 30-70 with a rolling angle  $\delta = 10^\circ$ : axonometry (a); side view (b)

Рис. 5. Адаптивная модель построенного валька-бочки типоразмера «30-70» с углом раскатки  $\delta = 10^\circ$ : аксонометрия (a); вид сбоку (b)

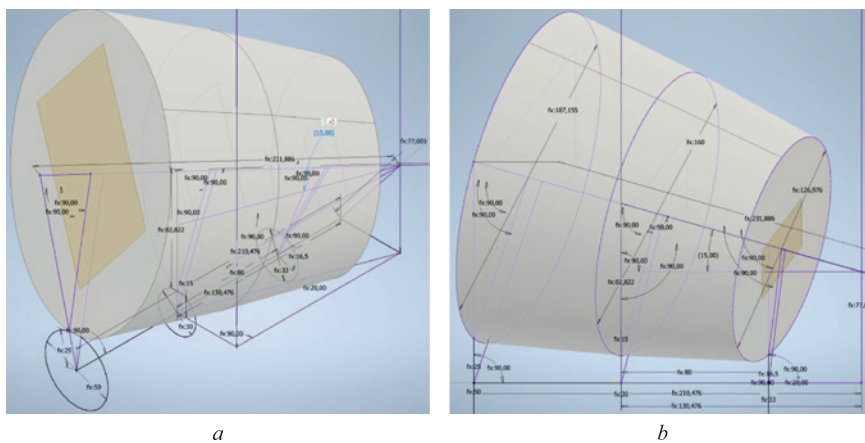


Fig. 6. Adaptive model of the constructed roll-barrel 30-70 with a rolling angle  $\delta = 15^\circ$ : axonometry (a); side view (b)

Рис. 6. Адаптивная модель построенного валька-бочки типоразмера «30-70» с углом раскатки  $\delta = 15^\circ$ : аксонометрия (a); вид сбоку (b)

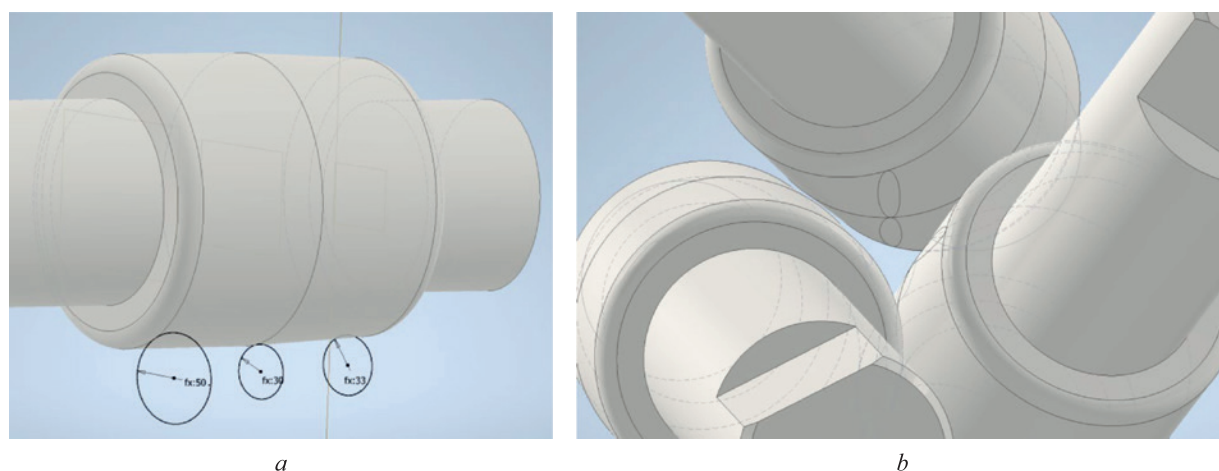


Fig. 7. Constructed parametric model of deformation focus: roll joint constructed by parametrization method (a); deformation focus obtained by an array of circular elements (b)

Рис. 7. Параметрическая модель очага деформации: валковое соединение, построенное с помощью метода параметризации (a); очаг деформации, полученный массивом круговых элементов (b)

Additionally, the constructed model ensures the production of high-quality items based on the specified initial model parameters ( $X$ ).

Fig. 7 illustrates the deformation zone consisting of three rollers. The deformation zone can be obtained by utilizing a circular array or creating an assembly by positioning the rollers around the sketch at a  $120^\circ$  angle, in accordance with the preset rolling and feed angles.

The parametrization method greatly facilitates the design process of roller joints and rolling mills, reducing the manual effort required for adjusting parts and angle ratios.

## CONCLUSIONS

By applying a parameterizable design algorithm, engineers can efficiently develop a computer model. Specifically, the method for plotting the deformation zone, based on the radii of the rolled ingot, roller, feed angle, and rolling angle, enables the rapid creation of a 3D model for roller calibration and the deformation zone. This model serves as a foundation for selecting other structural units of the mill.

The algorithm for designing the deformation zone was developed as a function of adjustable parameters, which are utilized for parametrization within a CAD system. The algorithm is based on the concept of virtual squeezes, which leverage the invariant relationships of RSR roller geometry in relation to the desired parameters of the technological squeeze. These parameters include the diameters of the roller and rod, as well as the feed and rolling angles along the rolling axis and/or roller axis. In the development of the computer model for the roll joint of the “30-70” mill, an explicit reference simulation methodology was employed, incorporating parameterizable properties that

can be varied based on the mill’s objectives and specific design requirements. The resulting model is adaptive, allowing for the easy determination of dimensions and spatial positions of rollers and the deformation zone in the mini-mill.

Further research efforts will focus on the development of an adaptive parametric model, encompassing the assembly of component units such as the shaft and body of working roller, bearing supports, pads, screw-down mechanism, and stands.

## REFERENCES / СПИСОК ЛИТЕРАТУРЫ

- Galkin S.P., Gamin Yu.V., Aleshchenko A.S., Romanov B.A. Modern development of elements of radial shift rolling theory, technology, and mini-rolling. *Chernye metally*. 2021;(12). (In Russ.).  
<https://doi.org/10.17580/chm.2021.12.09>  
Галкин С.П., Гамин Ю.В., Алешченко А.С., Романцев Б.А. Современное развитие элементов теории, технологии и мини-станов радиально-сдвиговой прокатки. *Черные металлы*. 2021;(12).  
<https://doi.org/10.17580/chm.2021.12.09>
- Galkin S.P. Radial shear rolling as an optimal technology for lean production. *Steel in Translation*. 2014;44(1):61–64.  
<https://doi.org/10.3103/S0967091214010069>  
Галкин С.П. Технология и мини-станы радиально-сдвиговой прокатки – оптимальная техника для создания бережливого производства. *Сталь*. 2014;(1):39–42.
- Naizabekov A., Lezhnev S., Arbuz A., Panin E., Koinov T. Simulation of radial-shear rolling of austenitic stainless steel AISI-321. *Journal of Chemical Technology and Metallurgy*. 2019;54(5):1086–1094.
- Arbuz A., Kawalek A., Ozhmegov K., Panin E., Magzhanov M., Lutchenko N., Yurchenko V. Obtaining an equiaxed ultrafine-grained state of the longlength bulk zirconium alloy bars by extralarge shear deformations with a vortex metal



- flow. *Materials*. 2023;16(3):1062.  
<https://doi.org/10.3390/ma16031062>
5. Mashekov S., Smailova G., Alshynova A., Uderbayeva A., Sembaev N., Zhaulyt A. Structure formation of aluminum alloy D16 while rolling bars in the radial shear mill. *Metallurgiya*. 2020;59(2):195–198.
  6. Diez M., Kim H.-E., Serebryany V., Dobatkin S., Estrin Y. Improving the mechanical properties of pure magnesium by three-roll planetary milling. *Materials Science and Engineering: A*. 2014;612:287–292.  
<https://doi.org/10.1016/j.msea.2014.06.061>
  7. Naizabekov A., Lezhnev S., Panin E. Formation of a gradient structure in austenitic stainless steel AISI 321 by radial-shear rolling. *Solid State Phenomena*. 2021;316:246–251.  
<https://doi.org/10.4028/www.scientific.net/ssp.316.246>
  8. Negodin D.A., Galkin S.P., Kharitonov E.A., Karpov B.V., Khar'kovskii D.N., Dubovitskaya I.A., Patrino P.V. Testing of radial-shear rolling technology and pre-project selection of mini rolling mills for flexible production of titanium rods of small cross sections in conditions of JSC “CMP”. *Metallurg*. 2018;(11):40–46. (In Russ.).  
Негодин Д.А., Галкин С.П., Харитонов Е.А., Карпов Б.В., Харьковский Д.Н., Дубовицкая И.А., Патрин П.В. Тестирование технологии радиально-сдвиговой прокатки и предпроектный выбор мини-станов для гибкого производства титановых прутков малых сечений в условиях АО ЧМЗ. *Металлург*. 2018;(11):40–46.
  9. Mishin I., Naydenkin E., Ratochka I., Lykova O., Vinokurov V., Manisheva A. Effect of radial shear rolling and aging on the structure and mechanical properties of titanium alloy VT35. *AIP Conference Proceedings*. 2020;2310(1):020206.  
<https://doi.org/10.1063/5.0034081>
  10. Shatalov R., Medvedev V., Bogdanov S. Development and use of an electromagnetic unit for controlling the mechanical properties along the steel vessel height at the exit from a rolling-pressing line. *Russian Metallurgy (Metally)*. 2022;2022(6):628–633.  
<https://doi.org/10.1134/S0036029522060210>
  11. Shatalov R., Medvedev V. Effect of deformed workpiece temperature inhomogeneity on mechanical properties of thin-walled steel vessels during treatment in a rolling and pressing line. *Metallurgist*. 2019;63(1–2):176–182.  
<https://doi.org/10.1007/s11015-019-00807-w>
  12. Stefanik A., Szota P., Mróz S. Analysis of the effect of rolling speed on the capability to produce bimodal-structure AZ31 alloy bars in the three-high skew rolling mill. *Archives of Metallurgy and Materials*. 2020;65(1):329–335.  
<https://doi.org/10.24425/amm.2020.131734>
  13. Galkin S.P., Fadeev V.A., Gusak A.Yu. Methodology of virtual squeezing for calculation of mini-mills of shear-radial (helical) rolling. *Proizvodstvo prokata*. 2016;(2):27–35. (In Russ.).  
Галкин С.П., Фадеев В.А., Гусак А.Ю. Методика виртуальных пережимов для расчета мини-станов радиально-сдвиговой (винтовой) прокатки. *Производство проката*. 2016;(2):27–35.
  14. Galkin S.P., Fadeev V.A., Gusak A.Yu. Comparative analysis of geometry of mini-mills of radial-shear (helical) rolling. *Proizvodstvo prokata*. 2015;(12):19–25. (In Russ.).  
Галкин С.П., Фадеев В.А., Гусак А.Ю. Сопоставительный анализ геометрии мини-станов радиально-сдвиговой (винтовой) прокатки. *Производство проката*. 2015;(12):19–25.
  15. Belevich A.V., Goncharuk A.V., Daeva E., Romantsev B.A. Study of technological and structural parameters of helical working stands with the help of modern finite element systems. *Izvestiya. Ferrous Metallurgy*. 2002;45(9):32–35.  
Белевич А.В., Гончарук А.В., Даева Е., Романцев Б.А. Исследование технологических и конструктивных параметров рабочих клетей винтовой прокатки с помощью современных конечно-элементных систем. *Известия вузов. Черная металлургия*. 2002;45(9):32–35.
  16. Company P., Naya F., Contero M., Camba D.J. On the role of geometric constraints to support design intent communication and model reusability. *Computer-Aided Design & Applications*. 2020;17(1):61–76.  
<https://doi.org/10.14733/cadaps.2020.61-76>
  17. Otey J., Company P., Contero M., Camba D.J. Revisiting the design intent concept in the context of mechanical CAD education. *Computer-Aided Design & Applications*. 2018;15(1):47–60.  
<https://doi.org/10.1080/16864360.2017.1353733>
  18. Bodein Y., Rose B., Caillaud E. Explicit reference modeling methodology in parametric CAD system. *Computers in Industry*. 2014;65(1):136–147.  
<https://doi.org/10.1016/j.compind.2013.08.004>
  19. Camba J.D., Contero M., Company P. Parametric CAD modeling: An analysis of strategies for design reusability. *Computer-Aided Design*. 2016;74:18–31.  
<https://doi.org/10.1016/j.cad.2016.01.003>
  20. Cheng Z., Ma Y. A functional feature modeling method. *Advanced Engineering Informatics*. 2017;33:1–15.  
<https://doi.org/10.1016/j.aei.2017.04.003>
  21. Aranburu A., Justel D., Contero M., Camba J.D. Geometric variability in parametric 3D models: Implications for engineering design. *Procedia CIRP*. 2022;109:383–388.  
<https://doi.org/10.1016/j.procir.2022.05.266>
  22. Amadori K., Tarkian M., Ölvander J., Krus P. Flexible and robust CAD models for design automation. *Advanced Engineering Informatics*. 2012;26(2):180–195.  
<https://doi.org/10.1016/j.aei.2012.01.004>
  23. Landers D.M., Khurana P. *Horizontally-structured CAD/CAM modeling for virtual concurrent product and process design*. Patent no. US6775581B2 USA. 10.08.2004.
  24. *Resilient Modeling Strategy*. 2018; URL: <https://www.resilientmodeling.net> (Дата обращения: 15.12.2022)
  25. Gebhard R. A resilient modeling strategy. *Solid Edge University 2013*. Siemens; 2013.
  26. Aranburu A., Cotillas J., Justel D., Contero D., Camba D.J. How does the modeling strategy influence design optimization and the automatic generation of parametric geometry variations? *Computer-Aided Design*. 2022;151:103364.  
<https://doi.org/10.1016/j.cad.2022.103364>
  27. Mironov Yu.M. Geometric parameters of skew rolling. *Proizvodstvo trub*. 1962;(6):37–46. (In Russ.).  
Миронов Ю.М. Геометрические параметры процесса косой прокатки. *Производство труб*. 1962;(6):37–46.
  28. Teterin P.K. *Theory of Cross Rolling*. Moscow: Metallurgiya; 1971:386. (In Russ.).  
Тетерин П.К. *Теория поперечно-винтовой прокатки*. Москва: Металлургия; 1971:386.



29. Budnikov A.S. *Improvement of tube rolling and sizing processes in three-roller helical rolling mills: Cand. Tech. Sci. Diss.* Moscow; 2020:147. (In Russ.).

Будников А.С. *Совершенствование процессов раскатки и калибрования труб в трехвалковых станах винтовой прокатки: Дисс. ... канд. техн. наук.* Москва: 2020:147.

## Information about the Authors

**Daniil V. Troitskii**, Postgraduate of the Chair “Metal Forming”, National University of Science and Technology “MISIS”

ORCID: 0009-0006-9930-5403

E-mail: d.v.troitskiy@gmail.com

**Yurii V. Gamin**, Cand. Sci. (Eng.), Assist. Prof. of the Chair “Metal Forming”, National University of Science and Technology “MISIS”

ORCID: 0000-0001-6654-4236

E-mail: y.gamin@mail.ru

**Sergei P. Galkin**, Dr. Sci. (Eng.), Prof. of the Chair “Metal Forming”, National University of Science and Technology “MISIS”

ORCID: 0000-0002-0853-3966

E-mail: glk-omd@yandex.ru

**Aleksei S. Budnikov**, Cand. Sci. (Eng.), Assist. Prof. of the Chair “Metal Forming”, National University of Science and Technology “MISIS”

ORCID: 0000-0002-2629-7741

E-mail: budnikov.as@sisis.ru

## Сведения об авторах

**Даниил Владимирович Троцкий**, аспирант кафедры «Обработка металлов давлением», Национальный исследовательский технологический университет «МИСИС»

ORCID: 0009-0006-9930-5403

E-mail: d.v.troitskiy@gmail.com

**Юрий Владимирович Гамин**, к.т.н., доцент кафедры «Обработка металлов давлением», Национальный исследовательский технологический университет «МИСИС»

ORCID: 0000-0001-6654-4236

E-mail: y.gamin@mail.ru

**Сергей Павлович Галкин**, д.т.н., профессор кафедры «Обработка металлов давлением», Национальный исследовательский технологический университет «МИСИС»

ORCID: 0000-0002-0853-3966

E-mail: glk-omd@yandex.ru

**Алексей Сергеевич Будников**, к.т.н., доцент кафедры «Обработка металлов давлением», Национальный исследовательский технологический университет «МИСИС»

ORCID: 0000-0002-2629-7741

E-mail: budnikov.as@sisis.ru

## Contribution of the Authors

**D. V. Troitskii** – writing the text, building three-dimensional adaptive models, preparation and design of the article.

**Yu. V. Gamin** – scientific guidance, formation of the idea of the work, setting research objectives, editing the text.

**S. P. Galkin** – scientific guidance, development of design and calculation methods, selection of methods for solving subproblems, editing and correcting the final version.

**A. S. Budnikov** – search and analysis of publications, collection and analysis of data, development of calculation of rolls permissible diameter, design of the article.

## Вклад авторов

**Д. В. Троцкий** – написание текста статьи, построение трехмерных адаптивных моделей, подготовка и оформление статьи.

**Ю. В. Гамин** – научное руководство, идея работы, постановка задач исследования, редактирование текста статьи.

**С. П. Галкин** – научное руководство, разработка методики проектирования и расчета, выбор методов решения подзадач, редактирование и корректировка финальной версии.

**А. С. Будников** – поиск и анализ публикаций, сбор и анализ данных, разработка расчета допустимого диаметра валков, оформление статьи.

Received 24.02.2023

Revised 07.03.2023

Accepted 11.04.2023

Поступила в редакцию 24.02.2023

После доработки 07.03.2023

Принята к публикации 11.04.2023

# НАУКОМЕТРИЧЕСКИЕ ПОКАЗАТЕЛИ ЖУРНАЛА

В 2017 году международная база данных Scopus возобновила индексирование журнала «Известия ВУЗов. Черная металлургия». На инфографике отражены текущие показатели.

Данные предоставлены сайтами <https://www.scopus.com>, <https://www.scimagojr.com> и <https://www.scival.com>



Над номером работали:

Л.И. Леонтьев, главный редактор

Е.В. Протопопов, заместитель главного редактора

Е.А. Ивани, заместитель главного редактора

Л.П. Бащенко, заместитель ответственного секретаря

Е.Ю. Потапова, заместитель главного редактора по развитию

О.А. Долицкая, научный редактор

Е.М. Запольская, ведущий редактор

А.О. Гашникова, ведущий редактор

В.В. Расенец, верстка, иллюстрации

Г.Ю. Острогорская, менеджер по работе с клиентами

---

Подписано в печать 25.06.2023. Формат 60×90 <sup>1</sup>/<sub>8</sub>. Бум. офсетная № 1.  
Печать цифровая. Усл. печ. л. 15,25. Заказ 17676. Цена свободная.

---

Отпечатано в типографии Издательского Дома МИСИС.  
119049, Москва, Ленинский пр-кт, д. 4, стр. 1.  
Тел./факс: (499) 236-76-17



Degree and depth of hardening under pendulum surface plastic deformation of carbon steel

Investigation of thermal mode of hot-rolling mill working rolls in order to improve the accuracy of calculating the thermal profile of their barrels' surface

Reserves for reducing energy consumption when rolling section bars on modern rolling mills

Structure formation of Np-30KhGSA alloy in wire and arc additive manufacturing

Electrospark deposition of metalloceramic Fe-Al/HfC coating on steel 1035

Effect of accelerated cooling after cross-helical rolling on formation of structure and low-temperature fracture toughness of low-carbon steel

Patterns of localized deformation at pre-fracture stage in carbon steel – stainless steel bimetal

Evolution of structural-phase state and properties of hypereutectoid steel rails at long-term operation

Wagner interaction coefficients of nitrogen with chromium and molybdenum in liquid nickel-based alloys


Using calcium-containing injection wire filled with electrolytic calcium in steel ladle treatment

Lead and zinc selective extraction from EAF dust while heating in resistance furnace with flowing argon

Structure and properties of steels for manufacture of core catcher vessel of nuclear reactor

A method for studying the frequency stability of materials during tests for multi-cycle fatigue of steel

Parametric model of a three-roll unit of radial-shear rolling mini-mill



**Зарегистрирован Федеральной службой  
по надзору в сфере связи, информационных  
технологий и массовых коммуникаций.  
Свидетельство о регистрации  
ПИ № ФС77-35456.**

**Подписной индекс 70383.**

